EMPIRICAL MODELING OF STRUCTURAL DISTORTIONS IN PEROVSKITE CERAMICS

by

Evan Connor Smith

A dissertation

submitted in partial fulfillment

of the requirements for the degree of

Doctor of Philosophy in Materials Science and Engineering

Boise State University

May 2020

BOISE STATE UNIVERSITY GRADUATE COLLEGE

DEFENSE COMMITTEE AND FINAL READING APPROVALS

of the dissertation submitted by

Evan Connor Smith

Dissertation Title: Empirical Modeling of Structural Distortions in Perovskite Ceramics

Date of Final Oral Examination: 21 April 2020

The following individuals read and discussed the dissertation submitted by student Evan Connor Smith, and they evaluated their presentation and response to questions during the final oral examination. They found that the student passed the final oral examination.

Rick Ubic, Ph.D.	Chair, Supervisory Committee
Lan Li, Ph.D.	Member, Supervisory Committee
Dmitri Tenne, Ph.D.	Member, Supervisory Committee
Brendan Kennedy, Ph.D.	External Examiner

The final reading approval of the dissertation was granted by Rick Ubic, Ph.D., Chair of the Supervisory Committee. The dissertation was approved by the Graduate College.

DEDICATION

I would like to dedicate this work to all my family and friends that have helped me along the way.

ACKNOWLEDGMENTS

I would like to thank my advisor, Prof. Rick Ubic, for his invaluable help and guidance with this work. It has been a privilege working with Prof. Ubic as a research assistant, editorial assistant, and teaching assistant over the past four years. I couldn't ask for a more supportive and helpful research advisor. It has also been a pleasure working with the rest of my committee members, Profs. Lan Li, Dmitri Tenne, and Brendan Kennedy over the last couple of years. I am also grateful to Dr. Karthik Chinnathambi of the Boise State Center for Materials Characterization (BSCMC) for his guidance and help with X-ray diffraction and transmission electron microscopy. I would also like to acknowledge my undergraduate research assistants, Claire Adams and Olivia Wander, for their dedication and hard work in the lab, which has undoubtedly contributed to the success of the work. Furthermore, I acknowledge that this work has been supported by the Micron School of Materials Science and Engineering at Boise State University.

ABSTRACT

Predictive models for composition-structure-property relationships are essential to realizing the full potential of electroceramic materials; however, the electroceramics industry has largely failed to invest in predictive models in favor of simple rules of thumb or expensive, time-consuming trial-and-error methods. Empirically derived predictive models have the potential to significantly improve and guide future research in a more cost-effective and timely manner. It may even be possible to predict some intrinsic properties (*e.g.*, polarization) on the order of a unit cell using only the charge and size of each chemical component. Scientists and researchers may ultimately be able to use these types of models to produce compositional recipes from desired property or structural data or conversely predict properties and structures from compositional data. Moreover, empirical models allow for the investigation and discovery of trends in properties and structures that would be practically unobservable via either expensive experimental or computationally demanding first-principles methods. The main focus of this work will be the use of empirical data to derive predictive models for ceramics with the perovskite crystal structure and thereby glean crystallochemical insights which explain them.

Chapter one lays the foundation for this work. A general overview of perovskites is provided and the seemingly endless degree of applications and properties that perovskite exhibit are explored including ferroelectricity, piezoelectricity, pyroelectricity, superconductivity, ionic conductivity, *etc*. It should be noted that the development of general correlative models which encompass all of these various properties and structural

effects would be well beyond the scope of this work. Instead, this work concentrates on developing models for the effects of layered A-site ordering, rock salt B-site ordering, trigonality, and oxygen vacancies on the perovskite structure. Additionally, previous empirical modeling efforts are introduced to lay the groundwork for the development of the correlative models within this work.

Chapter two examines the effect of layered A-site ordering on the perovskite structure. 15 compositions in the $[(Na_yLi_{1-y})_{(1-3x)/2}La_{(1+x)/2}]TiO_3$ (NLLT) system (y = 0.25, 0.5, and 0.75; x = 0, 0.0533, 0.1, 0.1733, and 0.225) were produced. Long-range ordering for $x \geq 0.1$ was observed via X-ray diffraction, while short-range ordering was shown to exist even for $x < 0.1$ via electron diffraction. Overall, the degree of ordering was observed to decrease as x increased. The A-site ordering parameter (η) and the resultant expansion (Δr_A) were each modeled for every y series of compositions in the NLLT system. Two general models were developed based on these system specific models, which allow for the prediction of η and Δr_A in layered A-site ordered perovskites with any arbitrary degree of ordering using only published ionic radii data.

Chapter three investigates the effects of 1:2 B-site ordering in the $BaMg_{1/3}Ta_{2/3}O_3$ (BMT) perovskite system. BMT is an ideal compound for the study B-site ordering because the degree of B-site ordering increases with increasing annealing time. Thus, BMT powders were synthesized and annealed incrementally from 0 to 40 hours at 1500°C. The resulting structures were increasingly ordered on the B-site, which also caused a trigonal distortion within the structure. An empirical model was developed which describes the degree of ordering in terms of the B-site shrinkage or the annealing time, which allows for the prediction of the ordering parameter (η) in BMT using only experimental input. This

work has major implications in that this modelling technique may be expanded to include other B-site ordered complex perovskites, which could allow for the prediction of the degree of ordering and resultant volume shrinkage in B-site ordered perovskites in general using only published ionic radii data or experimentally-derived pseudocubic lattice constants.

Chapter four analyzes the effects of 1:1 rock salt B-site ordering in general. Four compositions were synthesized in the $AZn_{0.5}Ti_{0.5}O_3$ system (A = Nd, Sm, $Nd_{0.5}La_{0.5}$, $Nd_{0.5}Gd_{0.5}$). Long-range 1:1 rock salt cation ordering on the B-site was shown to exist for all four compositions via X-ray diffraction. Additional data was mined from literature for another 38 rock salt B-site ordered perovskites. This data was sorted according to the B-site species and empirical models were developed which describe the B-site shrinkage (Δr_B) for each of these systems. From these system specific models, a general model was developed for rock salt B-site ordering, which allows for the prediction of Δr_B in rock salt B-site ordered perovskites using only published ionic radii data.

Chapter five focuses on the development of a general correlative model for perovskite trigonality. A data mining approach was employed to gather published structural data for trigonally distorted perovskites. These perovskites were sorted into specific systems, and empirical models were developed for the degree of trigonality for each of these systems, which can be expressed a function of the ratio of the pseudocubic lattice constant (a_{pc}) to the B-X bond length (r_{BX}). From these system specific models, general models were developed for trigonal perovskites with either $R3c$ or $R\bar{3}c$ symmetry which describe the degree of trigonality as a function of the modified tolerance factor.

Additionally, a general model was developed which allows for the prediction of the intrinsic polarization in *R*3*c* trigonal perovskites.

Chapter six describes the effects of oxygen vacancies in perovskite ceramics. Eight compositions in the $CaTi_{1-x}Fe_xO_{3-x/2}$ system (x = 0.05, 0.15, 0.20, 0.25, 0.30, 0.35, 0.40, and 0.45), and eleven compositions in the $SrTi_{1-x}Fe_xO_{3-x/2}$ system (x = 0, 0.025, 0.05, 0.10, 0.15, 0.20, 0.25, 0.30, 0.35, 0.40, and 0.45) were synthesized. A data mining approach was used to supplement this data with more oxygen vacant perovskite systems. Empirical models were developed for each of these oxygen-deficient systems which describe the effective oxygen vacancy size (r_V) and the bond deformation (D_B). In addition, a general model was developed for the modified tolerance factor, which allows for the prediction of the tolerance factor in oxygen vacant perovskites. In turn, this allows for the accurate prediction of the effective anion size (r_X) and pseudocubic lattice constant (a_{pc}) in oxygen vacant perovskites.

TABLE OF CONTENTS

DEDICATION iv

ACKNOWLEDGMENTS v

ABSTRACT vi

LIST OF TABLES xiii

LIST OF FIGURES xvi

LIST OF ABBREVIATIONS xx

CHAPTER ONE: INTRODUCTION 1

1.1 Perovskites in general 1

1.2 The Aristotypical Perovskite 1

1.3 The Hettotypical Perovskite 5

1.4 The Effect of Structural Distortions in Perovskites 7

1.4.1 Octahedral tilting 10

1.4.2 Cation Ordering 12

1.5 Predictive Modeling of Composition-Structure Relationships in Perovksites 15

1.5.1 Density Functional Theory 18

1.6 Aims and Objectives 18

1.7 References 19

CHAPTER TWO: EMPIRICAL MODELS FOR LAYERED A-SITE ORDERING IN PEROVSKITE TITANATES 25

2.1 Introduction 26

2.2 Materials and Methods....31

2.3 Results and Discussion....33

2.4 Conclusion....49

2.5 References....50

CHAPTER THREE: AN EMPIRICAL MODEL FOR B-SITE CATION ORDERING IN $Ba(Mg_{1/3}Ta_{2/3})O_3$....55

3.1 Introduction....56

3.2 Materials and Methods....61

3.3 Results and Discussion....62

3.4 Conclusion....70

3.5 References....71

CHAPTER FOUR: CORRELATIVE MODELS FOR PEROVSKITES WITH ROCK SALT B-SITE ORDERING....74

4.1 Introduction....75

4.2 Materials and Methods....80

4.3 Results and Discussion....81

4.4 Conclusion....95

4.5 References....97

CHAPTER FIVE: EMPIRICAL MODELS OF TRIGONAL DISTORTIONS AND POLARIZATION IN PEROVSKITES....102

5.1 Introduction....103

5.2 Materials and Methods....105

5.3 Results and Discussion....106

5.4 Conclusion....132

5.5 References....133

CHAPTER SIX: CORRELATIVE MODELS FOR OXGYEN VACANCIES IN PEROVSKITES 136

6.1 Introduction 137

6.2 Materials and Methods 141

6.3 Results and Discussion 142

6.4 Conclusions 168

6.5 References 169

CHAPTER SEVEN: CONCLUSIONS AND FUTURE WORK 173

7.1 Concluding Remarks 173

7.2 Future Work 177

7.2.1 Extend empirical model for A-site vacancies to perovskites with r_A < 1.34 Å (Ca^{2+}) 177

7.2.2 Extend all models with thermal variations 177

7.2.3 Develop an empirical model for simultaneous A- and B-site ordering 177

7.2.4 Develop a correlative model for simultaneous vacancies on both A and X 178

7.2.5 Extend B-site ordering model to include 1:2 and 1:3 B-site ordered perovskites 178

LIST OF TABLES

Table 1.1 Centrosymmetric and non-centrosymmetric point groups showing polar and non-polar point groups. 9

Table 2.1 $(Na_{0.25}Li_{0.75})_{(1-3x)/2}La_{(1+x)/2}TiO_3$ experimental and calculated pseudocubic lattice constants (Å) 40

Table 2.2 $(Na_{0.5}Li_{0.5})_{(1-3x)/2}La_{(1+x)/2}TiO_3$ experimental and pseudocubic lattice constants (Å) 40

Table 2.3 $(Na_{0.75}Li_{0.25})_{(1-3x)/2}La_{(1+x)/2}TiO_3$ experimental and calculated pseudocubic lattice constants (Å) 41

Table 2.4 $(Na_{0.25}Li_{0.75})_{(1-3x)/2}La_{(1+x)/2}TiO_3$ accounting for cation effective sizes (Å). 42

Table 2.5 $(Na_{0.5}Li_{0.5})_{(1-3x)/2}La_{(1+x)/2}TiO_3$ accounting for cation effective sizes (Å) ... 42

Table 2.6 $(Na_{0.75}Li_{0.25})_{(1-3x)/2}La_{(1+x)/2}TiO_3$ accounting for cation effective sizes (Å). 42

Table 2.7 Coefficients of Eq. 2.1 and the goodness of fit, R^2 46

Table 2.8 Coefficients of Eq. 2.2 and the goodness of fit, R^2 47

Table 3.1 B-site ordered compounds using ideal B-site sizes (Å). 65

Table 3.2 B-site ordered compounds accounting for cation effective sizes (Å). 65

Table 3.3 X-ray powder Rietveld refinement results for $Ba(Mg_{1/3}Ta_{2/3})O_3$ in space group $\boldsymbol{P\bar{3}m1}$ 66

Table 3.4 Crystallographic comparison of disordered and ordered forms of BMT.. 67

Table 4.1 Refinement Results for Zinc Titanates 84

Table 4.2 Experimental and calculated pseudocubic lattice constants (Å) for 42 rock salt B-site ordered perovskites. 86

87

Table 4.3 The 42 rock salt B-site ordered perovskites accounting for cation effective sizes (Å). 88

Table 4.4 Coefficients of Eq. 4.1 and the goodness of fit, R^2 91

Table 4.5 Coefficients of Eq. 4.2 and the goodness of fit, R^2. 93

Table 5.1 The 57 $\boldsymbol{R\bar{3}c}$ trigonal compositions used to derive the general trigonal model for $\boldsymbol{c/a<\sqrt{6}}$ (Fig. 5.1). 108

Table 5.2 Experimental and calculated trigonal lattice constants from Eqs. 5.4, 5.5, & 5.7 for the 57 $\boldsymbol{R\bar{3}c}$ trigonal compositions. 111

Table 5.3 Coefficients of Eq. 5.1 115

Table 5.4 Coefficients of Eq. 5.2 117

Table 5.5 The 31 *R*3*c* trigonal perovskites used to derive the general trigonal model for $\boldsymbol{c/a>\sqrt{6}}$ (Fig. 5.4). 121

Table 5.6 Experimental and calculated trigonal lattice constants from Eqs. 5.6-5.7 for the 31 *R*3*c* trigonal compositions. 122

Table 5.7 Room-temperature polarizations of 31 trigonal perovskites in space group *R*3*c*. 127

Table 5.8 Coefficients of Eq. 5.8. 130

Table 5.9 Coefficients of Eq. 5.9. 131

Table 6.1 $CaTi_{1-x}Fe_xO_{3-x/2}$ refinement results 146

Table 6.2 $SrTi_{1-x}Fe_xO_{3-x/2}$ refinement results 146

Table 6.3 Coefficients and goodness of fit for the linear trends in figure 6.4 149

Table 6.4 Experimental and predicted t' and r_X for $CaTi_{1-x}Fe_xO_{3-x/2}$. 156

Table 6.5 Experimental and predicted pseudocubic lattice constants for $CaTi_{1-x}Fe_xO_{3-x/2}$. 156

Table 6.6 Experimental and predicted t' and r_X for $SrTi_{1-x}Fe_xO_{3-x/2}$. 157

Table 6.7 Experimental and predicted pseudocubic lattice constants for $SrTi_{1-x}Fe_xO_{3-x/2}$. 158

Table 6.8 Experimental and predicted t' and r_X for $NaNb_{1-x}Ti_xO_{3-x/2}$. 158

Table 6.9 Experimental and predicted pseudocubic lattice constants for $NaNb_{1-x}Ti_xO_{3-x/2}$. 159

Table 6.10 Experimental and predicted t' and r_X for $BaCe_{1-x}Y_xO_{3-x/2}$..... 159

Table 6.11 Experimental and predicted pseudocubic lattice constants for $BaCe_{1-x}Y_xO_{3-x/2}$. 160

Table 6.12 Experimental and predicted t' and r_X for $BaSn_{1-x}Y_xO_{3-x/2}$..... 160

Table 6.13 Experimental and predicted pseudocubic lattice constants for $BaSn_{1-x}Y_xO_{3-x/2}$. 161

Table 6.14 Experimental and predicted t' and r_X for $BaZr_{1-x}Dy_xO_{3-x/2}$. 161

Table 6.15 Experimental and predicted pseudocubic lattice constants for $BaZr_{1-x}Dy_xO_{3-x/2}$..... 162

Table 6.16 Experimental and predicted t' and r_X for $(La_{1-x}Sr_x)(Ga_{1-y}Mg_y)O_{3-(x+y)/2}$.. 162

Table 6.17 Experimental and predicted pseudocubic lattice constants for $(La_{1-x}Sr_x)(Ga_{1-y}Mg_y)O_{3-(x+y)/2}$. 163

Table 6.18 Experimental and predicted anion sizes and pseudocubic lattice constants for the lanthanum ferrites with charge compensation via oxygen vacancies alone. 166

Table 6.19 Experimental and predicted anion sizes and pseudocubic lattice constants for the lanthanum ferrites with charge compensation via Fe^{3+} oxidation alone. 166

Table 6.20 Experimental and predicted anion size and pseudocubic lattice constant for the four lanthanum ferrites with the errors optimized using both oxygen vacancies and Fe^{4+} as charge compensating mechanisms. 167

LIST OF FIGURES

Figure 1.1 The ideal cubic perovskite structure ($\boldsymbol{Pm\bar{3}m}$), where the X anions are at the face centers of the unit cell, the B cation is at the body center of the unit cell, and the A cations are at the corners of the unit cell. The pseudocubic lattice constants $\boldsymbol{a}'_{\mathbf{pc}}$ and $\boldsymbol{a}''_{\mathbf{pc}}$ are shown by the green and blue arrows, respectively. 2

Figure 1.2 Coordination polyhedra for the XII-fold coordinated A cation (left), the VI-fold coordinated B cation (middle), and the II-fold coordinated X anion (right). 2

Figure 1.3 Four common pseudocubic to hettotype relationships. Relationships between the (a) orthorhombic, (b) tetragonal, (c) and rhombohedral unit cells to the pseudocubic unit cell. (d) Relationship between the rhombohedral and hexagonal unit cells. 7

Figure 1.4 Functional relationships for electroceramics. All ferroelectrics are dielectrics, but not all dielectrics are necessarily ferroelectrics. 10

Figure 1.5 Illustrations of octahedral tilting. (a) Untilted structure, $a^0a^0a^0$; (b) In-phase octahedral tilting, $a^+a^+a^+$; (c) Antiphase octahedral tilting, $a^-a^-a^-$. . 11

Figure 1.6 The group-subgroup relationships for all 15 perovskite tilt systems and their associated space groups. Second-order transitions are indicated by the solid lines and first-order transitions are indicated by the dashed lines. 12

Figure 1.7 Doubled perovskite unit cells showing layered A-site ordering (left) and rock salt B-site ordering (right). The ordering planes are shown in both cells. 13

Figure 1.8 (a) Cubic and (b), (c) monoclinically distorted rock salt B-site ordered perovskite structures showing all 4 ordering planes in each case. The anions are not shown in (a). 14

Figure 1.9 Perovskite unit cell showing an (001) plane. The A-X bonds that lie within this plane are shown. 15

Figure 2.1 X-ray diffraction of $(Na_{0.25}Li_{0.75})_{(1-3x)/2}La_{(1+x)/2}TiO_3$ for $0 \leq x \leq 0.225$. Peaks resulting from long-range A-site cation ordering are marked with a *..... 35

Figure 2.2 X-ray diffraction of $(Na_{0.5}Li_{0.5})_{(1-3x)/2}La_{(1+x)/2}TiO_3$ for $0 \leq x \leq 0.225$. Peaks resulting from long-range A-site cation ordering are marked with a *..... 36

Figure 2.3 X-ray diffraction of $(Na_{0.75}Li_{0.25})_{(1-3x)/2}La_{(1+x)/2}TiO_3$ for $0 \leq x \leq 0.225$. Peaks resulting from long-range A-site cation ordering are marked with a *..... 37

Figure 2.4 Selected area diffraction patterns for the x = 0, 0.0533, and 0.225 compositions in the $(Na_{0.5}Li_{0.5})_{(1-3x)/2}La_{(1+x)/2}TiO_3$ system with the associated pseudocubic indexing. Some α, β, and γ superlattice reflections are labeled. 43

Fig. 2.5 A-site size adjustment factors as functions of composition from experimentally collected data for $(Na_yLi_{1-y})_{(1-3x)/2}La_{(1+x)/2}TiO_3$ and A-site order parameter, η, as a function of composition. The y = 0 data are from Ref. [7]. 45

Figure 2.6 A-site order parameters as functions of Δr_A from experimentally collected data for $(Na_yLi_{1-y})_{(1-3x)/2}La_{(1+x)/2}TiO_3$. The y = 0 data are from Ref. [7]. ... 46

Figure 2.7 Coefficients of Eq. 2.1 (left) and Eq. 2.2 (right) as functions of A-site size, $r_{A(id)x=0}$. 47

Figure 2.8 $(Na_yLi_{1-y})_{(1-3x)/2}La_{(1+x)/2}TiO_3$ Δr_A values calculated from the data in Ref. [30] (squares) plotted against the results of Eq. 2.1 (circles) for x = 0 (top) and x = 0.2 (bottom). 49

Figure 3.1 Q and dielectric constant (ε_r) values vs. annealing time for $Ba(Mg_{1/3}Ta_{2/3})O_3$[1] 57

Figure 3.2 X-ray diffraction data of $Ba(Mg_{1/3}Ta_{2/3})O_3$ samples annealed for 0 – 40 hours. Peaks marked with a * result from long-range B-site cation ordering. 62

Figure 3.3 $Ba(Mg_{⅓}Ta_{⅔})O_3$ X-ray diffraction with annealing times of 0 and 40 hours. Peaks marked with a * result from long-range B-site cation ordering. The inset shows the trigonal distortion of the structure in the splitting of the 024_c peak into 226_t and 422_t peaks. 63

Figure 3.4 $Ba(Mg_{⅓}Ta_{⅔})O_3$ unit-cell volume (black curve) and order parameter (red curve) as a function of annealing time 68

Figure 3.5 $Ba(Mg_{1/3}Ta_{2/3})O_3$ order parameter (red curve) and B-site size adjustment (blue curve) as a function of annealing time. The inset shows the order parameter as a function of Δr_B and can be thought of as an empirical model for ordering (0 = disorder, 1 = fully ordered) 69

Figure 4.1 Rietveld plots of NLZT, NZT, SZT, and NGZT. The data points correspond to the observed intensities. Both refinement results and difference patterns are shown for each composition, and all peaks are indexed according to the pseudocubic unit cell. 82

Figure 4.2 Rietveld plots of NLZT, NZT, SZT, and NGZT in the range $15° \leq 2\theta \leq 28°$ showing the ½(111)pc peak fit. 83

Figure 4.3 B-site size adjustment factors as functions of the pseudocubic lattice constant (Eq. 1.19). 90

Figure 4.4 Coefficients of Eq. 4.1 as a function of charge (Z) and ionic radius of the smallest B-site species, $r_{B,small}$ 92

Figure 4.5 Coefficients of Eq. 4.1 as functions of one another. 93

Figure 4.6 Comparison of experimental a_{pc} values to a_{pc} calculated using Eq. 1.19. The triangles show a_{pc} before Δr_B has been applied and the circles show a_{pc} after Δr_B has been applied. The trend line represents a_{pc} (calc.) = a_{pc} (exptl.). 94

Figure 5.1 Linear fits describing c/a vs. $a_{pc(Exptl.)}/r_{BX(Exptl.)}$ for the (a) $\mathbf{La^{3+}_{1-x}A^{2+}_{x}Mn^{3+}_{1-x}Mn^{4+}_{x}O_3}$, $\mathbf{La^{3+}_{1-x}A^{1+}_{x}Mn^{3+}_{1-2x}Mn^{4+}_{2x}O_3}$, (b) $\mathbf{La^{3+}_{1-x}A^{2+}_{x}Fe^{3+}_{1-x}Fe^{4+}_{x}O_3}$, and (c) $\mathbf{La^{3+}_{1-x}A^{2+}_{x}Co^{3+}_{1-x}Co^{4+}_{x}O_3}$ systems. 114

Figure 5.2 Coefficients of Eq. 5.1 vs. tolerance factor[16]. 116

Figure 5.3 Linear correlation between the coefficients of Eq. 5.1. 117

Figure 5.4 Quadratic fit describing c/a vs. $a_{pc(Exptl.)}/r_{BX(Exptl.)}$ for the 31 $R3c$ trigonal perovskites 119

Figure 5.5 Predicted c/a values of trigonally distorted perovskites using Eqs. 5.4-5.6. 125

Figure 5.6 Predicted trigonal lattice constants of all 88 trigonally distorted perovskites. 126

Figure 5.7 Polarization of the 31 perovskites in space group $R3c$ of the form (a) $A^{1+}B^{5+}O_3$, (b) $A^{2+}B^{4+}O_3$, and (c) $A^{3+}B^{3+}O_3$ as a function of c/a. (d)

Calculated vs. experimental polarization values for all 31 *R*3*c* perovskites. All experimental data are from neutron diffraction. 129

Figure 5.8 Coefficients of Eq. 5.8 as functions of the charge difference between the A- and B-site cations, Δq. 130

Figure 5.9 Correlation between the coefficients of Eq. 5.9. 131

Figure 6.1 XRD patterns of $CaTi_{1-x}Fe_xO_{3-x/2}$ (x=0.05, 0.15, 0.20, 0.25, 0.30, 0.35, 0.40, and 0.45). All patterns are indexed according to the pseudocubic unit cell. 144

Figure 6.2 XRD patterns of $SrTi_{1-x}Fe_xO_{3-x/2}$ (x=0, 0.025, 0.05, 0.10, 0.15, 0.20, 0.25, 0.30, 0.35, 0.40, and 0.45). All patterns are indexed with cubic symmetry. 145

Figure 6.3 Non-ideality of the effective anion sizes (X-site) for all 50 oxygen-deficient perovksites in this work. 147

Figure 6.4 The size parameter, L, as a function of the composition, x. 149

Figure 6.5 The effective vacancy size, r_V, and bond deformation, D_B, as functions of the modified tolerance factor at x = 0. 150

Figure 6.6 The modified tolerance factor, t' (Eq. 1.9), as a function of the ideal Shannon[25] anion size, $r_{X(id)}$. 151

Figure 6.7 Coefficients of Eq. 6.8. 152

Figure 6.8 Correlation between the coefficients of Eq. 6.8. 152

Figure 6.9 Experimental pseudocubic lattice constants, $a_{pc(exptl.)}$, versus the predicted pseudocubic lattice constants, a_{pc} (Eq. 1.19), for all 5 $\mathbf{A^{2+}B^{4+}_{1-x}B^{3+}_{x}O_{3-x/2}}$ oxygen-deficient perovskite systems. 164

LIST OF ABBREVIATIONS

a_{pc}	Pseudocubic lattice constant calculated using unit-cell volume
a'	Pseudocubic lattice constant calculated using A-X bond length
a''	Pseudocubic lattice constant calculated using B-X bond length
t_0	Conventional Goldschmidt tolerance factor
t′	Tolerance factor calculated from an empirical model as a function of t_0
$[V_A]$	Concentration of cation vacancies on the A-site
$[V_O]$	Concentration of oxygen vacancies on the X-site

CHAPTER ONE: INTRODUCTION

1.1 Perovskites in general

Perovskites are growing increasingly important in modern electronic devices. In fact, perovskites are crucial in several multibillion dollar industries[1] primarily due to the fact that ceramics with the perovskite structure possess a wider range of properties than ceramics with almost any other crystal structure. For example, perovskites are known to exhibit ferroelectricity (*e.g.* $BaTiO_3$)[2], microwave resonance (e.g. $Ba(Zn_{1/3}Ta_{2/3})O_3$)[3], piezoelectricity (*e.g.* $PbZr_xTi_{1-x}O_3$)[4], magnetism (*e.g.* $BiCr_{1-x}Ga_xO_3$)[5], catalysis (*e.g.* $La_{1-x}K_xCo_{1-y}Fe_yO_3$)[6], photovoltaic properties (*e.g.* $CH_3NH_3PbI_3$)[7], electrical conduction (*e.g.* $LaCo_{0.5}Ni_{0.5}O_{3\pm\delta}$)[8], and many more useful electronic properties.

1.2 The Aristotypical Perovskite

The archetypal perovskite stoichiometry is ABX_3, but not all materials with ABX_3 stoichiometry are perovskites. For example, $MgTiO_3$ crystalizes in the ilmenite structure. Thus, there are more factors than just stoichiometry that determine whether a particular material is a perovskite or not.

The aristotypical perovskite exists in cubic space group $Pm\bar{3}m$ with A-site cations at each of the eight corners of the unit cell, B-site cations at the body center, and X-site anions at each of the six face centers, as can be seen in Fig. 1.1.

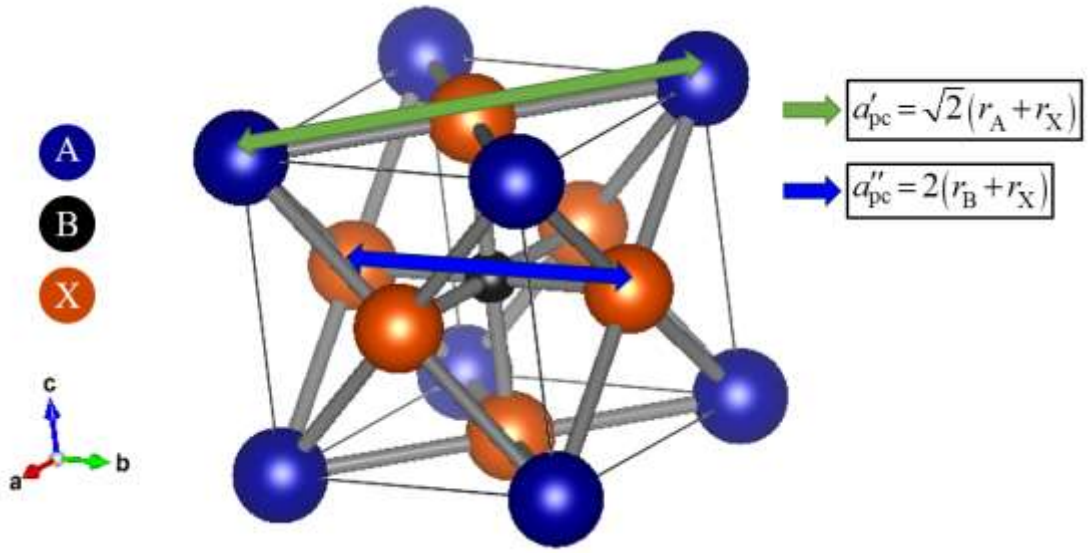

Figure 1.1 The ideal cubic perovskite structure ($Pm\bar{3}m$), where the X anions are at the face centers of the unit cell, the B cation is at the body center of the unit cell, and the A cations are at the corners of the unit cell. The pseudocubic lattice constants a'_{pc} and a''_{pc} are shown by the green and blue arrows, respectively.

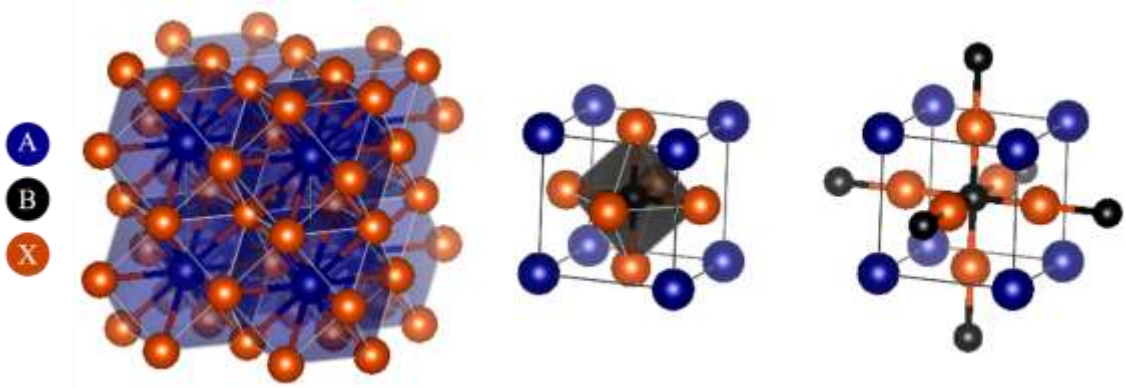

Figure 1.2 Coordination polyhedra for the XII-fold coordinated A cation (left), the VI-fold coordinated B cation (middle), and the II-fold coordinated X anion (right).

Additionally, Fig. 1.2 illustrates the different coordination environments for each species within the perovskite structure. The XII-coordinated A-site cations are within cuboctahedra, the VI-coordinated B-site cations are within octahedra, and each X-site anion is coordinated to two B-site cations resulting in II-fold coordination. A-site cations are second-nearest neighbors, about 41% further away.

Since most perovskites exist as hettotypes due to structural distortions, it is often useful to express the structure of the hettotypes in terms of the aristotype. Indeed, the following expression for the pseudocubic lattice constant, a_{pc}, is a useful technique for expressing non-cubic structures in terms of the cubic one:

$$a_{pc} = \left(\frac{V}{Z}\right)^{1/3} \tag{1.1}$$

where V is the unit-cell volume and Z is the number of formula units per unit cell. Moreover, the A-X bond length can be defined as follows:

$$r_{\text{A-X}} = \left(\frac{a_{\text{pc}}}{\sqrt{2}}\right) \tag{1.2}$$

and the B-X bond length can be defined as follows:

$$r_{\text{B-X}} = \left(\frac{a_{\text{pc}}}{2}\right) \tag{1.3}$$

where a_{pc} is the pseudocubic lattice constant; however, it is often convenient to express the pseudocubic lattice constant associated with the A-X bond length as a', and the pseudocubic lattice constant associated with the B-X bond length as a'', as defined in Fig. 1.1. Assuming a close-packed system of hard spheres with contact between both A and X as well as B and X, Eqs. 1.1 and 1.2 can now be redefined as:

$$a' = \sqrt{2}\left(r_{\text{A}} + r_{\text{B}}\right) \tag{1.4}$$

$$a'' = 2\left(r_{\text{B}} + r_{\text{X}}\right) \tag{1.5}$$

where r_{A}, r_{B}, and r_{X} are the effective ionic radii of each species in XII, VI, and II-fold coordination respectively.

Furthermore, Goldschmidt[9] developed the following relationship for the perovskite unit cell in 1926:

$$\left(r_A + r_X\right) = \alpha\sqrt{2}\left(r_B + r_X\right) \tag{1.6}$$

Eq. 1.6 can be rearranged using Eqs. 1.4 and 1.5 into what is commonly known as the Goldschmidt tolerance factor:

$$t_0 = \alpha = \frac{a'_{pc}}{a''_{pc}} = \frac{\left(r_A + r_X\right)}{\sqrt{2}\left(r_B + r_X\right)} \tag{1.7}$$

Tolerance factor is typically used as a measure of structural stability for perovskites. The most stable perovskites will exhibit a tolerance factor near unity. As t_0 decreases (*i.e.*, r_A becomes too small for regular cuboctahedral coordination), there is a driving force for octahedral tilting, which reduces the volume of cuboctahedra. At $t_0 < 0.985$ antiphase tilting of octahedra is generally observed, and when $t_0 < 0.965$ both in-phase and antiphase tilting are generally present.[10] If the A-site cation becomes too small (*e.g.* $t_0 < 0.8465$[11], then the structure becomes ilmenite (*e.g.* $MgTiO_3$). Although the conventional tolerance factor is a fairly reliable tool for predicting tilt transitions in perovskite structures, it cannot be used on its own because it does not account for chemical ordering or point defects such as vacancies.

Additionally, the concept of a bond-valence tolerance factor, t_{BV}, was developed by Lufaso and Woodward in 2001[12]. In particular, the bond-valence method is used to calculate the ionic radii which are used to determine t_{BV}. Although t_{BV} is a powerful tool for predicting perovskite stability, several of the drawbacks with using t_{BV} are that it does not account for some cation species, most polyatomic ions, nor extrinsic vacancies.

Another method for predicting perovskite stability was developed by Salinas-Sanchez[13] in 1992. Their method uses the differences between calculated and experimental bond valence sums to determine the likelihood that a perovskite structure will form. The resulting expression (Eq. 1.8) is referred to as the global instability index (GII). The GII also predicts the likelihood of octahedral tilting, and is defined as the following expression:

$$GII = \left[\left\{ \sum_{i=1}^{N} \left(d_i^2 \right) \right\} \Big/ N \right]^{1/2} \tag{1.8}$$

where d_i is the difference between the formal valence and calculated bond valence for the ith ion, and N is the number of ions in the unit cell. For untilted perovskites, the GII is usually < 0.1 v.u. (valence units); however, for tilted perovskites, the GII is usually < 0.2 v.u. Additionally, crystal structures are unstable when GII > 0.2 v.u.

1.3 The Hettotypical Perovskite

The vast majority of perovskites actually exist as hettotypes due to a variety of defects that cause slight structural deviations from the aristotype structure. These effects can arise due to differences in ionic sizes, differences in oxidation states, and/or cation or anion vacancies. Predicting lattice constants for these slightly distorted perovskites is becoming a more and more important issue for researchers in academia and industry alike. For instant, lattice matching parent materials with substrates used in the epitaxial growth of thin films or superlattices is incredibly important for appropriately bonding the film to the substrate without excessively straining the lattice of the deposited films[14-19]. Since there are currently no universal composition-structure models for predicting these lattice constants, large amounts of money and time are consumed trying to solve these structural problems.

The ability to detect minute distortions in the perovskite structure has increased dramatically over the last hundred years or so due to the significant improvement of characterization techniques and equipment. Of which, X-rays, electrons, and neutrons are currently the main types of diffraction sources for the characterization of perovskite materials. Basic structural data can readily be elucidated from X-ray diffraction data including lattice constants, cation positions, and phase purity (within ~ 1 at. wt.%); however, this technique is rather insensitive to most anions (*e.g.* oxygen). The resolution of X-ray diffraction data can further be improved by using synchrotron X-ray sources, which emit precisely controlled monochromatic X-rays, although the insensitivity to anions remains an issue. Additionally, important crystal symmetry and defect information can be determined by using electron diffraction, such as short-range ordering. Perhaps the most powerful characterization technique, neutron diffraction is sensitive cations positions, lattice constants, and phase purity similar to X-ray diffraction, yet it is also sensitive to anion positions and magnetic moments. It should also be noted that neutron scattering power varies randomly from one atomic species to another[20]. This means that neighboring elements on the periodic table may scatter neutrons in vastly different amounts; hence, those elements will be easily distinguishable from one another using neutron diffraction data[20]. Also, some heavier elements (*e.g.* W) scatter neutrons more weakly than lighter elements (*e.g.* H, C, O)[21]. Thus, even very small distortions in perovskite structures are easily discernable by using all three of these diffraction methods.

In total, there are 15 possible space groups for distorted perovskites encompassing six perovskite lattice systems[22-25], four of which are shown in Fig. 1.3. Additionally, Fig.

1.3 shows the relationship between the actual lattice parameters and the pseudocubic lattice parameters for each of these distortions.

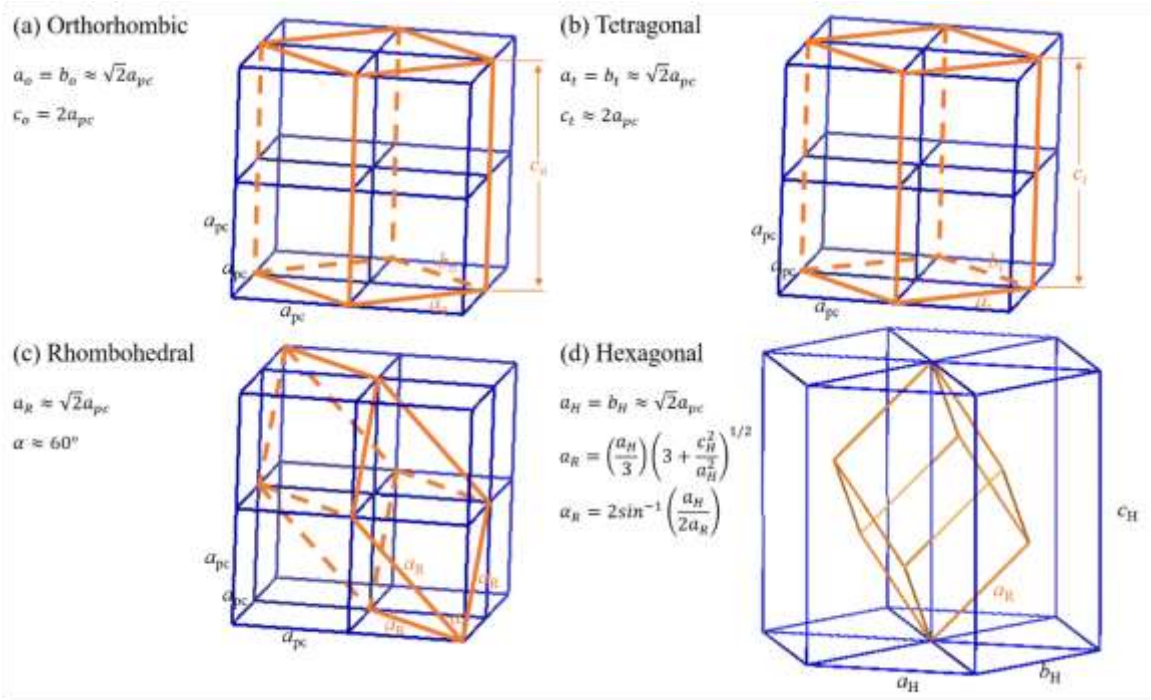

Figure 1.3 Four common pseudocubic to hettotype relationships. Relationships between the (a) orthorhombic, (b) tetragonal, (c) and rhombohedral unit cells to the pseudocubic unit cell. (d) Relationship between the rhombohedral and hexagonal unit cells.

1.4 The Effect of Structural Distortions in Perovskites

The vast majority of perovskites are distorted such that $t \neq 1$ (Eq. 1.7) and $a' \neq a''$ (Eqs. 1.4 and 1.5 respectively). Therefore, it is necessary to gain insight into how certain types of defects can impact these distortions and how they affect structure-composition relationships. It is rather simple to model properties in both bulk and nano scale materials that are undistorted, however modeling properties in distorted perovskites is significantly more challenging due to the complex ways in which certain defects tend to affect the structure. Predictive models based on empirical evidence for structures with defects have

the potential to significantly aid in the discovery of new electroceramic perovskites by reducing the amount of time and money required to discovery these materials.

The discovery of ferroelectrics was made by Joseph Valasek in the early 1920s in Rochelle salt (*e.g.* potassium sodium tartrate tetrahydrate $KNaC_4H_4O_6 \cdot 4H_2O$)[26]. Although he never referred to the effect as "ferroelectricity", his work in the area was groundbreaking nonetheless. Most notably, he was the first scientist to observe and report the Curie point, the reversible polarization, and the domain structure. Although Rochelle salt was the only known material at that time to exhibit these properties, he performed extensive research into this area and essentially fully characterized this phenomenon[27-30], which significantly helped to shape the future of the electroceramics industry. In fact, large amounts of time and money are still spent developing new ferroelectric ceramics for modern technological applications.

Table 1.1 lists the 32 crystallographic point groups, of which, 21 are non-centrosymmetric. All materials which possess non-centrosymmetric symmetry (except for cubic point group 432) will exhibit piezoelectricity, which is the phenomenon in which an applied mechanical strain induces a charge separation on the crystal faces. The reverse process can also occur, in which a mechanical strain is induced in the material by an applied electric field[31]. These two effects are widely used in the electroceramics industry for developing materials such as piezoelectric resonators used in electronic clocks and sonar equipment[32].

A subset of 10 of the 21 non-centrosymmetric point groups possess a unique axis of symmetry, which are defined as polar. These polar point groups are listed in table 1.1, and structures that fall into one of these point groups (*i.e.* polar structures) are referred to

as spontaneously polarized because their unit cells effectively have a dielectric polarization built into them. These spontaneously polarized structures are categorized generally as pyroelectrics because a change in temperature will cause a change in polarization within these structures. Sometimes the reverse process can happen in these structures and is referred to as the electrocaloric effect. Additionally, some of these pyroelectric materials possess the ability to change the direction of spontaneous polarization within the structure under an applied mechanical stress or electric field. If this effect occurs, the material is further classified as ferroelectric[31]. It is important to note that all ferroelectrics are pyroelectrics and piezoelectrics, but not all pyroelectrics and piezoelectrics are ferroelectrics.

Table 1.1 Centrosymmetric and non-centrosymmetric point groups showing polar and non-polar point groups.

Crystal system	Centrosymmetric	Non-centrosymmetric (non-polar)	Non-centrosymmetric (polar)
Triclinic	$\bar{1}$		1
Monoclinic	2/*m*		2, m
Orthorhombic	*mmm*	222	mm2
Tetragonal	4/*m*, 4/*mmm*	$\bar{4}$, 422, $\bar{4}2m$	4, 4mm
Trigonal	$\bar{3}$, $\bar{3}m$	32	3, 3m
Hexagonal	6/*m*, 6/*mmm*	$\bar{6}$, 622, $\bar{6}2m$	6, 6mm
Cubic	$m\bar{3}$, $m\bar{3}m$	23, 432, $\bar{4}3m$	

Fig. 1.4 shows the relationships between the different types of electroceramics. Defects can significantly affect these properties along with composition and structure. These defects cause small distortions to occur within the crystallographic structure, which can fundamentally alter these properties. For example, Ishihara *et al*.[33] found that slightly doping the A-site of $SrGa_{0.8}Mg_{0.2}O_{3-\delta}$ perovskites with rare earth cations effectively suppressed hole conduction without significantly reducing electrical conductivity.

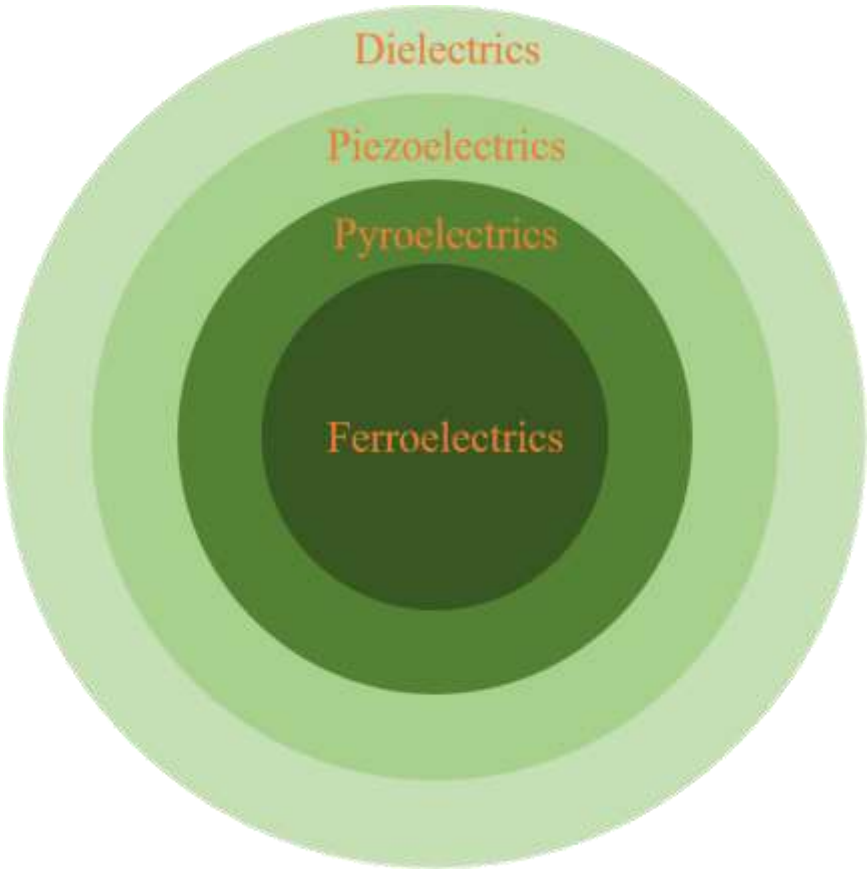

Figure 1.4 Functional relationships for electroceramics. All ferroelectrics are dielectrics, but not all dielectrics are necessarily ferroelectrics.

1.4.1 Octahedral tilting

Tilting of perovskite BO_6 octahedra along at least one pseudocubic axis is very common amongst perovskite distortions. In fact, it has been shown[10] that tilting typically occurs when $t < 0.985$. Glazer discovered[34] that there exists 23 possible octahedral tilt systems for perovskites. In fact, Glazer's notation for octahedral tilting has become the conventional method for describing tilting in perovskites, in which the three Cartesian axes are represented by *a*, *b*, and *c*; and each of the three axes is given a superscript denoting no tilting (0), in-phase octahedral tilting (+), and antiphase octahedral tilting (-) as shown in Fig. 1.5. The same symbol (*e.g. a*, *b*, or *c*) is used if the degree of tilting is the same along any two or three of the axes. Additionally, the tilting systems have been related to cation

ordering by Woodward *et al*.[35], and group theory has been used to show[22-25] that the total number of space groups for tilt systems can be reduced to 15 as shown in Fig. 1.6. Moreover, Carpenter *et al*. [36] have recently defined additional symmetry hierarchies for combinations of cooperative Jahn-Teller ordering and octahedral tilting in perovskites. Cooperative ordering and octahedral tilting may explain certain structural distortions associated with both A-site and B-site cation ordered perovskites.

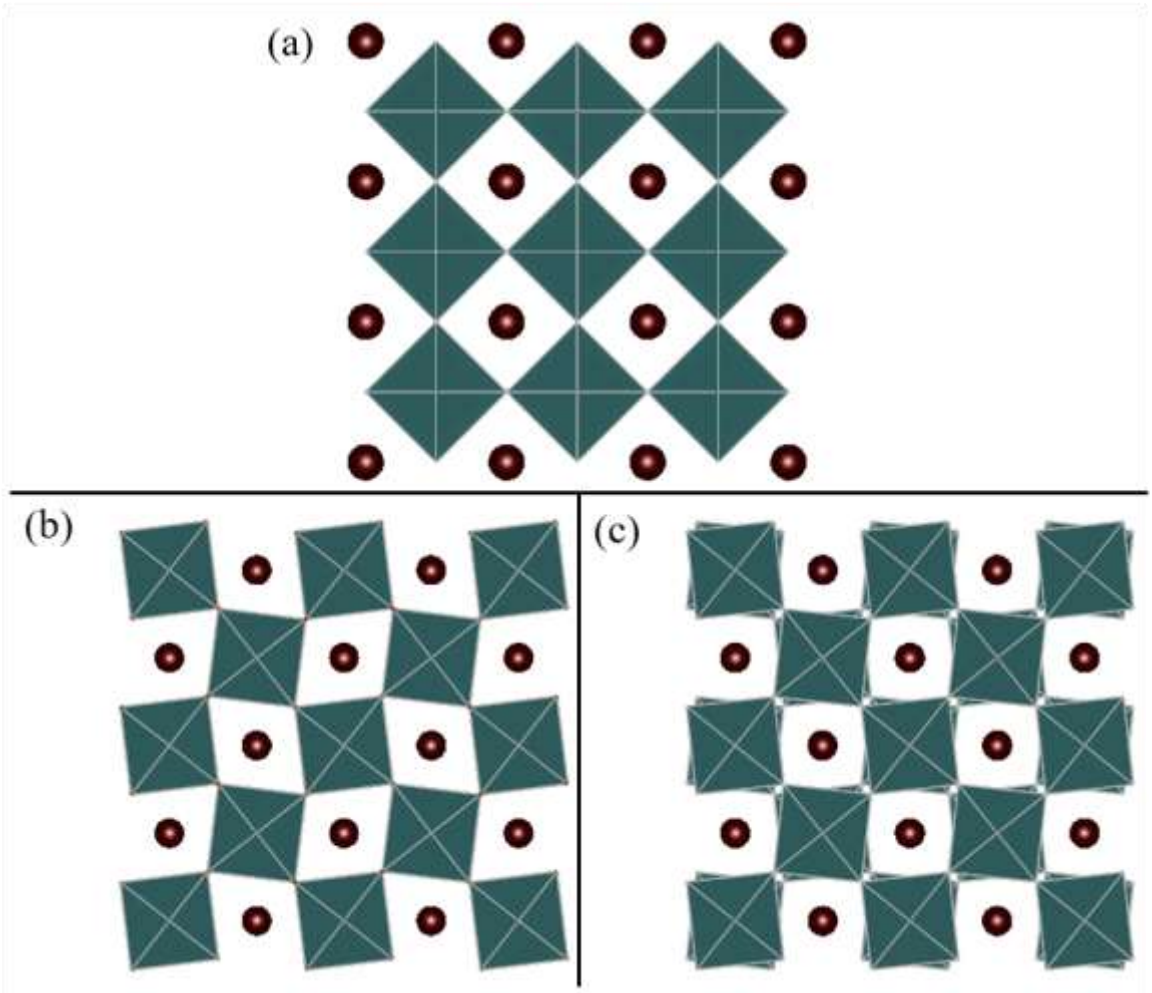

Figure 1.5 Illustrations of octahedral tilting. (a) Untilted structure, $a^0a^0a^0$; (b) In-phase octahedral tilting, $a^+a^+a^+$; (c) Antiphase octahedral tilting, $a^-a^-a^-$.

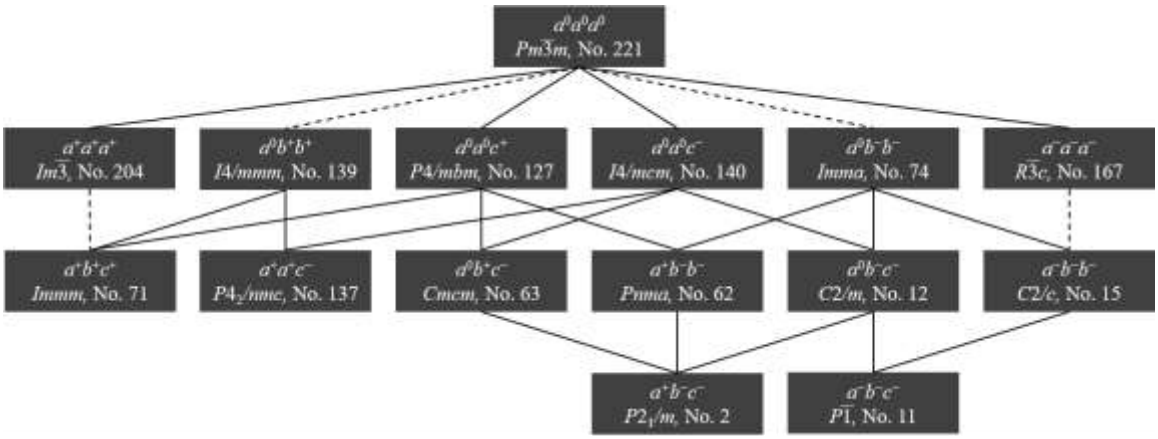

Figure 1.6 The group-subgroup relationships for all 15 perovskite tilt systems and their associated space groups. Second-order transitions are indicated by the solid lines and first-order transitions are indicated by the dashed lines.

1.4.2 Cation Ordering

As mentioned earlier, perovskites possess a wider range of functional properties than does almost any other mineral type; hence, predicting the structures and properties of perovskites without expensive trial-and-error experiments would save researchers and industry a significant amount of both time and money. For example, it can be shown that there is a direct link between the degree of cation ordering and the microwave dissipation factor or dielectric loss, tanδ, in complex perovskites; therefore, predicting the degree of ordering – and ultimately the quality factor, Q (where Q = 1/tanδ) – could eliminate the need for expensive measurements and unlock the full potential of these materials. As Q is a function of the frequency at which it is measured, it is often expressed as the product Q*f*, where *f* is the resonant frequency (in GHz). Other diagnostic properties of dielectrics include the dimensionless relative permittivity, ε_r, and temperature coefficient of resonant frequency, τ_f, typically expressed in units of ppm/°C or equivalently MK^{-1}.

Cation ordering on alternating {001}, {110}, or {111} pseudocubic planes is possible in both A-site substituted $A_{0.5}A'_{0.5}BX_3$ or B-site substituted $AB_{0.5}B'_{0.5}X_3$ complex

perovskites,[37] although layered {001} ordering tends to be preferred for the former and {111} ordering (so-called rock salt ordering) for the latter. In particular, layered A-site ordering in $A_{0.5}A'_{0.5}BX_3$ perovskites results in alternating layers of A and A′ ions along pseudocubic [001], as can be seen in Fig. 1.7. Similarly, rock salt B-site ordering in $AB_{0.5}B'_{0.5}X_3$ perovskites results in alternating layers of B and B′ ions along [111], resulting in a structure which resembles that of NaCl, as can be seen in Fig. 1.7. It should also be noted that there is only one unique ordering axis in layered A-site ordered structures, $[001]_{pc}$, whereas 1:1 rock salt B-site ordered perovskite structures have four ordering axes $[111]_{pc}$, $\left[\bar{1}11\right]_{pc}$, $\left[1\bar{1}1\right]_{pc}$, and $\left[11\bar{1}\right]_{pc}$ as illustrated in Fig. 1.8a. Even when the structures become distorted such as the monoclinically distorted $LaZn_{0.5}Ti_{0.5}O_3$ perovskite, the structure still has four ordering axes (*e.g.* the monoclinic [101], $\left[\bar{1}01\right]$, [110], and $\left[\bar{1}10\right]$) as illustrated in Fig. 1.8b and 1.8c.

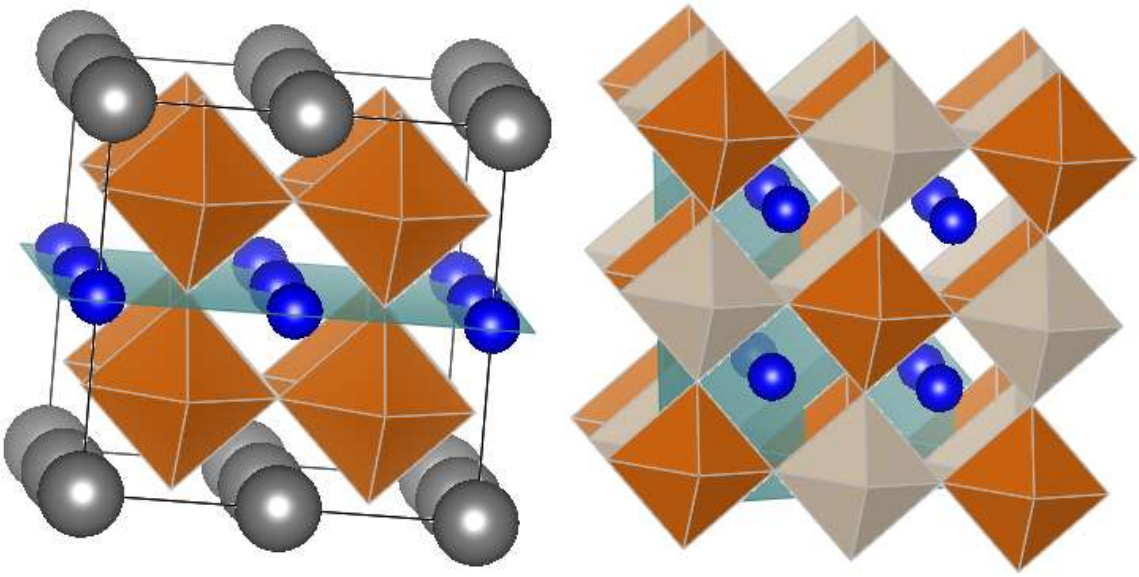

Figure 1.7 Doubled perovskite unit cells showing layered A-site ordering (left) and rock salt B-site ordering (right). The ordering planes are shown in both cells.

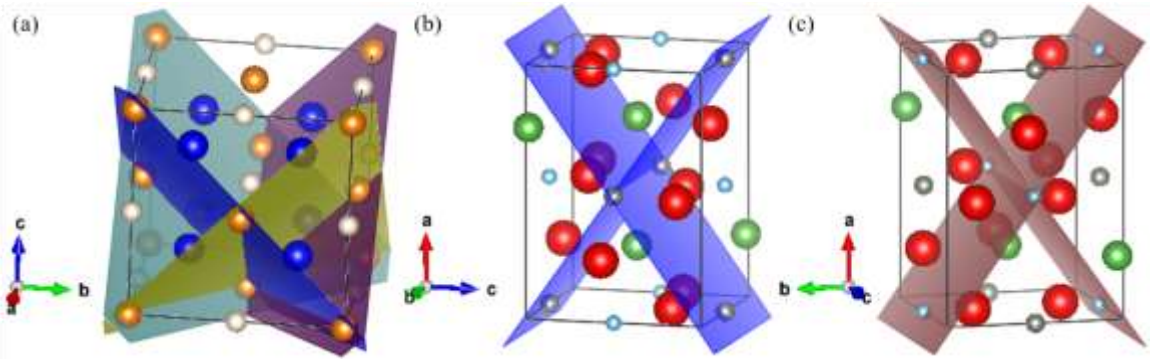

Figure 1.8 (a) Cubic and (b), (c) monoclinically distorted rock salt B-site ordered perovskite structures showing all 4 ordering planes in each case. The anions are not shown in (a).

In general, ordering is typically expected to produce structures that exhibit greater packing efficiency than disordered structures;[38] hence, ordering in complex perovskites should result in structures with smaller unit volumes than those of their disordered counterparts. With this reasoning, the expected trend would be a decrease in unit volume with increasing order. Indeed, this is typically the trend that is observed[39,40] for rock salt B-site ordering; however, the opposite trend is often observed in the case of layered A-site ordering, in which the unit-cell volume is commonly observed[39,40] to increase with increasing order.

In either case, the volume change may be due to the relative motion of ions in response to charge imbalances caused by the demixing of cations. A volume decrease can be understood in simple terms as resulting from a more efficient packing of ions, analogous to the discontinuous specific-volume shrinkage observed upon crystallization of a liquid; however, in the case of ionic solids, this shrinkage would only occur *within* the ordered planes. In the specific case of layered A-site ordering in an otherwise aristotypical perovskite, the greatest number of bonds an {001} plane could contain, when normalized per unit cell, is four (either four A-X or four B-X bonds) as can be seen in Fig. 1.9;

therefore, the resulting bond density (number of bonds per area) on {001} is $4/a^2$; however, there are twice as many A-X bonds out of these planes. Although, the bonds in the {001} would be shortened due to more efficient packing of ions within the ordered planes, repulsion between adjacent (001) planes due to the charge imbalances caused by ordering results in an overall volume *expansion* in systems like $(Li,Na)_{(1-3x)/2}La_{(1+x)/2}TiO_3$. On the other hand, although there are no B-X bonds on the $\{111\}_{pc}$ planes, the B-site species will inevitably pack more efficiently within the {111} upon ordering. Since there are 4 ordering planes in the case of 1:1 rock salt B-site ordering that are approximately perpendicular to one another, the unit cell must contract because a unit cell volume expansion in this case would imply that the B-site species pack less efficiently within the {111}; and, so explains the unit cell volume contraction observed in B-site ordered perovskite systems like $(Ca,Sr,Pb,Ba)(Mg_{1/2}W_{1/2})O_3$.[40]

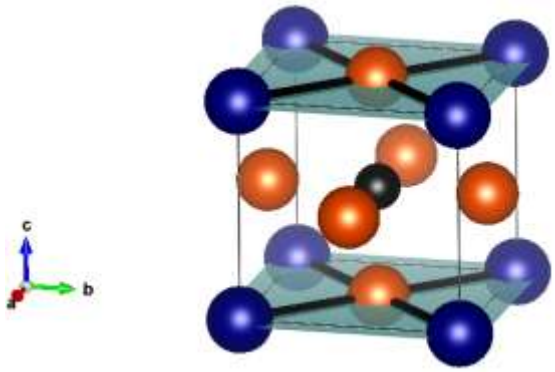

Figure 1.9 Perovskite unit cell showing an (001) plane. The A-X bonds that lie within this plane are shown.

1.5 Predictive Modeling of Composition-Structure Relationships in Perovksites

Recently, Ubic *et al.*[41,42] developed a new model for predicting the perovskite tolerance factor that accounts for extrinsic defects such as A-site vacancies and dopants. This model was later refined[43,44] as:

$$t_1 = \frac{a_{pc} - 0.011730139}{0.7209203\left(r_{\mathrm{B}} + r_{\mathrm{X}(id)}\right)} - 1.760998 \tag{1.9}$$

where r_{B} and r_{X} are the published Shannon radii of the B and X ions, respectively. This model has been proven[11] to be much better than t_0 at predicting octahedral distortions in perovskites. It also does not require knowledge of r_{A}, which eliminates the ambiguity in calculating the size of partially occupied sites; however, it does require foreknowledge of the pseudocubic lattice constant. In fact, Eq. 1.9 can be solved for a_{pc}:

$$a_{pc} = 0.7209203\left(t_1 + 1.760998\right)\left(r_{\mathrm{B}} + r_{\mathrm{X}(id)}\right) + 0.011730139 \tag{1.10}$$

Moreover, when $t \neq 1$ the bonds in perovskite structures undergo either compression or stretching. This stretching/compression effect is referred[11] to as bond deformation, D_B. An empirical model for predicting A-site size, r_{A}, that accounts for bond deformations, and A-site vacancy size, r_{V}, in $(\mathrm{A}^{2+}_{1-3x}\mathrm{A}'^{3+}_{2x})\mathrm{BX}_3$ perovskites has also recently been developed by Ubic *et al.*[11]:

$$r_{\mathrm{A}} = r_{\mathrm{A(id)}} + D_B + x r_{\mathrm{V}} \tag{1.11}$$

where

$$\mathrm{BD} = 7.4801 - 12.2139 t_0 + 4.8257 t_0^2 \tag{1.12}$$

$$r_{\mathrm{V}} = -20.8983 + 36.9417 t_0 - 14.4471 t_0^2 \tag{1.13}$$

and $r_{\mathrm{A(id)}}$ is the ideal Shannon radius. In this formulation, x is the concentration of vacancies on the A site, $x = [\mathrm{V_A}]$.

Moreover using the $(\mathrm{Ca,Sr,Pb,Ba})_{1-3x}\mathrm{La}_{2x}\mathrm{TiO}_3$ system, Ubic *et al.*[11] have developed a new model for the perovskite tolerance factor, t', as a function of the conventional tolerance factor.

$$t' = A + Bt_0 + Ct_0^2 \tag{1.14}$$

where,

$$A = -50.978 + 84.274 r_{\mathrm{A}(id)x=0} - 32.411 r^2_{\mathrm{A}(id)x=0} \tag{1.15}$$

$$B = 130.35 - 205.44 r_{\mathrm{A}(id)x=0} + 77.539 r^2_{\mathrm{A}(id)x=0} \tag{1.16}$$

$$C = -81.294 + 124.73 r_{\mathrm{A}(id)x=0} - 46.185 r^2_{\mathrm{A}(id)x=0} \tag{1.17}$$

where $r_{\mathrm{A(id)x=0}}$ is the average Shannon size of the A site when fully occupied (*i.e.*, the composition with no vacancies). This model is useful for calculating the tolerance factor due to the fact that the only variables that are needed are the conventional tolerance factor and the Shannon radius/radii for the A-site species at the x = 0 composition. Thus, this model allows for the prediction of the tolerance factor while accounting for extrinsic defects.

Furthermore, Ubic *et al.*[11] have developed a new model for effective anion size as a function of t' and the ideal Shannon size, $r_{\mathrm{X(id)}}$.

$$r_{\mathrm{X}'} = \left(0.42983 + 0.56696 t'\right) r_{\mathrm{X}(id)} \tag{1.18}$$

Eqs. 1.3, 1.4, and 1.10 can now be redefined in terms of t' and $r_{\mathrm{X}'}$.

$$a_{pc} = 0.7209203\left(t' + 1.760998\right)\left(r_{\mathrm{B}} + r_{\mathrm{X}(id)}\right) + 0.011730139 \tag{1.19}$$

$$a'_{pc} = \sqrt{2}\left(r_{\mathrm{A}} + r_{\mathrm{X}'}\right) \tag{1.20}$$

$$a''_{pc} = 2\left(r_{\mathrm{B}} + r_{\mathrm{X}'}\right) \tag{1.21}$$

where r_{A} is calculated using Eq. 1.11 and $r_{\mathrm{B}} = r_{\mathrm{B(id)}}$. Thus, Eqs. 1.19-1.21 allow for the prediction of the pseudocubic lattice constants using only the Shannon radii of the A-site, B-site, and X-site species, while simultaneously accounting for extrinsic defects.

1.5.1 Density Functional Theory

Accurately determining the structures of materials lies at the core of developing processing-structure-property relationships. Density functional theory (DFT) calculations can be used to validate these relationships by verifying experimentally determined structures and properties. For instance, Sausa *et al*.[45] used molecular DFT to predict the structure and properties of bis-oxadiazole-bis-methylene dinitrate, and they found that the most energetically favorable structure matches well with the experimental structure. Additionally, Pandey *et al*.[46] performed geometry optimizations according to density functional theory for the $CsPbCl_3$ and $CsPbBr_3$ perovskites. They found that not only did these calculations accurately predict the crystal structures of these two perovskites, they also found that the lattice parameters were accurately predicted. In both cases, DFT calculations were successfully used to validate experimental structures; hence, empirical models based on such experimental evidence can be validated using density functional theory calculations.

1.6 Aims and Objectives

Correlative models based on empirical evidence have the potential significantly improve the electroceramics industry, yet few of these predictive tools currently exist. This work attempts to fill this knowledge gap by developing predictive models to account for the effects of layered A-site ordering, rock salt B-site ordering, trigonality, and oxygen vacancies in distorted perovskite oxides using a combination of experimental data and published data from literature.

1.7 References

[1] Miller V, Tidrow S. Perovskites: Temperature and coordination dependent ionic radii. Integrated Ferroelectrics. 2013;148:1-16.

[2] Mazet L, Yang SM, Kalinin S V, Schamm-Chardon S, Dubourdieu C. A review of molecular beam epitaxy of ferroelectric $BaTiO_3$ films on Si, Ge and GaAs substrates and their applications. Sci Technol Adv Mater 2015;16(3):036005.

[3] Barwick M, Azough F, Freer R. Structure and dielectric properties of perovskite ceramics in the system $Ba(Ni_{1/3}Nb_{2/3})O_3$–$Ba(Zn_{1/3}Nb_{2/3})O_3$. J Eur Ceram Soc 2006;26(10–11):1767–73.

[4] Uchino K. Glory of piezoelectric perovskites. Sci Technol Adv Mater 2015;16(4):046001.

[5] Belik AA. Magnetic properties of solid solutions between $BiCrO_3$ and $BiGaO_3$ with perovskite structures. Sci Technol Adv Mater 2015;16(2):026003.

[6] Labhasetwar N, Saravanan G, Kumar Megarajan S, Manwar N, Khobragade R, Doggali P, et al. Perovskite-type catalytic materials for environmental applications. Sci Technol Adv Mater 2015;16(3):036002.

[7] Cui J, Yuan H, Li J, Xu X, Shen Y, Lin H, et al. Recent progress in efficient hybrid lead halide perovskite solar cells. Sci Technol Adv Mater 2015;16(3).

[8] Kozuka H, Ohbayashi K, Koumoto K. Electronic conduction in La-based perovskite-type oxides. Sci Technol Adv Mater 2015;16(2):026001.

[9] Goldschmidt VM. Die Gesetze der Krystallochemie. Naturwissenschaften 1926;14(21):477–85.

[10] Reaney IM, Colla EL, Setter N. Dielectric and Structural Characteristics of Ba- and Sr-based Complex Perovskites as a Function of Tolerance Factor. Jpn J Appl Phys 1994;33(7R):3984.

[11] Ubic R, Tolman K, Talley K, Joshi B, Schmidt J, Faulkner E, et al. Lattice-constant prediction and effect of vacancies in aliovalently doped perovskites. J Alloys Compd 2015;644:982–95.

[12] Lufaso M, Woodward P. Prediction of the crystal structures of perovskites using the software program SPuDS. Acta Cryst Sec B 2001;57:725-738.

[13] Salinas-Sanchez A, Garcia-Muñoz JL, Rodriguez-Carvajal J, Saez-Puche R, Martinez JL. Structural characterization of R_2BaCuO_5 (R = Y, Lu, Yb, Tm, Er, Ho, Dy, Gd, Eu and Sm) oxides by X-ray and neutron diffraction. J Solid State Chem 1992;100(2):201–11.

[14] Li F, Davidson B, Sutarto R, Shin H, Liu C, Elfimov I, *et al*. Epitaxial growth of perovskite $SrBiO_3$ film on $SrTiO_3$ by oxide molecular beam epitaxy. Phys Rev Mater. 2019;3:100802.

[15] Li G, Li X, Chen Y, Jia S, Xu X. Epitaxial growth mechanism of perovskite (111) $SrTiO_3$ on wurtzite (0002) GaN with single unit-cell TiN buffer layers. Appl Surf Sci. 2019;465:1055-1060.

[16] Wang X, Li Y, Xu Y, Pan Y, Wu Y, Li G, *et al*. Organometallic perovskite single crystals grown on lattice-matched substrate for photodetection. Nano Mater Sci. 2019;in-press.

[17] Tang G, You P, Tai Q, Yang A, Cao J, Zheng F, *et al*. Solution-phase epitaxial growth of perovskite films on 2D material flakes for high-performance solar cells. Adv Mater. 2019;31(24):1807689.

[18] Tenne D, Xi X. Raman spectroscopy of ferroelectric thin films and superlattices. J Am Ceram Soc. 2008;91(6):1820-1834.

[19] Tenne D, Lee H, Katiyar R, Xi X. Ferroelectric phase transitions in three-component short-period superlattices studied by ultraviolet raman spectroscopy. J Appl Phys. 2009;105:054106.

[20] Pecharsky VK, Zavalij PY. Fundamentals of powder diffraction and structural characterization of materials. 2nd ed. New York, NY: Springer Science+Business Media; 2009.

[21] Bacon GE. Neutron diffraction. Oxford, UK: Clarendon Press; 1955.

[22] Howard C, Stokes H. Group-theoretical analysis of octahedral tiliting in perovskites. Acta Cryst Sec B Struc Sci. 1998;54:782-789.

[23] Stokes H, Kisi E, Hatch D, Howard C. Group-theoretical analysis of octahedral tilting in ferroelectric perovskites. Acta Cryst Sec B 2002;58:934-938

[24] Howard C, Stokes H. Octahedral tilting in cation-ordered perovskites – a group-theoretical analysis. Acta Cryst Sec B Struc Sci. 2004;60:674-684.

[25] Howard C, Stokes H. Structures and phase transitions in perovksites – a group-theoretical approach. Acta Cryst Sec A 2005;61:93-111.

[26] Nier A, Goldman A. Joseph Valasek. Physics Today. 1994;47(8):76.

[27] Valasek J. Piezo-electric and allied phenomena in Rochelle salt. Phys Rev. 1921;17(4):475-481.

[28] Valasek J. Piezo-electric activity of Rochelle salt under various conditions. Phys Rev. 1922;19(5):478-491.

[29] Valasek J. Properties of Rochelle salt related to the piezo-electric effect. Phys Rev. 1922;20(6):639-664.

[30] Valasek J. Dielectric anomalies in Rochelle salt crystals. Phys Rev. 1924;24(5):560-568.

[31] Whatmore, R. Ferroelectric Materials. In: Kasap, S., Capper, P. Springer Handbook of Electronic and Photonic Materials. Springer Handbooks, Springer, Cham 2017.

[32] Erhart J, Pulpan P, Pustka M. Applications of piezoelectric resonators. In: Piezoelectric Ceramic Resonators. Topics in Mining, Metallurgy and Materials Engineering. Springer, Cham 2017.

[33] Ishihara T, Matsuda H, Takita Y. Effects of rare earth cations doped for La site on the oxide ionic conductivity of $LaGaO_3$-based perovskite type oxide. Solid State Ionics. 1995;79:147-151.

[34] Glazer AM. The classification of tilted octahedra in perovksites. Acta Cryst Sec B. 1972;28:3384-3392.

[35] Woodward P. Octahedral tilting in perovskites. I. Geometrical considerations. Acta Cryst Sec B. 1997;53:32-43.

[36] Carpenter A, Howard C. Symmetry rules and strain/order-parameter relatiohships for coupling between octahedral tilting and cooperative Jahn-Teller transitions in ABX_3 perovskites. I. Theory. Acta Cryst Sec B. 2009;65:134-146.

[37] King G, Woodward PM. Cation ordering in perovskites. J Mater Chem 2010;20(28):5785.

[38] Askeland D. The Science and Engineering of Materials. Boston: PWS-Kent Pub. Co.; 1989.

[39] Tolman K, Ubic R, Liu B, Williamson I, Bedke K, Nelson EB, et al. Empirical Evidence for A-Site Order in Perovskites. J Am Ceram Soc 2017;100(1):429–42.

[40] Smith E, Tolman KR, Ubic R. An empirical model for B-site cation ordering in Ba(Mg⅓Ta⅔)O3. J Alloys Compd 2018;735:2356–62.

[41] Ubic R. Revised method for the prediction of lattice constants in cubic and pseudocubic perovskites. J Am Ceram Soc 2007;90(10):3326–30.

[42] Ubic R, Subodh G, Sebastian MT, Gout D, Proffen T. Effective Size of Vacancies in the $Sr_{1-3x/2}Ce_xTiO_3$ Superstructure. In: Advances in Electroceramic Materials: Ceramic Transactions. Hoboken, NJ, USA: John Wiley & Sons, Inc.; 2009. page 177–85.

[43] Ubic R, Tolman K, Chan K, Lundy N, Letourneau S, Kriven WM. Effective size of vacancies in aliovalently doped $SrTiO_3$ perovskites. J Alloys Compd 2013;575:239–45.

[44] Tolman KR, Ubic R, Papac M, Seymour KC, McCormack SJ, Kriven WM, et al. Structural effect of aliovalent doping in lead perovskites. J Solid State Chem 2015;225:359–67.

[45] Sausa R, Batyrev I, Pesce-Rodriguez R, Byrd E. Density functional theory and experimental studies of the molecular, vibrational, and crystal structure of bis-oxadiazole-bis-methylene dinitrate (BODN). J Phys Chem A. 2018;122(46):9043-9053.

[46] Pandey N, Chakrabarti S. Density functional theory based study of $CsPb(Cl/Br)_3$ mixed halide perovskites with experimental validation. Proceedings Volume 11366, Photonics for Solar Energy Systems VIII; 2020;1136611

CHAPTER TWO: EMPIRICAL MODELS FOR LAYERED A-SITE ORDERING IN PEROVSKITE TITANATES

This chapter was published by John Wiley & Sons, Inc. in the Journal of the American Ceramic Society and should be referenced appropriately.

Reference: Smith, E., Ubic, R., "Empirical Models for Layered A-site Ordering in Perovskite Titanates," Journal of the American Ceramic Society 102, Issue 5, 2019, pp. 3019-3031, https://doi.org/10.1111/jace.16168

2.1 Introduction

The aristotype perovskite structure forms in cubic space group $Pm\bar{3}m$ with ABX_3 stoichiometry; however, there are a vast number of structural distortions that occur which can greatly affect properties. In particular, cation ordering on alternating {001}, {110}, or {111} pseudocubic planes is possible in both A-site substituted $A_{0.5}A'_{0.5}BX_3$ or B-site substituted $AB_{0.5}B'_{0.5}X_3$ complex perovskites,[2] although layered {001} ordering tends to be preferred for the former and {111} ordering (so-called rock salt ordering) tends to be more common for the latter.

Initially, $Na_yLa_{1-y}TiO_3$ ($y = 0.05 – 0.8$) perovskites were observed[3] to exhibit cubic symmetry with unit-cell volumes increasing with y for $0.05 \leq y < 0.1$ then decreasing for $y \geq 0.1$. It should be noted that this stoichiometry is problematic, as a fully occupied A site requires that the upper limit on y be 0.5. When $y < 0.5$, Ti exists as a mixture of Ti^{3+} and Ti^{4+} (pure Ti^{3+} at $y = 0$), but when $y > 0.5$ the only way to charge-balance would be to produce oxygen vacancies (not A-site vacancies as the authors propose). As there is a significant amount of TiO_2 in the XRD patterns for all samples with $y > 0.5$, it can be assumed that phase purity was not achieved for these compositions; instead, the following reaction is proposed:

$$Na_yLa_{1-y}TiO_3 \ (y \geq 0.5) \rightarrow 2(1-y)Na_{0.5}La_{0.5}TiO_3 + (2y-1)TiO_2 + (y-0.5)Na_2O\uparrow$$

The Na_2O phase melts at 1132°C and would likely have volatilized from calcined powders. Several years later, Ruiz *et al.*[4] studied various compositions in the vacancy-doped $Na_{(1-3x)/2}La_{(1+x)/2}TiO_3$ (NLT) system using neutron diffraction. This unconventional formulation, although not used by Ruiz *et al.*,[4] is convenient because the concentration of A-site vacancies, $[V_A]$, is identical to x, *i.e.*, $[V_A] = x$; so increasing x can be thought of as

doping with vacancies. They observed that both the x = 0.0533 and x = 0.1733 compositions exhibited orthorhombic symmetry in space groups *Ibmm* and *Pbmm*, respectively, and had a completely disordered arrangement of Na^+ and La^{3+} cations on the A site; however, upon re-examination[5] they determined that the x = 0.1733 composition exhibited some degree of layered A-site ordering. In addition, the x = 0.2233 composition showed[5] similar ordering. Knapp and Woodward[6] also studied $Na_{0.5}La_{0.5}TiO_3$ (x = 0) and observed no long-range cation ordering on the A site; however, the NLT system was recently re-examined by Tolman *et al.*[7] using electron diffraction, and short-range cation ordering was observed for x = 0 and attributed to the existence of ordered nanodomains, which explains why the ordering is not observed via X-ray diffraction (XRD). Furthermore, both $(Na_{0.5}La_{0.5})TiO_3$ and $(Na_{0.5}Tb_{0.5})TiO_3$ were later studied[8] via neutron diffraction; and while the latter was observed in orthorhombic space group *Pbnm*, the former crystallized in trigonal space group $R\bar{3}c$. The similar $(Na_yLa_yCa_{1-2y})TiO_3$ ($0 < y < 0.5$) system was also studied[9] via XRD and Raman spectroscopy, and the y = 0.5 composition ($Na_{0.5}La_{0.5}TiO_3$) was reported to exist with tetragonal symmetry in space group *I4/mcm*, whereas the y = 0 composition ($CaTiO_3$) exhibited orthorhombic symmetry in space group *Pbnm*. The tetragonal-to-orthorhombic phase transformation occurred between $0.34 \leq y \leq 0.39$. The NLT (x = 0) composition is well known for exhibiting quantum paraelectricity at low temperatures (< 50 K)[10] and is also reported to exhibit photoluminescent properties[11]. Its microwave dielectric properties have been reported[12,13] at its resonant frequency of 3 GHz as: ε_r = 122, Q = 3260, τ_f = 480 ppm/°C.

Initial studies[14-18] of the structure of $Li_{(1-3x)/2}La_{(1+x)/2}TiO_3$ (LLT) indicated that the symmetry remained tetragonal in space group *P4/mmm* for $0 \leq x \leq 0.244$. Later, the

structure of LLT was reported[19] to undergo a phase transformation from tetragonal (*P4/mmm*) to orthorhombic (*Pmmm*) as *x* increased to 0.13 – 0.19. The *x* = 0.213 composition was also reported[20] as orthorhombic, but in space group *Cmmm*, with layered ordering of the La^{3+} cations and vacancy-rich planes along the *c* axis. Several of these studies[14-16] showed that the Li^+ and La^{3+} cations order in layers along the *c* axis in the Li^+-rich (low-*x*) variants. This result was later supported by Ruiz *et al.*[17] who used neutron diffraction to determine that the *x* = 0.103 composition exhibited long-range cation ordering. In order to investigate high-temperature structures of LLT, several studies[18,21,22] used quenched LLT samples. These samples exhibited trigonal symmetry in space group $R\bar{3}c$ with Li^+ ions existing on four-coordinated interstitial sites (in the center of the square faces of the A-site coordination cuboctahedra). Similarly, samples[23-26] that underwent natural cooling in the furnace also contained Li^+ ions on the interstitial sites but formed with orthorhombic symmetry in space group *Cmmm*. Only samples cooled slowly[14-18,20] reach the equilibrium state in which Li^+ and La^{3+} ions form a layered ordered structure, although the short-range nature of that ordering has not always been recognized. Electron diffraction can be used to establish the existence of short-range A-site ordering as well as vacancy ordering, both of which can be difficult to determine from X-ray diffraction (XRD) alone. Short-range 1:1 A-site ordering typically results in diffuse pseudocubic ½{even,even,odd} β superlattice reflections in electron diffraction patterns. The LLT (*x* = 0) composition is known to exhibit high values for ionic conductivity.[19,27]

The complex perovskite $[(Na_yLi_{1-y})_{(1-3x)/2}La_{(1+x)/2}]TiO_3$ (NLLT) has an effective A-site cation size intermediate between that of NLT and LLT. Again, this formulation is unconventional but convenient, as the concentration of A-site vacancies, [V], is identical

to x. In 2002, Rivera *et al*.[28] were possibly the first to produce any type of NLLT hybrid composition. In particular, they analyzed the $x = 0$ compositions $[(Na_yLi_{1-y})_{0.5}La_{0.5}]TiO_3$ ($0 \leq y \leq 1$) via neutron and X-ray diffraction. They reported that all compositions in the series crystallized in space group $R\bar{3}c$, and they did not observe an appreciable difference in unit-cell parameters between any of the compositions. The lithium mobility was also reported to decrease by two orders of magnitude as the value of y increased, changing from values associated with fast ion conductors at $y = 0$ to those of insulators at $y = 1$. The intermediate $(Na_{0.3}Li_{0.2}La_{0.5})TiO_3$ ($y = 0.6$) composition was later analyzed[29] via neutron diffraction in the temperature range from 300 to 1073 K, with the room-temperature variant forming in rhombohedral space group $R\bar{3}c$ due to antiphase octahedral tilting about the pseudocubic [111].

Herrero *et al*.[30] appear to be the first to have analyzed vacancy-doped NLLT. They analyzed both the $[(Na_yLi_{1-y})_{0.5}La_{0.5}]TiO_3$ ($x = 0$) and $[(Na_yLi_{1-y})_{0.2}La_{0.6}]TiO_3$ ($x = 0.2$) series via neutron diffraction, impedance spectroscopy, nuclear magnetic resonance, and Monte Carlo simulations. The latter series was reported in the orthorhombic space group *Cmmm* with layered type vacancy ordering along the *c* axis, whereas the former was reported in the rhombohedral space group $R\bar{3}c$ with a completely disordered A site. Later work[22] on the $x = 0$ compositions at temperatures ranging from 300 K to 1073 K showed that all compositions exhibited a cubic structure ($Pm\bar{3}m$) near 1000 K; however, once the samples began to cool down, the octahedra exhibited antiphase tilting about [111], causing a rhombohedral distortion and resulting in space group $R\bar{3}c$ near room temperature. The $x = 0.2$ series $[(Na_yLi_{1-y})_{0.2}La_{0.6}]TiO_3$ ($0 \leq y \leq 1$) was again investigated[31] via neutron

diffraction at temperatures between 300 K and 1073 K; and in addition to the vacancy ordering, octahedral tilting along the *b* axis was also reported.

The ordering of cations on either A or B sites in a complex perovskite clearly has structural implications. It has also recently been established[7,32] using this model and verified via both density functional theory (DFT) and Rietveld refinements that, while rock salt ordering of the B site results in a *decrease* in the unit-cell volume with respect to the disordered state, A-site layered ordering can result in an *increase* in the unit-cell volume. This counterintuitive expansion was later explained crystalochemically[32] by the fact that ordering in perovskites causes more efficient packing – and so shrinkage – *within* ordered planes but an expansion of bonds *perpendicular* to them. This result could have implications for functional properties, especially ionic conduction. Specifically, large negative errors (-1% - -2%) in both a'_{pc} and a''_{pc}, caused by an underestimation of the A-X bond length, are indicative within this model of so-called layered A-site ordering.[7] In such systems, errors can be corrected by introducing a Δr_A correction term, which is a way of quantifying the degree of order as a function of composition. In the cases of both NLT and LLT, the Δr_A which resulted upon ordering could be expressed entirely as a function of vacancy concentration (x):

$$\Delta r_A = \frac{P}{1+\exp\left(\frac{x-Q}{S}\right)} \tag{2.1}$$

where P, Q, and S are coefficients. Likewise, the order parameter, η, could be derived from Δr_A with an equation of the form:

$$\eta = A + B\left(\ln\left[\left(\frac{C}{\Delta r_A}\right)-1\right]\right) \tag{2.2}$$

where *A*, *B*, and *C* are different coefficients. In this way, Δr_A can be used explicitly as a measure of A-site ordering. Interestingly, while no evidence of *long-range* A-site ordering has been observed in the NLT system via x-ray or neutron diffraction,[3-6,8,9,22,28,33-36] this model clearly shows the pattern of errors leading to the conclusion of order. In fact, electron diffraction shows[7] that the structure consists of nanodomains of order (short-range order); thus, even short-range order can be quantified with this model. Indeed, such regions of short-range order may be a more common phenomenon than is widely realized, as similar regions have also been found within long-range disordered spinel[37] and pyrochlore[38] structures. In both the NLT and LLT systems, the degree of vacancy ordering increases with *x* while the degree of cation ordering decreases.[7]

Here, four similar models have been derived for the $[(Na_yLi_{1-y})_{(1-3x)/2}La_{(1+x)/2}]TiO_3$ (NLLT) solid solution using 15 compositions (y = 0.25, 0.5, and 0.75; and x = 0, 0.0533, 0.1, 0.1733, and 0.225). From these data, two generalized empirical models have been developed which predict both the A-site size correction factor, Δr_A, and the A-site ordering parameter, η, for perovskite titanates.

2.2 Materials and Methods

Fifteen compositions in the system $(Na_yLi_{1-y})_{(1-3x)/2}La_{(1+x)/2}TiO_3$ (NLLT) with five x values (x = 0, 0.0533, 0.1, 0.1733 and 0.225) for each of three y values (y = 0.25, 0.5, and 0.75) were synthesized via the solid-state mixed-oxide route. As-received La_2O_3 (99.9%, Alfa-Aesar, Ward Hill, MA) powder was first hydroxylated by mixing with an excess of deionized water and drying overnight, forming $La(OH)_3$. Stoichiometric amounts of Na_2CO_3 (99.5%, Thermo Fisher Scientific Inc., Pittsburgh, PA), Li_2CO_3 (99.5%, Thermo Fisher Scientific Inc., Pittsburgh, PA), TiO_2 (99.9%, Aldrich Chemical Co., Milwaukee,

WI), and $La(OH)_3$ were then ball-milled with yttria-stabilized ZrO_2 (YSZ) media using deionized water in a high-density nylon pot for ~6 hours. Powders were then dried overnight in an atmospheric drying oven at ~98°C until all the water was evaporated. Calcination was conducted for three hours in a box furnace (1807FL, CM Furnaces Inc., Bloomfield, NJ) at 1100°C for the $x \leq 0.0533$ compositions, 1150°C for $x = 0.1$ and $x = 0.1733$, and 1200°C for $x = 0.225$. A pre-contaminated crucible was used to inhibit sodium- and lithium-loss into the crucible walls. No excess sodium or lithium was added to the compositions. After calcination, the powders were ball-milled again with YSZ media using deionized water in a high-density nylon pot for ~24 hours, adding 2 wt% polyethylene glycol (PEG 10 000, Alfa-Aesar, Heysham, UK) powder for the final 5 minutes. The mixture was then dried overnight in an atmospheric drying oven at ~98°C until all the water was evaporated. Cylindrical green compacts 8-10 mm in height and 10 mm in diameter were then formed by applying a uniaxial pressure of 63 MPa. Compacts were placed on bed of sacrificial calcined powders with the same composition on a Y_2O_3 plate, and were completely covered with the same sacrificial powder to induce a sodium- and lithium-rich closed atmosphere during sintering. An inverted 250 mL Al_2O_3 crucible was placed over the Y_2O_3 plate containing the compacts and sacrificial powder. Compacts were sintered for three hours at 1300°C ($x \leq 0.0533$), 1350°C ($x = 0.1733$), and 1400°C ($x = 0.225$).

Powder XRD measurements were performed in a diffractometer (Miniflex-600, Rigaku, Woodlands, TX) operating with convergent-beam geometry and CuKα radiation. Le Bail refinements were performed on the XRD patterns using GSAS II (Argonne National Laboratory, IL). The background was fitted with a twelfth-order Chebyshev

polynomial. All compositions were refined with either orthorhombic or tetragonal symmetry.

Specimens for transmission electron microscopy (TEM) (JEM-2100 HR, JEOL, Japan) were prepared from sintered pellets by mechanically cutting them with a diamond wafering blade then polishing the faces via conventional ceramographic techniques, finishing with a precision ion polisher (Model 691, Gatan, Pleasanton, CA) at low ion-beam angles to achieve electron transparency (*i.e.*, thickness ~100 nm). Amorphous material caused by ion damage was removed using a plasma cleaner (Model 1400, E. A. Fischione Instruments Inc., Export, PA) prior to observation in the TEM.

2.3 Results and Discussion

Figs. 2.1-2.3 show the XRD traces for each of the *y* series of compositions in the NLLT system that were produced. These figures clearly show that there are no secondary phases in any of the compositions. It can also be seen that none of the $x \leq 0.0533$ compositions show any superlattice reflections, indicating a lack of detectable long-range A-site ordering. In the cases of $y = 0.25$ and $y = 0.5$, such ordering seems to disappear below $x = 0.1$, and for $y = 0.75$ it is absent below $x = 0.1733$. The reason the degree of ordering seems to counter-intuitively increase as *x* increases (*i.e.*, as the stoichiometry diverges from the ideal 1:1 ratio for Na_yLi_{1-y}:La) can be explained by the size of ordered domains. At low *x* values the degree of ordering is high but ordered domains are small and so undetectable via XRD, although the order is detectable via electron diffraction as seen in Fig. 2.4. As *x* increases, the degree of order decreases ($\eta = 1 - 3x$) but the range of ordering grows so that it becomes more detectable via XRD. The same phenomenon was previously observed in pure NLT.[7,39] As in the NLT and LLT systems,[7] the degree of

cation ordering in NLLT decreases as x increases while the degree of vacancy ordering increases.

Figs. 2.1-2.3 also suggest that there is a structural transformation from orthorhombic to tetragonal between $0.1 \leq x \leq 0.1733$ for both the $y = 0.25$ and $y = 0.5$ variants and between $0.1733 \leq x \leq 0.225$ for the sodium-rich $y = 0.75$ variant, as seen for example in the splitting of the pseudocubic 200 peak from a doublet to a triplet. This structural transformation can be understood in the light of previous work in which pure NLT has been reported[5] to exhibit orthorhombic symmetry throughout the range of compositions, whereas conventionally processed pure LLT tends to exhibit tetragonal symmetry for Li-rich compositions ($x \lesssim 0.19$) and orthorhombic symmetry for Li-poor ones ($x \gtrsim 0.19$).[14-20] Thus, all three NLLT hybrid compositions exhibit certain symmetry elements of both end members.

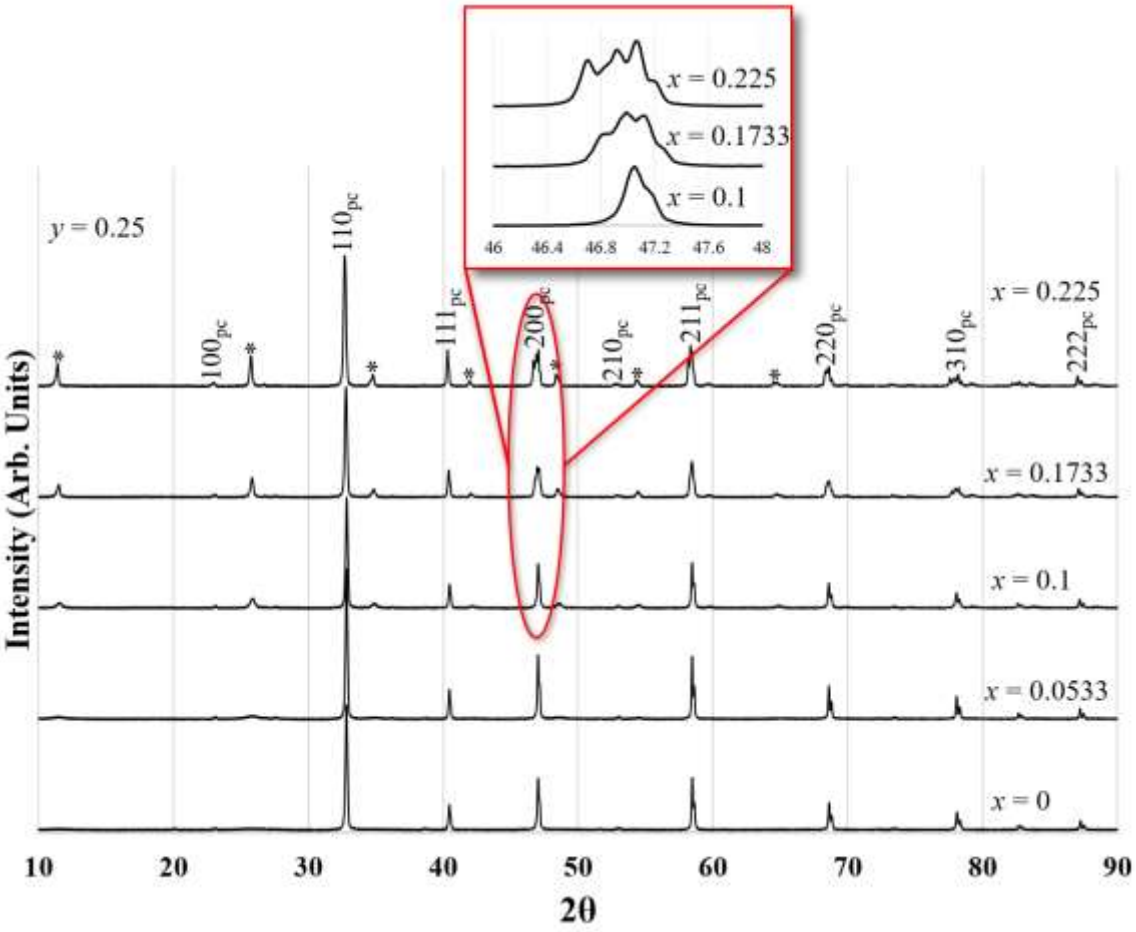

Figure 2.1 X-ray diffraction of $(Na_{0.25}Li_{0.75})_{(1-3x)/2}La_{(1+x)/2}TiO_3$ for $0 \leq x \leq 0.225$. Peaks resulting from long-range A-site cation ordering are marked with a *.

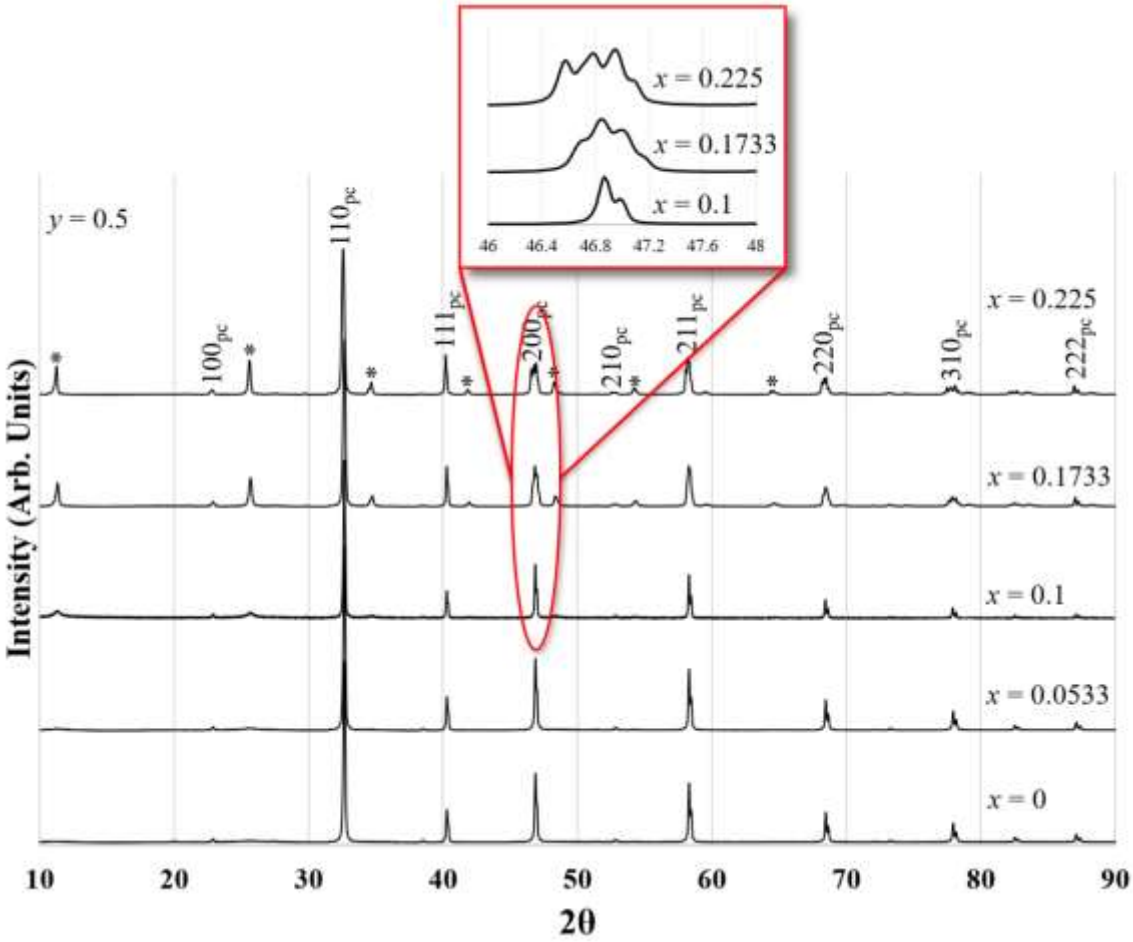

Figure 2.2 X-ray diffraction of $(Na_{0.5}Li_{0.5})_{(1-3x)/2}La_{(1+x)/2}TiO_3$ for $0 \leq x \leq 0.225$. Peaks resulting from long-range A-site cation ordering are marked with a *.

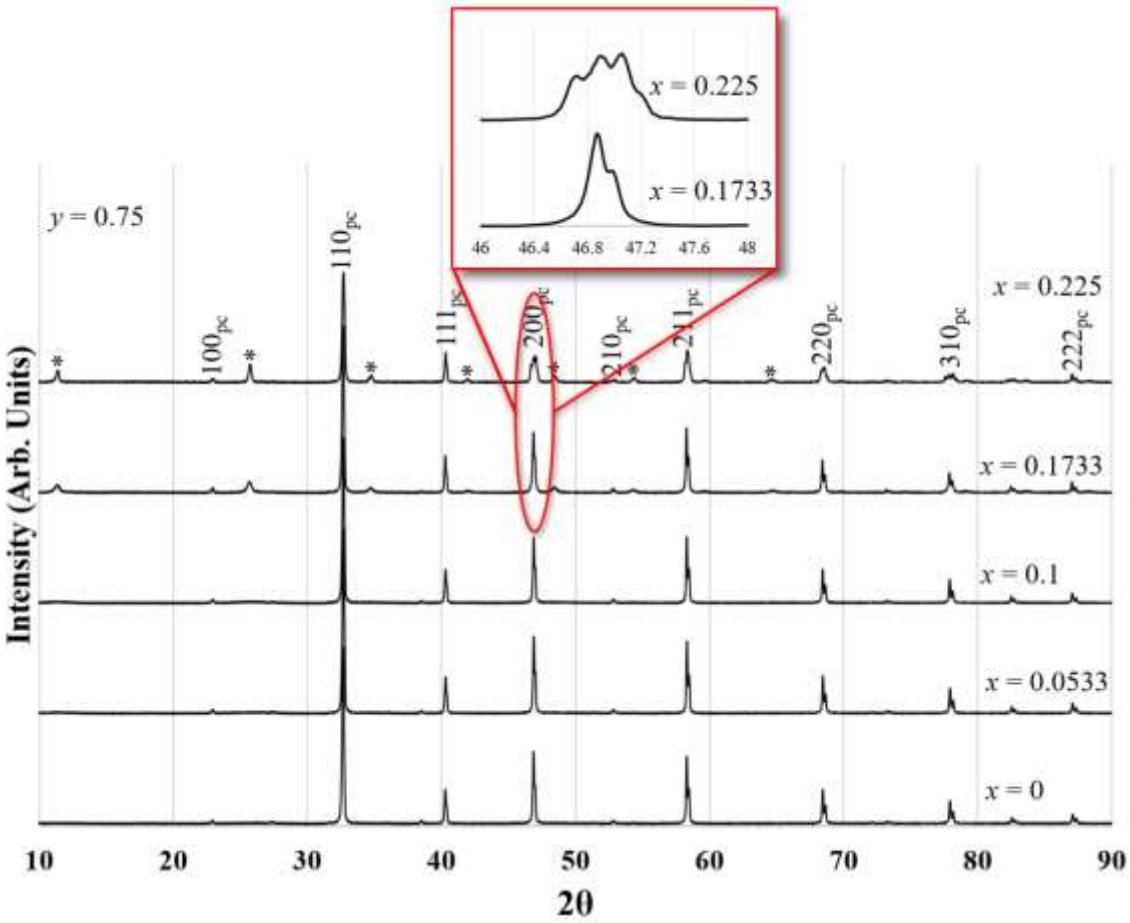

Figure 2.3 X-ray diffraction of $(Na_{0.75}Li_{0.25})_{(1-3x)/2}La_{(1+x)/2}TiO_3$ for $0 \leq x \leq 0.225$. Peaks resulting from long-range A-site cation ordering are marked with a *.

The refinements in tables 2.1-2.3 show that, in general, the model increasingly underestimates the pseudocubic lattice constant as the degree of cation ordering increases. This effect can be seen in Fig. 2.5 and tables 2.4-2.6 by the increase in the A-site size correction factor, Δr_A, as the cation ordering parameter, η, increases (or x decreases). This result seems to support the hypothesis[32] that electrostatic repulsions pushing ordered planes apart will dominate over the effects of the shrinking bonds within ordered planes for this type of layered ordering. This repulsion, in turn, causes the unit-cell volume to be larger than that for a random distribution of cations.

The change in unit-cell volume can then be explained by the relative motion of ions in response to charge imbalances caused by the demixing of cations. Cations will pack more efficiently within ordered planes, but electrostatic repulsion will result in less efficient packing outside of these planes. The aristotypical perovskite {001} planes can contain at most four A-X bonds per unit cell; however, there are twice as many A-X bonds out of this plane, resulting in a net volume expansion upon ordering. Thus, the overall trend favors volume *expansion* with increasing layered type A-site cation ordering. By contrast, the contraction of B-X bonds due to more efficient packing of B-site species within ordered $(111)_{pc}$ planes in conjunction with the contraction of A-X bonds within ordered $(111)_{pc}$ planes, despite the lower bond density on $\{111\}_{pc}$ than on {001}, results in a net volume *shrinkage* observed in rock salt ordered perovskites like, for example, $Ba(Mg_{1/3}Ta_{2/3})O_3$.[32]

The trend in error values seen in tables 2.1-2.3, *i.e.*, large negative errors at low x values gradually increasing to large positive errors as x increases, is indicative of an underestimation of r_A. It can also be observed from tables 2.1-2.3 that the model produces much larger absolute errors in a'_{pc} for smaller A-site cation sizes than for larger ones. It produces an error of -1.035% for the $x = 0$ composition in the Li-rich $y = 0.25$ series, whereas the error for the $x = 0$ composition in the Na-rich $y = 0.75$ series is merely -0.476%. The model also appears to increase in accuracy for all y values as vacancy concentration increases due to fact that the overall degree of 1:1 cation order decreases the further the composition is removed from the ideal 1:1 stoichiometry.

In order to account for the volume expansion upon ordering and minimize resultant errors, values of r_A were increased by an amount Δr_A. At $x = 0$, Δr_A was

determined by incrementally increasing r_A (effectively increasing the Shannon[40] radii) until the errors in both a'_{pc} (Eq. 1.3) and a''_{pc} (Eq. 1.4) were minimized. The resultant $r_{A(x=0)}$ value is necessary to subsequently derive values of t' and thus a_{pc} (Eq. 1.19). For $x > 0$, r_A was increased until errors in a'_{pc} were minimized due to the fact that a'_{pc} is far more sensitive to the A-site size than is a''_{pc}. The results of this process can be seen in tables 2.4-2.6. It should be noted that a_{pc} in tables 2.1-2.6 is calculated from Eq. 1.19, where t_0 and $r_{A(x=0)}$ are used to calculate t' via an empirical model[41] (Eq. 1.14).

Table 2.1 **$(Na_{0.25}Li_{0.75})_{(1-3x)/2}La_{(1+x)/2}TiO_3$ experimental and calculated pseudocubic lattice constants (Å)**

					a_{pc}		a'_{pc}		a''_{pc}	
x	***a* (Å)**	***b* (Å)**	***c* (Å)**	$a_{pc(Exptl.)}$	**Eq. 1.19**	**Error%**	**Eq. 1.3**	**Error%**	**Eq. 1.4**	**Error%**
0	5.4714	5.4714	7.7431	3.8709	3.8154	-1.398	3.8294	-1.035	3.8061	-1.639
0.0533	5.4744	5.4777	7.7396	3.8714	3.8254	-1.186	3.8396	-0.820	3.8170	-1.404
0.100	3.8715	3.8715	7.7520	3.8730	3.8379	-0.908	3.8513	-0.560	3.8305	-1.098
0.1733	3.8682	3.8682	7.7717	3.8741	3.8565	-0.454	3.8748	0.019	3.8590	-0.390
0.225	3.8667	3.8667	7.7777	3.8740	3.8875	0.349	3.8952	0.547	3.8845	0.269
0.3333[a]	3.8565	3.8565	24.645	3.9384	3.9499	0.293	3.9482	0.248	3.9522	0.352

[a]Ref. [42].

Table 2.2 **$(Na_{0.5}Li_{0.5})_{(1-3x)/2}La_{(1+x)/2}TiO_3$ experimental and pseudocubic lattice constants (Å)**

					a_{pc}		a'_{pc}		a''_{pc}	
x	***a* (Å)**	***b* (Å)**	***c* (Å)**	$a_{pc(Exptl.)}$	**Eq. 1.19**	**Error%**	**Eq. 1.3**	**Error%**	**Eq. 1.4**	**Error%**
0	5.4741	5.4746	7.7446	3.8718	3.8322	-1.021	3.8398	-0.825	3.8244	-1.224
0.0533	5.4762	5.4756	7.7470	3.8719	3.8379	-0.877	3.8471	-0.641	3.8306	-1.067
0.100	5.4743	5.4781	7.7409	3.8724	3.8470	-0.655	3.8566	-0.408	3.8404	-0.825
0.1733	3.8723	3.8723	7.7753	3.8742	3.8689	-0.136	3.8773	0.081	3.8604	-0.257
0.225	3.8747	3.8747	7.7956	3.8739	3.8899	0.415	3.8963	0.579	3.8871	0.341
0.3333[a]	3.8565	3.8565	24.645	3.9384	3.9492	0.273	3.9476	0.233	3.9514	0.330

[a]Ref. [42].

Table 2.3 **$(Na_{0.75}Li_{0.25})_{(1-3x)/2}La_{(1+x)/2}TiO_3$ experimental and calculated pseudocubic lattice constants (Å)**

					a_{pc}		a'_{pc}		a''_{pc}	
x	***a* (Å)**	***b* (Å)**	***c* (Å)**	$a_{pc(Exptl.)}$	**Eq. 1.19**	**Error%**	**Eq. 1.3**	**Error%**	**Eq. 1.4**	**Error%**
0	5.4751	5.4751	7.7442	3.8709	3.8508	-0.518	3.8524	-0.476	3.8446	-0.679
0.0533	5.4729	5.4771	7.7470	3.8721	3.8520	-0.519	3.8565	-0.403	3.8459	-0.677
0.100	5.4743	5.4788	7.7500	3.8733	3.8576	-0.407	3.8635	-0.253	3.8519	-0.553
0.1733	5.4747	5.4762	7.7543	3.8734	3.8748	0.037	3.8811	0.198	3.8707	-0.071
0.225	7.7205	7.7462	7.7766	3.8741	3.8932	0.495	3.8982	0.624	3.8906	0.428
0.3333[a]	3.8565	3.8565	24.645	3.9384	3.9485	0.257	3.9476	0.220	3.9507	0.312

[a]Ref. [42].

Table 2.4 **$(Na_{0.25}Li_{0.75})_{(1-3x)/2}La_{(1+x)/2}TiO_3$ accounting for cation effective sizes (Å)**

x	Δr_A	a_{pc} Eq. 1.19	Error%	a'_{pc} Eq. 1.3	Error%	a''_{pc} Eq. 1.4	Error%
0	0.06850	3.8739	0.115	3.8693	-0.005	3.8696	0.005
0.0533	0.05888	3.8699	-0.038	3.8714	0.000	3.8653	-0.157
0.100	0.04765	3.8713	-0.044	3.8730	0.000	3.8668	-0.160
0.1733	0.02293	3.8846	0.271	3.8741	0.000	3.8813	0.185
0.225	0	3.9037	0.765	3.8745	0.012	3.9020	0.721
0.3333[a]	0	3.9479	0.242	3.9466	0.209	3.9501	0.296

[a]Ref. [42].

Table 2.5 **$(Na_{0.5}Li_{0.5})_{(1-3x)/2}La_{(1+x)/2}TiO_3$ accounting for cation effective sizes (Å)**

x	Δr_A (Å)	a_{pc}	Error%	a'_{pc}	Error%	a''_{pc}	Error%
0	0.04885	3.8764	0.120	3.8712	-0.015	3.8723	0.015
0.0533	0.04275	3.8718	-0.002	3.8719	0.000	3.8674	-0.117
0.100	0.03223	3.8729	0.013	3.8724	0.000	3.8685	-0.100
0.1733	0.01273	3.8855	0.293	3.8742	0.000	3.8823	0.209
0.225	0	3.9025	0.738	3.8824	0.219	3.9007	0.692
0.3333[a]	0	3.9479	0.241	3.9466	0.208	3.9500	0.295

[a]Ref. [42].

Table 2.6 **$(Na_{0.75}Li_{0.25})_{(1-3x)/2}La_{(1+x)/2}TiO_3$ accounting for cation effective sizes (Å)**

x	Δr_A (Å)	a_{pc}	Error%	a'_{pc}	Error%	a''_{pc}	Error%
0	0.0266	3.8754	0.118	3.8704	-0.011	3.8713	0.011
0.0533	0.02356	3.8711	-0.027	3.8721	0.000	3.8666	-0.143
0.100	0.01805	3.8722	-0.028	3.8733	0.000	3.8678	-0.142
0.1733	0.00197	3.8853	0.307	3.8734	0.000	3.8820	0.222
0.225	0	3.9004	0.680	3.8912	0.444	3.8984	0.629
0.3333[a]	0	3.9479	0.241	3.9466	0.208	3.9500	0.295

[a]Ref. [42].

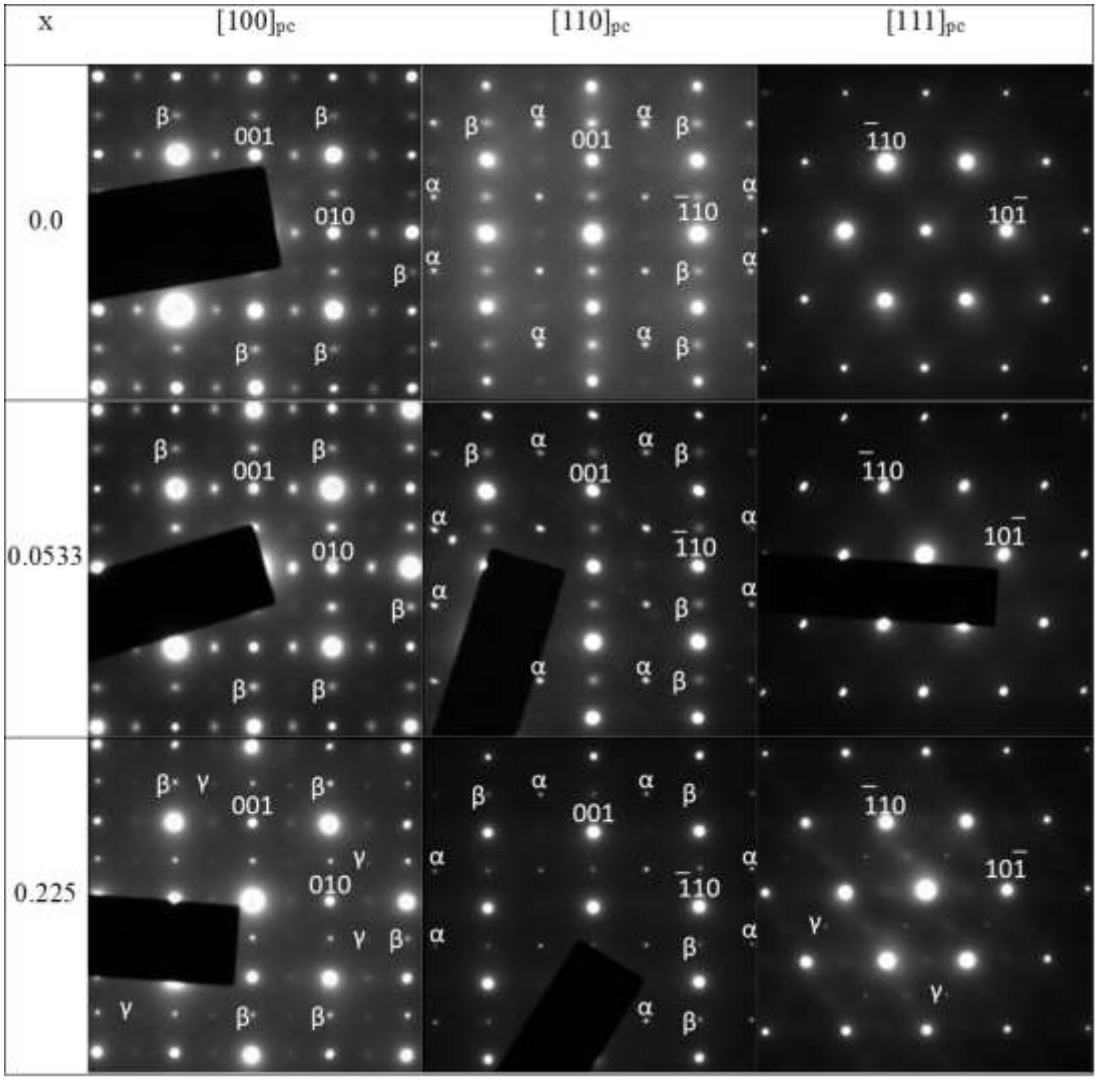

Figure 2.4 Selected area diffraction patterns for the x = 0, 0.0533, and 0.225 compositions in the $(Na_{0.5}Li_{0.5})_{(1-3x)/2}La_{(1+x)/2}TiO_3$ system with the associated pseudocubic indexing. Some α, β, and γ superlattice reflections are labeled.

Fig. 2.4 shows the presence of three types of superlattice reflections in the electron diffraction patterns of $(Na_{0.5}Li_{0.5})_{(1-3x)/2}La_{(1+x)/2}TiO_3$. The α superlattice labels correspond to ½{odd, odd, odd} reflections with mixed indices. Such reflections are typically associated with either antiphase octahedral tilting or rock-salt cation ordering. Reflections marked β correspond to ½{even, even, odd} indices. Specifically, ½{001} reflections correspond solely to layered cation ordering[7] whereas the intensity of reflections for

which both even indices are not 0 may also contain a component from antiparallel A-site cation displacements. The presence of ½{001} β reflections in all $[100]_{pc}$ and $[110]_{pc}$ patterns indicates some degree of layered ordering in every composition. The different intensities of the β reflections within the same $[100]_{pc}$ pattern may be further evidence of layered ordering within nanodomains. For example, while the intensities of ½{even, even, odd} and ½{even, odd, even } reflections are roughly equal for $x \leq 0.0533$ due to the nanosize of ordered regions, at $x = 0.225$ the ½{even, even, odd} reflections are clearly stronger, indicating both a single plane of order and an increase in the size of ordered domains. Although not technically α type, ½{111} reflections are specific to rock-salt ordering but can also occur via double diffraction if β reflections are also present, as they are here. The γ reflections are of the type ½{odd, odd, even}, where the two odd indices are not equal, and correspond to in-phase octahedral tilting. Although they might also contain a component from columnar A-site order, as layered ordering is clearly evident here, this possibility can be discounted. In the case of $x \leq 0.0533$, γ reflections are not observed in $[111]_{pc}$ patterns and are very weak in $[100]_{pc}$ patterns, where they probably occur via double diffraction; however, at $x = 0.225$ γ reflections also occur in $[111]_{pc}$ patterns in which there is no route for double diffraction. In this case, discreet γ reflections of the type ½{even, odd, odd} can be seen, indicating the presence of in-phase tilting about the pseudocubic *a* axis. Although not technically γ type, ½{even, odd, odd} reflections for which the two odd indices are equal may correspond to columnar A-site cation ordering (which possibility can be discounted for reasons explained above) but may also occur via double diffraction, and such reflections for which the even index is not 0 may also correspond to antiparallel A-site cation displacement. All these observations agree with

those previously observed in pure NLT;[7] however, whereas three sets of discreet γ reflections were observed in NLT for $x \geq 0.1733$, here only diffuse intensity can be seen in ½{odd, even, odd } and ½{odd, odd, even} positions, suggesting some degree of aperiodicity along the *b* and *c* axes.

Fig. 2.5 shows the value of Δr_A and the A-site order parameter, η, as functions of vacancy concentration, *x*, for $(Na_yLi_{1-y})_{(1-3x)/2}La_{(1+x)/2}TiO_3$ (y = 0, 0.25, 0.5, 0.75, 1). Fig. 2.6 shows η as a function of Δr_A. These figures clearly show that the empirical model[41] based on random ionic occupancies increasingly underestimates the unit-cell volume as the degree of cation ordering increases. On the other hand, the model appears surprisingly insensitive to vacancy ordering, as the error in the model decreases to nearly zero as the vacancy concentration increases, as illustrated in Fig. 2.5.

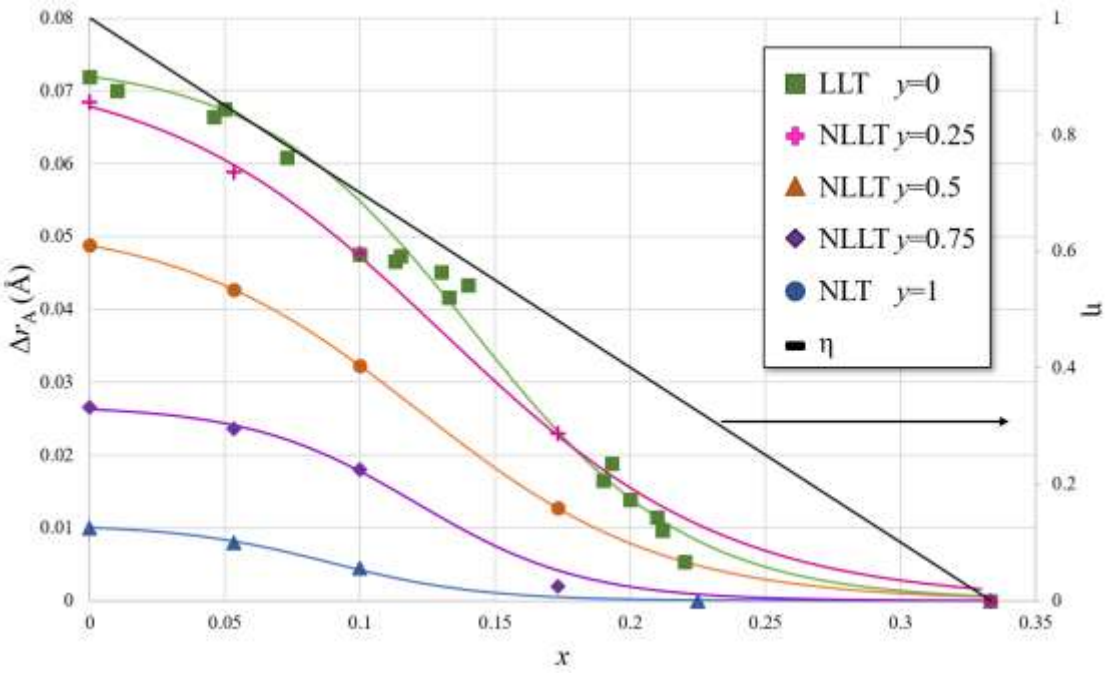

Fig. 2.5 A-site size adjustment factors as functions of composition from experimentally collected data for $(Na_yLi_{1-y})_{(1-3x)/2}La_{(1+x)/2}TiO_3$ and A-site order parameter, η, as a function of composition. The y = 0 data are from Ref. [7].

All the curves in Fig. 2.5 can be described using Eq. 2.1, and Table 2.7 lists all the associated coefficients. These curves demonstrate that, for a given x, the magnitude of the Δr_A required decreases as the size of the A-site species increases.

Table 2.7 Coefficients of Eq. 2.1 and the goodness of fit, R^2

	y	***P***	***Q***	***S***
	0	0.0740887	0.141918	0.0399016
	0.25	0.0735582	0.130847	0.0525141
	0.5	0.0521042	0.121984	0.0451441
	0.75	0.0268138	0.12089	0.0309928
	1	0.0105	0.089	0.028
	R^2	0.9998	0.9994	0.9999

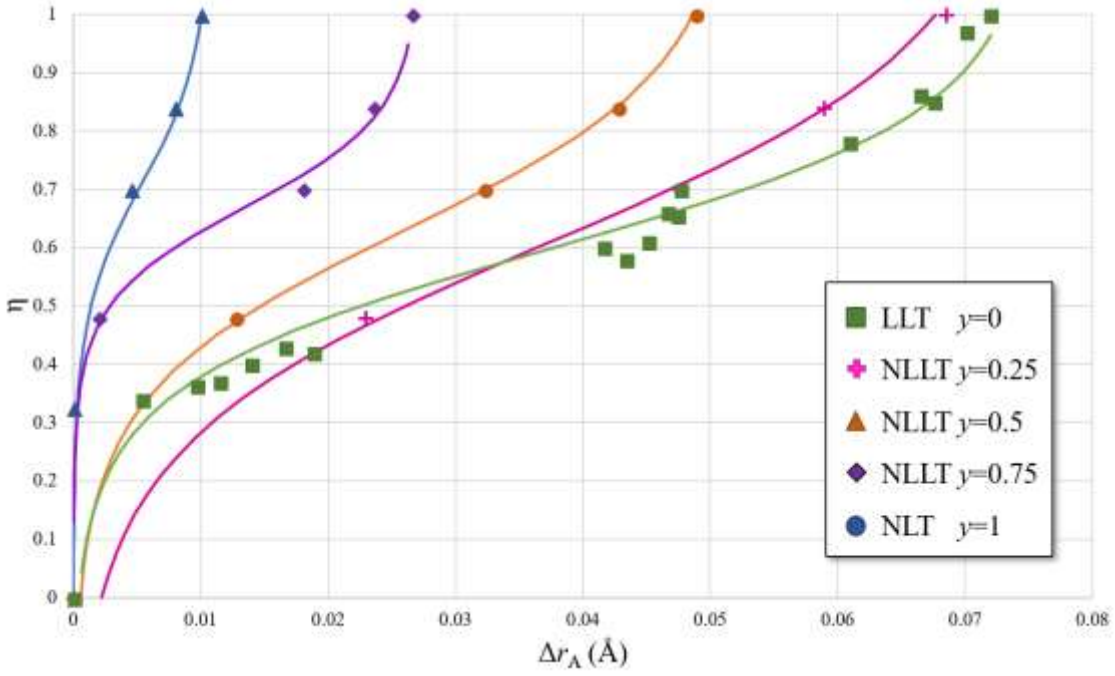

Figure 2.6 A-site order parameters as functions of Δr_A from experimentally collected data for $(Na_yLi_{1-y})_{(1-3x)/2}La_{(1+x)/2}TiO_3$. The y = 0 data are from Ref. [7].

Similarly, the curves in Fig. 2.6 can be described using Eq. 2.2, and Table 2.8 lists all the associated coefficients.

Table 2.8 Coefficients of Eq. 2.2 and the goodness of fit, R^2

y	*A*	*B*	*C*
0	0.6	0.118	0.0753
0.25	0.61	0.175	0.075
0.5	0.63	0.14	0.0521
0.75	0.67	0.08	0.0271
1	0.71	0.11	0.0108
R^2	0.9999	1	0.9998

The curve fits in Fig. 2.7 demonstrate trigonometric relationships between all these coefficients (*A*, *B*, *C*, *P*, *Q*, *S*) and the ideal A-site size when $x = 0$ ($r_{A(id)x=0}$) which are summarized in Eqs. 2.3-2.8. Importantly, Eqs. 2.1-2.8 allow for the prediction of both Δr_A and η using just published ionic radii data.

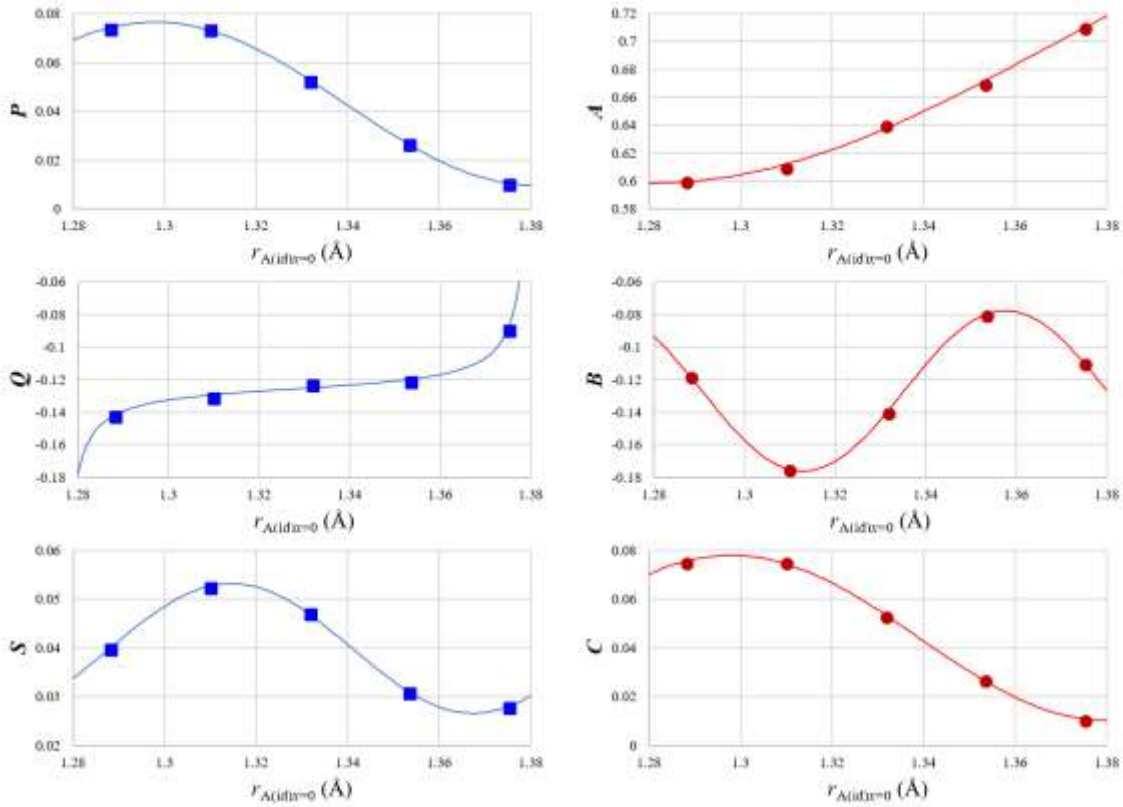

Figure 2.7 Coefficients of Eq. 2.1 (left) and Eq. 2.2 (right) as functions of A-site size, $r_{A(id)x=0}$.

$$A = 0.0959983\cos(-18.3005 r_{\mathrm{A}(id)x=0} + 20.2936) + 0.694574 \quad \left(R^2 = 0.9999\right) \qquad (2.3)$$

$$B = 0.049293\sin(70.2849 r_{\mathrm{A}(id)x=0} - 93.8517) - 0.12697 \quad \left(R^2 = 1\right) \qquad (2.4)$$

$$C = 0.0338009\cos(38.1898 r_{\mathrm{A}(id)x=0} - 49.5677) + 0.044067 \quad \left(R^2 = 0.9998\right) \qquad (2.5)$$

$$P = 0.0334125\sin(37.7844 r_{\mathrm{A}(id)x=0} - 47.4713) + 0.043107 \quad \left(R^2 = 0.9998\right) \qquad (2.6)$$

$$Q = 0.006164\tan(30.0708 r_{\mathrm{A}(id)x=0} - 36.8021) - 0.125554 \quad \left(R^2 = 0.9994\right) \qquad (2.7)$$

$$S = 0.0132533\sin(-59.3986 r_{\mathrm{A}(id)x=0} + 73.3694) + 0.039914 \quad \left(R^2 = 0.9999\right) \qquad (2.8)$$

As the data in tables 2.7 and 2.8 have been derived for the NLLT system, $0 \leq y \leq 1$, these general equations have an accuracy range for titanates in which 1.288 Å $\leq r_{\mathrm{A}} \leq$ 1.375 Å. While the model *may* be more generally applicable, the nature of empirical models makes it impossible to extrapolate beyond this range with *certainty*; and new data would be required in order to validate/revise the model.

Finally, Eq. 2.1 was used with the coefficients in table 2.7 to predict the A-site size correction factor for all of the compositions reported in Ref. [30] (x = 0, y = 0, 0.4, 0.6, 1 and x = 0.2, y = 0, 0.5, 0.65, 0.8). The experimental Δr_{A} (derived from data in Ref. [30]) and predicted Δr_{A} values are shown in Fig. 2.8. The discrepancy in the data points at $x = y = 0$ may be due to the fact that these samples in Ref. [30] were quenched in liquid nitrogen, which resulted in a trigonal unit cell with Li^+ on interstitial sites as previously discussed. On the other hand, the model employed here was developed using data from slowly cooled samples, which results in a layered ordered structure in which Li^+ resides on the A sites. The apparent divergence at x = 0.2, y = 0 may be due to experimental error or a difference in the degree of ordering caused by different cooling rates. In any event, the model

accurately predicts Δr_A to within ~0.01 Å for all of the compositions regardless of processing method.

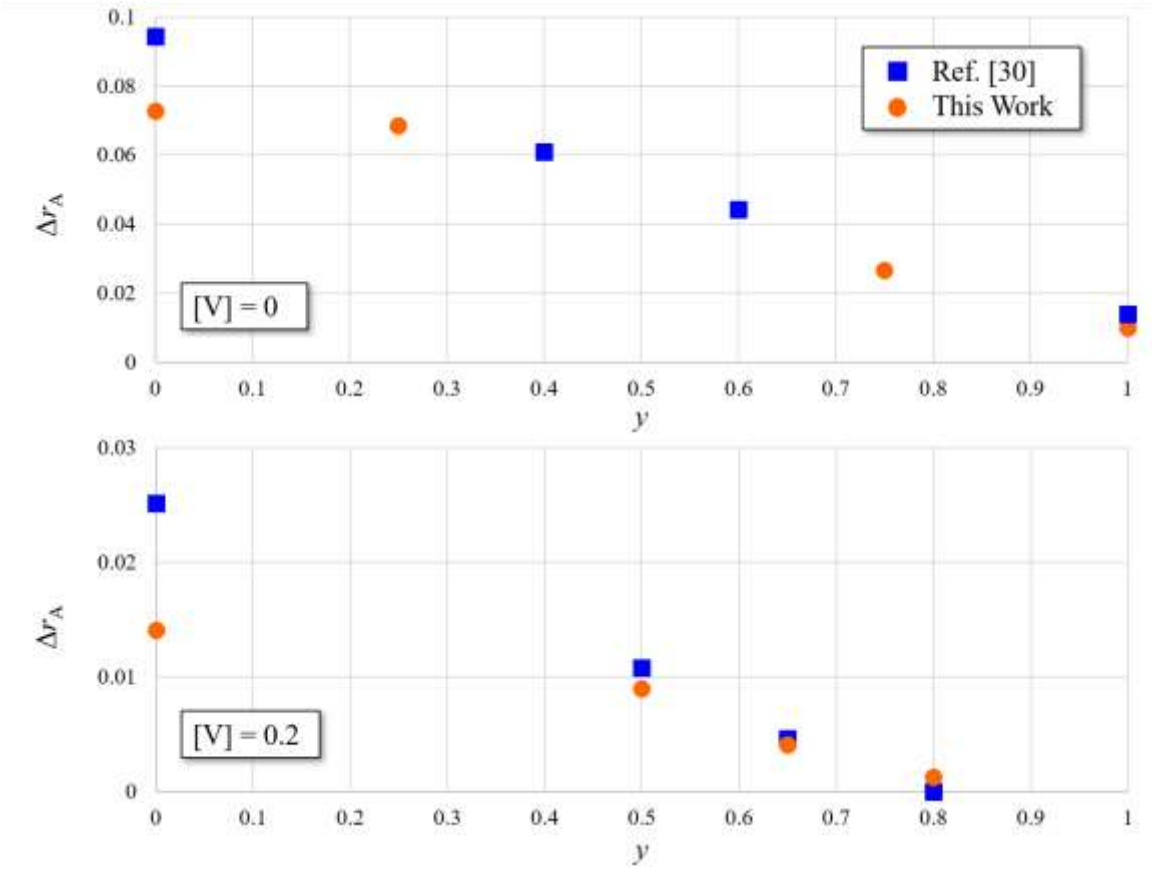

Figure 2.8 $(Na_yLi_{1-y})_{(1-3x)/2}La_{(1+x)/2}TiO_3$ Δr_A values calculated from the data in Ref. [30] (squares) plotted against the results of Eq. 2.1 (circles) for x = 0 (top) and x = 0.2 (bottom).

2.4 Conclusion

Fifteen compositions within the $(Na_yLi_{1-y})_{(1-3x)/2}La_{(1+x)/2}TiO_3$ system (y = 0.25, 0.5, and 0.75; and x = 0, 0.0533, 0.1, 0.1733, and 0.225) were successfully synthesized via a solid-state mixed-oxide route. It can be seen from the XRD patterns that some degree of long-range order exists as x increases; however, electron diffraction patterns show that there is some degree of order present in all compositions. This ordering results in a net increase in cell volume with respect to the disordered state, and several specific models

were developed to describe the A-site size adjustment factor, Δr_A, and A-site ordering parameter, η. Based upon these equations, two general models were developed to describe Δr_A and η as functions of ionic radii in this system. The significance of these models is that they accurately predict/verify the degree of layered A-site ordering in perovskite titanates; and a major implication of this empirical modeling method is that it can potentially be applied to predict the degree of ordering in many other complex perovskite systems.

2.5 References

[1] Miller V, Tidrow S. Perovskites: Temperature and coordination dependent ionic radii. Integrated Ferroelectrics. 2013;148:1-16.

[2] King G, Woodward P. Cation ordering in perovskites. J of Mater Chem. 2010;20:5785-5796.

[3] Miao J, Li L, Liu H, et al. Structure characteristics and valence state study for $La_{1-x}Na_xTiO_3$ synthesized under high-pressure and high-temperature conditions. Mater Lett. 2000;42:1-6.

[4] Ruiz A, López M, Pico C, Veiga M. New $La_{2/3}TiO_3$ derivatives: Structure and impedance spectroscopy. J Solid State Chem. 2002;163:472-278.

[5] Ruiz A, López M, Pico C, Veiga M. Structural modification induced by composition in the $La_{1.33-x}Na_{3x}Ti_2O_6$ perovskites: A neutron diffraction study. Chem Mater. 2005;17:1391-1397.

[6] Knapp M, Woodward P. A-site cation ordering in AA′BB′O_6 perovskites. J Solid State Chem. 2006;179:1076-1085.

[7] Tolman K, Ubic R, Liu B, et al. Empirical evidence for A-site order in perovskites. J Am Ceram Soc. 2017;100:429-442.

[8] Ranjan R, Senyshyn A, Boysen H, Baehtz C, Frey F. Crystal structures of $Na_{1/2}Ln_{1/2}TiO_3$ (Ln: La, Eu, Tb). J Solid State Chem. 2007;180:995-1001.

[9] Li Y, Qin S, Seifert F. Phase transitions in A-site substituted perovskite compounds: The $(Ca_{1-2x}Na_xLa_x)TiO_3$ ($0 \le x \le 0.5$) solid solution. J Solid State Chem. 2007;180:824-833.

[10] Sun P, Nakamura T, Shan Y, Inaguma Y, Itoh M. High temperature quantum paraelectricity in perovskite-type titanates $Ln_{(1/2)}Na_{(1/2)}TiO_3$ (Ln = La, Pr, Nd, Sm, Eu, Gd and Tb). Ferroelectrics. 1997;200:93-107.

[11] Inaguma Y, Tsuchiya T, Katsumata T. Systematic study of photoluminescence upon band gap excitation in perovskite-type titanates $R_{1/2}Na_{1/2}TiO_3$: Pr(R=La, Gd, Lu, and Y). J Solid State Chem. 2007;180:1678-1687.

[12] Takahashi H, Baba Y, Ezaki K, et al. Dielectric characteristics of $(A_{1/2}^{1+}A_{1/2}^{3+})TiO_3$ ceramics at microwave frequencies. Japanese J App Phys. 1991;30(9B):2339-2342.

[13] Ichinose N, Mutoh K. Microwave dielectric properties in the $(1-x)(Na_{1/2}La_{1/2})TiO_3$-$x(Li_{1/2}Sm_{1/2})TiO_3$ ceramic system. J European Ceram Soc. 2003;23:2455-2459.

[14] Fourquet JL, Duroy H, Crosnier-Lopez MP. Structure and microstructural studies of the series $La_{2/3-x}Li_{3x}\square_{1/3-2x}TiO_3$. J Solid State Chem. 1996;127:283-294.

[15] Bhuvanesh N, Bohnké O, Duroy H, Crosnier-Lopez MP, Emery J, Fourquet JL. Topotactic H^+/Li^+ ion exchange on $La_{2/3-x}Li_{3x}TiO_3$: New metastable perovskite phases $La_{2/3-x}TiO_{3-3x}(OH)_{3x}$ and $La_{2/3-x}TiO_{3-3x/2}$ obtained by further dehydration. Mater Res Bull. 1998;33:1681-1691.

[16] Ruiz A, López M, Veiga M, Pico C. Electrical properties of $La_{1.33-x}Li_xTi_2O_6$ ($0.1 < x < 0.3$). Solid State Ionics. 1998;112:291-297.

[17] Ruiz A, López M, Veiga M, Pico C. Structural refinement by neutron diffraction of $La_{1.12}Li_{0.62}Ti_2O_6$. J Solid State Chem. 1999;148:329-332.

[18] Kang E, Kwon Y. The structure of $La_{2/3-x}Li_{3x}\square_{1/3-2x}TiO_3$ by the powder neutron and X-ray diffraction. J Korean Ceram Soc. 2003;40:513-518.

[19] Ibarra J, Várez A, León C, Santamaría J, Torres-Martínez LM, Sanz J. Influence of composition on the structure and conductivity of the fast ionic conductors $La_{2/3-x}Li_{3x}TiO_3$ ($0.03 \leq x \leq 0.167$). Solid State Ionics. 2000;134:219-228.

[20] Sanz J, Várez A, Alonso J, Fernández MT. Structural changes produced during heating of the fast ion conductor $Li_{0.18}La_{0.61}TiO_3$. A neutron diffraction study. J Solid State Chem. 2004;177:1157-1164.

[21] Alonso J, Sanz J, Santamaría J, León C, Várez A, Fernández-Díaz MT. On the location of Li^+ cations in the fast Li-cation conductor $La_{0.5}Li_{0.5}TiO_3$ perovskite. Angew Chem Int Ed. 2000;39:619-621.

[22] Jiménez R, Rivera A, Várez A, Sanz J. Li mobility in $Li_{0.5-x}Na_xLa_{0.5}TiO_3$ perovskites ($0 \leq x \leq 0.5$) influence of structural compositional parameters. Solid State Ionics. 2009;180:1362-1371.

[23] Inaguma Y, Katsumata T, Itoh M, Morii Y. Crystal structure of a lithium ion-conducting perovskite $La_{2/3-x}Li_{3x}TiO_3$ (x=0.5). J Solid State Chem. 2002;166:67-72.

[24] Inaguma Y, Katsumata T, Itoh M, Morii Y, Tsurui T. Structural investigations of migration pathways in lithium ion-conducting $La_{2/3-x}Li_{3x}TiO_3$ perovskites. Solid State Ionics. 2006;177:3037-3044.

[25] Yashima M, Itoh M, Inaguma Y, Morii Y. Crystal structure and diffusion path in the fast lithium-ion conductor $La_{0.62}Li_{0.16}TiO_3$. J Am Ceram Soc. 2005;127:3491-3495.

[26] Sommariva M, Catti M. Neutron diffraction study of quenched $Li_{0.3}La_{0.567}TiO_3$ lithium ion conducting perovskite. Chem Mater. 2006;18:2411-2417.

[27] Stramare S, Thangadurai V, Weppner W. Lithium lanthanum titanates: A review. Chem Mater. 2003;15:3974-3990.

[28] Rivera A, León C, Santamaría J, et al. Percolation-limited ionic diffusion in $Li_{0.5-x}Na_xLa_{0.5}TiO_3$ perovskties ($0 \leq x \leq 0.5$). Chem Mater. 2002;14:5148-5152.

[29] Várez A, Fernández-Diaz MT, Sanz J. Rhombohedral-cubic Transition in $Li_{0.2}Na_{0.3}La_{0.5}TiO_3$ Perovskite. J Solid State Chem. 2004;177:4665-4671.

[30] Herrero CP, Várez A, Rivera A, et al. Influence of Vacancy Ordering on the Percolative Behavior of $(Li_{1-x}Na_x)_{3y}La_{2/3-y}TiO_3$ Perovskites. J Phys Chem B. Materials, Surfaces, Interfaces, & Biophysical. 2005;109:3262-3268.

[31] Jiménez R, Várez A, Sanz J. Influence of octahedral tilting and composition on electrical properties of the $Li_{0.2-x}Na_xLa_{0.6}TiO_3$ ($0 \leq x \leq 0.2$) series. Solid State Ionics. 2008;179:495-502.

[32] Smith E, Tolman K, Ubic R. An empirical model for B-site cation ordering in $Ba(Mg_{1/3}Ta_{2/3})O_3$. J Alloys Compd. 2018;735:2356-2362.

[33] Brous J, Fankuchen I, Banks E. Rare earth titanates with a perovskite structure. Acta Crystallogr Sec A. 1953;6:67-70.

[34] Agranovskaya A. Physical-chemical investigation of the formation of complex ferroelectrics with perovskite structure. Izv Akad Nau. SSSR Ser Fiz. 1960;24:1275-1281.

[35] Garg R, Senyshyn A, Boysen H, Ranjan R. Structure and phase transition of $Na_{(0.5)}La_{(0.5)}TiO_{(3)}$. J Phys Condens Matter. 2008;20:1-6.

[36] Harusani M, Woodward D, Peel M, Ashbrook S, Walton R. Investigation of the hydrothermal crystallization of the perovskite solid solution $NaCe_{1-x}La_xTi_2O_6$ and its defect chemistry. J Solid State Chem. 2013;207:117-125.

[37] O'Quinn EC, Shamblin J, Perlov B, et al. Inversion in $Mg_{1-x}Ni_xAl_2O_4$ spinel: New insight into local structure. J Am Chem Soc. 2017;139:10395-10402.

[38] Karthik C, Anderson T, Gout D, Ubic R. Transmission electron microscopic study of pyrochlore to defect-fluorite transition in rare-earth pyrohafnates. J Solid State Chem. 2012;194:168-172.

[39] García-Martín S, Urones-Garrote E, Knapp M, King G, Woodward P. Structural complexity in $AA'BB'O_6$ perovskites. A transmission electron microscopy study. Mater Res Soc Symp Proc. 2009;1148:15-05.

[40] Shannon R. Revised Effective Ionic-Radii and Systematic Studies of Interatomic Distances in Halides and Chalcogenides. Acta Crystallogr Sec A. 1976;32:751-767.

[41] Ubic R, Tolman K, Talley K, et al. Lattice-constant prediction and effect of vacancies in aliovalently doped perovskites. J Alloys Compd. 2015;644:982-995.

[42] Gönen Z, Paluchowski D, Zavalij P, Eichhorn B, Gopalakrishnan J. Reversible cation/anion extraction from $K_2La_2Ti_3O_{10}$: Formation of new layered titanates, $KLa_2Ti_3O_{9.5}$ and $La_2Ti_3O_9$. Inorg Chem. 2006;45:8736-8742.

CHAPTER THREE: AN EMPIRICAL MODEL FOR B-SITE CATION ORDERING IN $Ba(Mg_{1/3}Ta_{2/3})O_3$

This Chapter was published by Elsevier in the Journal of Alloys and Compounds and should be reference appropriately.

Reference: Smith, E., Tolman, K., Ubic, R., "An Empirical Model for B-site Cation Ordering in $Ba(Mg_{1/3}Ta_{2/3})O_3$," Journal of Alloys and Compounds 735, 2018, pp. 2356-2362, https://doi.org/10.1016/j.jallcom.2017.11.333

3.1 Introduction

The perovskite $Ba(Mg_{1/3}Ta_{2/3})O_3$ (BMT) is known for developing long-range 1:2 cation ordering on the B site after sintering or annealing for long periods of time. In its ordered form it exhibits exceptional microwave dielectric properties.[1,2] In particular, BMT is known in the electroceramics industry to exhibit high Q*f* values (maximum of 430,000 GHz)[2] after long sintering times (>20 hours),[1] making it especially attractive for satellite communications systems; and many pieces of this ceramic currently orbit the earth.

In general, X-ray diffraction (XRD) is a sensitive technique for analyzing B-site long-range cation ordering, which lowers the symmetry with respect to the disordered form and thus gives rise to weak superlattice (ordering) peaks in the XRD patterns.

Nomura *et al.*[3] may have been the first to report that dense samples of BMT had useful properties for microwave dielectric-resonator applications. In order to enhance sinterability, a small amount of Mn was used as a sintering aid, after which they measured Q = 16,800±300 at 10.5 GHz, $\varepsilon_r = 25$, and $\tau_f = 2.7$ MK^{-1}. Sugiyama *et al.*[4] were possibly the first to note that BMT slowly orders with increasing annealing time. They reported the degree of ordering increased from completely disordered in the pre-annealed state to almost completely ordered after 16 hours annealing time at 1600°C. They also noted a trend of increasing Q with increasing annealing time.

The formation mechanisms of BMT during solid-state and wet-chemical synthesis were later analyzed by Surendran *et al.*[5] who observed that the particle size and calcination temperature were both significantly higher for solid-state synthesis. For wet-chemical synthesis, BMT was reported to calcine at 600°C and have an average particle size of 18 nm; whereas, solid-state synthesis required calcination at 1100°C and resulted in an

average particle size of 220 nm. As a result, the solid-state synthesis route resulted in ceramics with larger grains upon sintering. Since the microwave dielectric properties are generally better for larger grain sizes, these samples had better microwave dielectric properties than those produced via the wet-chemical method.

In 1982, Kawashima *et al.*[6] analyzed the microwave dielectric properties of the similar compound $Ba(Zn_{1/3}Ta_{2/3})O_3$ (BZT) and observed that increasing sintering time increased Q. It was also found that Q improved with increasing Zn^{2+} and Ta^{5+} ordering on the B site. In particular, Q increased from near 0 to 14,000 at 12 GHz as sintering time increased (hence, ordering increased) from 0 to 120 hours at 1350°C. A similar study on the microwave dielectric properties of BMT was performed by Kim and Yoon[1] a decade later. They found a small linear correlation between annealing time and the dielectric constant and a much stronger relationship between annealing time and Q. The ordering parameter was found to be maximized after annealing for 20 hours at 1500°C (Fig. 3.1).

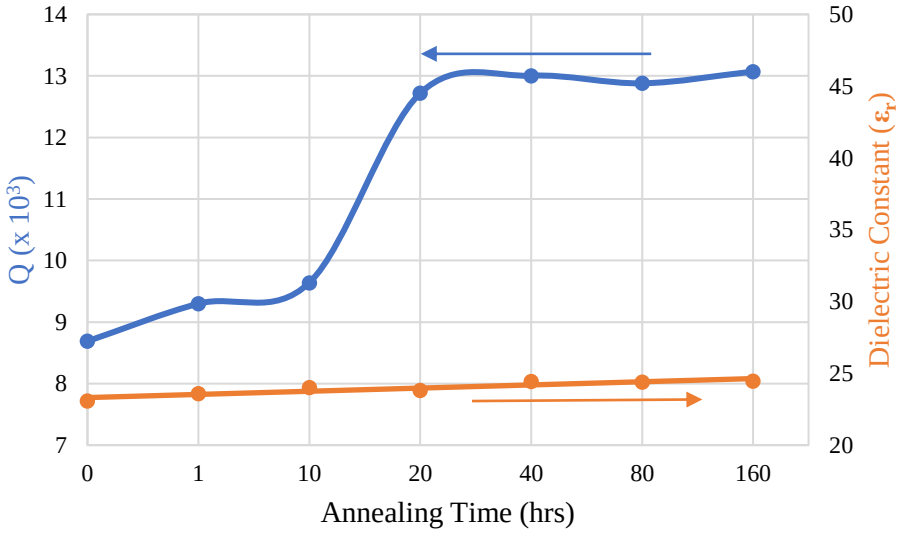

Figure 3.1 Q and dielectric constant (ε_r) values vs. annealing time for $Ba(Mg_{1/3}Ta_{2/3})O_3$[1]

Li *et al.*[7] analyzed the microwave dielectric characteristics of $Ca(Mg_{1/3}Nb_{2/3})O_3$ (CMN) and $Ba(Zn_{1/3}Nb_{2/3})O_3$ (BZN) perovskites. They stacked thin slices of sintered pellets inside a shielded cavity in three arrangements: CMN/BZN, CMN/BZN/CMN, and BZN/CMN/BZN. Finite-element analysis and dielectric-composite models were used to analyze the effect of stacking schemes and volume fraction of BZN on microwave dielectric properties. They reported effective relative permittivities of 34.33-34.52, Q*f* values of 58,800-62,080 GHz, and near-zero temperature coefficients of resonant frequency for these structures.

Structure-dielectric property relationships of five compositions of the perovskite $Ba(M_{⅓}M'_{⅔})O_3$ (M = Mg, Ni, Zn; M′ = Nb, Ta) were analyzed by Lufaso.[2] Rietveld refinements were performed on neutron-diffraction data for these perovskites, and crystal structure models were made from the refinements. On average M-O and M′-O bonds were stretched, whereas the Ba-O bonds were compressed based on calculated bond valence sums. The d^0 M′ ions (Ta^{5+}, Nb^{5+}) reportedly shifted out of their ideal positions at the center of the M′-O octahedra, indicating that second-order Jahn-Teller distortions affect the $M'O_6$ octahedra, which causes three short and three long M′-O bonds to form. A correlation was found between the divalent B-site cation (M^{2+}) and τ_f. Specifically, it was noted that as M^{2+} became more underbonded, τ_f would become more negative. A higher Q*f* was observed if B-site cations exhibited bond valence sums near their formal oxidation states, and the highest Q*f* value (430,000 GHz) was reported for BMT.

Kim *et al.*[8] analyzed the structure and properties of the perovskites $(A_{½}La_{½})(Mg_{½}Ta_{½})O_3$ (A = Ba, Sr, Ca) and $La(Mg_{⅔}Ta_{⅓})O_3$ (LMT) and reported that these compounds exhibited band gaps of 4.6-4.8 eV, dielectric permittivities of ε_r = 18-23, tanδ

= 0.004-0.007, and temperature coefficients of capacitance (τ_c) less than 100 MK^{-1} over the temperature range 20-150°C. In particular, $(Ba_{½}La_{½})(Mg_{½}Ta_{½})O_3$ (BLMT) was reported with a near-zero τ_c. The space groups of these perovskites were reported to be $Fm\bar{3}m$ for BLMT and $P2_1/n$ for $(Sr_{½}La_{½})(Mg_{½}Ta_{½})O_3$ (SLMT), $(Ca_{½}La_{½})(Mg_{½}(Ta_{½})O_3$ (CLMT), and LMT.

In 1997, Janaswamy *et al.*[9] reported $Ba(Mg_{⅓}Ta_{(2-x)/3}Nb_{x/3})O_3$ (BMTN) calcined at 1400°C with a disordered cubic phase. Later it was reported[10] that an ordered trigonal phase begins to appear at higher calcination temperatures, with the degree of order dependent upon the calcination temperature. In 2008, Janaswamy *et al.*[11] reported that the disordered cubic phase appeared at 1300°C. As calcination temperature increased to 1600°C, the concentration of the ordered trigonal phase increased. A fully ordered trigonal phase was observed only for the $x = 0$ (BMT) and $x = 0.4$ compositions. The rest of the solid-solution series contained some degree of disorder.

In 1980, Setter and Cross[12] were the first to analyze the effect of cation size and charge on the degree of ordering in $A(B'B'')O_3$ perovskites. According to their study, large differences in either charge or size of B′ and B″ ions tend to lead to a higher degree of cation ordering. Over a decade later, work by Zhang *et al.*[13] and Gui *et al.*[14] seemed to corroborate these findings. Zhang *et al.*[13] derived an ordering structure factor, F_0, which was determined from the charge difference and size difference of the B-site ions. F_0 is larger when charge and size differences are small, but is more strongly affected by charge differences.

Lei *et al.*[15] analyzed the ordering transition in BMT particularly. They observed diffuse superlattice reflections along all <111> directions in electron-diffraction patterns

of unannealed BMT, indicative of ordered nano-domains (*i.e.*, short-range ordering). They attributed this short-range order to defects on the B-site cation sublattice, which resulted in local excesses of Mg^{2+} or Ta^{5+}. As annealing time increased, 1:2 ordered nuclei appeared; and long-range order appeared only after long annealing times.

Recently, Tolman *et al.*[16] derived empirical models for A-site ordering of two perovskite systems. First, four compositions in the $Na_{(1-3x)/2}La_{(1+x)/2}TiO_3$ (NLT) system (x = 0.0, 0.0533, 0.1733 and 0.225) were synthesized. It was shown via electron diffraction that these perovskites contain a layered short-range order on the A site, and the degree of ordering decreases as x increases. Interestingly, they reported that the ordered form had a larger unit volume than did its disordered counterpart. Furthermore, various compositions in the $Li_{(1-3x)/2}La_{(1+x)/2}TiO_3$ (LLT) system reported in the literature were analyzed. Unlike NLT, these perovskites have been reported with A-site long-range order.[17,18]

The A-site ordering model derived by Tolman *et al.*[16] and both specific examples show a somewhat counterintuitive trend of volume *increase* with increase in A-site order. This phenomenon is in contrast to the trend generally observed for ordering on the B-site, in which case an overall volume *decrease* is typically observed, as demonstrated by Tolman *et al*.[16] Despite the opposite nature of the effect with respect to A-site ordering, one would expect both to be equally amenable to empirical modeling.

This work focuses on developing an empirical model for B-site ordering in $Ba(Mg_{1/3}Ta_{2/3})O_3$ (BMT). This compound was chosen because the extended annealing treatments required to produce full order enable several intermediate partially-ordered states to be easily investigated in order to unambiguously support the prediction that B-site ordering is the cause of the volume shrinkage. In order to develop a model that can predict

the ordering parameter as a function of annealing time or Δr_B, specimens were annealed at 1500°C for five different times (5, 10, 20, 30, and 40 hours). As the degree of order in perovskites is directly related to Q, such a model would be a quick diagnostic for high-Q BMT materials and, if generalized, could be extended to other complex perovskite systems.

3.2 Materials and Methods

A series of $Ba(Mg_{⅓}Ta_{⅔})O_3$ (BMT) samples were synthesized via the solid-state mixed-oxide route. Stoichiometric amounts of $BaCO_3$ (99.95%, Alfa-Aesar, Thermo Fisher Scientific, Tewksbury, MA), $4MgCO_3•Mg(OH)_2•4H_2O$ (43.5%, Alfa-Aesar, Thermo Fisher Scientific, Tewksbury, MA), and Ta_2O_5 (99.95%, Alfa-Aesar, Thermo Fisher Scientific, Tewksbury, MA) were then ball milled with yttria-stabilized ZrO_2 (YSZ) media using deionized water in a high-density nylon pot for ~24 hours. Powders were then dried overnight in an atmospheric drying oven at 95°C until the water was evaporated. The powders were placed in an alumina crucible for calcination, which was conducted in a box furnace (1807FL, CM Furnaces Inc., Bloomfield, NJ) at 1200°C for 12 hours. Calcined powders were then sieved to under 250 μm and re-milled in deionized water for 24 hours adding 2 wt% polyethylene glycol (PEG 10,000, Alfa-Aesar, Heysham, UK) in a water solution for the last three minutes of milling. The mixture was then dried overnight in an atmospheric drying oven at 95°C until all the water had evaporated. Cylindrical pellets 8-10 mm in height and 10 mm in diameter were then formed via uniaxial pressing at 63 MPa. One pellet and some unpressed powder were then subjected to each of six heat treatments: 5, 10, 15, 20, 30 or 40 hours at 1500°C.

Powder XRD measurements were performed in a diffractometer (Miniflex-600, Rigaku, Woodlands, TX) operating with convergent-beam geometry and Cu Kα radiation

(λ=1.540593 Å). Refinements of the XRD data were performed using FULLPROF. The background was fitted with a sixth-order Chebyshev polynomial.

3.3 Results and Discussion

No secondary phases were detected in $Ba(Mg_{1/3}Ta_{2/3})O_3$ samples via XRD (Fig. 3.2). The superlattice reflections resulting from long-range ordering are not present in XRD patterns of specimens annealed for less than 20 hours, in agreement with Lei *et al.*[15] who reported that BMT contained short-range-ordered nanodomains in similar samples, with long-range order beginning to appear on the B-site only after 20 hours. The XRD patterns in Fig. 3.2 were all indexed in the pseudocubic setting, with ordering peaks, which can only be indexed according to the trigonal unit cell, starred.

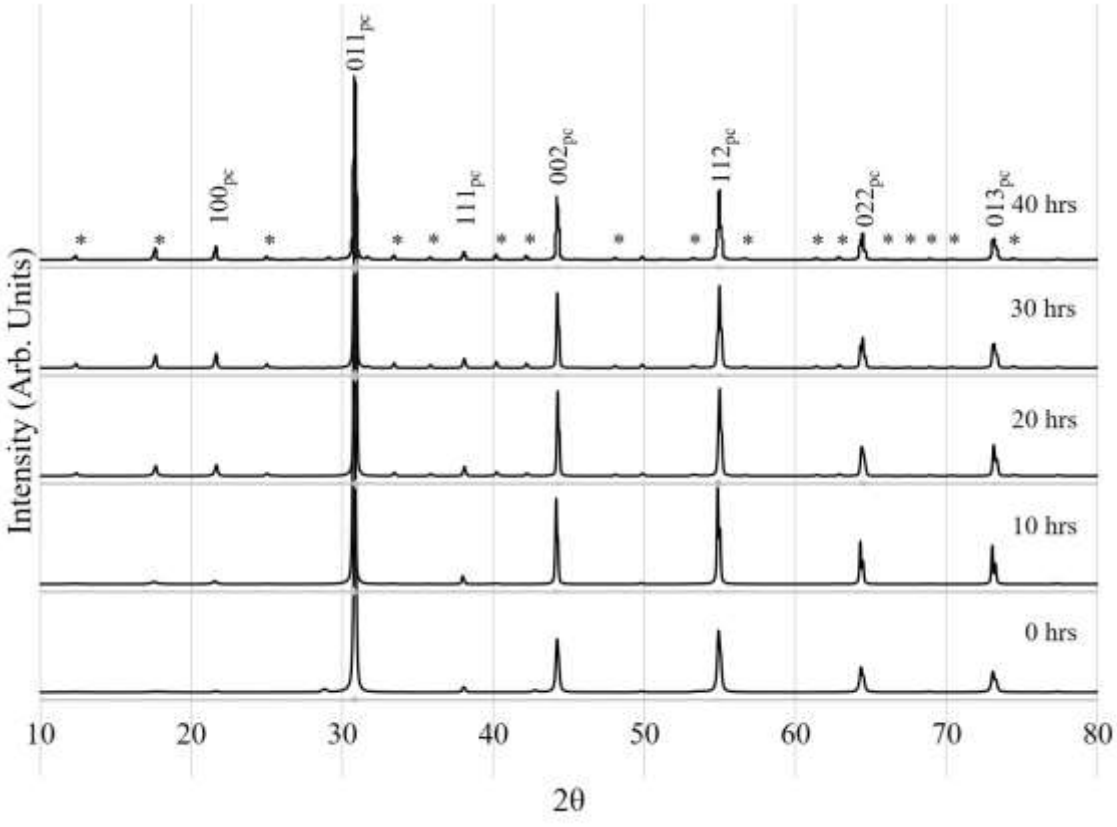

Figure 3.2 X-ray diffraction data of $Ba(Mg_{1/3}Ta_{2/3})O_3$ samples annealed for 0 – 40 hours. Peaks marked with a * result from long-range B-site cation ordering.

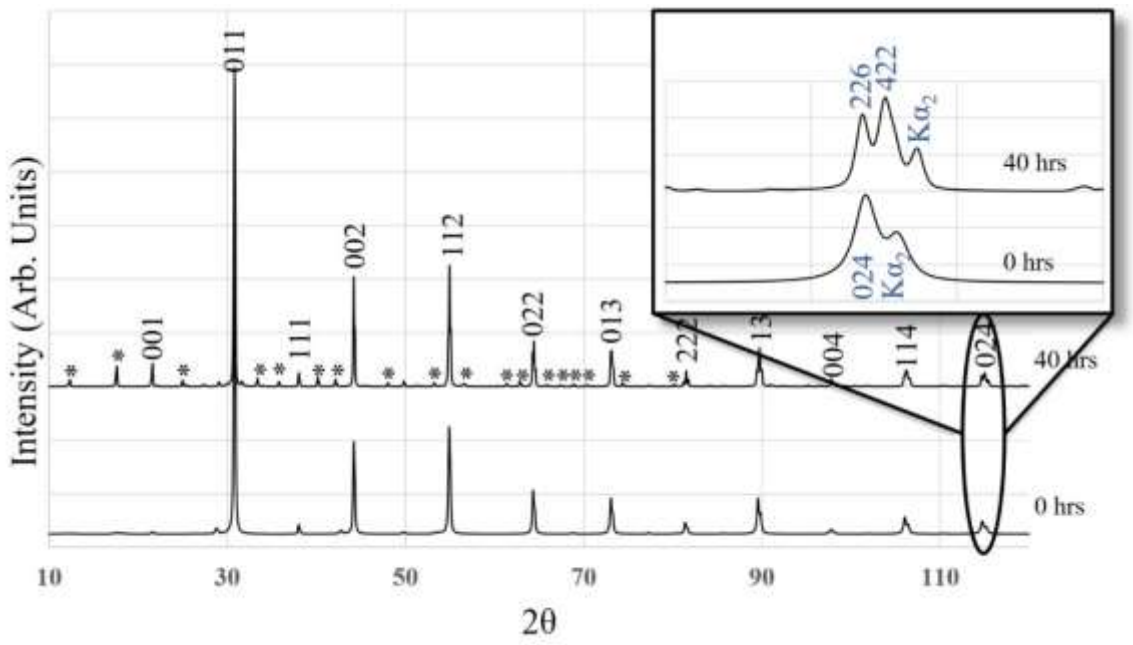

Figure 3.3 $Ba(Mg_{⅓}Ta_{⅔})O_3$ X-ray diffraction with annealing times of 0 and 40 hours. Peaks marked with a * result from long-range B-site cation ordering. The inset shows the trigonal distortion of the structure in the splitting of the 024_c peak into 226_t and 422_t peaks.

Close inspection of the XRD peaks in Fig. 3.3 reveals that BMT exhibits a trigonally distorted lattice after 40 hours of annealing. In particular, the 024 cubic peak at 114.74°, which occurs for unannealed samples, splits into trigonal 226 and 422 peaks at 114.71° and 115.01°, respectively, after annealing for 40 hours, as previously reported.[10,11]

Ordering is typically expected to produce structures that exhibit greater packing efficiency than disordered structures;[19] hence, ordering in complex perovskites should result in structures with smaller unit volumes than those of their disordered counterparts. With this reasoning, the expected trend would be a decrease in unit volume with increasing order.

In the case of B-site ordered $Ba(Mg_{1/3}Ta_{2/3})O_3$, Mani *et al.*[20] reported a unit cell with a_{pc} = 4.0868 Å; however, using this value, the modeling technique of Ubic *et al.*[21]

results in unexpectedly large positive errors in both a'_{pc} (0.952%) and a''_{pc} (1.595%), suggesting an overestimation of r_B caused by the volume shrinkage induced by ordering, as discussed by Tolman *et al.*[16] Other examples are listed in Tables 3.1 and 3.2. Table 3.1 shows the results without correcting for B-site shrinkage while Table 3.2[20-26] shows the results after adding a correction term, Δr_B, effectively removing the errors in both a'_{pc} and a''_{pc}. The phenomenon of volume shrinkage upon B-site ordering has already been demonstrated[16] via DFT in the case of $La(Zn_{0.5}Ti_{0.5})O_3$, which reportedly[26] forms with 1:1 B-site ordering in space group $P2_1/n$. These calculations showed that the unit volume does, in fact, decrease upon ordering, validating the empirical modeling technique.[21] Specifically, the disordered form had a calculated unit volume at 0 K of 253.27 $Å^3$ compared to the ordered variant which had a unit volume of 252.24 $Å^3$. The relative energies of the ordered and disordered forms were 0.0952 eV and -0.2131 eV, respectively, indicating that the ordered form is the more stable, as observed experimentally.[26]

Table 3.1 B-site ordered compounds using ideal B-site sizes (Å).

Composition	$a_{pc(exptl)}$ Eq. 1.5	$a_{pc}=f(t')$ Eq. 1.19	Error (%)	a'_{pc} Eq. 1.3	Error (%)	a''_{pc} Eq. 1.4	Error (%)
[a]$Ca(Mg_{1/2}W_{1/2})O_3$	3.8707	3.9515	2.086	3.9628	2.379	3.9468	1.966
[b]$Sr(Mg_{1/2}W_{1/2})O_3$	3.9530	4.0298	1.942	4.0129	1.515	4.0295	1.936
[c]$Ba(Mg_{1/2}W_{1/2})O_3$	4.0542	4.1339	1.966	4.1152	1.506	4.1395	2.105
[d]$Pb(Mg_{1/2}W_{1/2})O_3$	3.9996	4.0724	1.821	4.0469	1.183	4.0746	1.875
[e]$La(Zn_{1/2}Ti_{1/2})O_3$	3.9503	3.9903	1.011	3.9966	1.170	3.9868	0.924
[f]$Ba(Mg_{1/3}Ta_{2/3})O_3$	4.0868	4.1467	1.467	4.1257	0.952	4.1519	1.595

[a]Ref. [22]; [b]Ref. [23]; [c]Ref. [24]; [d]Ref. [25]; [e]Ref. [26]; [f]Ref. [20].

Table 3.2 B-site ordered compounds accounting for cation effective sizes (Å).

Composition	Δr_B	$a_{pc(exptl)}$ Eq. 1.5	$a_{pc}=f(t')$ Eq. 1.19	Error (%)	a'_{pc} Eq. 1.3	Error (%)	a''_{pc} Eq. 1.4	Error (%)
[a]$Ca(Mg_{1/2}W_{1/2})O_3$	-0.036137	3.8707	3.8771	0.165	3.8842	0.348	3.8707	0.000
[b]$Sr(Mg_{1/2}W_{1/2})O_3$	-0.044354	3.9530	3.9524	-0.016	3.9359	-0.433	4.9530	0.000
[c]$Ba(Mg_{1/2}W_{1/2})O_3$	-0.045825	4.0542	4.0458	-0.208	4.0459	-0.203	4.0542	0.000
[d]$Pb(Mg_{1/2}W_{1/2})O_3$	-0.045877	3.9996	3.9953	-0.109	3.9743	-0.632	3.9996	0.000
[e]$La(Zn_{1/2}Ti_{1/2})O_3$	-0.017712	3.9503	3.9544	0.104	3.9588	0.213	3.9503	0.000
[f]$Ba(Mg_{1/3}Ta_{2/3})O_3$	-0.035005	4.0868	4.0794	-0.179	4.0718	-0.365	4.0868	0.000

[a]Ref. [22]; [b]Ref. [23]; [c]Ref. [24]; [d]Ref. [25]; [e]Ref. [26]; [f]Ref. [20].

The results of annealing time for BMT are shown in Figs. 3.4 and 3.5. Fig. 3.4 demonstrates that, as the order parameter increases, the volume of the unit cell shrinks. The order parameter, η, was calculated by the difference of the occupancies of the two B-site species in the two relevant Wyckoff positions in $P\bar{3}m1$:

$$\eta = |[Mg]_{1b} - [Mg]_{2d}| = |[Ta]_{2d} - [Ta]_{1b}| \quad (3.1)$$

Table 3.3 X-ray powder Rietveld refinement results for $Ba(Mg_{1/3}Ta_{2/3})O_3$ in space group $P\bar{3}m1$.

Anneal time (hr)	***a* (Å)**	***c* (Å)**	**Vol (Å^3)**	**η**
Unannealed	5.7823(7)	7.0748(6)	204.855(67)	0.248
5	5.7767(4)	7.0816(6)	204.656(34)	0.454
10	5.7728(4)	7.0839(8)	204.442(39)	0.677
15	5.7726(7)	7.0898(6)	204.602(68)	0.725
20	5.7726(5)	7.0883(8)	204.559(39)	0.860
30	5.7722(5)	7.0914(7)	204.617(42)	0.939
40	5.7709(4)	7.0899(6)	204.483(32)	0.945

The refinements in Table 3.3 clearly show that, while *c* generally increases with increasing η, *a* decreases such that an overall decrease in unit-cell volume is observed. This result is illustrated in Fig. 3.4 and supports the hypothesis that, while ionic displacements push successive ordered planes apart (ordering in BMT is normal to *c*), as also observed in cases of A-site ordering, ionic spacings *within* ordered planes decrease due to more efficient packing. In the case of A-site ordering, it seems that the former effect dominates while, for B-site ordering, the latter dominates.

In the specific case of BMT, the disordered form reported by Janaswamy *et al.*[9-11] has a cubic lattice constant of a = 4.0893 – 4.0884 Å and so contains a {111} spacing of ~2.3604 – 2.3610 Å. On the other hand, the ordered form reported by, for example, Mani *et al.*,[20] can be described with a smaller *pseudocubic* lattice constant of a_{pc} = 4.0868 Å,

with an average spacing of ordered planes parallel to (001) of 2.3638 Å. Additionally, the spacing between a Mg^{2+} (001) plane and a Ta^{5+} (001) plane is 2.2875 Å, whereas the spacing between two adjacent Ta^{5+} (001) planes is 2.5188 Å; therefore, although the structure expands overall along [001] upon ordering, the reason that it expands is due entirely to the two adjacent Ta^{5+} (001) ordered planes (ionic demixing). This is most likely due to the very high oxidation state of Ta^{5+}, which will create two very highly charged (001) planes that mutually repel. This explanation supports the hypothesis that in a 1:1 rock salt B-site ordered compound, the structure actually shrinks along the $[111]_{pc}$ because the spacing between adjacent Mg^{2+}-rich and Ta^{5+}-rich $(111)_{pc}$ planes is smaller (2.2875 Å) than the average $(111)_{pc}$ spacing in the disordered variant of BMT (~2.3604 – 2.3610 Å). Additionally, the interatomic distance between two nearest B-site atoms within the $(111)_{pc}$ planes in the disordered variant of BMT is ~5.7831 Å – 5.7819 Å, whereas the interatomic distance between nearest B-site atoms (both Ta^{5+} and Mg^{2+}) within the $(111)_{pc}$ ordered planes is 5.7743 Å, which supports the hypothesis that the structure packs more efficiently within the ordering planes.

Table 3.4 Crystallographic comparison of disordered and ordered forms of BMT

$Pm\bar{3}m$ (disordered)	$P\bar{3}m1$ (ordered)
	a = 5.77428 Å, c = 7.09139 Å;
a = 4.0893 Å	a_{pc} = 4.0868 Å
$d_{\{111\}}$ = 2.3610 – 2.3604 Å	$d_{(001)}$ = 2.3638 Å

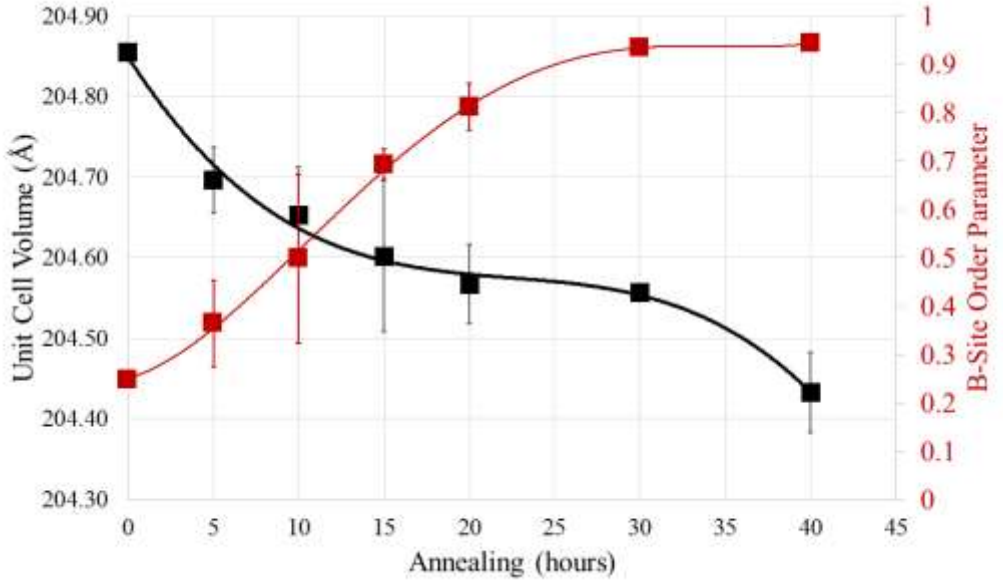

Figure 3.4 Ba(Mg⅓Ta⅔)O3 unit-cell volume (black curve) and order parameter (red curve) as a function of annealing time

It is clear from Fig. 3.4 that the volume shrinkage is directly related to increasing B-site order caused by increased annealing time. Eq. 3.2 describes the black curve in Fig. 3.4, which relates the unit-cell volume ($Å^3$) to annealing time in hours, t:

$$Vol = 204.85 - 0.0332t + 0.0014t^2 - 2x10^{-5}t^3 \quad \left(R^2 = 0.9917\right) \tag{3.2}$$

Furthermore, Eq. 3.3 relates η to the annealing time in hours, t (red curve in Fig. 3.4):

$$\eta = \frac{0.973062}{1+\exp\left(\frac{8.72456-t}{7.37166}\right)} \quad \left(R^2 = 0.9989\right) \tag{3.3}$$

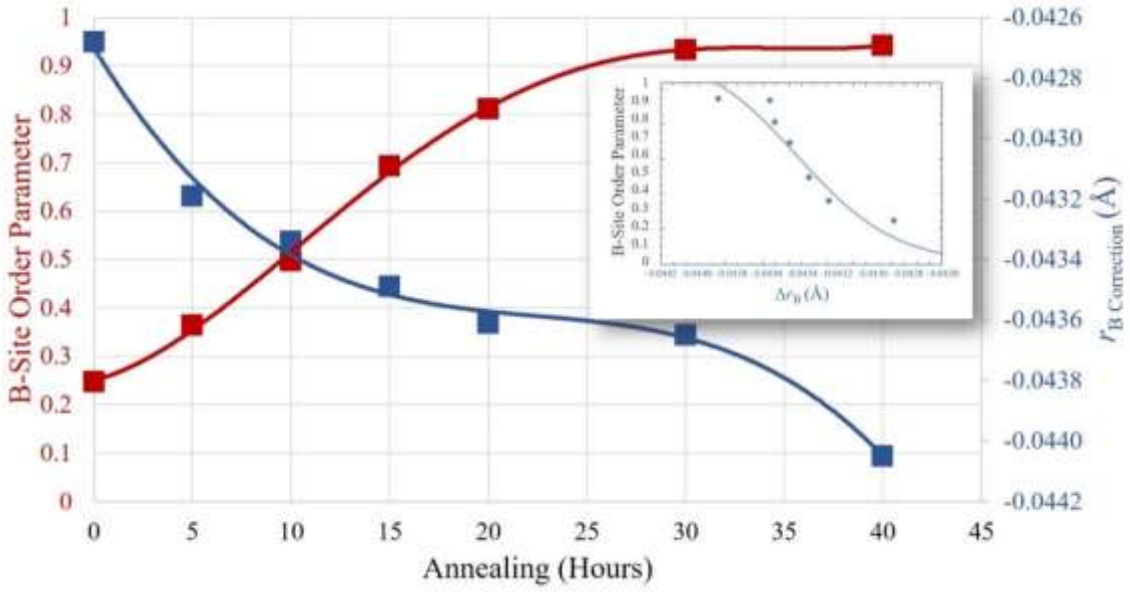

Figure 3.5 $Ba(Mg_{⅓}Ta_{⅔})O_3$ order parameter (red curve) and B-site size adjustment (blue curve) as a function of annealing time. The inset shows the order parameter as a function of Δr_B and can be thought of as an empirical model for ordering (0 = disorder, 1 = fully ordered)

Fig. 3.5 shows the inherent relationships between η, Δr_B, and t. In particular, the inset shows that η decreases as Δr_B increases, corresponding to an increasing unit-cell volume. Eq. 3.4 describes the blue curve in Fig. 3.5 which relates Δr_B to t.

$$\Delta r_B = -0.0427 - 0.0001t + 5x10^{-6}t^2 - 7x10^{-8}t^3 \quad \left(R^2 = 0.9952\right) \tag{3.4}$$

Eq. 3.5 describes the relationship between η and Δr_B (inset in Fig. 3.5).

$$\eta = \frac{1.22869}{1 + \exp\left(\frac{0.0434304 + \Delta r_B}{3.83894x10^{-4}}\right)} \tag{3.5}$$

The increase in the order parameter shown in Figs. 3.4 and 3.5 corresponds to the increase in Q with annealing time depicted in Fig. 3.1, thus providing a clear link between η and Q, as expected. Furthermore, as Fig. 3.4 clearly relates η to volume shrinkage, there is also a link between volume shrinkage and Q.

Of course, it is also possible to simply quantify the relationship between η and either a_{pc} or trigonality (c/a) without ever invoking the model of Ubic *et al.*;[21] however, such a model would necessarily be unique to BMT and could not be generalized to other systems.

3.4 Conclusion

$Ba(Mg_{1/3}Ta_{2/3})O_3$ was synthesized using a conventional solid-state mixed-oxide method and subsequently annealed at 1500°C. The unit-cell volume was found to decrease as the degree of B-site ordering increased. Analysis of the XRD patterns showed a structural transition from cubic to trigonal with increasing annealing time, and it was shown that while ordering caused a shrinkage within the ordered planes, it caused an expansion perpendicular to the ordered planes due to charge imbalances in this case. This observation explains both the volume shrinkage observed upon B-site rock salt ordering and the volume expansion reported in layered A-site ordered perovskites. An empirical model which relates the shrinkage to the degree of order in BMT has been developed. This model could potentially be extended in order to enable the prediction of ordering parameters in other complex perovskite systems from ionic-radii data and experimentally-derived pseudocubic lattice constants alone. It may also be possible to predict the degree of order-induced volume contraction, which has implications for functional properties like Q or ionic conductivity.

3.5 References

[1] E. Kim, K. Yoon, Microwave dielectric properties of complex perovskite $Ba(Mg_{1/3}Ta_{2/3})O_3$, Ferroelectrics, 133 (1992) 187-192.

[2] M. Lufaso, Crystal structures, modeling, and dielectric property relationships of 2:1 ordered $Ba_3MM'_2O_9$ (M = Mg, Ni, Zn; M′ = Nb, Ta) perovskites, Chem. Mater. 16 (2004) 2148-2156.

[3] S. Nomura, K. Toyama, K. Kaneta, $Ba(Mg_{1/3}Ta_{2/3})O_3$ ceramics with temperature-stable high dielectric constant and low microwave loss, Japanese J. Appl. Phys. 21 (1982) L624-L626.

[4] K. Surendran, P. Varma, M. Varma, Solid state synthesis of $Ba(Mg_{1/3}Ta_{2/3})O_3$: a comparative study, Mater. Res. Bull. 42 (2007) 1831-1844.

[5] M. Sugiyama, T. Inuzuka, H. Kubo, Effects of processing on microstructure and dielectric properties in $Ba(Mg_{1/3}Ta_{2/3})O_3$ ceramics, Ceram. Trans. 15 (1990) 153-166.

[6] S. Kawashima, M. Nishida, I. Ueda, H. Ouchi, $Ba(Zn_{1/3}Ta_{2/3})O_3$ ceramics with low dielectric loss at microwave frequencies, J. Am. Ceram. Soc. 66 (1983).

[7] L. Li, X. Chen, Effects of stacking scheme on microwave dielectric characteristics of $Ca(Mg_{1/3}Nb_{2/3})O_3$-$Ba(Zn_{1/3}Nb_{2/3})O_3$ layered dielectric resonators, J. Am. Ceram. Soc. 89 (2006) 2514-2520.

[8] Y. I. Kim, P. Woodward, Crystal structures and dielectric properties of ordered double perovskites containing Mg^{2+} and Ta^{5+}, J. of Solid State Chem. 180 (2007) 2798-2807.

[9] S. Janaswamy, E. Dias, G Murthy, Crystal structure of $Ba(Mg_{1/3}Ta_{2/3})O_3$ calcinated at 1400°C, Bull. Mater. Sci. 20 (1997) 23-25.

[10] S. Janaswamy, G. Murthy, E. Dias, V. Murthy, Structural analysis of $BaMg_{1/3}(Ta,Nb)_{2/3}O_3$ ceramics, Mater. Lett. 55 (2002) 414-419.

[11] S. Janaswamy, G. Murthy, E. Dias, V. Murthy, Structure analysis on the $Ba_3Mg(Ta_{1-x}Nb_x)_2O_9$ ceramics: coexistence of order and disorder, Mater. Res. Bull. 43 (2008) 655-664.

[12] N. Setter, L.E. Cross, The contribution of structural disorder to diffuse phase transitions in ferroelectrics, J. Mater. Science 15 (1980) 2478-2482.

[13] X. Zhang, Q. Wang, Study of the order-disorder transition in $A(B'B'')O_3$ perovskite type ceramics, J. Am. Ceram. Soc. 74 (1991) 2846-2850.

[14] H. Gui, B. Gu, Order-disorder transition in $(A'A'')BO_3$ and $A(B'B'')O_3$ complex perovskite crystals, J. Am. Ceram. Soc. 79 (1996) 381-384.

[15] C. Lei, S. Amelinckx, G. Tendeloo, Disordered $Ba(Mg_{1/3}Ta_{2/3})O_3$ and its ordering transition, Philosophical Magazine A 82 (2002) 2321-2332.

[16] K. Tolman, R. Ubic, B. Liu, I. Williamson, K. Bedke, E. Nelson, L. Li, X. Chen, Empirical evidence for A-site order in perovskites, J. Am. Ceram. Soc. 100 (2017) 429-442.

[17] Y. Inaguma, T. Katsumata, M. Itoh, Y. Morii, Crystal structure of a lithium ion-conducting perovskite $La_{2/3-x}Li_{3x}TiO_3$ (x=0.05), J. Solid State Chem. 166 (2002) 67-72.

[18] A. Ruiz, M. Lopez, M. Viega, C. Pico, Structural refinement by neutron diffraction of $La_{1.12}Li_{0.62}Ti_2O_6$, J. Solid State Chem. 148 (1999) 329-332.

[19] D.R. Askeland, The science and engineering of materials, PWS-Kent Pub. Co., Boston, 1989.

[20] R. Mani, N. Bhuvanesh, K. Ramanujachary, W. Green, S. Lofland, J. Gopalakrishnan, A novel one-pot metathesis route for the synthesis of double perovskites, Ba3MM'2O9 (M = Mg, Ni, Zn; M ' = Nb, Ta) with 1:2 ordering of M and M ' atoms, J. Mater. Chem. 17 (16) (2007) 1589-1592.

[21] R. Ubic, K. Tolman, K. Talley, B. Joshi, J. Schmidt, E. Faulkner, J. Owens, M. Papac, A. Garland, C. Rumrill, K. Chan, N. Lundy, H. Kungl, Lattice-constant prediction and effect of vacancies in aliovalently doped perovskites, J. Alloys Compd. 644 (2015) 982-995.

[22] J. Yang, W. Choo, C. Lee, Ca_2MgWO_6 from neutron and X-ray powder data, Acta Crystallogr. Section C-Crystal Structure Communications 59 (2003) i86-i88.

[23] Mishra, H. Poswal, S. Acharya, A. Tyagi, S. Sharma, Structural evolution of double perovskite Sr(2)MgWO(6) under high pressure, Phys. Status Solidi B-Basic Solid State Physics 247 (7) (2010) 1773-1777.

[24] B. Day, N. Bley, H. Jones, R. McCullough, H. Eng, S. Porter, P. Woodward, P. Barnes, Structure of ordered tungsten- or molybdenum-containing quarternary perovskite oxides, J. Solid State Chem. 185 (2012) 107-116.

[25] G. Baldinozzi, P. Sciau, M. Pinot, D. Grebille, Crystal-Structure of the Antiferroelectric Perovskite Pb2MgWO6, Acta Crystallogr. Section B-Structural Science 51 (1995) 668-673.

[26] R. Ubic, Y. Hu, I. Abrahams, Neutron and electron diffraction studies of La(Zn1/2Ti1/2)O3 perovskite, Acta Crystallogr. Section B-Structural Science 62 (2006) 521-529.

CHAPTER FOUR: CORRELATIVE MODELS FOR PEROVSKITES WITH ROCK SALT B-SITE ORDERING

This chapter was published by John Wiley & Sons, Inc. in the Journal of the American Ceramic Society and should be referenced appropriately.

Reference: Smith, E., Adams, C., Ubic, R., "Correlative Models for Perovskites with Rock Salt B-site Ordering," Journal of the American Ceramic Society 103, Issue 1, 2020, pp. 577-588, https://doi.org/10.1111/jace.16695

4.1 Introduction

Predictive models for composition-structure-property relationships are essential to realizing the full potential of electroceramic materials. Ceramics with the perovskite structure possess a wider range of properties (*e.g.*, pyroelectricity, ferroelectricity, piezoelectricity, superconductivity, *etc*.) than ceramics with almost any other type of crystal structure;[1] thus, eliminating the need for expensive trial-and-error experiments by instead using predictive models to predict structures and properties is key to the future of the electroceramics industry.

There are a vast number of structural distortions in perovskites which cause deviations from the aristotypical perovskite structure in cubic space group $Pm\bar{3}m$. These structural distortions, such as cation ordering, can have significant implications for the materials properties, such as ionic conduction. In perovskites, cation ordering often occurs on alternating {001}, {110}, or {111} pseudocubic planes for both A-site substituted $A'_{0.5}A''_{0.5}BX_3$ or B-site substituted $AB'_{0.5}B''_{0.5}O_3$ complex perovskites[2]. Ordering on {111} (rock salt ordering) is typically preferred for B-site ordering, whereas {001} ordering (layered ordering) tends to be preferred for A-site ordering.

In 1980, Setter and Cross[3] were the first to study cation size and charge effects on the degree of ordering in $AB'_{0.5}B''_{0.5}O_3$ perovskites. According to their study, large differences in either charge or size of B′ and B″ ions tend to lead to a higher degree of cation ordering. Over the next couple of decades, these findings were seemingly corroborated by many studies[4-7]. In particular, Woodward *et al*.[6] observed that if the B′ and B″ cations have a charge difference larger than two, then they will tend to form highly

ordered structures; however, if the charge difference is equal to or less than two, then various degrees of ordering among the B cations will exist.

Interestingly, the large majority of rock salt B-site ordered perovskite oxides seem to prefer monoclinic symmetry in space group $P2_1/n$, with the second most preferential symmetry being cubic $Fm\bar{3}m$;[7-9] however, Howard *et al.*[9] note that many of the perovskites listed with $P2_1/n$ symmetry may actually have higher symmetry, and many of the perovskites listed with $Fm\bar{3}m$ symmetry may have lower symmetry due to varying degrees of octahedral tilting. This discrepancy is primarily due to the fact that the majority of the B-site ordered perovskites reported to date have been studied using X-ray diffraction, but octahedral tilting is notoriously difficult to detect via X-ray diffraction. It is typically visible via electron diffraction, but neutron diffraction would most likely be necessary to accurately quantify the degree of octahedral tilting in such cases.

The $(Ca,Sr,Pb,Ba)(Mg_{1/2}W_{1/2})O_3$ perovskite systems lend themselves particularly well to the study of B-site ordering due to the fact that they are reported[10-25] to exhibit long-range rock salt type ordering of Mg^{2+} and W^{6+} cations on the B site. The $CaMg_{1/2}W_{1/2}O_3$ (CMW) composition has been studied[10,11] via neutron and X-ray diffraction (XRD) and has been reported to exist in monoclinic space group $P2_1/n$. The low symmetry was attributed[10] to tilting of the BO_6 octahedra and an antiparallel shift of the A-site cations along the monoclinic [010]. Moreover, the $SrMg_{1/2}W_{1/2}O_3$ (SMW) perovskite has been investigated[12-16] via neutron diffraction and XRD, and it has been reported with tetragonal symmetry in space group $I4/m$. Likewise, $BaMg_{1/2}W_{1/2}O_3$ (BMW) has been studied[16-20] using neutron diffraction and XRD, but it has been reported with cubic symmetry in space group $Fm\bar{3}m$. In addition, the well-studied $PbMg_{1/2}W_{1/2}O_3$

(PMW) composition was initially reported[21] in cubic space group $Pm\bar{3}m$ but was later reported[22] with orthorhombic symmetry in space group *Pmmm*. Several more studies[23,24] seem to verify that PMW exhibits orthorhombic symmetry at room temperature, but in space group *Pmcn*; however, the most recent study[25] performed on PMW suggests that it crystalizes in cubic space group $Fm\bar{3}m$ at room temperature but transitions to orthorhombic space group *Pmcn* below 8°C.

The $A^{3+}Zn_{0.5}Ti_{0.5}O_3$ perovskite system is an important system for many dielectric applications,[26-28] and it seems to readily display[26-29] long range rock salt B-site ordering. Ubic *et al.*[26] reported a monoclinic symmetry in space group $P2_1/n$ for $LaZn_{0.5}Ti_{0.5}O_3$ (LZT) and observed a completely ordered B site via neutron diffraction. A seemingly different result was later observed by Aguadero *et al.*,[29] who also used neutron diffraction but observed about 10% disorder on the B site; however, the difference is reconcilable considering the difference in experimental processes between the two studies. Aguadero *et al.*[29] used soft-chemistry processing procedures and annealed their samples at 1150°C, whereas Ubic *et al.*[26] used solid-state processing procedures and annealed their samples at 1400°C. The dielectric properties reported by Ubic *et al.*[26] at 4.25 GHz were $\varepsilon_r = 34$, $Qf = 36{,}090$ GHz, and $\tau_f = -70$ MK^{-1}.

$NdZn_{0.5}Ti_{0.5}O_3$ has been reported[27] to exist with monoclinic symmetry with a fully ordered B site. The following dielectric properties were also reported[27] at 8.5 GHz: $\varepsilon_r = 31.6$, $Qf = 170{,}000$ GHz, and $\tau_f = -42$ ppm/°C. Additionally, $PrZn_{0.5}Ti_{0.5}O_3$ (PZT) and $GdZn_{0.5}Ti_{0.5}O_3$ (GZT) were studied[28] via X-ray and electron diffraction. Both compounds were observed[28] with monoclinic symmetry in space group $P2_1/n$, but GZT was reported with a fully ordered B site while PZT was reported with a 95% ordered B site. The B-site

ordering was attributed to a large charge and size difference between the B-site cations (Zn^{2+} and Ti^{4+}). The following dielectric properties were also observed[28] at 1MHz: ε_r = 27 & tanδ = 0.003 for PZT, and ε_r = 17 & tanδ = 0.005 for GZT.

Interestingly, $BiZn_{0.5}Ti_{0.5}O_3$ (BZT) was studied[30] using X-ray and electron diffraction and was reported[30] to exist with a completely disordered arrangement of Zn^{2+} and Ti^{4+} cations on the B site, which would seem to contradict the conclusions of Woodward *et al*.[6] Room temperature dielectric properties of ε_r = 250 and tanδ = 0.1 were observed[30] at 1 MHz.

$AR_{0.5}Ir_{0.5}O_6$ (A = Sr, Ba; R = Sc, Y, La, Lu)[31] and $SrCu_{0.5}Ir_{0.5}O_3$[32] perovskites were studied via X-ray diffraction and were all determined to exhibit a fully ordered B site. All of these compounds are reported with monoclinic symmetry except for $SrCu_{0.5}Ir_{0.5}O_3$, which was reported with tetragonal symmetry in space group *I*4/*m*. Moreover, these perovskites were observed to exhibit paramagnetic properties down to 4.5 K, and $SrCu_{0.5}Ir_{0.5}O_3$ was observed to exhibit magnetic properties above 15 K.

$SrY_{0.5}Ta_{0.5}O_3$[33,34] and $SrY_{0.5}Nb_{0.5}O_3$[33] were both studied via X-ray diffraction and they were observed with a fully ordered B site in monoclinic space group $P2_1/n$. $BaLn_{0.5}Nb_{0.5}O_3$ (Ln = Y, La, Pr, Nd, Sm, Eu, Gd, Tb, Dy, Ho, Er, Tm, Yb, Lu),[35] $BaLn_{0.5}Ta_{0.5}O_3$ (Ln = Y, all lanthanide species),[36] $SrLn_{0.5}Ta_{0.5}O_3$ (Ln = Nd, Pm, Sm, Eu, Gd, Tb, Dy, Ho, Er, Tm, Yb, Lu),[37] and $AIn_{0.5}Nb_{0.5}O_3$ (A = Ca, Sr, Ba)[38] perovskites were all studied using X-ray diffraction[35-37] or neutron diffraction[38]. All compositions were observed in monoclinic space group $P2_1/n$, except for members of the Ln = Dy-Lu series of the $BaLn_{0.5}Ta_{0.5}O_3$ system, which were reported in cubic space group $Fm\bar{3}m$. All compositions were also reported with long range rock salt ordering on the B site. In

addition, all of the compositions, except for the $AIn_{0.5}Nb_{0.5}O_3$ system, were reported with paramagnetic properties down to 5 K.

Interestingly compounds in the $SrM_{0.5}Mo_{0.5}O_3$ (M = Mg, Mn, Fe, Co, Ni, Zn)[39] system were determined via X-ray diffraction to exhibit triclinic symmetry in space group $P\bar{1}$ with nearly fully ordered B sites; however, the similar $SrCa_{0.5}Mo_{0.5}O_3$ perovskite compound has been studied[40] via neutron diffraction and was also reported[40] with a fully ordered B site but in monoclinic space group $P2_1/n$.

It has recently been established[41-43] that, while layered A-site ordering results in a counterintuitive unit-cell volume *increase* compared to the disordered structure, rock salt B-site ordering results in the expected unit-cell volume *decrease* compared to the disordered structure. This result was explained crystalochemically[41] by the fact that ordering causes more efficient packing in perovskites *within* ordered planes but an expansion of bonds *perpendicular* to them. In other words, bonds which lie in or near the ordering planes will contract whereas those more perpendicular will tend to expand. For this reason, a strong indicator of rock salt B-site ordering within this model[42] is an overestimation of B-X bond length, which results in large positive errors (1% - 3%) in both a'_{pc} and a''_{pc}. In these cases, a negative Δr_B correction term can be introduced to effectively correct for these errors.

In this work, four compositions within the $A(Zn_{0.5}Ti_{0.5})O_3$ (A = Nd, Sm, $Nd_{0.5}La_{0.5}$, and $Nd_{0.5}Gd_{0.5}$) (NZT, SZT, NLZT, and NGZT) perovskite system were produced. Another 38 rock salt B-site ordered perovskites were also mined from literature. Empirical models were derived for each specific B-site ordered system. From these data, a general empirical

model has been derived for the B-site size correction factor, Δr_B, similar to the A-site model recently derived by Smith *et al*.[43]

4.2 Materials and Methods

Four compositions in the system $A(Zn_{0.5}Ti_{0.5})O_3$ (A = Nd, Sm, $Nd_{0.5}La_{0.5}$, $Nd_{0.5}Gd_{0.5}$) were synthesized via the solid-state mixed-oxide route. As-received La_2O_3 (99.9%, Acros Organics, Fair Lawn, NJ), Nd_2O_3 (99%, Alfa-Aesar, Ward Hill, MA), and Sm_2O_3 (99.9%, Alfa-Aesar, Ward Hill, MA) powders were first hydroxylated by mixing with an excess of deionized water and drying overnight, forming $La(OH)_3$, $Nd(OH)_3$, or $Sm(OH)_3$. Stoichiometric amounts of ZnO (99.9%, Alfa-Aesar, Ward Hill, MA), TiO_2 (99.5%, Alfa-Aesar, Ward Hill, MA), Gd_2O_3 (99.9%, Alfa-Aesar, Ward Hill, MA) $La(OH)_3$, $Nd(OH)_3$, and $Sm(OH)_3$ were then ball-milled with yttria-stabilized ZrO_2 (YSZ) media using deionized water in a high-density nylon pot for ~6 hours. Powders were then dried overnight in an atmospheric drying oven at ~98°C until all the water was evaporated. An initial dehydroxylation heat treatment was conducted in an open crucible at 600°C for 2 hours. Calcination was subsequently conducted in a closed crucible for two hours in a box furnace (1807FL, CM Furnaces Inc., Bloomfield, NJ) at 1200°C. After calcination, the powders were ground using a porcelain mortar and pestle. Powders were then re-calcined in a closed crucible for two hours at 1400°C, after which they were ball-milled again with YSZ media using deionized water in a high-density nylon pot for ~24 hours. The mixture was then dried overnight in an atmospheric drying oven at ~98°C until all the water had evaporated. The mixture was then ground again using a mortar and pestle and finally sieved to under 250 μm.

Powder XRD measurements were performed in a diffractometer (Miniflex-600, Rigaku, Woodlands, TX) operating with convergent-beam geometry and CuKα radiation. Rietveld refinements were performed on the XRD patterns using GSAS II (Argonne National Laboratory, IL). The background was fitted with a Debye diffuse scattering function with six terms. All compositions were refined in monoclinic space group $P2_1/n$ allowing the cation occupancies and the coordinates of the A-site species in the 4*e* sites to vary.

4.3 Results and Discussion

Figs. 4.1 and 4.2 show the XRD patterns and refinement fits for each of the four compositions that were produced within the $A(Zn_{0.5}Ti_{0.5})O_3$ system, clearly showing that all the compositions had successfully been produced with complete phase purity. Fig. 4.1 also shows that the 110 pseudocubic peak is split into a triplet, which is one of the characteristics of an orthorhombic distortion. This triplet arises due to slight differences in the spacings of the $(0\bar{1}1)_{pc}$, $\{110\}_{pc}/\{101\}_{pc}$, and $(011)_{pc}$; however, the structure is actually monoclinic in space group $P2_1/n$ due to the presence of long-range rock salt ordering of Zn^{2+} and Ti^{4+} cations on the B site.

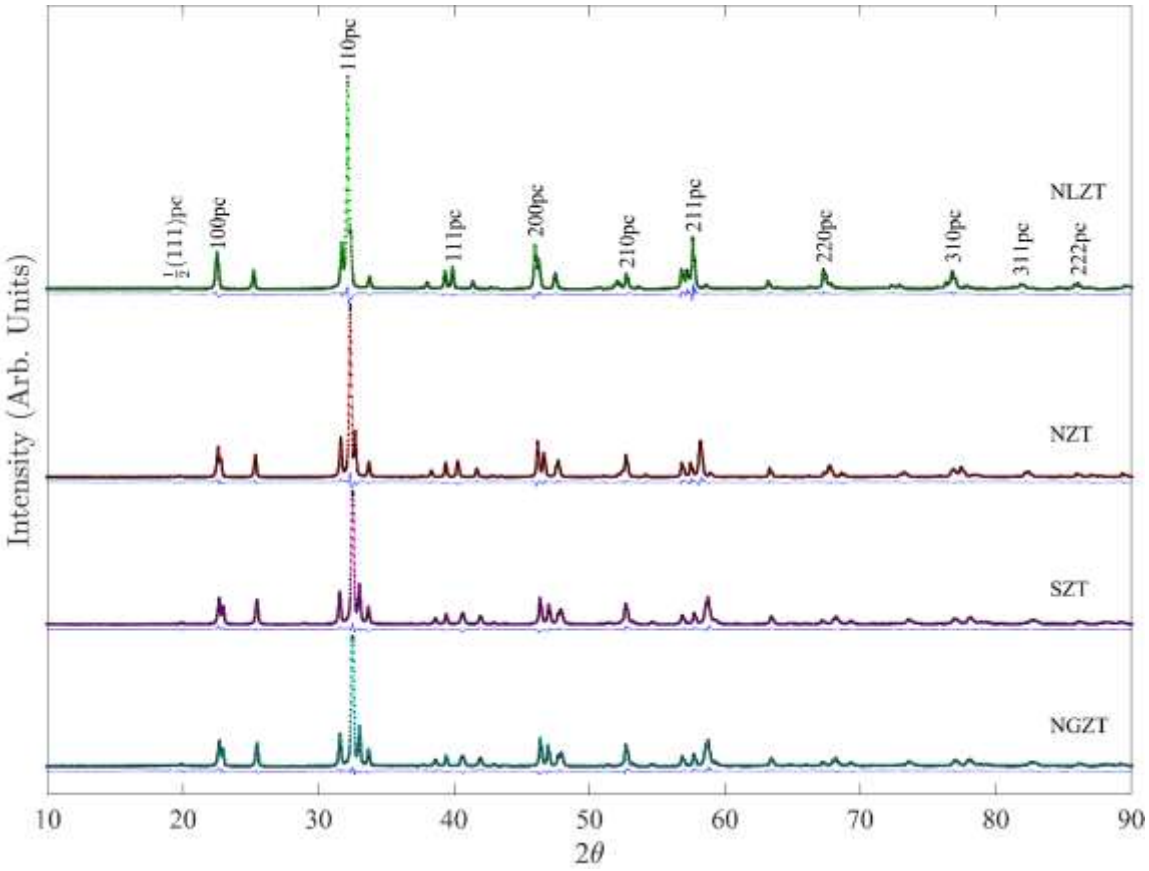

Figure 4.1 Rietveld plots of NLZT, NZT, SZT, and NGZT. The data points correspond to the observed intensities. Both refinement results and difference patterns are shown for each composition, and all peaks are indexed according to the pseudocubic unit cell.

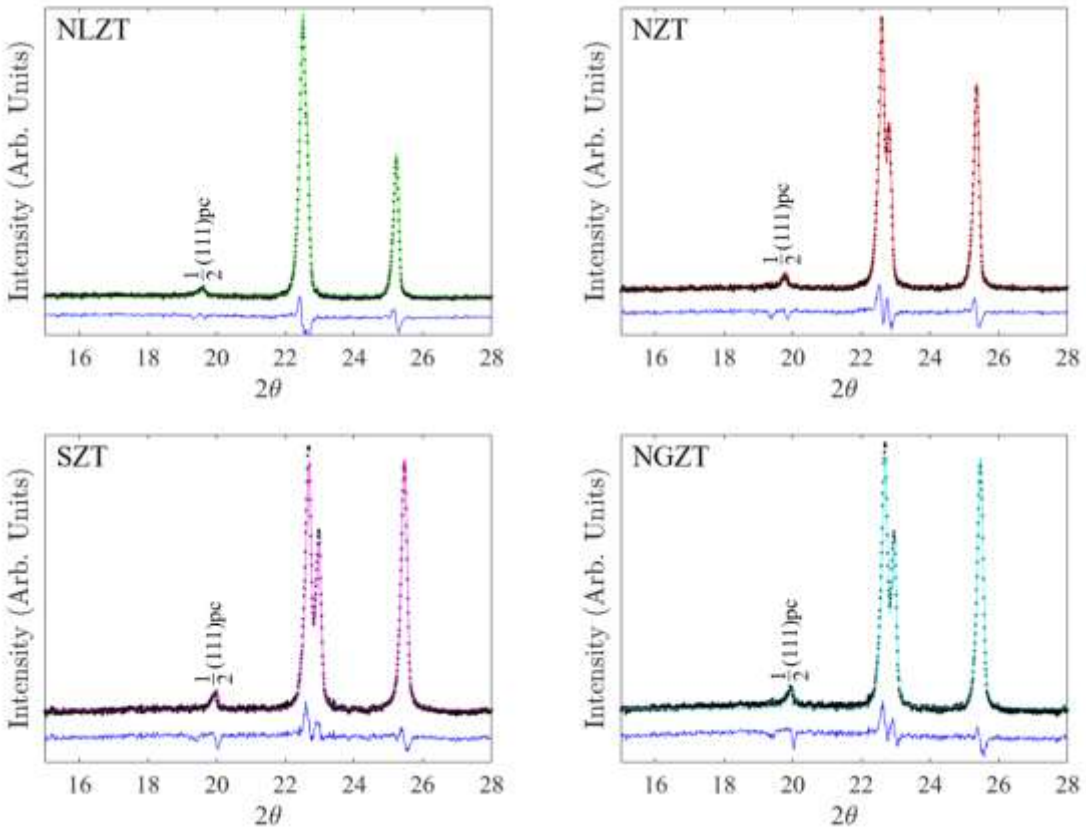

Figure 4.2 Rietveld plots of NLZT, NZT, SZT, and NGZT in the range 15° ≤ 2θ ≤ 28° showing the ½(111)pc peak fit.

The existence of ½{odd,odd,odd}$_{pc}$ peaks may indicate 1:1 B-site ordering; however, ½{odd,odd,odd}$_{pc}$ superlattice reflections are also commonly associated with anti-phase octahedral tilting, which makes it difficult to unambiguously identify the origin of these superlattice reflections via XRD alone; nevertheless, Rietveld analyses of the XRD patterns do suggest that all four of these perovskites exhibit fully ordered B sites.

Table 4.1 shows the results of the Rietveld refinements performed on each of the four compositions within the A($Zn_{0.5}Ti_{0.5}$)O_3 system. The refinements suggest that all four of these perovskites exhibit monoclinic symmetry in space group $P2_1/n$ and display full rock salt ordering of Zn^{2+} and Ti^{4+} cations on the B site. These results also suggest that the

samples become increasingly monoclinic (*i.e.*, β increases) as the size of the A-site species decreases (*i.e.*, as the tolerance factor decreases).

Table 4.1 Refinement Results for Zinc Titanates

A-site species	$(Nd_{0.5}La_{0.5})$	Nd	Sm	$(Nd_{0.5}Gd_{0.5})$
***a* (Å)**	7.84135(8)	7.78132(7)	7.72469(9)	7.73249(9)
***b* (Å)**	5.63482(5)	5.64713(4)	5.65861(6)	5.65563(6)
***c* (Å)**	5.52172(5)	5.46671(5)	5.41550(7)	5.41560(6)
β (°)	90.021(4)	90.099(1)	90.184(1)	90.211(1)
***x* (4(*e*) A-site)**	0.2510(3)	0.2504(4)	0.2500(3)	0.2505(3)
***y* (4(*e*) A-site)**	0.0456(1)	0.0535(1)	0.0602(1)	0.0593(1)
***z* (4(*e*) A-site)**	0.9895(2)	0.9876(2)	0.9851(2)	0.9851(2)
***wR*%**	7.81	5.78	3.58	3.71

Table 4.2 shows the errors in a'_{pc}, a''_{pc}, and a_{pc}, (Eqs. 1.3, 1.4, and 1.19) with respect to the experimental pseudocubic lattice constants. Table 4.3 shows the B-site size correction parameters and the resultant reduced errors in Eqs. 1.3, 1.4, and 1.19. The data from Table 4.2 shows that, in general, the model overestimates the pseudocubic lattice constant for rock salt B-site ordered perovskites, which supports the hypothesis[41] that shrinking bonds within ordered planes will dominate over the effects electrostatic repulsions pushing ordered planes apart.

The large positive errors in pseudocubic lattice constants predicted from the uncorrected model (Table 4.2) result from an apparent overestimation of r_B. Somewhat predictably, the uncorrected model seems to be less accurate for compounds with large differences in B-site cation sizes, whereas it appears to be far more accurate for compounds with similar B-site cation sizes. For instance, the model produces an error of 4.506% when predicting a''_{pc} in $Sr(Ca_{0.5}Mo_{0.5})O_3$, in which the size difference between Ca^{2+} and Mo^{6+}

ions is 0.41 Å; however, the model only produces a 0.170% error in a''_{pc} for $Sr(Cr_{0.5}Ir_{0.5})O_3$, in which the size difference between Cr^{3+} and Ir^{5+} ions is just 0.015 Å.

To effectively minimize and account for the errors coming from the volume contraction upon ordering, the values of r_B were decreased by an amount Δr_B. The value of Δr_B was determined by incrementally decreasing the value of r_B until the errors in a_{pc} (Eq. 1.19), a'_{pc} (Eq. 1.3), and a''_{pc} (Eq. 1.4) were simultaneously minimized. It should be noted that a_{pc} and a''_{pc} are more sensitive to changes in B-site size than is a'_{pc} due to the fact that both a_{pc} and a''_{pc} depend directly on r_B. Thus, the errors in a'_{pc} (Eq. 1.3) tend to be the largest in this case. Table 4.3 displays the results of this iterative process. Also, Eq. 1.19 is used to calculate a_{pc} in tables 4.2 and 4.3, where t' is determined from t_0 and r_A via an empirical model[44] (Eq. 1.14). Additionally, Eqs. 1.3 and 1.4 are used to determine a'_{pc} and a''_{pc} in tables 4.2 and 4.3, where the effective r_X is calculated from a correlative model[44] (Eq. 1.18) using t' and the Shannon radius of the X-site species.

Table 4.2 Experimental and calculated pseudocubic lattice constants (Å) for 42 rock salt B-site ordered perovskites.

ICSD #	Composition	$a_{pc(exptl.)}$ (Å)	a_{pc} Eq. 1.19	Error%	a'_{pc} Eq. 1.3	Error%	a''_{pc} Eq. 1.4	Error%
172775	**$La(Zn_{0.5}Ti_{0.5})O_3$**	3.9503	3.9903	1.0114	3.9966	1.1701	3.9868	0.9240
251934	**$Gd(Zn_{0.5}Ti_{0.5})O_3$**	3.8755	3.9794	2.6795	4.0703	5.0255	3.9754	2.5763
251933	**$Pr(Zn_{0.5}Ti_{0.5})O_3$**	3.9264	3.9508	0.6226	3.9854	1.5034	3.9454	0.4845
*	**$(Nd_{0.5}La_{0.5})(Zn_{0.5}Ti_{0.5})O_3$**	3.9364	3.9646	0.7177	3.9861	1.2627	3.9599	0.5974
*	**$Nd(Zn_{0.5}Ti_{0.5})O_3$**	3.9161	3.9488	0.8370	3.9863	1.7937	3.9433	0.6960
*	**$Sm(Zn_{0.5}Ti_{0.5})O_3$**	3.8969	3.9447	1.2249	3.9930	2.4664	3.9389	1.0778
*	**$(Nd_{0.5}Gd_{0.5})(Zn_{0.5}Ti_{0.5})O_3$**	3.8976	3.9481	1.2953	4.0120	2.9363	3.9425	1.1527
155217	**$Ca(Mg_{0.5}W_{0.5})O_3$**	3.8741	3.9515	1.9985	3.9628	2.2903	3.9468	1.8781
151703	**$Sr(Mg_{0.5}W_{0.5})O_3$**	3.9570	4.0298	1.8398	4.0129	1.4134	4.0295	1.8335
262318	**$Ba(Mg_{0.5}W_{0.5})O_3$**	4.0542	4.1339	1.9660	4.1153	1.5055	4.1395	2.1047
262284	**$Pb(Mg_{0.5}W_{0.5})O_3$**	3.9996	4.0724	1.8213	4.0469	1.1834	4.0746	1.8753
170684	**$Sr(Y_{0.5}Nb_{0.5})O_3$**	4.1263	4.2362	2.6632	4.2257	2.4083	4.2360	2.6592
193235	**$Sr(Yb_{0.5}Nb_{0.5})O_3$**	4.1028	4.2050	2.4913	4.1931	2.2029	4.2047	2.4846
247459	**$Sr(Y_{0.5}Ta_{0.5})O_3$**	4.1237	4.2362	2.7286	4.2257	2.4735	4.2360	2.7246
88838	**$Ba(Pr_{0.5}Nb_{0.5})O_3$**	4.2878	4.4298	3.3114	4.3766	2.0707	4.4279	3.2687
95524	**$Sr(Tm_{0.5}Ta_{0.5})O_3$**	4.1117	4.2166	2.5532	4.2053	2.2772	4.2164	2.5475
172169	**$Sr(In_{0.5}Nb_{0.5})O_3$**	4.0568	4.1399	2.0498	4.1256	1.6973	4.1395	2.0389
290859	**$Ba(La_{0.5}Ta_{0.5})O_3$**	4.3198	4.4696	3.4688	4.4143	2.1878	4.4670	3.4087
88152	**$Sr(Sc_{0.5}Ir_{0.5})O_3$**	3.9917	4.0253	0.8413	4.0084	0.4177	4.0251	0.8358
88153	**$Ba(Sc_{0.5}Ir_{0.5})O_3$**	4.0738	4.1291	1.3574	4.1113	0.9214	4.1349	1.4991
88154	**$Sr(Y_{0.5}Ir_{0.5})O_3$**	4.0923	4.1684	1.8596	4.1551	1.5351	4.1680	1.8502
88155	**$Ba(Y_{0.5}Ir_{0.5})O_3$**	4.1745	4.2775	2.4674	4.2373	1.5063	4.2791	2.5063
88156	**$Ba(La_{0.5}Ir_{0.5})O_3$**	4.2836	4.4032	2.7915	4.3517	1.5892	4.4019	2.7514

88157	**$Sr(Lu_{0.5}Ir_{0.5})O_3$**	4.0642	4.1315	1.6551	4.1169	1.2963	4.1310	1.6439
88158	**$Ba(Lu_{0.5}Ir_{0.5})O_3$**	4.1461	4.2402	2.2691	4.2047	1.4123	4.2428	2.3316
192738	**$Sr(Cu_{0.5}Ir_{0.5})O_3$**	3.9471	3.9640	0.4263	3.9472	0.0027	3.9644	0.4372
246736	**$Sr(Cr_{0.5}Sb_{0.5})O_3$**	3.9328	3.9386	0.1475	3.9224	-0.2633	3.9395	0.1696
157007	**$Sr(Ga_{0.5}Sb_{0.5})O_3$**	3.9284	3.9428	0.3658	3.9265	-0.0486	3.9436	0.3857
33623	**$Ba(Sc_{0.5}Sb_{0.5})O_3$**	4.1015	4.1579	1.3746	4.1349	0.8140	4.1628	1.4942
246959	**$Sr(Sm_{0.5}Sb_{0.5})O_3$**	4.1607	4.2539	2.2409	4.2442	2.0066	4.2539	2.2385
247246	**$Sr(In_{0.5}Sb_{0.5})O_3$**	4.0508	4.1026	1.2788	4.0871	0.8971	4.1021	1.2672
262994	**$Sr(Sc_{0.5}Sb_{0.5})O_3$**	4.0172	4.0522	0.8728	4.0357	0.4600	4.0519	0.8637
50040	**$Ba(Bi_{0.5}Sb_{0.5})O_3$**	4.2750	4.4298	3.6205	4.3766	2.3761	4.4279	3.5777
84660	**$Ba(Tl_{0.5}Sb_{0.5})O_3$**	4.1905	4.2918	2.4180	4.2501	1.4222	4.2930	2.4482
97487	**$La(Li_{0.5}Ru_{0.5})O_3$**	3.9364	3.9700	0.8536	3.9751	0.9845	3.9662	0.7567
90653	**$Sr(Ho_{0.5}Ru_{0.5})O_3$**	4.0833	4.1646	1.9913	4.1512	1.6627	4.1642	1.9817
93361	**$Sr(Tb_{0.5}Ru_{0.5})O_3$**	4.1019	4.1857	2.0419	4.1730	1.7344	4.1853	2.0337
153132	**$Sr(Tb_{0.5}Ru_{0.5})O_3$**	4.0976	4.1857	2.1484	4.1730	1.8406	4.1853	2.1402
380254	**$Sr(Ca_{0.5}Mo_{0.5})O_3$**	4.1010	4.2857	3.5056	4.2774	4.3023	4.2858	4.5061
247346	**$Sr(Mg_{0.5}Mo_{0.5})O_3$**	3.9501	4.0209	1.7929	4.0039	1.3640	4.0207	1.7882
247350	**$Sr(Ni_{0.5}Mo_{0.5})O_3$**	3.9323	3.9945	1.5792	3.9775	1.1469	3.9945	1.5803
247351	**$Sr(Zn_{0.5}Mo_{0.5})O_3$**	3.9627	4.0387	1.9193	4.0220	1.4960	4.0384	1.9117

*** This work**

Table 4.3 The 42 rock salt B-site ordered perovskites accounting for cation effective sizes (Å).

ICSD #	Composition	Δr_B	a_{pc} Eq. 1.19	Error%	a'_{pc} Eq. 1.3	Error%	a''_{pc} Eq. 1.4	Error%
172775	**$La(Zn_{0.5}Ti_{0.5})O_3$**	-0.01977	3.9503	-0.0006	3.9544	0.1033	3.9461	-0.1062
251934	**$Gd(Zn_{0.5}Ti_{0.5})O_3$**	-0.04341	3.8501	-0.6558	3.9329	1.4816	3.8412	-0.8848
251933	**$Pr(Zn_{0.5}Ti_{0.5})O_3$**	-0.01416	3.9174	-0.2284	3.9498	0.5954	3.9109	-0.3939
*	**$(Nd_{0.5}La_{0.5})(Zn_{0.5}Ti_{0.5})O_3$**	-0.01500	3.9316	-0.1215	3.9509	0.3697	3.9259	-0.2645
*	**$Nd(Zn_{0.5}Ti_{0.5})O_3$**	-0.01773	3.9065	-0.2452	3.9411	0.6387	3.8995	-0.4222
*	**$Sm(Zn_{0.5}Ti_{0.5})O_3$**	-0.02397	3.8843	-0.3232	3.9287	0.8140	3.8764	-0.5263
*	**$(Nd_{0.5}Gd_{0.5})(Zn_{0.5}Ti_{0.5})O_3$**	-0.02527	3.8799	-0.4544	3.9394	1.0718	3.8717	-0.6627
155217	**$Ca(Mg_{0.5}W_{0.5})O_3$**	-0.03775	3.8738	-0.0058	3.8808	0.1732	3.8674	-0.1724
151703	**$Sr(Mg_{0.5}W_{0.5})O_3$**	-0.03852	3.9624	0.1360	3.9457	-0.2859	3.9628	0.1475
262318	**$Ba(Mg_{0.5}W_{0.5})O_3$**	-0.04279	4.0516	-0.0635	4.0504	-0.0937	4.0598	0.1396
262284	**$Pb(Mg_{0.5}W_{0.5})O_3$**	-0.03986	4.0052	0.1401	3.9835	-0.4030	4.0092	0.2401
170684	**$Sr(Y_{0.5}Nb_{0.5})O_3$**	-0.05453	4.1314	0.1239	4.1168	-0.2295	4.1310	0.1129
193235	**$Sr(Yb_{0.5}Nb_{0.5})O_3$**	-0.05100	4.1081	0.1305	4.0928	-0.2425	4.1076	0.1190
247459	**$Sr(Y_{0.5}Ta_{0.5})O_3$**	-0.05591	4.1288	0.1247	4.1142	-0.2310	4.1284	0.1136
88838	**$Ba(Pr_{0.5}Nb_{0.5})O_3$**	-0.06781	4.3007	0.3020	4.2580	-0.6935	4.3018	0.3264
95524	**$Sr(Tm_{0.5}Ta_{0.5})O_3$**	-0.05227	4.1169	0.1281	4.1019	-0.2377	4.1165	0.1168
172169	**$Sr(In_{0.5}Nb_{0.5})O_3$**	-0.04185	4.0625	0.1399	4.0461	-0.2644	4.0621	0.1300
290859	**$Ba(La_{0.5}Ta_{0.5})O_3$**	-0.07127	4.3342	0.3331	4.2882	-0.7315	4.3344	0.3387
88152	**$Sr(Sc_{0.5}Ir_{0.5})O_3$**	-0.01580	3.9974	0.1422	3.9804	-0.2838	3.9974	0.1425
88153	**$Ba(Sc_{0.5}Ir_{0.5})O_3$**	-0.02925	4.0729	-0.0226	4.0667	-0.1734	4.0804	0.1624
88154	**$Sr(Y_{0.5}Ir_{0.5})O_3$**	-0.03759	4.0978	0.1331	4.0822	-0.2479	4.0973	0.1217
88155	**$Ba(Y_{0.5}Ir_{0.5})O_3$**	-0.05043	4.1810	0.1571	4.1542	-0.4865	4.1853	0.2585
88156	**$Ba(La_{0.5}Ir_{0.5})O_3$**	-0.05611	4.2963	0.2977	4.2541	-0.6880	4.2975	0.3246

88157	**$Sr(Lu_{0.5}Ir_{0.5})O_3$**	-0.03330	4.0698	0.1387	4.0536	-0.2612	4.0694	0.1284
88158	**$Ba(Lu_{0.5}Ir_{0.5})O_3$**	-0.04671	4.1507	0.1116	4.1290	-0.4128	4.1559	0.2350
192738	**$Sr(Cu_{0.5}Ir_{0.5})O_3$**	-0.00677	3.9524	0.1330	3.9359	-0.2852	3.9530	0.1485
246736	**$Sr(Cr_{0.5}Sb_{0.5})O_3$**	-0.00047	3.9378	0.1275	3.9217	-0.2828	3.9387	0.1499
157007	**$Sr(Ga_{0.5}Sb_{0.5})O_3$**	-0.00559	3.9334	0.1256	3.9174	-0.2817	3.9343	0.1503
33623	**$Ba(Sc_{0.5}Sb_{0.5})O_3$**	-0.02868	4.1028	0.0319	4.0902	-0.2746	4.1094	0.1924
246959	**$Sr(Sm_{0.5}Sb_{0.5})O_3$**	-0.04558	4.1654	0.1129	4.1520	-0.2089	4.1650	0.1035
247246	**$Sr(In_{0.5}Sb_{0.5})O_3$**	-0.02517	4.0564	0.1407	4.0399	-0.2669	4.0561	0.1313
262994	**$Sr(Sc_{0.5}Sb_{0.5})O_3$**	-0.01635	4.0229	0.1432	4.0060	-0.2783	4.0227	0.1381
50040	**$Ba(Bi_{0.5}Sb_{0.5})O_3$**	-0.07484	4.2873	0.2885	4.2461	-0.6761	4.2887	0.3206
84660	**$Ba(Tl_{0.5}Sb_{0.5})O_3$**	-0.04904	4.1980	0.1811	4.1685	-0.5237	4.2018	0.2705
97487	**$La(Li_{0.5}Ru_{0.5})O_3$**	-0.01660	3.9367	0.0076	3.9401	0.0941	3.9323	-0.1045
90653	**$Sr(Ho_{0.5}Ru_{0.5})O_3$**	-0.04045	4.0888	0.1351	4.0730	-0.2524	4.0883	0.1239
93361	**$Sr(Tb_{0.5}Ru_{0.5})O_3$**	-0.04146	4.1073	0.1307	4.0919	-0.2430	4.1068	0.1193
153132	**$Sr(Tb_{0.5}Ru_{0.5})O_3$**	-0.04375	4.1030	0.1318	4.0876	-0.2452	4.1026	0.1203
380254	**$Sr(Ca_{0.5}Mo_{0.5})O_3$**	-0.09296	4.1063	0.1309	4.0910	-0.2435	4.1059	0.1195
247346	**$Sr(Mg_{0.5}Mo_{0.5})O_3$**	-0.03762	3.9554	0.1339	3.9388	-0.2855	3.9559	0.1482
247350	**$Sr(Ni_{0.5}Mo_{0.5})O_3$**	-0.03323	3.9374	0.1274	3.9212	-0.2827	3.9382	0.1500
247351	**$Sr(Zn_{0.5}Mo_{0.5})O_3$**	-0.04017	3.9681	0.1375	3.9513	-0.2861	3.9685	0.1468

*** This work**

It should be noted that all 42 compositions in Tables 4.2 and 4.3 were sorted into series based upon the smallest B-site cation in each, $r_{B,small}$, in order to develop a model for the B-site size adjustment factor with relation to the B-site size. This process created seven unique series of data (*i.e.* compounds with Mo, Ru, Sb, Ir, Nb or Ta, $Mg_{½}W_{½}$, or $Zn_{½}Ti_{½}$ on the B site). A correlative model was then developed for each series.

The fact that Nb^{5+} and Ta^{5+} have the same charge and ionic size makes it impossible to isolate the effects of size and charge in compounds containing either of these species; however, compounds containing either Nb^{5+} or Ta^{5+} as the smallest B-site species produced very similar Δr_B vs. a_{pc} curves. Despite the fact that Nb and Ta have very different atomic masses (m_{Nb} = 92.906 amu and m_{Ta} = 180.95 amu), it would appear that the model is only sensitive to size and charge differences between two species. Thus, it was possible to consider these compounds together in a single series.

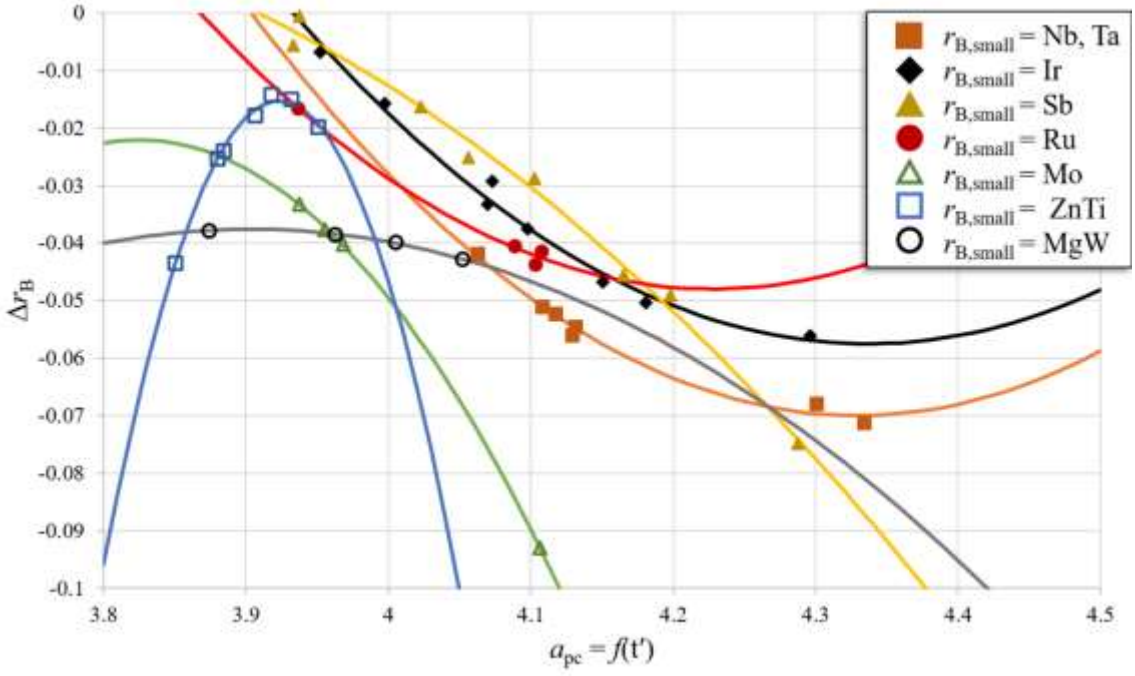

Figure 4.3 B-site size adjustment factors as functions of the pseudocubic lattice constant (Eq. 1.19).

Fig. 4.3 shows the relationship between the B-site size correction factor, Δr_B, and pseudocubic lattice constant, a_{pc}. These curves demonstrate that the general trend is clearly a quadratic polynomial and can be represented generically by Eq. 4.1:

$$\Delta r_B = A a_{pc}^2 + B a_{pc} + C, \tag{4.1}$$

where a_{pc} is calculated from Eq. 1.19. Since Eq. 1.19 predicts a_{pc} using solely ionic radii data[45], Δr_B can be predicted only using ionic radii data[45] as well. The coefficients and goodness of fit for all seven of these curves are listed in table 4.4.

Table 4.4 Coefficients of Eq. 4.1 and the goodness of fit, R^2

$r_{B,small}$	A	B	C	R^2
Nb, Ta	0.3858	-3.3406	7.1619	0.9809
Ir	0.3529	-3.0608	6.5796	0.9889
Sb	-0.1986	1.4324	-2.5646	0.9908
Ru	0.3707	-3.1345	6.5778	0.9922
Mo	-0.8958	6.8529	-13.1282	0.9999
MgW	-0.2328	1.8175	-3.5842	0.9970
ZnTi	-5.3117	41.6784	-81.7733	0.9836

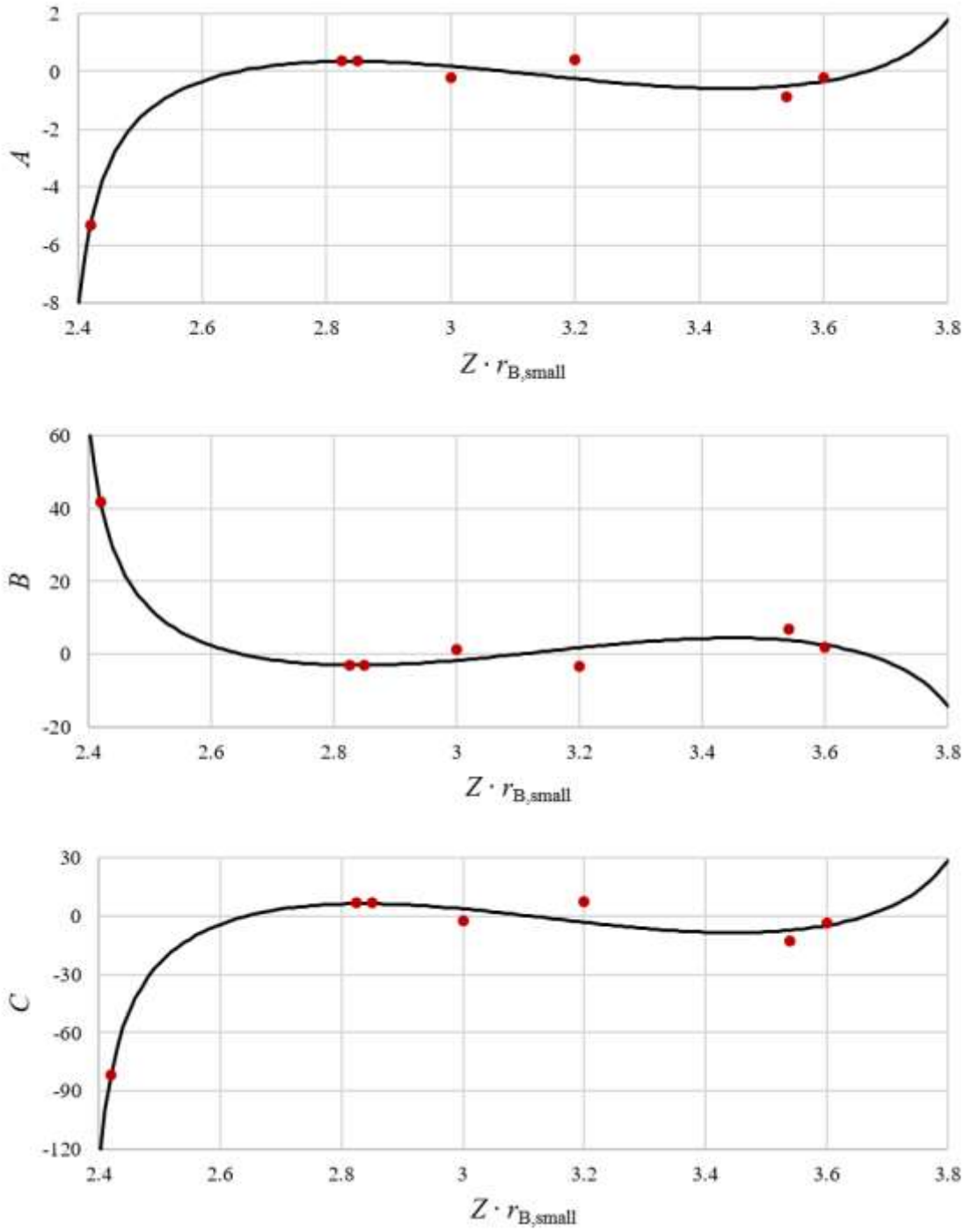

Figure 4.4 Coefficients of Eq. 4.1 as a function of charge (*Z*) and ionic radius of the smallest B-site species, $r_{B,small}$.

Fig. 4.4 shows the relationship between the coefficients of Eq. 4.1 and the product of charge and size of the smallest B-site cation, $Z \cdot r_{B,small}$. Not only is this model sensitive

to both the size and charge of B-site cations, but all three of the coefficients (*A*, *B*, and *C*) are related to the charge and size of the smallest B-site species in each composition by the same trigonometric function:

$$Coeff = a + b\tan\left(2Zr_{\mathrm{B,small}}\right) + c\sin\left(3Zr_{\mathrm{B,small}}\right), \tag{4.2}$$

where *Coeff* = *A*, *B*, or *C*. Table 4.5 lists all the coefficients of Eq. 4.2 and the goodness of fit.

Table 4.5 Coefficients of Eq. 4.2 and the goodness of fit, R^2.

Coefficient	*a*	*b*	*c*	R^2
A	-0.11987	0.80266	1.29757	0.9715
B	0.75396	-6.33299	-10.29258	0.9709
C	-1.12758	12.49349	20.42735	0.9701

It appears from Fig. 4.4 that the *A*, *B*, and *C* coefficients are not independent parameters but are actually highly correlated. Specifically, *A* and *C* differ by a scale factor while *B* is a mirror image of *A* and *C* with a constant scale factor. This correlation is demonstrated in Fig. 4.5.

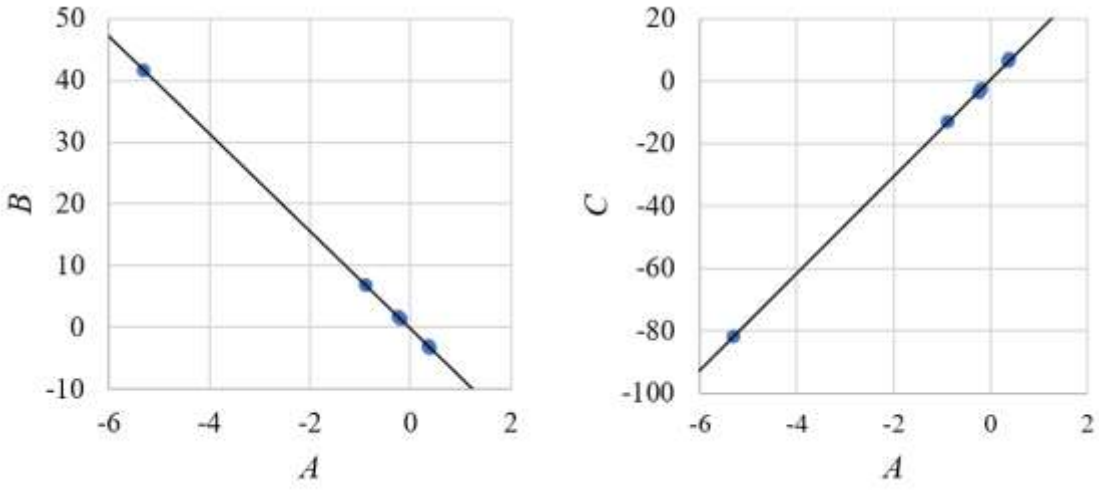

Figure 4.5 Coefficients of Eq. 4.1 as functions of one another.

The linear correlations of Fig. 4.5 can be represented by Eqs. 4.3-4.4:

$$B = -7.88736882A - 0.19527227 \quad \left(R^2 = 1\right) \tag{4.3}$$

$$C = 15.55306591A + 0.75275399 \quad \left(R^2 = 0.9999\right) \tag{4.4}$$

Substituting Eqs. 4.3 and 4.4 into Eq. 4.1 yields Eq. 4.5:

$$\Delta r_B = A\left(a_{pc}^2 - 7.88736882a_{pc} + 15.55306591\right) - 0.19527227a_{pc} + 0.75275399, \tag{4.5}$$

where a_{pc} is calculated using Eq. 1.19. The advantage of Eq. 4.5 is that it allows for the prediction of the B-site size correction factor, Δr_B, using only a single coefficient, A, which can be easily calculated from Eq. 4.2 and the coefficients in Table 4.5 as

$$A = -0.11987 + 0.80266\tan\left(2Zr_{B,small}\right) + 1.29757\sin\left(3Zr_{B,small}\right) \tag{4.6}$$

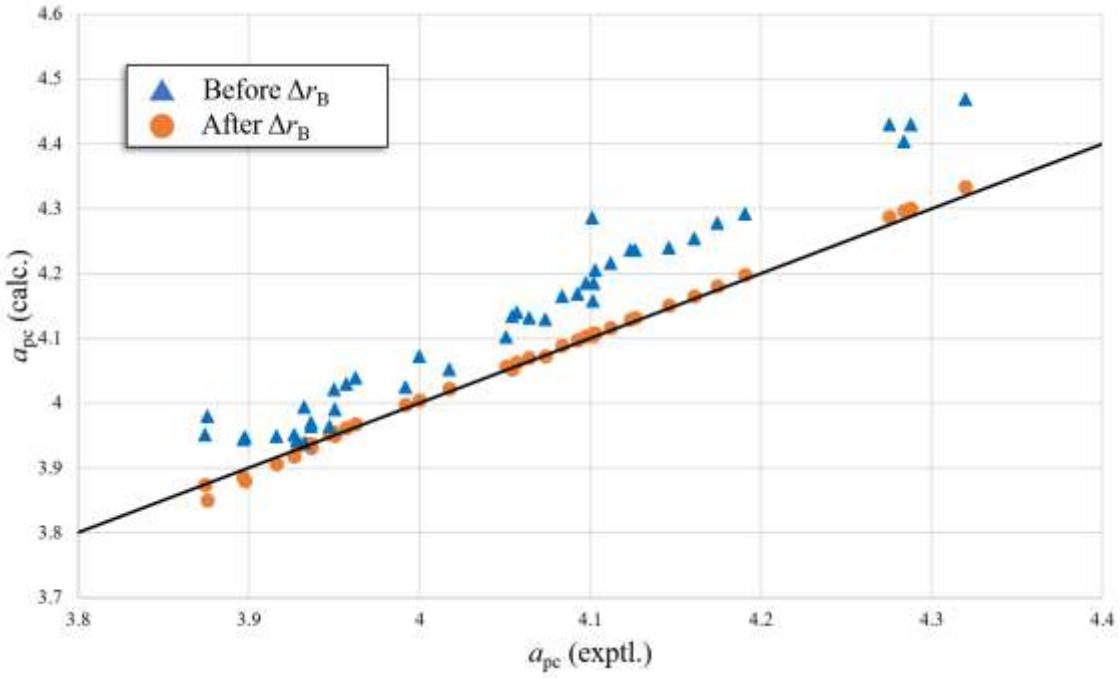

Figure 4.6 Comparison of experimental a_{pc} values to a_{pc} calculated using Eq. 1.19. The triangles show a_{pc} before Δr_B has been applied and the circles show a_{pc} after Δr_B has been applied. The trend line represents a_{pc} (calc.) = a_{pc} (exptl.).

Since Eq. 1.19 was developed from perovskite data which contained random distributions of cations on both the A and B sites, it does not accurately predict a_{pc} in B-site ordered perovskites, as Table 4.1 and Fig. 4.6 demonstrate. The pseudocubic lattice constant calculated from Eq. 1.19 tends to be larger than the experimental pseudocubic lattice constant, which further demonstrates that the model overestimates the unit cell volume for B-site ordered perovskites; however, Fig. 4.6 also shows that after the volume shrinkage resulting from B-site ordering has been accounted for, Eq. 1.19 is still an accurate predictor of the pseudocubic lattice constant. Thus, the model as developed previously[44] has been effectively extended to account for rock salt B-site ordering.

A major implication of this model is that it can be used to accurately predict the volume shrinkage as the result of rock salt B-site ordering in perovskites; however, it should be noted that the model is only generally applicable to rock salt B-site ordered perovskites with the smallest B-site species between 0.565 (Ru^{5+}) and 0.64 (Nb^{5+}, Ta^{5+}) and ionic charges between 4+ and 6+. Although the model *may* be more generally applicable, like all empirical models, it cannot be extrapolated beyond the upper and lower bounds in the data set with any degree of certainty.

4.4 Conclusion

Using a solid-state mixed-oxide method, four compositions within the $A(Zn_{0.5}Ti_{0.5})O_3$ system (A = Nd, Sm, $La_{0.5}Nd_{0.5}$, $Nd_{0.5}Gd_{0.5}$) were successfully synthesized. The XRD patterns show long-range rock salt B-site order is present within all of the compositions. Seven system-specific models were derived for the B-site size adjustment factor, Δr_B, as a function of a_{pc}. A general model for rock salt B-site ordering in perovskites, which accounts for both the charge and size of the smallest B-site species, was derived

based upon these specific models. One of the major implications of this model is that it accurately predicts the volume shrinkage, and so pseudocubic lattice constant, for any $A_2(B'B'')O_6$ rock salt B-site ordered perovskites using only readily available ionic radii data. Conversely, it might be used to determine the degree of order in a given perovskite from experimental measurements of lattice constants. It may even be possible with more data to extend this model to predict volume shrinkage in other B-site ordered perovskite systems (*e.g.*, those with 1:2 ordering).

4.5 References

[1] Miller V, Tidrow S. Perovskites: Temperature and coordination dependent ionic radii. Integrated Ferroelectrics. 2013;148:1-16.

[2] King G, Woodward P. Cation ordering in perovskites. J of Mater Chem. 2010;20:5785-5796.

[3] Setter N, Cross LE. The contribution of structural disorder to diffuse phase transitions in ferroelectrics. J Mater Sci 1980;15(10):2478-82.

[4] Zhang X, Wang Q, Gu B. Study of the Order-Disorder Transition in $A(B'B'')O_3$ Perovskite Type Ceramics. J Am Ceram Soc 1991;74(11):2846-50.

[5] Gui H, Gu B, Zhang X. Order-Disorder Transition in $(A'A'')BO_3$ and $A(B'B'')O_3$ Complex Perovskite Crystals. J Am Ceram Soc 1996;79(2):381-4.

[6] Woodward P, Hoffmann R, Sleight A. Order-disorder in $A_2M^{3+}M^{5+}O_6$ perovskites. J Mater Res. 1994;9(8):2118-27.

[7] Lufaso M, Barnes P, Woodward P. Structure prediction of ordering and disordered multiple octahedral cation perovskites using SPuDS. Acta Crystallogr Sect B Struct Sci. 2006;62(3):397-410.

[8] Anderson M, Greenwood K, Taylor G, Poeppelmeier K. B-cation arrangements in double perovksites. Prog. in Solid State Chem. 1993;22(3):197-233.

[9] Howard C, Kennedy B, Woodward P. Ordered double perovskites – a group-theoretical analysis. Acta Crystallogr Sect B Struct Sci. 2003;59(4):463-471.

[10] Yang JH, Choo WK, Lee CH. Ca_2MgWO_6 from neutron and X-ray powder data. Acta Crystallogr Sect C Cryst Struct Commun 2003;59(8):i86-8.

[11] Patwe SJ, Achary SN, Mathews MD, Tyagi AK. Crystal structure and thermal expansion behavior of Ca_2MgWO_6. Mater Chem Phys 2006;98(2-3):486-93.

[12] Mishra AK, Poswal HK, Acharya SN, Tyagi AK, Sharma SM. Structure evolution of double perovskite Sr_2MgWO_6 under high pressure. Phys status solidi 2010;247(7):1773-7.

[13] Khalyavin DD, Senos AMR, Mantas PQ. Crystal structure of Sr_2MgWO_6 and Ba_2MgWO_6 determined by powder X-ray diffraction. Powder Diffr 2004;19(03):280-3.

[14] Achary SN, Chakraborty KR, Patwe SJ, Shinde AB, Krishna PSR, Tyagi AK. Anisotropic thermal expansion behavior in tetragonal Sr_2MgWO_6. Mater Res Bull 2006;41(3):674-82.

[15] Vasala S, Lehtimäki M, Haw SC, Chen JM, Liu RS, Yamauchi H, et al. Isovalent and aliovalent substitution effects on redox chemistry of $Sr_2MgMoO_{6-\delta}$ SOFC-anode material. Solid State Ionics 2010;181(15-16):754-9.

[16] Patwe SJ, Achary SN, Mathews MD, Tyagi AK. Synthesis, phase transition and thermal expansion studies on M_2MgWO_6 ($M=Ba^{2+}$ and Sr^{2+}) double perovskites. J Alloys Compd 2005;390(1-2):100-5.

[17] Bugaris DE, Hodges JP, Huq A, zur Loye H-C. Crystal growth, structures, and optical properties of the cubic double perovskites Ba_2MgWO_6 and Ba_2ZnWO_6. J Solid State Chem 2011;184(8):2293-8.

[18] Day BE, Bley ND, Jones HR, McCullough RM, Eng HW, Porter SH, et al. Structures of ordered tungsten- or molybdenum-containing quaternary perovskite oxides. J Solid State Chem 2012;185:107-16.

[19] Filip'ev VS, Shatalova GE, Fesenko EG. Determination of bond lengths in tungstates with Perovskite-type structure. Kristallografiya 1974;19(2):386-7.

[20] Meenakshi S, Vijayakumar V, Achary SN, Tyagi AK. High pressure investigation on double perovskite Ba_2MgWO_6. J Phys Chem Solids 2011;72(6):609-12.

[21] Agranovskaya AI. Physical-chemical investigation of the formation of complex ferroelectrics with perovskite structure. Izv Akad Nauk SSSR, Seriya Fiz 1960;24:1275-81.

[22] Zaslavskii AI, Bryzhina MF. An X-ray structural investigation of the antiferroelectric Pb_2MgWO_6 and the system of the solid solutions Pb_2MgWO_6-$PbTiO_3$. Kristallografiya 1962;7:709-17.

[23] Baldinozzi G, Sciau P, Buffat P-A. Investigation of the orthorhombic structures of Pb_2MgWO_6 and Pb_2CoWO_6. Solid State Commun 1993; 86(9):541-4.

[24] Baldinozzi G, Sciau P, Pinot M, Grebille D. Crystal structure of the antiferroelectric perovskite Pb_2MgWO_6. Acta Crystallogr Sect B Struct Sci 1995;51(5):668-73.

[25] Singh AK, Singh AK. Low temperature phase transition studies on $Pb(Mg_{0.5}W_{0.5})O_3$ ceramic. Solid State Sci 2012;14(1):100-5.

[26] Ubic R, Hu Y, Abrahams I. Neutron and electron diffraction studies of $La(Zn_{1/2}Ti_{1/2})O_3$ perovskite. Acta Crystallogr Sec B Struc Sci. 2006;62:521-9.

[27] Tseng C, Huang C, Yang W. Dielectric characteristics of $Nd(Zn_{1/2}Ti_{1/2})O_3$ ceramics at microwave frequencies. J Am Ceram Soc. 2006;89(4):1465-70.

[28] Das N, Nath M, Thakur G, Thirumal M, Ganguli A. Monoclinically distorted perovskites, A_2ZnTiO_6 (A=Pr, Gd): Rietveld refinement, and dielectric studies. J Solid State Chem. 2015;229:97-102.

[29] Aguadero A, Alonso J, Martínez-Lopez M, Fernández-Díaz M. Crystallo-chemical evolution of the La_2ZnTiO_6 double perovskite upon reduction: A structural study. Solid State Sciences 2011;13:13-8.

[30] Suchomel M, Fogg A, Allix M, Niu H, Claridge J, Rosseinsky M. Bi_2ZnTiO_6: A lead-free closed-shell polar perovskite with a calculated ionic polarization of 150 μC cm^{-2}. Chem Mater. 2006;18:4987-9.

[31] Wakeshima M, Harada D, Hinatsu Y. Crystal structures and magnetic properties of ordered perovskites $A_2R^{3+}Ir^{5+}O_6$ (A=Sr, Ba; R=Sc, Y, La, Lu). J Alloy Compd. 1999;287:130-6.

[32] Vasala S, Yamauchi H, Karppinen M. Synthesis, crystal structure and magnetic properties of a new B-site ordered double perovskite Sr_2CuIrO_6. J Solid State Chem. 2014;220:28-31.

[33] Howard C, Barnes P, Kennedy B, Woodward P. Structures of the ordered double perovskites Sr_2YTaO_6 and Sr_2YNbO_6. Acta Crystallogr Sec B Struc Sci. 2005;61:258-62.

[34] Zhou Q, Kennedy B, Avdeev M. Structural studies of the disorder and phase transitions in the double perovskite Sr_2YTaO_6. J Solid State Chem. 2010;183:1741-6.

[35] Henmi K, Hinatsu Y, Masaki N. Crystal structures and magnetic properties of ordered perovskites Ba_2LnNbO_6 (Ln = lanthanide elements). J Solid State Chem. 1999;148:353-60.

[36] Doi Y, Hinatsu Y. Manetic properties of ordered perovskites Ba_2LnTaO_6 (Ln = Y, lanthanides). J Phys: Condens Matter 2001;13:4191-202.

[37] Kanaiwa Y, Wakeshima M, Hinatsu Y. Synthesis, crystal structure, and magnetic properties of ordered perovskites Sr_2LnTaO_6 (Ln = lanthanides). Mater Res Bull. 2002;37:1825-36.

[38] Ting V, Liu Y, Withers R, Norén L, James M, FitzGerald J. A structure and phase analysis investigation of the 1:1 ordered A_2InNbO_6 perovskites ($A = Ca^{2+}$, Sr^{2+}, Ba^{2+}). J Solid State Chem. 2006;179:551-62.

[39] Vasala S, Lehtimäki M, Huang Y, Yamauchi H, Goodenough J, Karppinen M. Degree of order and redox balance in B-site ordered double-perovskite oxides, $Sr_2MMoO_{6-\delta}$ (M=Mg, Mn, Fe, Co, Ni, Zn). J Solid State Chem. 2010;183:1007-12.

[40] Prior T, Couper V, Battle P. Structural chemistry of the cation-ordered perovskites $Sr_2CaMo_{1-x}Te_xO_6$ ($0 \leq x \leq 1$). J Solid State Chem. 2005;178:153-7.

[41] Smith E, Tolman K, Ubic R. An empirical model for B-site cation ordering in $Ba(Mg_{1/3}Ta_{2/3})O_3$. J Alloys Compd. 2018;735:2356-2362.

[42] Tolman K, Ubic R, Liu B, et al. Empirical evidence for A-site order in perovskites. J Am Ceram Soc. 2017;100:429-442.

[43] Smith E, Ubic R. Empirical models for layered A-site ordering in perovskite titanates. J Am Ceram Soc. 2019;102:3019-31.

[44] Ubic R, Tolman K, Talley K, et al. Lattice-constant prediction and effect of vacancies in aliovalently doped perovskites. J Alloys Compd. 2015;644:982-995.

[45] Shannon R. Revised Effective Ionic-Radii and Systematic Studies of Interatomic Distances in Halides and Chalcogenides. Acta Crystallogr Sec A. 1976;32:751-767.

CHAPTER FIVE: EMPIRICAL MODELS OF TRIGONAL DISTORTIONS AND POLARIZATION IN PEROVSKITES

This chapter has been submitted for publication in the Journal of the American Ceramic Society.

Reference: Smith, E., Wander, O., Ubic, R., "Empirical Models of Trigonal Distortions and Polarization in Perovskites," Journal of the American Ceramic Society, submitted.

5.1 Introduction

Correlative models describing composition-structure relationships are the keys to unlocking the full potential of many materials, including electroceramics. Perovskite ceramics exhibit an expansive range of properties, and examples of trigonally distorted perovskites alone exhibit colossal magnetoresistance (*e.g.*, $La_{0.6-x}Pr_xSr_{0.4}MnO_3$)[1], magnetocaloric effects (*e.g.*, $La_{0.65}Sr_{0.35}V_{0.1}Mn_{0.9}O_3$)[2], catalysis (*e.g.*, $La_{1-x}Ag_xMnO_3$)[3], and ferroelectricity (*e.g.*, $BiFeO_3$)[4]. Thus, predictive models linking structure to properties are needed to minimize expensive and time-consuming trial-and-error experiments, allowing for a more cost-effective future for the electroceramics industry, with all the concomitant benefits for society which that entails.

Generally, perovskites are defined as compounds with ABX_3 stoichiometry in which large A-site cations exist on cuboctahedral sites between corner-sharing anion octahedra, each of which contains a smaller B-site cation. Trigonal distortion in perovskites occurs when the BO_6 octahedra undergo equal anti-phase octahedral tilting about all three crystallographic pseudocubic axes ($a^-a^-a^-$ in Glazer's notation[5]). This tilting results in the vast majority of trigonally distorted perovskites crystallizing in the centrosymmetric space group $R\bar{3}c$; although it is also possible for these perovskites to crystallize in the non-centrosymmetric space group *R*3*c*. Both $R\bar{3}c$ and *R*3*c* trigonal perovskites can be described with either a rhombohedral or hexagonal cell; however, a hexagonal cell is most often chosen for the sake of convenience; thus, all of the trigonally distorted perovskites in this work were considered in the hexagonal setting.

Additionally, the A site for all the trigonal perovskites that have been analyzed in this work contain a trivalent cation (*e.g.*, La^{3+}) and have been doped with either a divalent

cation (*e.g.*, Sr^{2+}) or a monovalent cation (*e.g.*, Na^{+}) according to the following stoichiometries: $A^{3+}_{1-x}A^{2+}_{x}B^{3+}_{1-x}B^{4+}_{x}O_3$ or $A^{3+}_{1-x/2}A^{1+}_{x/2}B^{3+}_{1-x}B^{4+}_{x}O_3$. Using these formulas, a divalent cation species can completely replace the trivalent one ($x = 1$) without the need for oxygen vacancies for charge compensation; however, a monovalent A-site dopant can only be used to replace half of the trivalent one before intrinsic oxygen vacancies or second phases would begin to form.

Many of the trigonal perovskites that have been produced to date contain manganese on the B site due to its useful magnetic properties. Mn^{3+} is a well-known Jahn-Teller ion, and the Mn^{3+} cation is known to exist purely in its high-spin (HS) state $\left(t^3_{2g}e^1_g\right)$ at room temperature and atmospheric pressure[6]. Furthermore, the Mn^{3+} cation is well known for its ability to change oxidation states, which allows for series such as $LnMnO_3$ to be doped with divalent or monovalent cations while maintaining fully occupied anion sites. For instance, doping $LaMnO_3$ with a quantity of Sr^{2+} causes the formation of an equal amount of Mn^{4+}. Interestingly, electrons can migrate between Mn^{3+} and Mn^{4+} cations via the double exchange mechanism; thus, if the dopant reaches sufficient concentration (*i.e.*, the Mn^{4+} concentration reaches sufficient concentration), it can cause the electrons to delocalize from these cations and allow the sample to exhibit metallic conductivity[6].

On the other hand, the spin state of the Co^{3+} cation in the $LnCoO_3$ series of compounds is a bit ambiguous. Current research[6] suggests that Co^{3+} exists in its low-spin (LS) state $\left(t^6_{2g}\right)$ at room temperature and atmospheric pressure but transitions to an intermediate-spin (IS) state $\left(t^5_{2g}e^1_g\right)$ at higher temperatures and pressures. Furthermore, Fe^{3+} is known to exist purely in its high-spin state $\left(t^3_{2g}e^2_g\right)$ at room temperature and

atmospheric pressure[7]. Thus, for the sake of choosing the appropriate ionic radii, Mn^{3+} and Fe^{3+} were considered in their high-spin states and Co^{3+} was considered in its low-spin state for the perovskites in this work.

There currently exist several correlative models for predicting both cubic[8-10] and orthorhombic[11,12] perovskite lattice parameters. There even exists an empirical model for predicting tetragonal lattice parameters in perovskites[13]; however, there are currently no empirical models for predicting lattice constants in trigonally distorted perovskites, arguably a larger and more commercially relevant class of perovskite.

In 2001, Lufaso and Woodward developed[14] a program called SPuDS (Structure Prediction Diagnostic Software) for predicting perovskite structures. It was based on the concept of the global-instability-index (GII) as developed by Salinas-Sanchez *et al.*[15]. SPuDS is a very powerful tool, and it is currently one of the only methods available for predicting the stability of trigonal perovskites; however, because SPuDS relies solely on the GII, it cannot unambiguously predict the most stable perovskite structures in many cases. It also fails to account for B-site octahedral distortions and does not account for some atomic species (*e.g.*, Pm^{3+} and Ra^{2+}).

5.2 Materials and Methods

In this work, 57 trigonally distorted perovskites in space group $R\bar{3}c$ and 31 trigonally distorted perovskites in space group *R*3*c* were mined from literature. A total of 10 compositional series were analyzed for the perovskites in space group $R\bar{3}c$: $La_{1-x}Sr_xFeO_3$ (LSF), $La_{1-x}Sr_xCoO_3$ (LSC), $La_{1-x}Ba_xCoO_3$ (LBC), $La_{1-x}Sr_xMnO_3$ (LSM), $La_{1-x}Ba_xMnO_3$ (LBM), $La_{1-x}Ca_xMnO_3$ (LCM), $La_{1-x}Na_xMnO_3$ (LNM), $La_{1-x}K_xMnO_3$ (LKM),

$La_{1-x}Ag_xMnO_3$ (LAM), and $La_{1-x}Pb_xMnO_3$ (LPM). Using the data from these perovskites, system-specific models were developed for the perovskites in space group $R\bar{3}c$ which describe the degree of trigonality as a function of the ratio of the pseudocubic lattice constant to the B-X bond length. From the system-specific models, a general model describing perovskite trigonality for perovskites in space group $R\bar{3}c$ in terms of the modified tolerance factor[16] was derived. In addition, a general model was developed for both trigonality and intrinsic polarization in perovskites with space group *R*3*c*.

5.3 Results and Discussion

Table 5.1 shows the data for all 57 compounds used to derive the general trigonal model for perovskites with $R\bar{3}c$ symmetry and the predicted perovskite trigonality, *c*/*a*, using this model. Values of t' were determined from an empirical model[16] using only the values of t_0 and Shannon[17] values of r_A for each compound. After applying the trigonal model to each compound, the average global absolute error between the experimental and predicted *c*/*a* values is 0.1348%. The two systems producing the most error are $La_{1-x}Sr_xCoO_3$ (0.3187%) and $La_{1-x}Pb_xMnO_3$ (0.2968%), whereas the system producing the least amount of error is $La_{1-x}Sr_xFeO_3$ (0.0529%).

Table 5.2 shows the experimental and predicted trigonal lattice constants using Eqs. 5.4-5.7 for all 57 $R\bar{3}c$ trigonal compounds used in this model. The average global absolute error for *a* and *c* is 0.0449% and 0.0898%, respectively. Again, the two systems producing the most error are $La_{1-x}Sr_xCoO_3$ (0.1060% for *a* and 0.2123% for *c*) and $La_{1-x}Pb_xMnO_3$ (0.0993% for *a* and 0.1981% for *c*), and the system producing the least amount of error is $La_{1-x}Sr_xFeO_3$ (0.0176% for *a* and 0.0352% for *c*). It should be noted that the errors are very good overall; however, one of the reasons that the $La_{1-x}Pb_xMnO_3$ compound has the largest

errors may be due to the fact that Pb is volatile during the calcination and sintering stages of processing. Thus, if care is not taken to minimize the amount of lead loss in these compounds, it can cause oxygen vacancies and/or multiple phases to form.

Table 5.1 The 57 $R\bar{3}c$ trigonal compositions used to derive the general trigonal model for $c/a < \sqrt{6}$ (Fig. 5.1).

ICSD #	Compound	$a_{pc\ (exptl.)}$ (Å)	$r_{B\text{-}X(exptl.)}$ (Å)	t'	$c/a_{\ exptl}$	$c/a_{\ calc}$	|Error%|
98069	$La_{0.6}Sr_{0.4}FeO_3$	3.8998	1.964	0.9868	2.4288	2.4269	0.0800
163227	$La_{0.5}Sr_{0.5}FeO_3$	3.8889	1.954	0.9928	2.4343	2.4339	0.0161
78067	$La_{0.4}Sr_{0.6}FeO_3$	3.8802	1.946	0.9992	2.4411	2.4397	0.0570
160591	$La_{0.333}Sr_{0.667}FeO_3$	3.8733	1.938	1.0036	2.4491	2.4470	0.0851
190643	$La_{0.33}Sr_{0.67}FeO_3$	3.8711	1.938	1.0038	2.4463	2.4452	0.0447
78068	$La_{0.3}Sr_{0.7}FeO_3$	3.8715	1.937	1.0058	2.4479	2.4471	0.0342
Average systematic absolute error							0.0529
82814	$La_{0.9}Sr_{0.1}CoO_3$	3.7756	1.901	0.9795	2.4225	2.4284	0.2435
164487	$La_{0.85}Sr_{0.15}CoO_3$	3.8293	1.930	0.9830	2.4156	2.4247	0.3768
82815	$La_{0.8}Sr_{0.2}CoO_3$	3.8029	1.913	0.9865	2.4247	2.4315	0.2837
156454	$La_{0.7}Sr_{0.3}CoO_3$	3.8369	1.928	0.9937	2.4260	2.4354	0.3881
237871	$La_{0.6}Sr_{0.4}CoO_3$	3.8344	1.926	1.0009	2.4306	2.4367	0.2542
93380	$La_{0.5}Sr_{0.5}CoO_3$	3.8337	1.921	1.0082	2.4422	2.4453	0.1237
167257	$LaCoO_3$	3.8243	1.932	0.9726	2.4056	2.4191	0.5607
Average systematic absolute error							0.3187
189376	$La_{0.99}Ba_{0.01}CoO_3$	3.8265	1.929	0.9747	2.4138	2.4135	0.0091
157894	$La_{0.97}Ba_{0.03}CoO_3$	3.8314	1.931	0.9789	2.4096	2.4145	0.2046
157895	$La_{0.95}Ba_{0.05}CoO_3$	3.8356	1.933	0.9832	2.4123	2.4147	0.1013
157896	$La_{0.92}Ba_{0.08}CoO_3$	3.8406	1.936	0.9896	2.4161	2.4138	0.0967
157897	$La_{0.9}Ba_{0.1}CoO_3$	3.8447	1.936	0.9939	2.4188	2.4179	0.0374
157898	$La_{0.88}Ba_{0.12}CoO_3$	3.8469	1.935	0.9982	2.4211	2.4220	0.0382
157899	$La_{0.85}Ba_{0.15}CoO_3$	3.8518	1.936	1.0047	2.4247	2.4249	0.0062
157900	$La_{0.82}Ba_{0.18}CoO_3$	3.8557	1.936	1.0111	2.4285	2.4287	0.0099

157901	$La_{0.8}Ba_{0.2}CoO_3$	3.8585	1.936	1.0154	2.4310	2.4314	0.0162
157902	$La_{0.75}Ba_{0.25}CoO_3$	3.8635	1.935	1.0261	2.4370	2.4383	0.0539
157903	$La_{0.72}Ba_{0.28}CoO_3$	3.8666	1.936	1.0324	2.4410	2.4394	0.0643
157904	$La_{0.7}Ba_{0.3}CoO_3$	3.8685	1.936	1.0365	2.4437	2.4413	0.0990
167257	$LaCoO_3$	3.8243	1.932	0.9726	2.4056	2.4191	0.5607
Average systematic absolute error							0.0998
91179	$La_{0.875}Ba_{0.125}MnO_3$	3.9095	1.973	0.9854	2.4187	2.4224	0.1522
91180	$La_{0.85}Ba_{0.15}MnO_3$	3.9049	1.968	0.9897	2.4219	2.4257	0.1577
159742	$La_{0.825}Ba_{0.175}MnO_3$	3.9328	1.981	0.9940	2.4288	2.4271	0.0718
91182	$La_{0.8}Ba_{0.2}MnO_3$	3.9093	1.965	0.9986	2.4286	2.4323	0.1525
91183	$La_{0.775}Ba_{0.225}MnO_3$	3.9094	1.966	1.0032	2.4301	2.4311	0.0380
91184	$La_{0.75}Ba_{0.25}MnO_3$	3.9081	1.965	1.0079	2.4324	2.4315	0.0359
82104	$La_{0.7}Ba_{0.3}MnO_3$	3.9097	1.962	1.0175	2.4380	2.4363	0.0690
185842	$La_{0.67}Ba_{0.33}MnO_3$	3.9073	1.958	1.0235	2.4409	2.4398	0.0425
96038	$LaMnO_3$	3.8705	1.960	0.9667	2.4135	2.4163	0.1161
Average systematic absolute error							0.0929
97865	$La_{0.82}Sr_{0.18}MnO_3$	3.8924	1.969	0.9754	2.4159	2.4127	0.1354
97866	$La_{0.8}Sr_{0.2}MnO_3$	3.8899	1.967	0.9765	2.4175	2.4140	0.1453
162762	$La_{0.7}Sr_{0.3}MnO_3$	3.8812	1.955	0.9826	2.4268	2.4278	0.0407
160750	$La_{0.67}Sr_{0.33}MnO_3$	3.8853	1.956	0.9848	2.4290	2.4297	0.0286
95568	$La_{0.64}Sr_{0.36}MnO_3$	3.8805	1.954	0.9867	2.4290	2.4290	0.0026
99555	$La_{0.6}Sr_{0.4}MnO_3$	3.8708	1.944	0.9895	2.4359	2.4384	0.1012
236939	$La_{0.55}Sr_{0.45}MnO_3$	3.8656	1.940	0.9932	2.4372	2.4410	0.1541
96038	$LaMnO_3$	3.8705	1.960	0.9667	2.4135	2.4163	0.1161
Average systematic absolute error							0.0905
155413	$La_{0.95}Ca_{0.05}MnO_3$	3.8873	1.967	0.9661	2.4158	2.4204	0.1904

238369	$La_{0.8}Ca_{0.2}MnO_3$	3.8784	1.959	0.9644	2.4347	2.4384	0.1548
161685	$La_{0.7}Ca_{0.3}MnO_3$	3.8676	1.953	0.9633	2.4436	2.4412	0.0977
258206	$La_{0.6}Ca_{0.4}MnO_3$	3.8637	1.952	0.9623	2.4418	2.4361	0.2312
96038	$LaMnO_3$	3.8705	1.960	0.9667	2.4135	2.4163	0.1161
Average systematic absolute error							0.1580
257499	$La_{0.9}Na_{0.1}MnO_3$	3.8761	1.955	0.9685	2.4202	2.4213	0.0457
161362	$La_{0.67}Na_{0.33}MnO_3$	3.8711	1.939	0.9772	2.4254	2.4299	0.1871
96038	$LaMnO_3$	3.8705	1.960	0.9667	2.4135	2.4163	0.1161
Average systematic absolute error							0.1163
185478	$La_{0.9}K_{0.1}MnO_3$	3.8938	1.964	0.9842	2.4222	2.4177	0.1869
185479	$La_{0.875}K_{0.125}MnO_3$	3.8928	1.960	0.9893	2.4221	2.4210	0.0460
185480	$La_{0.85}K_{0.15}MnO_3$	3.8884	1.957	0.9948	2.4249	2.4217	0.1299
96038	$LaMnO_3$	3.8705	1.960	0.9667	2.4135	2.4163	0.1161
Average systematic absolute error							0.1197
168695	$La_{0.95}Ag_{0.05}MnO_3$	3.8809	1.958	0.9698	2.4222	2.4201	0.0879
168696	$La_{0.9}Ag_{0.1}MnO_3$	3.8801	1.958	0.9735	2.4233	2.4196	0.1523
241662	$La_{0.85}Ag_{0.15}MnO_3$	3.8899	1.964	0.9778	2.4218	2.4183	0.1420
153552	$La_{0.8}Ag_{0.2}MnO_3$	3.8729	1.953	0.9826	2.4268	2.4212	0.2301
96038	$LaMnO_3$	3.8705	1.960	0.9667	2.4135	2.4163	0.1161
Average systematic absolute error							0.1457
96039	$La_{0.9}Pb_{0.1}MnO_3$	3.8733	1.957	0.9788	2.4155	2.4140	0.0593
167676	$La_{0.67}Pb_{0.33}MnO_3$	3.9116	1.956	1.0041	2.4429	2.4241	0.7683
95498	$La_{0.65}Pb_{0.35}MnO_3$	3.8795	1.955	1.0064	2.4225	2.4166	0.2435
96038	$LaMnO_3$	3.8705	1.960	0.9667	2.4135	2.4163	0.1161
Average systematic absolute error							0.2968
Global average absolute error							0.1348

Table 5.2 Experimental and calculated trigonal lattice constants from Eqs. 5.4, 5.5, & 5.7 for the 57 $R\bar{3}c$ trigonal compositions.

ICSD #	Compound	a (Exptl.) (Å)	a (Calc.) (Å)	|Error%|	c (Exptl.) (Å)	c (Calc.) (Å)	|Error%|
98069	$La_{0.6}Sr_{0.4}FeO_3$	5.5308	5.5323	0.0267	13.4334	13.4262	0.0533
163227	$La_{0.5}Sr_{0.5}FeO_3$	5.5111	5.5114	0.0054	13.4158	13.4143	0.0108
78067	$La_{0.4}Sr_{0.6}FeO_3$	5.4937	5.4947	0.0190	13.4106	13.4055	0.0380
160591	$La_{0.33}Sr_{0.67}FeO_3$	5.4780	5.4796	0.0284	13.4160	13.4084	0.0568
190643	$La_{0.33}Sr_{0.67}FeO_3$	5.4769	5.4777	0.0149	13.3980	13.3940	0.0298
78068	$La_{0.3}Sr_{0.7}FeO_3$	5.4762	5.4769	0.0114	13.4055	13.4025	0.0228
Average systematic absolute error				0.0176			0.0352
82814	$La_{0.9}Sr_{0.1}CoO_3$	5.3594	5.3550	0.0810	12.9828	13.0039	0.1623
164487	$La_{0.85}Sr_{0.15}CoO_3$	5.4406	5.4338	0.1253	13.1423	13.1753	0.2511
82815	$La_{0.8}Sr_{0.2}CoO_3$	5.3964	5.3913	0.0944	13.0844	13.1092	0.1890
156454	$La_{0.7}Sr_{0.3}CoO_3$	5.4437	5.4367	0.1290	13.2062	13.2404	0.2586
237871	$La_{0.6}Sr_{0.4}CoO_3$	5.4367	5.4321	0.0846	13.2142	13.2366	0.1694
93380	$La_{0.5}Sr_{0.5}CoO_3$	5.4270	5.4248	0.0412	13.2540	13.2649	0.0825
167257	$LaCoO_3$	5.4410	5.4309	0.1862	13.0890	13.1379	0.3734
Average systematic absolute error				0.1060			0.2123
189376	$La_{0.99}Ba_{0.01}CoO_3$	5.4380	5.4382	0.0030	13.1260	13.1252	0.0061
157894	$La_{0.97}Ba_{0.03}CoO_3$	5.4482	5.4445	0.0681	13.1280	13.1459	0.1364
157895	$La_{0.95}Ba_{0.05}CoO_3$	5.4521	5.4503	0.0338	13.1520	13.1609	0.0675
157896	$La_{0.92}Ba_{0.08}CoO_3$	5.4563	5.4581	0.0323	13.1830	13.1745	0.0645
157897	$La_{0.9}Ba_{0.1}CoO_3$	5.4602	5.4609	0.0125	13.2070	13.2037	0.0249
157898	$La_{0.88}Ba_{0.12}CoO_3$	5.4616	5.4609	0.0127	13.2230	13.2264	0.0255
157899	$La_{0.85}Ba_{0.15}CoO_3$	5.4658	5.4657	0.0021	13.2530	13.2536	0.0041
157900	$La_{0.82}Ba_{0.18}CoO_3$	5.4685	5.4683	0.0033	13.2800	13.2809	0.0066

157901	$La_{0.8}Ba_{0.2}CoO_3$	5.4705	5.4702	0.0054	13.2990	13.3004	0.0108
157902	$La_{0.75}Ba_{0.25}CoO_3$	5.4731	5.4721	0.0180	13.3380	13.3428	0.0360
157903	$La_{0.72}Ba_{0.28}CoO_3$	5.4745	5.4757	0.0214	13.3630	13.3573	0.0428
157904	$La_{0.7}Ba_{0.3}CoO_3$	5.4752	5.4757	0.0330	13.3800	13.3712	0.0660
167257	$LaCoO_3$	5.4410	5.4309	0.1862	13.0890	13.1379	0.3734
Average systematic absolute error				0.0332			0.0665
91179	$La_{0.875}Ba_{0.125}MnO_3$	5.5522	5.5494	0.0507	13.4290	13.4426	0.1014
91180	$La_{0.85}Ba_{0.15}MnO_3$	5.5432	5.5403	0.0525	13.4250	13.4391	0.1051
159742	$La_{0.825}Ba_{0.175}MnO_3$	5.5776	5.5789	0.0240	13.5470	13.5405	0.0479
91182	$La_{0.8}Ba_{0.2}MnO_3$	5.5444	5.5416	0.0508	13.4650	13.4787	0.1017
91183	$La_{0.775}Ba_{0.225}MnO_3$	5.5433	5.5426	0.0126	13.4710	13.4744	0.0253
91184	$La_{0.75}Ba_{0.25}MnO_3$	5.5398	5.5405	0.0120	13.4750	13.4718	0.0239
82104	$La_{0.7}Ba_{0.3}MnO_3$	5.5378	5.5391	0.0230	13.5011	13.4949	0.0460
185842	$La_{0.67}Ba_{0.33}MnO_3$	5.5322	5.5330	0.0142	13.5034	13.4996	0.0283
96038	$LaMnO_3$	5.5008	5.4987	0.0387	13.2760	13.2863	0.0774
Average systematic absolute error				0.0309			0.0619
97865	$La_{0.82}Sr_{0.18}MnO_3$	5.5300	5.5325	0.0452	13.3600	13.3480	0.0903
97866	$La_{0.8}Sr_{0.2}MnO_3$	5.5253	5.5280	0.0485	13.3577	13.3448	0.0969
162762	$La_{0.7}Sr_{0.3}MnO_3$	5.5059	5.5052	0.0135	13.3619	13.3655	0.0271
160750	$La_{0.667}Sr_{0.333}MnO_3$	5.5100	5.5095	0.0095	13.3840	13.3866	0.0191
95568	$La_{0.64}Sr_{0.36}MnO_3$	5.5032	5.5032	0.0009	13.3675	13.3673	0.0017
99555	$La_{0.6}Sr_{0.4}MnO_3$	5.4843	5.4825	0.0337	13.3594	13.3684	0.0675
236939	$La_{0.55}Sr_{0.45}MnO_3$	5.4760	5.4732	0.0513	13.3461	13.3598	0.1027
96038	$LaMnO_3$	5.5008	5.4987	0.0387	13.2760	13.2863	0.0774
Average systematic absolute error				0.0302			0.0603
155413	$La_{0.95}Ca_{0.05}MnO_3$	5.5229	5.5194	0.0634	13.3420	13.3589	0.1269

238369	$La_{0.8}Ca_{0.2}MnO_3$	5.4960	5.4932	0.0515	13.3810	13.3948	0.1031
161685	$La_{0.7}Ca_{0.3}MnO_3$	5.4740	5.4758	0.0326	13.3760	13.3673	0.0652
258206	$La_{0.6}Ca_{0.4}MnO_3$	5.4698	5.4740	0.0772	13.3559	13.3353	0.1542
96038	$LaMnO_3$	5.5008	5.4987	0.0387	13.2760	13.2863	0.0774
Average systematic absolute error				0.0527			0.1054
257499	$La_{0.9}Na_{0.1}MnO_3$	5.5037	5.5029	0.0152	13.3199	13.3240	0.0304
161362	$La_{0.67}Na_{0.33}MnO_3$	5.4926	5.4892	0.0623	13.3217	13.3383	0.1247
96038	$LaMnO_3$	5.5008	5.4987	0.0387	13.2760	13.2863	0.0774
Average systematic absolute error				0.0387			0.0775
185478	$La_{0.9}K_{0.1}MnO_3$	5.5273	5.5307	0.0624	13.3883	13.3716	0.1246
185479	$La_{0.875}K_{0.125}MnO_3$	5.5259	5.5267	0.0153	13.3842	13.3801	0.0306
185480	$La_{0.85}K_{0.15}MnO_3$	5.5176	5.5200	0.0434	13.3796	13.3680	0.0866
96038	$LaMnO_3$	5.5008	5.4987	0.0387	13.2760	13.2863	0.0774
Average systematic absolute error				0.0399			0.0798
168695	$La_{0.95}Ag_{0.05}MnO_3$	5.5090	5.5106	0.0293	13.3440	13.3362	0.0586
168696	$La_{0.9}Ag_{0.1}MnO_3$	5.5070	5.5098	0.0508	13.3450	13.3315	0.1015
241662	$La_{0.85}Ag_{0.15}MnO_3$	5.5220	5.5246	0.0474	13.3730	13.3603	0.0947
153552	$La_{0.8}Ag_{0.2}MnO_3$	5.4941	5.4984	0.0768	13.3332	13.3127	0.1535
96038	$LaMnO_3$	5.5008	5.4987	0.0387	13.2760	13.2863	0.0774
Average systematic absolute error				0.0486			0.0971
96039	$La_{0.9}Pb_{0.1}MnO_3$	5.5033	5.5044	0.0198	13.2930	13.2877	0.0395
167676	$La_{0.67}Pb_{0.33}MnO_3$	5.5368	5.5511	0.2574	13.5258	13.4564	0.5129
95498	$La_{0.65}Pb_{0.35}MnO_3$	5.5068	5.5113	0.0813	13.3401	13.3184	0.1624
96038	$LaMnO_3$	5.5008	5.4987	0.0387	13.2760	13.2863	0.0774
Average systematic absolute error				0.0993			0.1981
Global average absolute error				0.0449			0.0898

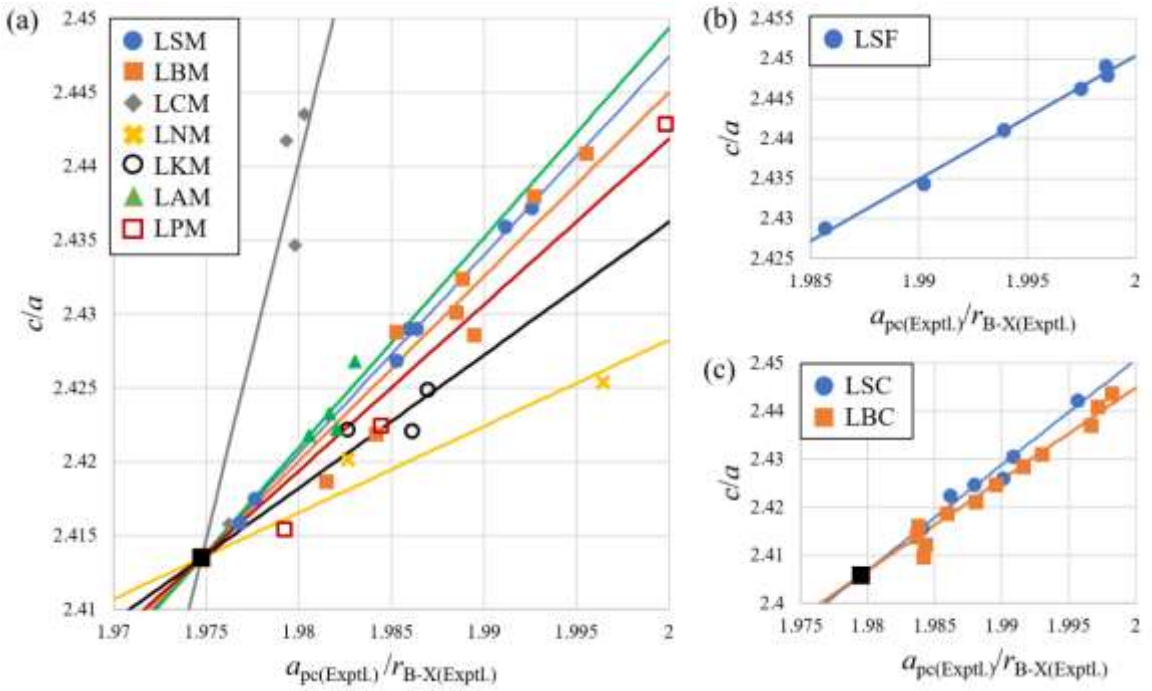

Figure 5.1 Linear fits describing *c*/*a* vs. $a_{pc(Exptl.)}/r_{BX(Exptl.)}$ for the (a) $La^{3+}_{1-x}A^{2+}_{x}Mn^{3+}_{1-x}Mn^{4+}_{x}O_3$, $La^{3+}_{1-x}A^{1+}_{x}Mn^{3+}_{1-2x}Mn^{4+}_{2x}O_3$, (b) $La^{3+}_{1-x}A^{2+}_{x}Fe^{3+}_{1-x}Fe^{4+}_{x}O_3$, and (c) $La^{3+}_{1-x}A^{2+}_{x}Co^{3+}_{1-x}Co^{4+}_{x}O_3$ systems.

Fig. 5.1 shows the relationship between the degree of trignonality, *c*/*a*, and the ratio of the pseudocubic lattice constant, a_{pc}, to the B-X bond length, r_{BX}. These fits clearly show that this trend is linear so can be represented by Eq. 5.1:

$$\frac{c}{a} = A\left(\frac{a_{pc}}{r_{BX}}\right) + B, \tag{5.1}$$

Fig. 5.1 also shows that the seven series with Mn on the B site clearly converge at $LaMnO_3$ and the two series with Co on the B site converge at $LaCoO_3$. Table 5.3 shows all of the coefficients and the goodness of fits for the trends represented by Eq. 5.1.

Table 5.3 Coefficients of Eq. 5.1

Composition	*A*	*B*	R^2
$La_{1-x}Sr_xFeO_3$	1.543171	-0.635964	0.9937
$La_{1-x}Sr_xCoO_3$	2.191690	-1.932677	0.9809
$La_{1-x}Ba_xCoO_3$	1.907794	-1.370724	0.9728
$La_{1-x}Sr_xMnO_3$	1.343478	-0.239554	0.9977
$La_{1-x}Ba_xMnO_3$	1.249331	-0.053637	0.9273
$La_{1-x}Ca_xMnO_3$	5.104347	-7.666295	0.9075
$La_{1-x}Na_xMnO_3$	0.584690	1.258855	0.9320
$La_{1-x}K_xMnO_3$	0.900957	0.634310	0.9244
$La_{1-x}Ag_xMnO_3$	1.420578	-0.391807	0.9464
$La_{1-x}Pb_xMnO_3$	1.124310	0.193246	0.9737

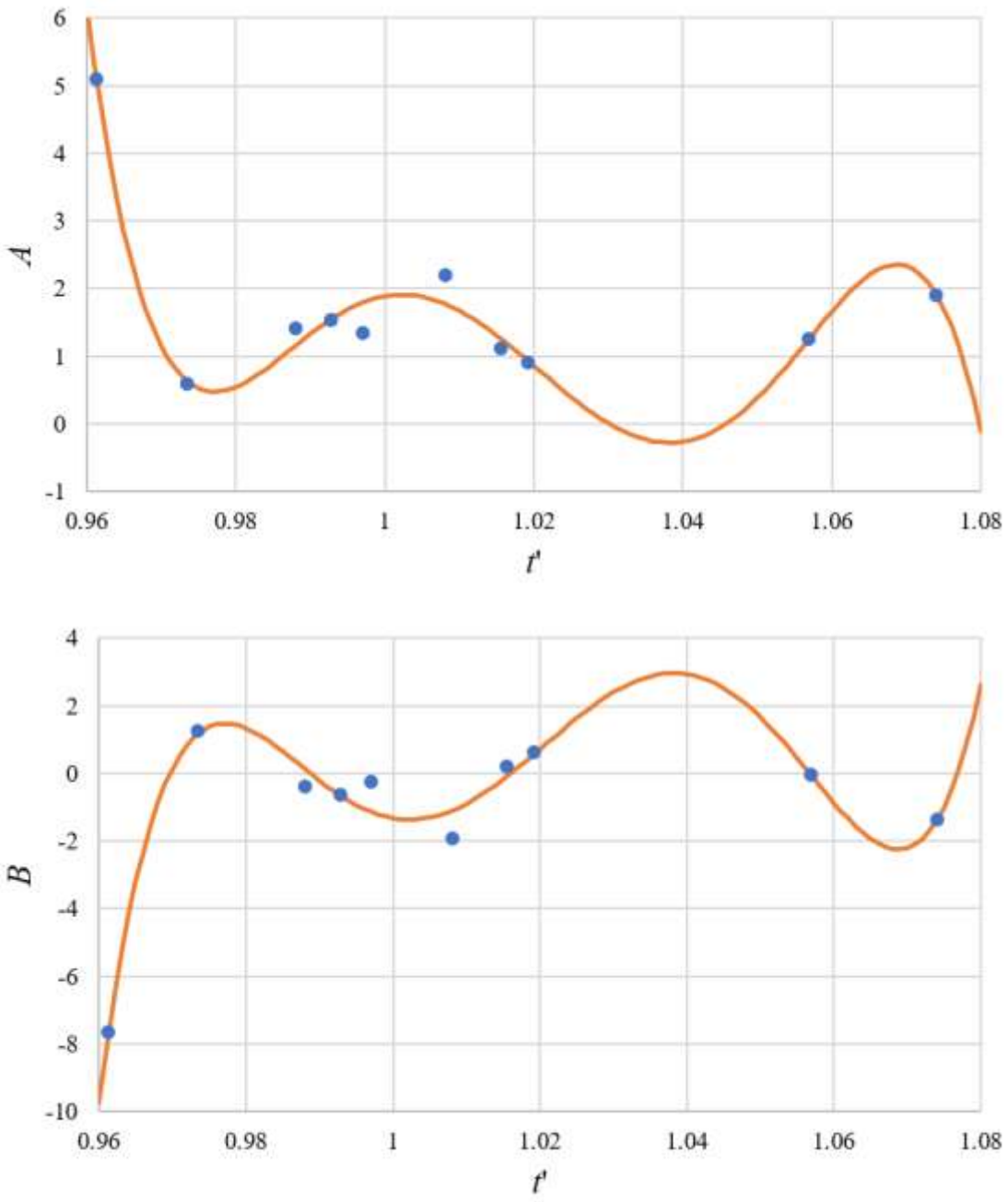

Figure 5.2 Coefficients of Eq. 5.1 vs. tolerance factor[16].

Fig. 5.2 demonstrates the relationship between the modified tolerance factor[16] and the coefficients of Eq. 5.1. Both coefficients of Eq. 5.1 (*A* and *B*) can be represented by the same fifth-order polynomial as a function of *t′*:

$$Coeff = at'^5 + bt'^4 + ct'^3 + dt'^2 + et' + f \tag{5.2}$$

where *Coeff* = *A* or *B*, and *t'* is determined via an empirical model[16] at the compositions that are 50% doped on the A site for divalent dopants and 25% doped on the A site for monovalent dopants (*i.e.* $A^{3+}_{0.5}A^{2+}_{0.5}B^{3+}_{0.5}B^{4+}_{0.5}O_3$ or $A^{3+}_{0.75}A^{1+}_{0.25}B^{3+}_{0.5}B^{4+}_{0.5}O_3$). For instance, the compound $La_{0.8}Sr_{0.2}MnO_3$ has an *x* value of 0.2, but Eq. 5.2 would be applied to the $La_{0.5}Sr_{0.5}MnO_3$ composition to determine the values of *A* and *B*. Then, Eq. 5.1 can be applied to the actual composition, $La_{0.8}Sr_{0.2}MnO_3$, to predict its *c*/*a* value. Table 5.4 lists the goodness of fits and the coefficients of Eq. 5.2.

Table 5.4 Coefficients of Eq. 5.2

Coeff	*a* (×10⁸)	*b* (×10⁸)	*c* (×10⁸)	*d* (×10⁸)	*e* (×10⁸)	*f* (×10⁸)	R^2
A	-0.279599	1.428203	-2.917000	2.977727	-1.519272	0.309941	0.9674
B	0.552473	-2.822077	5.763927	-5.883965	3.002091	-0.612450	0.9669

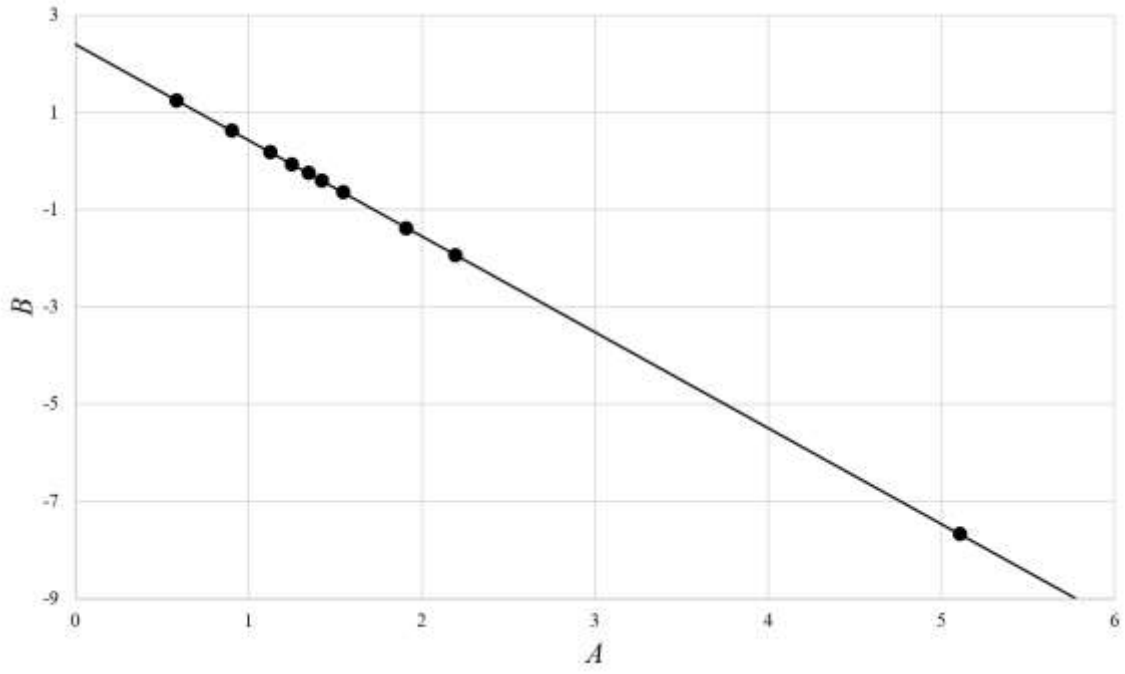

Figure 5.3 Linear correlation between the coefficients of Eq. 5.1.

It is also apparent from Fig. 5.2 that *A* and *B* are not independent parameters; instead, it appears that they are highly correlated and are, in fact, displaced mirror images

of each other. Fig. 5.3 shows the correlation between *A* and *B*, which is linear. It can be represented by Eq. 5.3:

$$B = -1.975479A + 2.411050 \quad \left(R^2 = 1\right) \tag{5.3}$$

Eq. 5.3 can be substituted into Eq. 5.1; thus, simplifying the model even further as shown in Eq. 5.4:

$$\frac{c}{a} = A\left(\frac{a_{\mathrm{pc}}}{r_{\mathrm{BX}}} - 1.975479\right) + 2.411050 \tag{5.4}$$

Now, Eq. 5.4 allows for the prediction of the perovskite trigonality, *c*/*a*, using only a single coefficient, *A*. This coefficient can now be easily calculated using Eq. 5.2 and the coefficients of Table 5.4 as:

$$A = \left(-0.279599t'^5 + 1.428203t'^4 - 2.917000t'^3 + 2.977727t'^2 - 1.519272t' + 0.309941\right) \times 10^8 \tag{5.5}$$

Interestingly, perovskites with *R*3*c* symmetry tend to exhibit *c*/*a* values greater than $\sqrt{6}$, which is beyond the range of Eqs. 5.4-5.5. Thus, another general model was developed to describe the perovskite trigonality for these compounds.

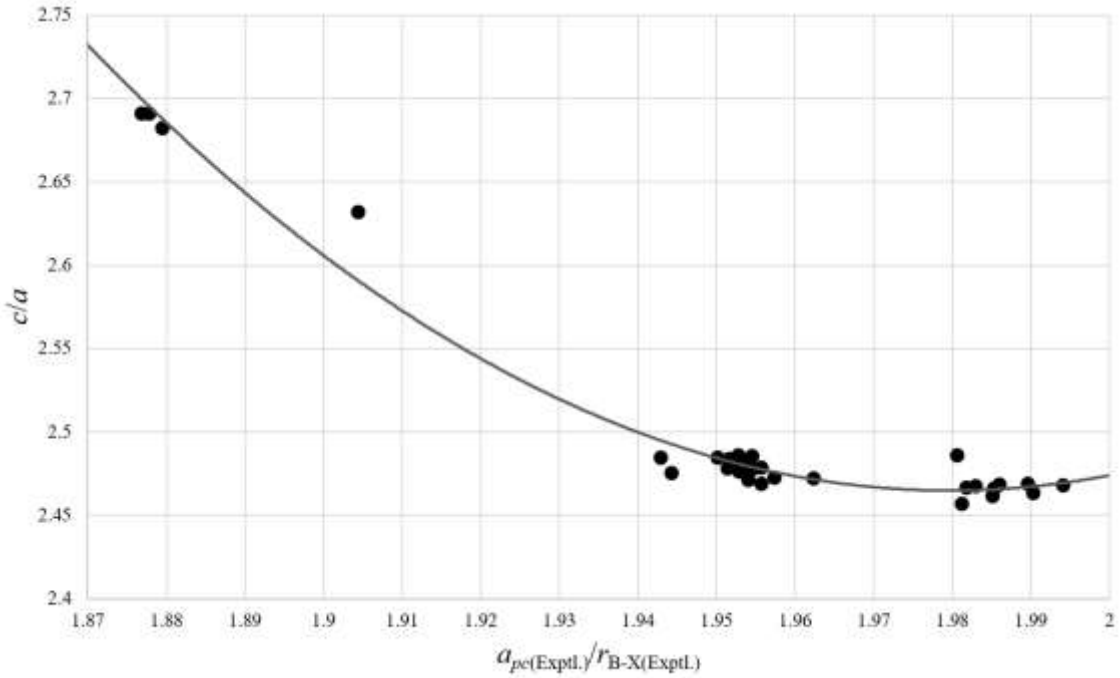

Figure 5.4 Quadratic fit describing c/a vs. $a_{pc(Exptl.)}/r_{BX(Exptl.)}$ for the 31 $R3c$ trigonal perovskites

Fig. 5.4 shows that the trigonality for all 31 $R3c$ perovskites can be represented by the same general quadratic function (Eq. 5.6) in terms of the ratio of the experimental pseudocubic lattice constant, $a_{pc(Exptl.)}$, to the experimental B-X bond length, $r_{B\text{-}X(Exptl.)}$.

$$\frac{c}{a} = 22.211002\left(\frac{a_{pc}}{r_{BX}}\right)^2 - 87.942060\left(\frac{a_{pc}}{r_{BX}}\right) + 89.514066 \quad \left(R^2 = 0.9783\right) \tag{5.6}$$

Table 5.5 shows the experimental data and the predicted trigonality for all 31 $R3c$ trigonal perovskites using Eq. 5.6. Overall, this model is very accurate. The average error is 0.2380%. Only the $LiReO_3$ composition produces a rather large error of 1.5779%.

Table 5.6 shows the experimental and predicted lattice constants for all 31 $R3c$ trigonal perovskites. The average error for a and c are 0.0795% and 0.1587%, respectively. Again, the $LiReO_3$ composition produces the most error (0.5316% for a and 1.0547% for c). One of the reasons $LiReO_3$ produces the largest error may be due to the fact that ReO_3

is actually a perovskite[18] with a completely vacant A-site. Thus, the Li ions may not necessarily occupy the A-site in these perovskites. It is entirely possible that some of the Li ions may occupy interstitial sites. Another possibility is that there are some Li vacancies in this perovskite because Li tends to volatilize at the high temperatures associated with the calcination and sintering processes if care is not taken to mitigate this volatilization. A third possibility is that displacive disorder is occurring in this perovskite. In any of these cases, the degree of trigonality will be significantly affected and cause large errors in the prediction of the trigonality and lattice constants.

Table 5.5 The 31 *R*3*c* trigonal perovskites used to derive the general trigonal model for $c/a > \sqrt{6}$ (Fig. 5.4).

ICSD #	Compound	$a_{pc(Exptl.)}$ (Å)	$r_{B\text{-}X(Exptl.)}$ (Å)	c/a Exptl	c/a Calc	|Error%|
250775	$LiNbO_3$	3.9651	2.002	2.4862	2.4648	0.8585
35012	$LiReO_3$	3.6879	1.937	2.6323	2.5907	1.5779
98123	$(Li_{0.937}Zn_{0.063})(Nb_{0.979}Zn_{0.021})O_3$	3.7602	2.004	2.6913	2.6999	0.3177
98125	$(Li_{0.94}Zn_{0.06})(Nb_{0.98}Zn_{0.02})O_3$	3.7602	2.003	2.6913	2.6956	0.1592
250774	$Li_{0.96}Na_{0.04}NbO_3$	3.7645	2.003	2.6824	2.6882	0.2159
280368	$PbHf_{0.8}Ti_{0.2}O_3$	4.1050	2.063	2.4635	2.4673	0.1543
46024	$PbZr_{0.9}Ti_{0.1}O_3$	4.1406	2.077	2.4681	2.4694	0.0526
86131	$PbZr_{0.871}Ti_{0.129}O_3$	4.1432	2.087	2.4663	2.4655	0.0327
86132	$PbZr_{0.838}Ti_{0.162}O_3$	4.1370	2.087	2.4670	2.4649	0.0837
86133	$PbZr_{0.796}Ti_{0.204}O_3$	4.1282	2.082	2.4678	2.4650	0.1102
86134	$PbZr_{0.745}Ti_{0.255}O_3$	4.1213	2.075	2.4684	2.4657	0.1118
86135	$PbZr_{0.7}Ti_{0.3}O_3$	4.1128	2.067	2.4691	2.4670	0.0850
237367	$BiFeO_3$	3.9651	2.031	2.4862	2.4809	0.2103
193811	$Bi_{0.5}Na_{0.5}TiO_3$	3.8870	1.962	2.4569	2.4648	0.3250
237369	$BiFe_{0.8}Co_{0.2}O_3$	3.9436	2.017	2.4788	2.4776	0.0491
261637	$Bi_{0.95}Tb_{0.05}FeO_3$	3.9587	2.029	2.4837	2.4824	0.0538
261638	$Bi_{0.9}Tb_{0.1}FeO_3$	3.9587	2.029	2.4837	2.4824	0.0538
261639	$Bi_{0.85}Tb_{0.15}FeO_3$	3.9484	2.023	2.4807	2.4821	0.0568
182003	$Bi_{0.88}Sm_{0.12}FeO_3$	3.9535	2.026	2.4781	2.4826	0.1796
194413	$Bi_{0.9}La_{0.1}FeO_3$	3.9585	2.036	2.4754	2.4927	0.7007
181565	$Bi_{0.815}La_{0.185}FeO_3$	3.9465	2.018	2.4693	2.4776	0.3382
193639	$BiFe_{0.98}Co_{0.02}O_3$	3.9655	2.029	2.4855	2.4790	0.2631
82615	$Bi_{0.93}La_{0.07}FeO_3$	3.9554	2.026	2.4765	2.4809	0.1759
51662	$BiFe_{0.8}Mn_{0.2}O_3$	3.9559	2.024	2.4780	2.4789	0.0367
51663	$BiFe_{0.9}Mn_{0.1}O_3$	3.9624	2.029	2.4834	2.4802	0.1289
192514	$Bi_{0.95}Dy_{0.05}FeO_3$	3.9596	2.031	2.4848	2.4843	0.0208
165908	$Bi_{0.85}La_{0.15}FeO_3$	3.9596	2.038	2.4848	2.4949	0.4056

187231	$Bi_{0.87}La_{0.13}FeO_3$	3.9577	2.022	2.4728	2.4759	0.1259
188046	$BiFe_{0.9}Ti_{0.1}O_3$	3.9580	2.017	2.4721	2.4715	0.0234
252624	$Bi_{0.9}Pb_{0.1}FeO_3$	3.9583	1.994	2.4619	2.4654	0.1451
163686	$Bi_{0.9}Ca_{0.1}FeO_3$	3.9481	2.021	2.4714	2.4794	0.3251
Average absolute error						0.2380

Table 5.6 Experimental and calculated trigonal lattice constants from Eqs. 5.6-5.7 for the 31 *R*3*c* trigonal compositions.

ICSD #	**Compound**	***a*** **(Exptl.) (Å)**	***a*** **(Calc.) (Å)**	**|Error%|**	***c*** **(Exptl.) (Å)**	***c*** **(Calc.) (Å)**	**|Error%|**
250775	$LiNbO_3$	5.5797	5.5958	0.2878	13.8721	13.7926	0.5731
35012	$LiReO_3$	5.0918	5.1189	0.5316	13.4030	13.2616	1.0547
98123	$(Li_{0.937}Zn_{0.063})(Nb_{0.979}Zn_{0.021})O_3$	5.1534	5.1480	0.1057	13.8696	13.8990	0.2117
98125	$(Li_{0.94}Zn_{0.06})(Nb_{0.98}Zn_{0.02})O_3$	5.1534	5.1507	0.0530	13.8696	13.8843	0.1061
250774	$Li_{0.96}Na_{0.04}NbO_3$	5.1650	5.1613	0.0719	13.8545	13.8744	0.1439
280368	$PbHf_{0.8}Ti_{0.2}O_3$	5.7943	5.7913	0.0514	14.2742	14.2889	0.1029
46024	$PbZr_{0.9}Ti_{0.1}O_3$	5.8410	5.8400	0.0175	14.4160	14.4211	0.0351
86131	$PbZr_{0.871}Ti_{0.129}O_3$	5.8461	5.8467	0.0109	14.4182	14.4151	0.0218
86132	$PbZr_{0.838}Ti_{0.162}O_3$	5.8367	5.8383	0.0279	14.3989	14.3909	0.0558
86133	$PbZr_{0.796}Ti_{0.204}O_3$	5.8238	5.8259	0.0368	14.3716	14.3610	0.0735
86134	$PbZr_{0.745}Ti_{0.255}O_3$	5.8134	5.8156	0.0373	14.3500	14.3393	0.0746
86135	$PbZr_{0.7}Ti_{0.3}O_3$	5.8010	5.8026	0.0283	14.3230	14.3149	0.0567
237367	$BiFeO_3$	5.5797	5.5836	0.0702	13.8721	13.8526	0.1403
193811	$Bi_{0.5}Na_{0.5}TiO_3$	5.4916	5.4857	0.1081	13.4921	13.5213	0.2165
237369	$BiFe_{0.8}Co_{0.2}O_3$	5.5551	5.5560	0.0164	13.7700	13.7655	0.0328
261637	$Bi_{0.95}Tb_{0.05}FeO_3$	5.5726	5.5737	0.0179	13.8409	13.8359	0.0359
261638	$Bi_{0.9}Tb_{0.1}FeO_3$	5.5726	5.5737	0.0179	13.8409	13.8359	0.0359
261639	$Bi_{0.85}Tb_{0.15}FeO_3$	5.5603	5.5593	0.0189	13.7937	13.7989	0.0379
182003	$Bi_{0.88}Sm_{0.12}FeO_3$	5.5695	5.5662	0.0598	13.8020	13.8185	0.1197
194413	$Bi_{0.9}La_{0.1}FeO_3$	5.5786	5.5656	0.2325	13.8090	13.8734	0.4666

181565	$Bi_{0.815}La_{0.185}FeO_3$	5.5663	5.5600	0.1125	13.7447	13.7757	0.2254
193639	$BiFe_{0.98}Co_{0.02}O_3$	5.5809	5.5858	0.0879	13.8714	13.8471	0.1755
82615	$Bi_{0.93}La_{0.07}FeO_3$	5.5734	5.5701	0.0586	13.8025	13.8187	0.1172
51662	$BiFe_{0.8}Mn_{0.2}O_3$	5.5729	5.5722	0.0122	13.8097	13.8131	0.0245
51663	$BiFe_{0.9}Mn_{0.1}O_3$	5.5780	5.5804	0.0430	13.8525	13.8406	0.0860
192514	$Bi_{0.95}Dy_{0.05}FeO_3$	5.5730	5.5734	0.0069	13.8480	13.8461	0.0138
165908	$Bi_{0.85}La_{0.15}FeO_3$	5.5730	5.5655	0.1348	13.8480	13.8854	0.2702
187231	$Bi_{0.87}La_{0.13}FeO_3$	5.5793	5.5770	0.0419	13.7967	13.8083	0.0839
188046	$BiFe_{0.9}Ti_{0.1}O_3$	5.5804	5.5808	0.0078	13.7951	13.7930	0.0156
252624	$Bi_{0.9}Pb_{0.1}FeO_3$	5.5885	5.5858	0.0483	13.7582	13.7715	0.0967
163686	$Bi_{0.9}Ca_{0.1}FeO_3$	5.5670	5.5609	0.1081	13.7581	13.7879	0.2166
Average absolute error				0.0795			0.1587

Eq. 5.7 describes the mathematical relationship between the degree of trigonality, c/a, and the pseudocubic lattice constant, a_{pc}:

$$\frac{c}{a} = 4\sqrt{3}\left(\frac{a_{pc}}{a}\right)^3 \tag{5.7}$$

From this expression, it can be shown that the trigonal-to-cubic transition occurs at $c/a = \sqrt{6}$, where the structure is considered trigonal if $c/a \neq \sqrt{6}$. It should also be noted that using Eqs. 5.4-5.7 to predict lattice constants for the cubic perovskite $SrTiO_3$ ($t' = 1$, $a_{pc}/r_{BX} = 2$), the model predicts $c/a = 2.4561$, which is very near the experimental value of 2.4495 (0.270% error). Thus, the model can accurately predict the composition at which a trigonal-to-cubic transition occurs. The trigonal lattice constants can now be derived using Eqs. 5.4-5.7. Fig. 5.6 and Tables 5.2 and 5.6 show the predicted trigonal lattice constants using this model and demonstrate that the model is an effective predictive tool at least within the ranges $5.3594 \leq a \leq 5.5776$ and $12.9828 \leq c \leq 13.5470$ provided that $2.406 \leq c/a \leq 2.4495$ for $R\bar{3}c$ symmetry; and $5.0918 \leq a \leq 5.8461$ and $13.4030 \leq c \leq 14.4182$ provided that $2.4495 \leq c/a \leq 2.6913$ for $R3c$ symmetry.

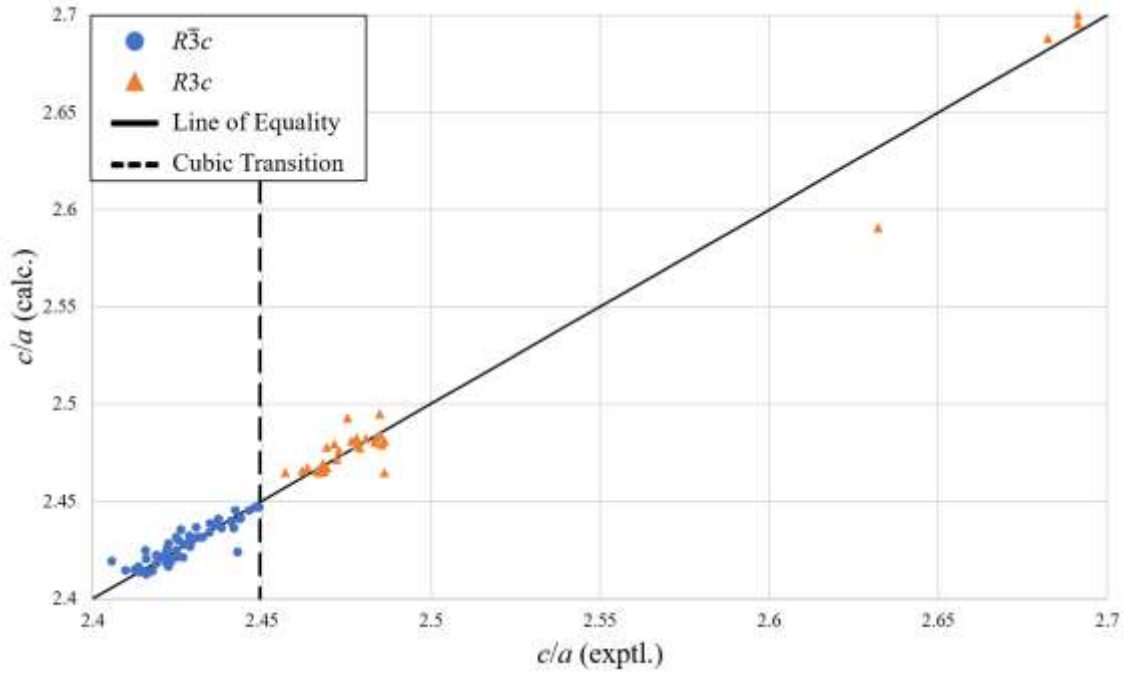

Figure 5.5 Predicted *c*/*a* values of trigonally distorted perovskites using Eqs. 5.4-5.6.

Fig. 5.5 shows the predicted trigonality using the general models. The accuracy of the models appears to be very good for all 88 trigonally distorted perovskites analyzed in this work. It shows that the models can be applied even to compositions that are severely distorted on either side of the cubic transition. There appears to be an outlier at *c*/*a* ~ 2.42, which corresponds to $La_{0.67}Pb_{0.33}MnO_3$[19]. The underestimation of the trigonality in this case may be due to excessive lead volatilization during sintering, especially as this sample was sintered five times in an open environment, likely causing the formation of oxygen vacancies which would be virtually undetectable via XRD. The reasons for the outlier at *c*/*a* ~ 2.63, which corresponds to $LiReO_3$; have already been addressed.

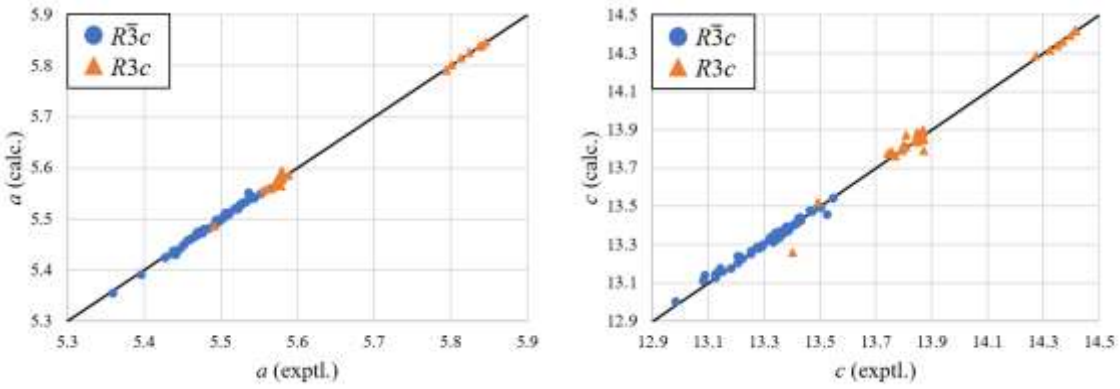

Figure 5.6 Predicted trigonal lattice constants of all 88 trigonally distorted perovskites.

It is also useful to relate trigonality to polarization, which is the intrinsic component of the relative permittivity - the key to unlocking the ferroelectric, piezoelectric, and pyroelectric properties of a material. The dipole moment of a material arises from the separation of the two oppositely charged sublattices. There is obviously no net dipole moment for perovskites in the centrosymmetric space group $R\bar{3}c$, in which the charge centers of the two sublattices coincide. On the other hand, space group *R*3*c* is non-centrosymmetric; thus, perovskites with *R*3*c* symmetry can have non-zero dipole moments. Table 5.7 shows the derived polarizations for 31 *R*3*c* trigonal perovskites which are the direct result of their trigonal distortion. Fig. 5.7 shows that there are three distinct trends in polarization which coincide with $A^{1+}B^{5+}O_3$, $A^{2+}B^{4+}O_3$, and $A^{3+}B^{3+}O_3$ structures. This distinction between perovskites with larger charge differences between the A and B cations and ones with equally charged A and B cations makes sense because the charge centers for the cation sublattices will be different depending upon the ionic charges of the A- and B-site cations. The trends in each of these cases are described by Eqs. 5.8-5.10.

Table 5.7 Room-temperature polarizations of 31 trigonal perovskites in space group *R*3*c*.

ICSD#	Data Type	Compound	$c/a_{(exptl.)}$	Polarization ($\mu C/cm^2$)$_{(exptl.)}$	Polarization ($\mu C/cm^2$)$_{(calc.)}$	|Error%|
250775	neutron	$LiNbO_3$	2.6869	66.2863	61.5224	7.19
35012	neutron	$LiReO_3$	2.6323	20.1141	23.0340	14.52
98123	neutron	$(Li_{0.937}Zn_{0.063})(Nb_{0.0979}Zn_{0.021})O_3$	2.6913	62.1352	66.6244	7.23
98125	neutron	$(Li_{0.94}Zn_{0.06})(Nb_{0.98}Zn_{0.02})O_3$	2.6913	62.9878	66.6244	5.77
250774	neutron	$Li_{0.96}Na_{0.04}NbO_3$	2.6824	62.3474	56.7818	8.93
46024	neutron	$PbZr_{0.9}Ti_{0.1}O_3$	2.4681	41.9707	41.6220	0.83
193811	neutron	$Bi_{0.5}Na_{0.5}TiO_3$	2.4569	16.1952	16.9870	4.89
280368	neutron	$PbHf_{0.8}Ti_{0.2}O_3$	2.4635	34.5167	31.5550	8.58
86131	neutron	$PbZr_{0.871}Ti_{0.129}O_3$	2.4663	37.7467	37.7171	0.08
86132	neutron	$PbZr_{0.838}Ti_{0.162}O_3$	2.4670	42.4012	39.1793	7.60
86133	neutron	$PbZr_{0.796}Ti_{0.204}O_3$	2.4678	42.6230	40.9237	3.99
86134	neutron	$PbZr_{0.745}Ti_{0.255}O_3$	2.4684	41.0485	42.4230	3.35
86135	neutron	$PbZr_{0.7}Ti_{0.3}O_3$	2.4691	38.4811	43.7901	13.80
237367	neutron	$BiFeO_3$	2.4862	72.0989	71.2317	1.20
237369	neutron	$BiCo_{0.2}Fe_{0.8}O_3$	2.4788	67.9923	65.3965	3.82
261637	neutron	$Bi_{0.95}Tb_{0.05}FeO_3$	2.4837	69.8951	69.7663	0.18
261638	neutron	$Bi_{0.9}Tb_{0.1}FeO_3$	2.4837	67.6325	69.7663	3.16
261639	neutron	$Bi_{0.85}Tb_{0.15}FeO_3$	2.4807	67.5440	67.2695	0.41
182003	neutron	$Bi_{0.88}Sm_{0.12}FeO_3$	2.4781	57.2301	64.6766	13.01
194413	neutron	$Bi_{0.9}La_{0.1}FeO_3$	2.4754	55.9634	61.6084	10.09
181565	neutron	$Bi_{0.815}La_{0.185}FeO_3$	2.4693	45.1479	53.9537	19.50
193689	neutron	$BiFe_{0.98}Co_{0.02}O_3$	2.4855	70.2511	70.9030	0.93
82615	neutron	$Bi_{0.93}La_{0.07}FeO_3$	2.4765	65.8305	62.9056	4.44
51662	neutron	$BiMn_{0.2}Fe_{0.8}O_3$	2.4780	68.4157	64.5531	5.65
51663	neutron	$BiMn_{0.1}Fe_{0.9}O_3$	2.4834	70.4312	69.5379	1.27
192514	neutron	$Bi_{0.95}Dy_{0.05}FeO_3$	2.4848	69.6892	70.5094	1.18

165908	neutron	$Bi_{0.85}La_{0.15}FeO_3$	2.4848	71.8443	70.5094	1.86
187231	neutron	$Bi_{0.87}La_{0.13}FeO_3$	2.4728	61.0800	58.5831	4.09
188046	neutron	$BiFe_{0.9}Ti_{0.1}O_3$	2.4721	59.0363	57.6591	2.33
252624	neutron	$Bi_{0.9}Pb_{0.1}FeO_3$	2.4619	42.9346	41.7655	2.73
163686	neutron	$Bi_{0.9}Ca_{0.1}FeO_3$	2.4714	64.4325	56.7831	11.87

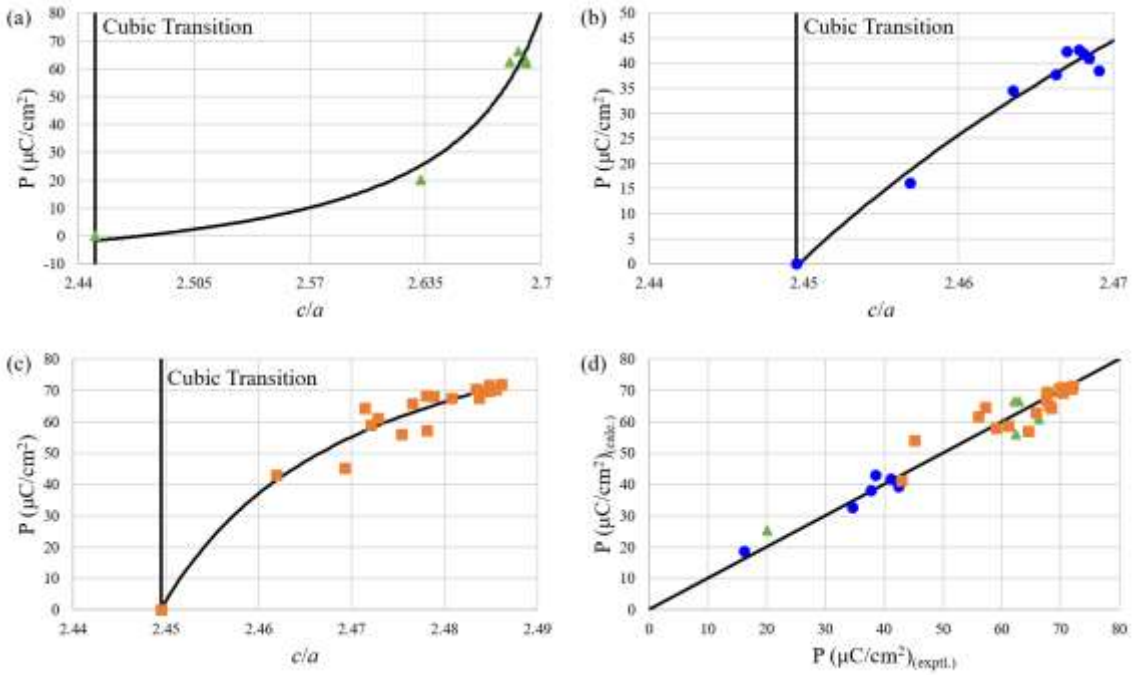

Figure 5.7 Polarization of the 31 perovskites in space group *R*3*c* of the form (a) $A^{1+}B^{5+}O_3$, (b) $A^{2+}B^{4+}O_3$, and (c) $A^{3+}B^{3+}O_3$ as a function of *c*/*a*. (d) Calculated vs. experimental polarization values for all 31 *R*3*c* perovskites. All experimental data are from neutron diffraction.

Fig. 5.7 shows that all three polarization trends can be described by the same general equation:

$$\mathrm{P}\left[\frac{\mu\mathrm{C}}{\mathrm{cm}^2}\right] = G\tan\left(H\left(\frac{c}{a}\right) - \sqrt{6}\right) + K, \tag{5.8}$$

where $H(c/a) - \sqrt{6}$ is in radians. It should be noted that the P = 0 data point at $c/a = \sqrt{6}$ was assumed in all three cases because the polarization will be zero when the structure transitions from trigonal to the centrosymmetric cubic space group $Pm\bar{3}m$. Table 5.8 lists the coefficients for each series.

Table 5.8 Coefficients of Eq. 5.8.

Series	*G*	*H*	*K*	R^2
$A^{+}B^{5+}O_3$	-4.515086	-0.821300	-19.295296	0.9675
$A^{2+}B^{4+}O_3$	18.720362	1.683688	178.895349	0.9749
$A^{3+}B^{3+}O_3$	18.581938	8.123501	108.231639	0.9469

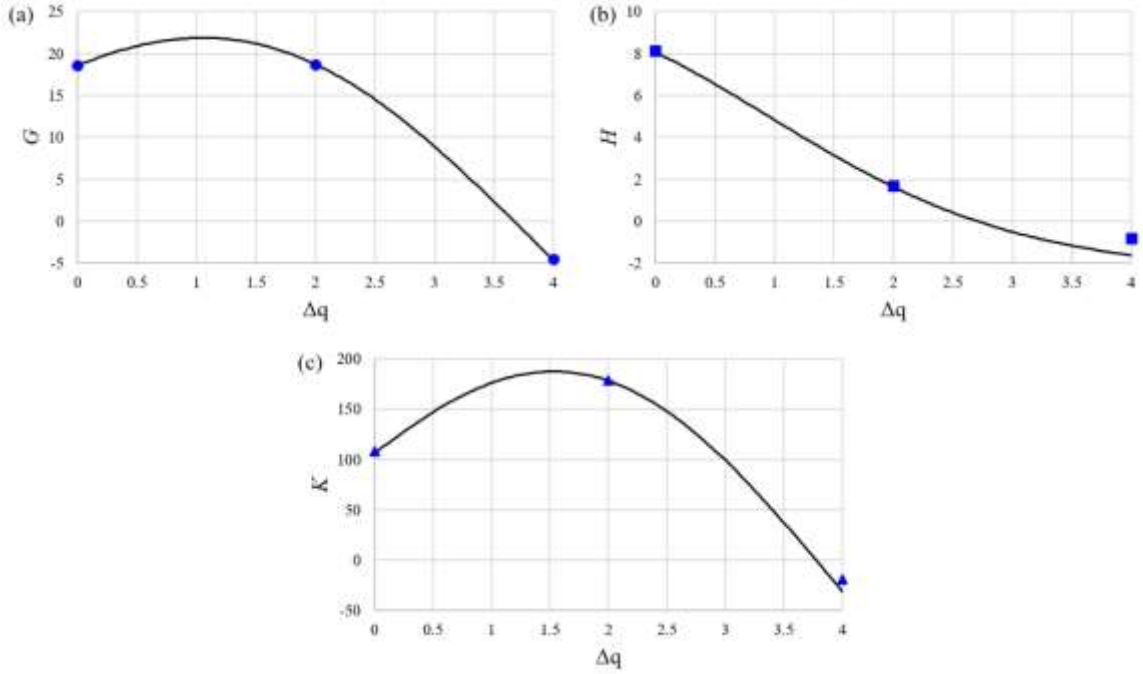

Figure 5.8 Coefficients of Eq. 5.8 as functions of the charge difference between the A- and B-site cations, Δq.

Fig. 5.8 shows that all three coefficients of Eq. 5.8 can be represented by the same expression as a function of the charge difference between the A- and B-site species, Δq:

$$Coeff = M\sin(0.8\Delta q) + Q\cos(0.45\Delta q) \tag{5.9}$$

where *Coeff* = *G*, *H*, or *K*. Table 5.9 shows the coefficients of Eq. 5.9.

Table 5.9 Coefficients of Eq. 5.9.

Coefficient	*M*	*Q*	R^2
G	7.179977	18.558904	1.0000
H	-3.374372	8.058375	0.9842
K	112.350064	106.062864	0.9933

Although Fig. 5.8 clearly shows that *G*, *H*, and *K* are not correlated, the coefficients of those fits (*M* and *Q*) are, in fact, highly correlated, as shown in Fig. 5.9, and can be represented by Eq. 5.10.

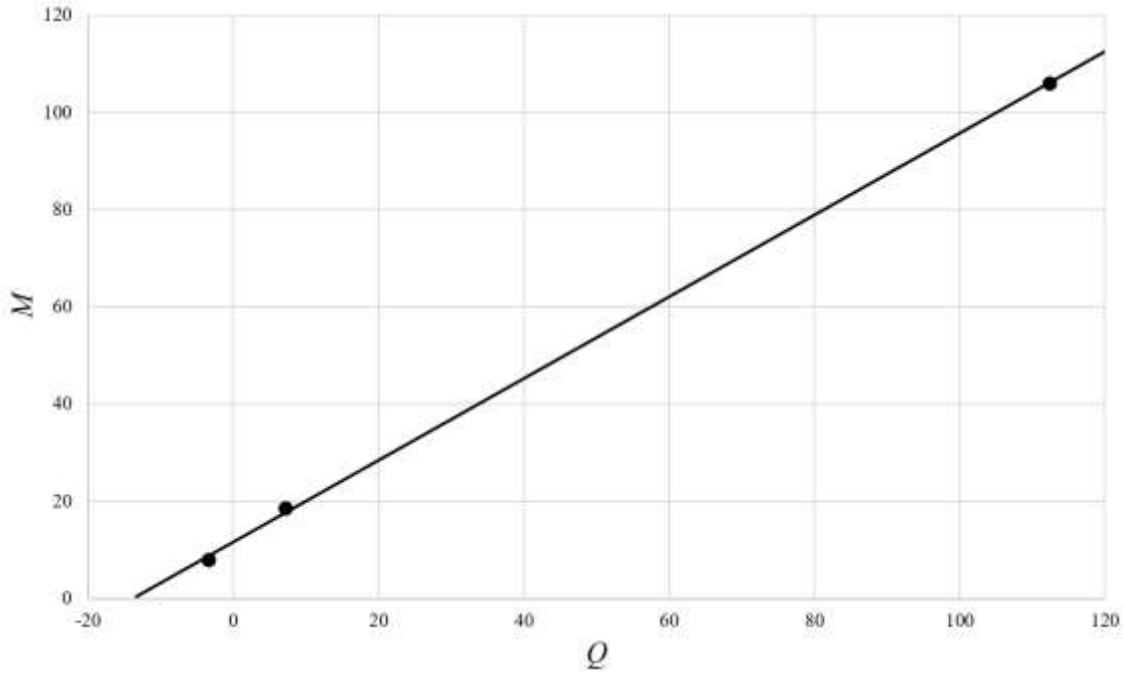

Figure 5.9 Correlation between the coefficients of Eq. 5.9.

Fig. 5.9 clearly shows that *M* and *Q* can be represented in terms of one another as illustrated by Eq. 5.10:

$$Q = 0.840861M + 11.669807 \tag{5.10}$$

Thus, Eq. 5.9 can be simplified as follows:

$$Coeff = M\left(\sin(0.8\Delta q) + 0.840861\cos(0.45\Delta q)\right) + 11.669807\cos(0.45\Delta q) \tag{5.11}$$

Although $Bi_{0.9}Pb_{0.1}FeO_3$ and $Bi_{0.9}Ca_{0.1}FeO_3$ are not exactly $A^{3+}B^{3+}O_3$ type perovskites, their ionic charges are very close; hence, they fit the trend very well. It should also be noted that all the data used for deriving the polarization trends are from neutron diffraction experiments because, unlike XRD, neutron diffraction is sensitive to oxygen positions. Thus, structural data derived from neutron diffraction experiments will provide the most accurate positions for the oxygen sublattice, which will allow for the polarization to be more accurately calculated from that structural data.

5.4 Conclusion

Using data mined from literature for several specific systems, general models were derived for the trigonality of perovskites in both $R\bar{3}c$ and *R*3*c* as a function of the ratio of pseudocubic lattice constant, a_{pc}, to B-X bond length, r_{BX}. A major implication of these models is that they allow for the accurate prediction of trigonal lattice parameters in trigonally distorted perovskites. In addition, these models successfully predicted the trigonal-to-cubic phase transition at room temperature. It may even be possible to extend these models, in conjunction with other empirical models, to predict temperature-dependent trigonal phase transitions in perovskites (*e.g.*, T_C). Moreover, a general model has been developed for predicting the polarization in trigonal perovskites of the forms $A^{1+}B^{5+}O_3$, $A^{2+}B^{4+}O_3$, and $A^{3+}B^{3+}O_3$ in *R*3*c*. This model has major implications in the electroceramics industry because it allows for the accurate prediction of intrinsic polarization using only the degree of trigonality, *c*/*a*, which itself can be accurately predicted using the models presented here.

5.5 References

[1] Zenmi S, Dhahri Ja, Cherif K, Dhahri Je, Oummezzine M, Ghedira M, Vincent H. The effect of a cation radii on structural, magnetic and electrical properties of doped manganites $La_{0.6-x}Pr_xSr_{0.4}MnO_3$. J. Solid State Chem. 2004;177:2387-2393.

[2] Anwar M, Kumar S, Ahmed F, Arshi N, Koo B. Structural, magnetic and magnetocaloric properties of $La_{0.65}Sr_{0.35}V_{0.1}Mn_{0.9}O_3$ perovksite. Mater. Res. Bull. 2012;47:2977-2979.

[3] Ifrah S, Kaddouri A, Gelin P, Leonard D. Hydrothermal synthesis of $La_{1-x}Ag_xMnO_3$ (x = 0,0.2) perovskites used in methane combustion. C. R. Chimie 2007;10:1216-1226.

[4] Sosnowska I, Azuma M, Przenioslo R, Wardecki D, Chen W, Oka K, Shimakawa Y. Crystal and magnetic structure in Co-substituted $BiFeO_3$. Inorg Chem. 2013;52:13269-13277.

[5] Glazer AM. The classification of tilted octahedra in perovskites. Acta Crystallogr Sec B. 1972;28:3384-3392.

[6] Tilley JD. Perovskites: structure-property relationships. West Sussex, UK: John Wiley & Sons, Ltd; 2016.

[7] Grocholski B, Shim S, Sturhahn W, Zhao J, Xiao Y, Chow P. Spin and valence states of iron in $(Mg_{0.8}Fe_{0.2})SiO_3$ perovskite. Geophys. Res. Lett. 2009;36(24):L24303.

[8] Sidey V. A simplified empirical model for predicting the lattice parameters of the cubic/pseudocubic perovskites. J Solid State Chem. 2019;279:120951.

[9] Jiang L, Guo J, Liu H, Zhu M, Zhou X, Wu P, Li C. Prediction of lattice constant in cubic perovskites. J. Phys. Chem. Solids 2006;67(7):1531-1536.

[10] Ubic R. Revised method for the prediction of lattice constants in cubic and pseudocubic perovskites. J. Am. Ceram. Soc. 2007;90(10):3326-3330.

[11] Ubic R, Subodh G. The prediction of lattice constants in orthorhombic perovskites. J. Alloys Compd. 2009;488(1):374-379.

[12] Kumar A, Verma A. Lattice constant of orthorhombic perovskite solids. J. Alloys Compd. 2009;480(2):650-657.

[13] Tolman K, Ubic R. An empirical model for perovskite tetragonality. J. Alloys Compd. 2017;690:825-835.

[14] Lufaso M, Woodward P. Prediction of the crystal structures of perovskites using the software program SPuDS. Acta Crystallogr. Sect. B Struct. Sci. 2001;57:725-738.

[15] Salinas-Sanchez A, Garcia-Munoz J, Rodriguez-Carvajal J, Saez-Puche R, Martinez J. Structural characterization of R2BaCuO5 (R = Y, Lu, Yb, Tm, Er, Ho, Dy, Gd, Eu and Sm) oxides by X-ray and neutron diffraction. J. Solid State Chem. 1992;100(2):201-211.

[16] Ubic R, Tolman K, Talley K, et al. Lattice-constant prediction and effect of vacancies in aliovalently doped perovskites. J Alloys Compd. 2015;644:982-995.

[17] Shannon R. Revised effective ionic-radii and systematic studies of interatomic distances in halides and chalcogenides. Acta Crystallogr Sec A. 1976;32:751-67.

[18] Jorgensen JE, Jorgensen JD, Batlogg B, Remeika JP, Axe JD. Order parameter and critical exponent for the pressure-induced phase transitions in ReO_3. Phys Rev B. 1986;33:4793-4798.

[19] Dhahri N, Dhahri A, Cherif K, Dhahri J, Taibi K, Dhahri E. Structural, magnetic and electrical properties of $La_{0.67}Pb_{0.33}Mn_{1-x}Co_xO_3$ ($0 \leq x \leq 0.3$). J Alloys Compd. 2010;496:69-74.

CHAPTER SIX: CORRELATIVE MODELS FOR OXGYEN VACANCIES IN PEROVSKITES

This Chapter was published by Elsevier in the Journal of Alloys and Compounds and should be reference appropriately.

Reference: Smith, E., Skapin, S., Ubic R., "Correlative Models for Oxygen Vacancies in Perovskites," Journal of Alloys and Compounds 836, 2020, 155475, https://doi.org/10.1016/j.jallcom.2020.155475

6.1 Introduction

Correlative models describing composition-structure-property relationships are the keys to unlocking the full potential of electroceramics. Perovskite ceramics display a larger range of properties (*e.g.*, superconductivity, piezoelectricity, ferromagnetism, pyroelectricity, *etc.*) than do ceramics of almost any other structure type[1]. Within the perovskite structure, many types of structural distortions which cause deviations from the aristotypical cubic structure in space group $Pm\bar{3}m$ are possible. They can also be deleterious to certain properties (*e.g.*, dielectric properties), yet beneficial for others (*e.g.*, thermoelectric properties[2]).

One of the structural effects that oxygen vacancies can exhibit in perovskites is ordering[3,4]. At low concentrations they exist as isolated point defects; however, it has been reported[3,4] that as their concentration increases, they can begin to arrange themselves into linear chains along $[101]_{pc}$ directions. When the concentration gets sufficiently high, those chains begin to merge, which eventually results in alternating $(101)_{pc}$ planes of oxygen vacancies; therefore, a perovskite with a high concentration of oxygen vacancies may exhibit layered type ordering amongst the $(101)_{pc}$ planes.[3.4]

Oxygen vacancies also play an important role in certain electroceramic properties. For instance, an increase in the number of oxygen vacancies can lead to an increase in the spontaneous normal-to-relaxor ferroelectric phase transition[5,6]. Thermoelectric properties can also be improved by an increase in the concentration of oxygen vacancies[2]. It was reported[2] that such vacancies cause the carrier mobility to increase whilst simultaneously causing a decrease in the thermal conductivity. This effect was attributed[7] to the oxygen vacancies effectively suppressing heat transfer within the material, inherently causing an

increase in the thermoelectricity. It was also observed[2] that increasing the oxygen-vacancy concentration leads to an increase in the electrical conductivity without significantly effecting the Seebeck coefficient in the oxygen-deficient $SrTiO_{3\pm\delta}$ perovskite system. The increase in conductivity is particularly useful in organic-inorganic halide perovskite solar cells[8] because it causes an improvement in the power conversion efficiency.

Oxygen vacancies play an instrumental role in solid-oxide fuel cells (SOFCs). For example, $SrTi_{1-x}Fe_xO_{3-x/2+\delta}$ and $SrSn_{1-x}Fe_xO_{3-x/2+\delta}$ are both known[9] to be good cathode materials in SOFCs because the oxygen vacancies create pathways for the ions to more easily diffuse, which leads to an increase in the ionic conduction. Oxygen vacancies in $La_{0.6}Sr_{0.4}CoO_{3-\delta}$ SOFC cathodes reportedly[10] act as immoblizers in lithium-sulfur batteries. The oxygen vacancies increase the bond strength between polysulfide compounds and the $La_{0.6}Sr_{0.4}CoO_{3-\delta}$, which effectively traps the sulfur and prevents it from migrating out of the cathode. Oxygen-deficient perovskites can also be used as catalysts. In particular, several oxygen-deficient perovskites were studied[11] for use as catalysts in the decomposition of NO gas. It was observed that two NO molecules would be simultaneously adsorbed onto two neighboring oxygen vacancies, resulting in the activation of the two nitrogen atoms, which then bond with each other to form N_2 gas. The leftover oxygen atoms would then bond with each other to form O_2 gas.

In addition, oxygen vacancies play an important role in perovskite memory cells. In particular, oxygen vacancies in single crystal $SrTiO_3$ substrates with graphene nanoribbon (GNR) electrodes have been linked[12] to bipolar resistive switching properties in resistive random access memory (RRAM) devices. The mechanism for this process has

been attributed to oxygen vacancies on the surface of the $SrTiO_3$ substrate creating conduction pathways for the electrons.

In A-site or B-site doped perovskite ferrites (*e.g.*, $A^{3+}_{1-x}A^{2+}_{x}FeO_3$, $A^{2+}B^{4+}_{1-x}Fe_xO_3$, *etc*.), charge balancing occurs either via oxygen vacancies and/or an increase in iron valence from Fe^{3+} to Fe^{4+} according to:

$$\left(A^{3+}_{1-x}A^{2+}_{x}\right)\left(Fe^{3+}_{1-y}Fe^{4+}_{y}\right)O_{3-\left(\frac{x-y}{2}\right)} \quad (x \geq y) \text{ or } A^{2+}\left[B^{4+}_{1-x}\left(Fe^{3+}_{1-y}Fe^{4+}_{y}\right)_x\right]O_{3-x(1-y)}$$

Beausoleil *et al.*[13] have analyzed the effects of divalent A-site cation doping in lanthanum ferrite ($LaFeO_3$). Their results were compared to the values predicted by an empirical model developed by Ubic *et al*.[14] While the errors (-0.746% to -0.445%) were all well within the expected accuracy of the model, it was observed that they were all negative. Thus, the experimental values were consistently larger than the values predicted by the model. As Fe^{4+} is even smaller than Fe^{3+}, which would result in a volume *shrinkage*, this result supports the hypothesis that oxygen vacancies were the principle cause of the underestimation; however, for Ca-doped $LaFeO_3$ they reported only the oxidation of Fe^{3+} to Fe^{4+}. For Sr- or Ba-substituted $LaFeO_3$ they conjectured that charge compensation was accomplished via *both* the oxidation of Fe^{3+} to Fe^{4+} and the formation of oxygen vacancies.

Recently, it was noted[15] that as the oxygen vacancy content in $SrFeO_{3-\delta}$ (SFO) thin films increased above about 17% (*i.e.* $SrFeO_{2.5}$) the structure changed from perovskite to brownmillerite. Interestingly, as the oxygen content decreased, the tetragonality was observed to increase causing a net unit-cell volume increase. In fact, this trend is corroborated by another study[16] using neutron diffraction, and it is also seen in several other oxygen-deficient perovskite systems like $BaSn_{1-x}Y_xO_{3-x/2}$[17] (BSYO) and $BaZr_{1-x}Dy_xO_{3-x/2}$[18] (BZDO); however, this trend of unit cell volume expansion with increasing

oxygen vacancy concentration is by no means universal. In fact, the opposite trend is observed in the $NaNb_{1-x}Ti_xO_{3-x/2}$[19] (NNTO) and $BaCe_{1-x}Y_xO_{3-x/2}$[20] (BCYO) systems.

Recently, an empirical model was developed[21] which predicts the lattice parameters in oxygen-deficient perovskites. Unlike most predictive models that currently exist, this model accounts for the sizes of the cations and anions in their correct coordination environments (XII, VI, and II for A-, B-, and X-site species, respectively). This model is also accurate with an average error of 0.83% when predicting the lattice parameters of oxygen-deficient perovskites; however, it has some significant drawbacks. For instance, it relies on a combination of experimental lattice constants as well as lattice constants from theoretical perovskite compounds calculated via density functional theory (DFT). Additionally, this model was not derived from a large range of compositions. The majority of the compositions used in its derivation exist in the $(La_{1-x}Sr_x)(Ga_{1-y}Mg_y)O_{3-(x+y)/2}$ (LSGMO) system, which means that it can only be applied with any degree of certainty to a narrow range of compositions. Thus, another empirical model is needed in order to effectively calculate the tolerance factor for a broader range of oxygen-deficient perovskites.

In this work, eight compositions in the $CaTi_{1-x}Fe_xO_{3-x/2}$ (CTFO) system and eleven compositions in the $SrTi_{1-x}Fe_xO_{3-x/2}$ (STFO) were produced. An additional 32 oxygen-deficient perovskite compositions were mined from literature, and correlative models were developed for each system. From these models, general models describing the effective vacancy size and bond deformation as functions of t' were developed. Models were also developed for t' as a function of the ideal anion size. From these system-specific models, a general model was then developed.

6.2 Materials and Methods

Eight compositions in the system $Ca(Ti_{1-x}Fe_x)O_{3-x/2}$ (x = 0.05, 0.15, 0.2, 0.25, 0.30, 0.35, 0.40, and 0.45) and eleven compositions in the system $Sr(Ti_{1-x}Fe_x)O_{3-x/2}$ (x = 0, 0.025, 0.05, 0.10, 0.15, 0.2, 0.25, 0.30, 0.35, 0.40, and 0.45) were synthesized via the solid-state mixed-oxide route. Stoichiometric amounts of $SrCO_3$ (99.9%, Sigma-Aldrich, St. Louis, MO), $CaCO_3$ (99.9%, Sigma-Aldrich, St. Louis, MO), TiO_2 (99.9%, Sigma-Aldrich, St. Louis, MO), and Fe_2O_3 (99%, Merck, Darmstadt, Germany) were ball-milled in a planetary mill with yttria-stabilized ZrO_2 (YSZ) media using ethanol in a YSZ jar at 250 revolutions per minute for 30 minutes. Powders were then dried overnight in an atmospheric drying oven at ~75°C until all the ethanol had evaporated. The dried powders were then uniaxially pressed into pellets which were then calcined at 1100°C in air for twelve hours in an open boat. After calcination, the pellets were pulverized using an agate mortar and pestle and ball-milled again in a planetary mill with YSZ media using ethanol in a YSZ jar at 250 revolutions per minute for 30 minutes. The mixture was then dried overnight in an atmospheric drying oven at ~75°C until all the ethanol had evaporated. Again, the dried powders were uniaxially pressed into pellets before being sintered at 1400°C for twelve hours in air, after which the samples were allowed to cool to room temperature slowly inside the furnace.

XRD measurements were performed on the sintered pellets in a diffractometer (Empyrean, PANalytical, Malvern, UK) operating with convergent-beam geometry and CuKα radiation. Le Bail refinements were performed on the XRD patterns using GSAS II[22] (Argonne National Laboratory, IL). The background was fitted with a third-order

Chebyshev polynomial. $CaTi_{1-x}Fe_xO_{3-x/2}$ compositions were refined with orthorhombic and tetragonal symmetry, and $SrTi_{1-x}Fe_xO_{3-x/2}$ compositions were refined with cubic symmetry.

6.3 Results and Discussion

Figs. 6.1 and 6.2 show the X-ray diffraction (XRD) patterns for the $CaTi_{1-x}Fe_xO_{3-x/2}$ (CTFO) and $SrTi_{1-x}Fe_xO_{3-x./2}$ (STFO) systems, respectively. The lack of secondary-phase peaks indicate that all the compositions in both series have successfully been produced with complete phase purity. Fig. 6.1 shows that there is a structural transition from orthorhombic to tetragonal in the CTFO system between $0.25 \leq x \leq 0.30$ as indicated[23] by the reversal in the asymmetry of the 211_{pc} doublet. Fig. 6.2 shows that all eleven compositions produced in the STFO series exhibit cubic symmetry.

Tables 6.1 and 6.2 show the results of the Le Bail refinements for all eight CTFO and eleven STFO compositions that were produced. Table 6.1 further illustrates the phase transition from orthorhombic to tetragonal near the $x = 0.25$ composition in the CTFO system. The pseudocubic lattice constant in this system systematically increases with increasing oxygen vacancy concentration. Interestingly, the refinement results in Table 6.2 show that the cubic lattice constant for STFO initially increases slightly upon doping with Fe^{3+}, which may be due to the fact that Fe^{3+} (0.645 Å) is larger than Ti^{4+} (0.605 Å), before gradually decreasing as the oxygen vacancy concentration continues to increase. The fact that the trend in pseudocubic lattice constant versus oxygen-vacancy concentration is different in these two systems may imply that the size of the A-site species plays an important role in how the structure distorts as a function of oxygen-vacancy concentration. It may also be possible that the anion vacancies order to some extent, which may cause the unit cell volume to increase or decrease with respect to the disordered structure similar to

the effects of A-site and B-site cation ordering; however, since the concentration of vacancies in these perovskites are all below 8%, the likelihood that the vacancies become ordered to any degree is very low. Individual vacancies would, on average, be far too well separated to interact, and even if some degree of order did exist, the scale of the ordering would be negligible. Thus, the potential effects on these structures due to vacancy ordering will be very minimal at best.

Additionally, $CaFeO_3$ is a well-known perovskite with Fe^{4+} occurring on the B-site at room temperature; although, charge disproportionation of the iron to Fe^{3+} and Fe^{5+} has also been observed[24] in this perovskite below room temperature; however, $CaFeO_3$ has only been synthesized[25] under a high-oxygen pressure atmosphere. Thus, the fact that Fe^{4+} exists in these perovskites is due to the high-pressure synthesis procedure. Synthesis of oxide materials under normal atmospheric conditions usually results in iron forming with either a 2+ or 3+ valence state; therefore, as the starting material included Fe_2O_3, only Fe^{3+} was assumed to be present in the $CaTi_{1-x}Fe_xO_{3-x/2}$ and $SrTi_{1-x}Fe_xO_{3-x/2}$ perovskites.

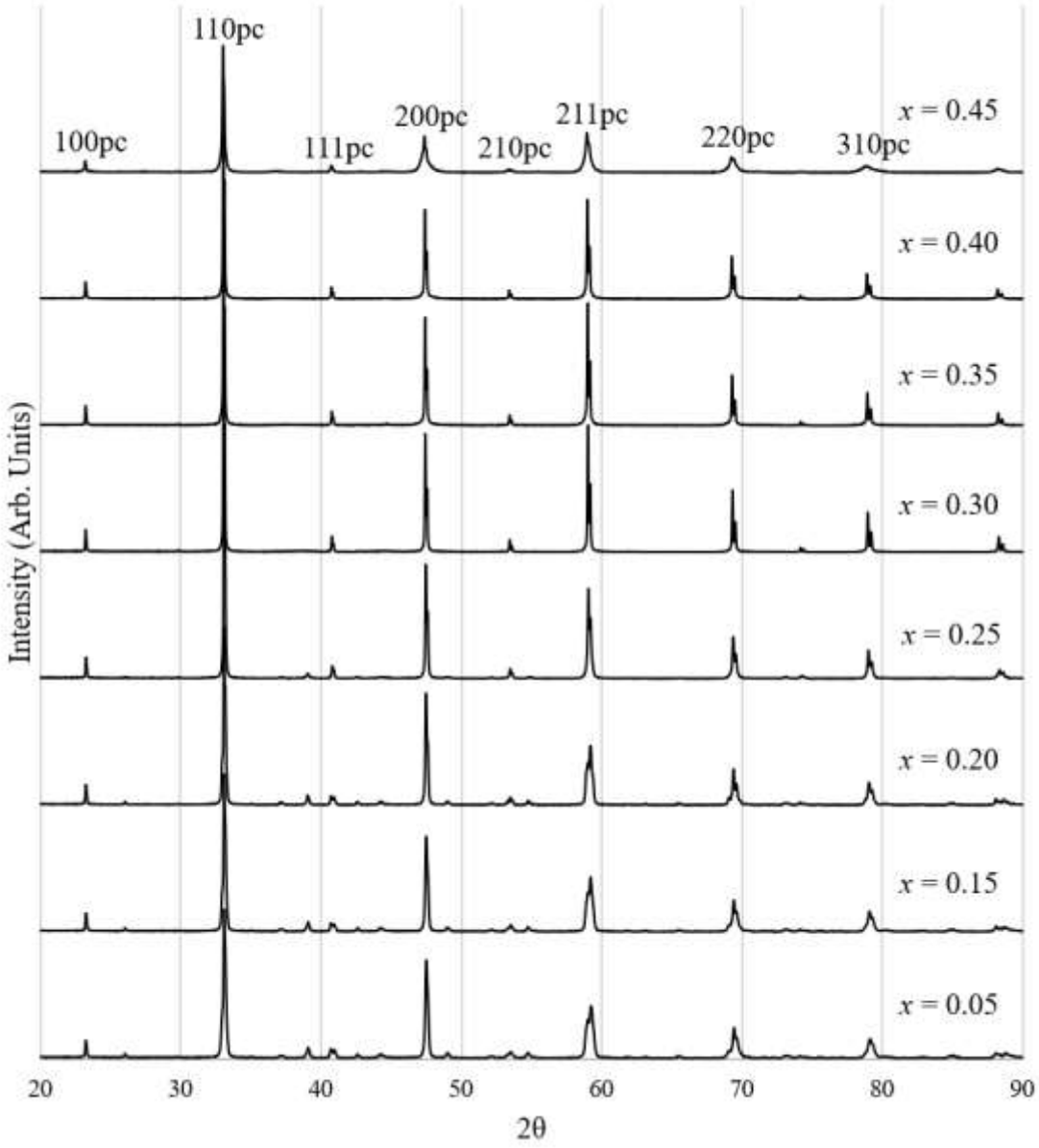

Figure 6.1 XRD patterns of $CaTi_{1-x}Fe_xO_{3-x/2}$ (x=0.05, 0.15, 0.20, 0.25, 0.30, 0.35, 0.40, and 0.45). All patterns are indexed according to the pseudocubic unit cell.

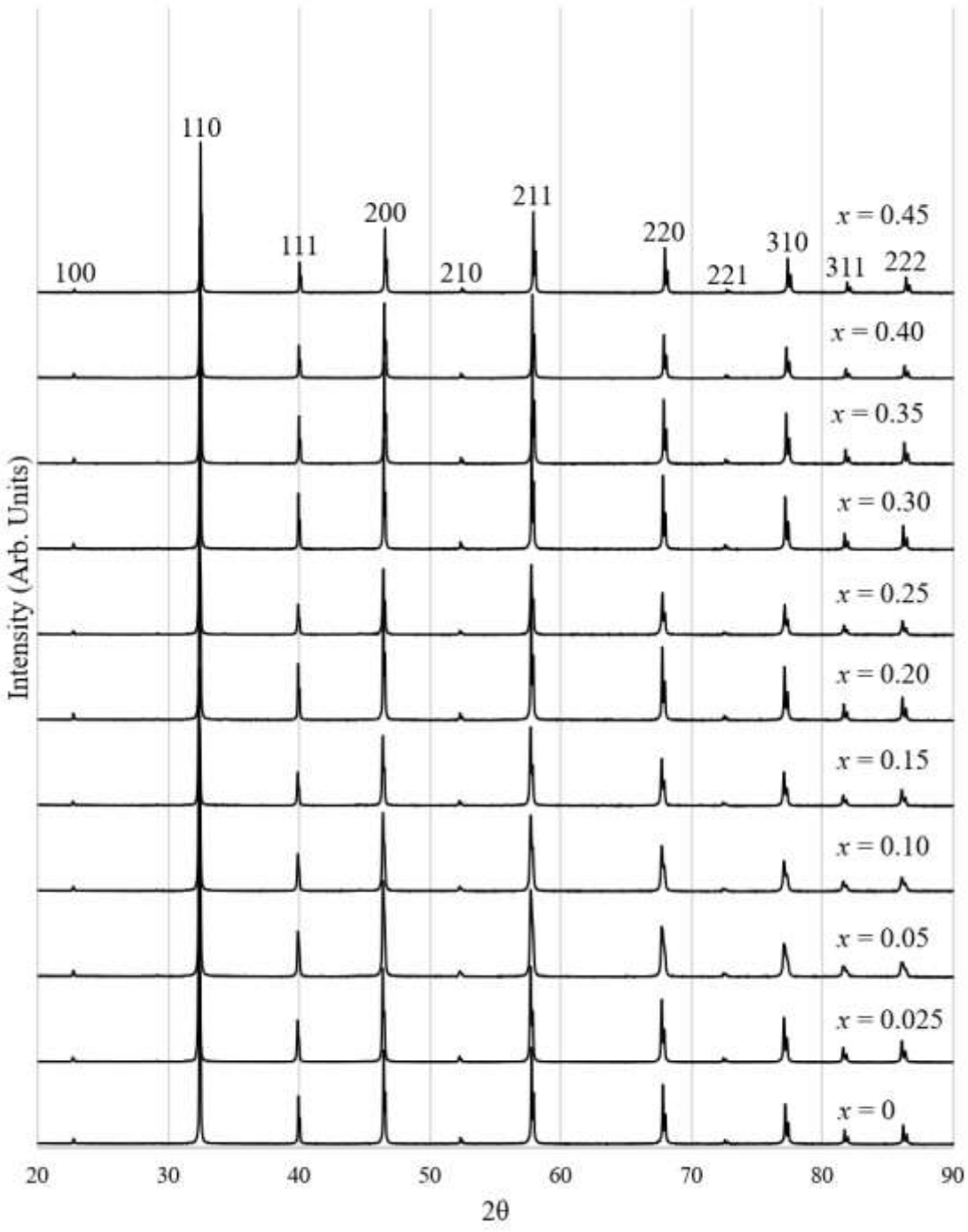

Figure 6.2 XRD patterns of $SrTi_{1-x}Fe_xO_{3-x/2}$ (x=0, 0.025, 0.05, 0.10, 0.15, 0.20, 0.25, 0.30, 0.35, 0.40, and 0.45). All patterns are indexed with cubic symmetry.

Table 6.1 $CaTi_{1-x}Fe_xO_{3-x/2}$ refinement results

Composition	Crystal System	*a* (Å)	*b* (Å)	*c* (Å)	Z	$a_{pc(exptl)}$ (Å)
***x* = 0.05**	Orthorhombic	5.3913	5.4391	7.6494	4	3.8276
***x* = 0.15**	Orthorhombic	5.3964	5.4372	7.6530	4	3.8290
***x* = 0.20**	Orthorhombic	5.3978	5.4364	7.6562	4	3.8297
***x* = 0.25**	Tetragonal	3.8307	3.8307	3.8324	1	3.8314
***x* = 0.30**	Tetragonal	3.8331	3.8331	3.8298	1	3.8320
***x* = 0.35**	Tetragonal	3.8333	3.8333	3.8345	1	3.8337
***x* = 0.40**	Tetragonal	3.8357	3.8357	3.8337	1	3.8350
***x* = 0.45**	Tetragonal	3.8364	3.8364	3.8420	1	3.8383

Table 6.2 $SrTi_{1-x}Fe_xO_{3-x/2}$ refinement results

Composition	Crystal System	*a* (Å)	*b* (Å)	*c* (Å)	Z	$a_{pc(exptl)}$ (Å)
***x* = 0**	Cubic	3.9088	3.9088	3.9088	1	3.9088
***x* = 0.025**	Cubic	3.9085	3.9085	3.9085	1	3.9085
***x* = 0.05**	Cubic	3.9115	3.9115	3.9115	1	3.9115
***x* = 0.10**	Cubic	3.9098	3.9098	3.9098	1	3.9098
***x* = 0.15**	Cubic	3.9087	3.9087	3.9087	1	3.9087
***x* = 0.20**	Cubic	3.9089	3.9089	3.9089	1	3.9089
***x* = 0.25**	Cubic	3.9072	3.9072	3.9072	1	3.9072
***x* = 0.30**	Cubic	3.9066	3.9066	3.9066	1	3.9066
***x* = 0.35**	Cubic	3.9041	3.9041	3.9041	1	3.9041
***x* = 0.40**	Cubic	3.9031	3.9031	3.9031	1	3.9031
***x* = 0.45**	Cubic	3.8980	3.8980	3.8980	1	3.8980

To develop a workable model for the effect of oxygen vacancies in perovskites, several reasonable assumptions are necessary. The first assumption is that increasing the number of oxygen vacancies does not affect the B-site size, r_B. The second assumption is that the oxygen anions are in contact with both the A-site and B-site cations. Under these conditions, the effective size of the X-site anion, r_X, is represented by the difference between the B-site cation and half the pseudocubic lattice constant, a_{pc}:

$$r_{X(exptl)} = \frac{a_{pc}}{2} - r_B \tag{6.1}$$

where r_B is the Shannon[26] size of the B-site cation in six-fold coordination.

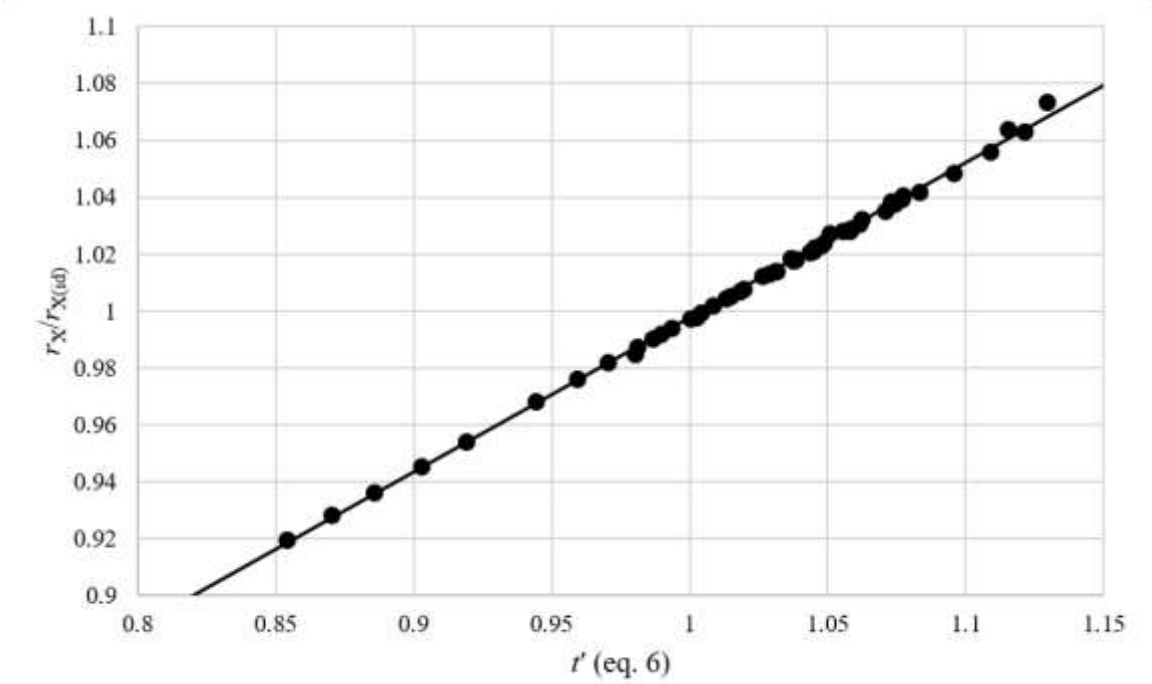

Figure 6.3 Non-ideality of the effective anion sizes (X-site) for all 50 oxygen-deficient perovksites in this work.

The ratio of r_X (Eq. 6.1) to $r_{X(id)}$ can be expressed as a function of t' (Eq. 1.9) as shown in Fig. 6.3. This relationship is described mathematically by Eq. 6.2:

$$\frac{r_X}{r_{X(id)}} = 0.544008t' + 0.453751 \quad \left(R^2 = 0.9987\right) \tag{6.2}$$

As expected, $r_X = r_{X(id)}$ only when $t' = 1$. It should be noted that this expression is very similar to that derived previously by Ubic *et al.*[27] for ABX_3 perovskites in general; however, that model was not developed using oxygen-deficient perovskites. Thus, although Eq. 6.2 is very similar to Eq. 12 in the previous work,[27] it is slightly different, presumably because it accounts for the effects of oxygen vacancies in the perovskite structure.

Now, the anion size is composed of three components: the ideal (Shannon) size, the deviation from ideality caused by bond deformation (including the effect of partial covalency) when $t' \neq 1$, and the effect of vacancies:

$$r_{\mathrm{X}} = \left(1 - \frac{x}{6}\right) r_{\mathrm{X(id)}(x=0)} + \left(r_{\mathrm{X}(exptl)} - r_{\mathrm{X(id)}(x=0)}\right) + \frac{x}{6} r_{\mathrm{V}} \tag{6.3}$$

It should be noted again that the term "bond deformation" in this work is used to describe the difference between the actual ionic size and the Shannon size. It includes the effect of partial covalency and is non-zero even for untilted perovskites. The "deformation" implies stretching or compression of bonds rather than angular distortions. In Eq. 6.3 the three terms on the right-hand side represent, respectively, the ideal (Shannon) size, bond deformation, and the effect of vacancies. This equation can be re-written more succinctly as:

$$6\left(r_{\mathrm{X}(exptl)} - r_{\mathrm{X(id)}(x=0)}\right) + x r_{\mathrm{X(id)}(x=0)} = x r_{\mathrm{V}} + 6D_B \tag{6.4}$$

For convenience, the left-hand side of this equation can be considered a size parameter, L. So, by graphing L vs x, as in Fig. 6.4, one obtains a line in which the slope is r_{V} and the intercept is $6D_B$.

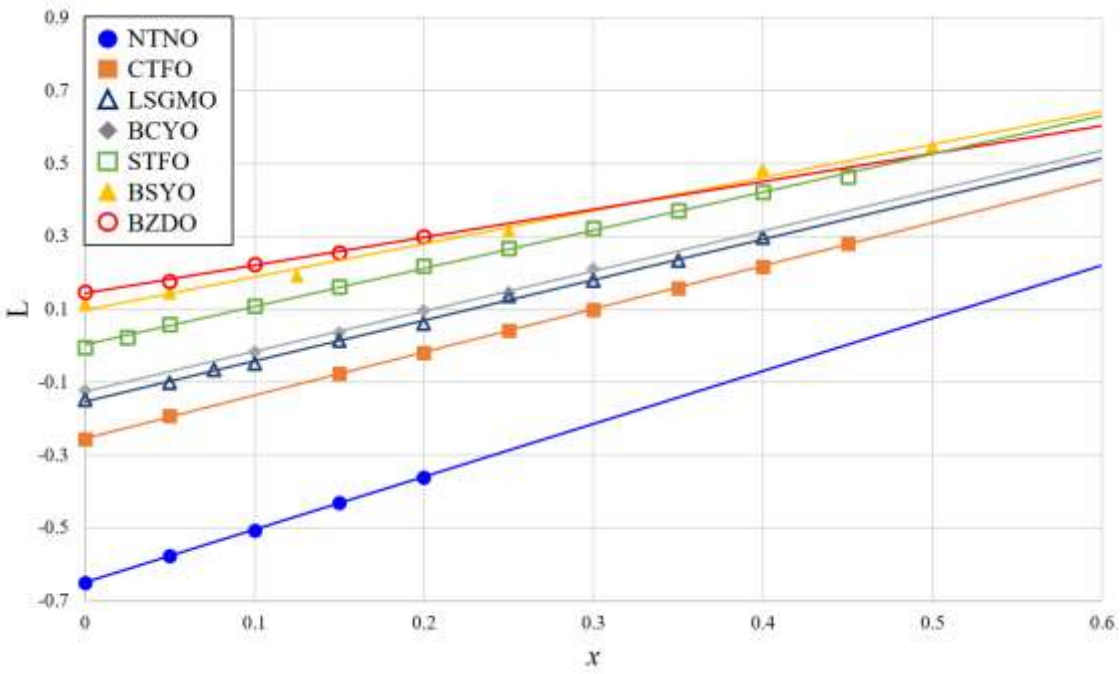

Figure 6.4 The size parameter, L, as a function of the composition, *x*.

Table 6.3 shows the coefficients of Eq. 6.4 and goodness of fits for all seven oxygen-deficient perovskite systems.

Table 6.3 Coefficients and goodness of fit for the linear trends in figure 6.4

Composition	$t'_{(x=0)}$ **(Eq. 1.9)**	r_V	D_B	R^2
$NaTi_{1-x}Nb_xO_{3-x/2}$	0.8540	1.4524	-0.1084	0.9988
$CaTi_{1-x}Fe_xO_{3-x/2}$	0.9444	1.1850	-0.0424	0.9999
$(La_{1-x}Sr_x)(Ga_{1-y}Mg_y)O_{3-(x+y)/2}$	0.9705	1.1156	-0.0256	0.9983
$BaCe_{1-x}Y_xO_{3-x/2}$	0.9803	1.1046	-0.0211	0.9988
$SrTi_{1-x}Fe_xO_{3-x/2}$	1.0041	1.0463	0.0006	0.9992
$BaSn_{1-x}Y_xO_{3-x/2}$	1.0311	0.9082	0.0165	0.9924
$BaZr_{1-x}Dy_xO_{3-x/2}$	1.0382	0.7680	0.0240	0.9954

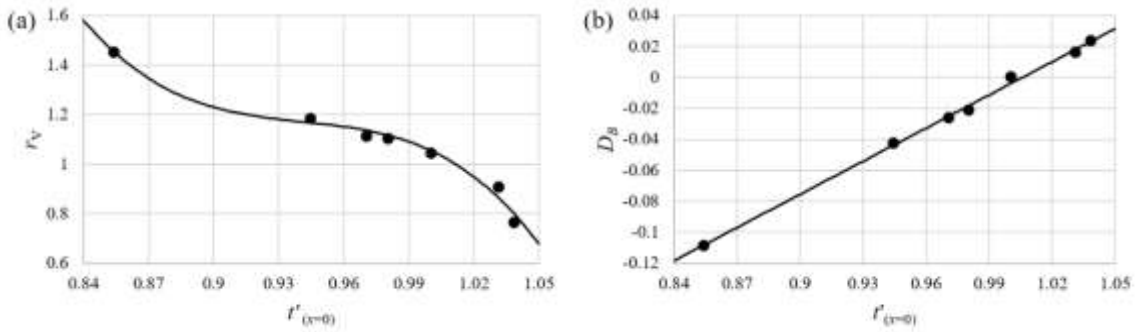

Figure 6.5 The effective vacancy size, r_V, and bond deformation, D_B, as functions of the modified tolerance factor at $x = 0$.

Fig. 6.5a shows that the vacancy size, r_V, can be represented by a third order polynomial as a function of the modified tolerance factor:

$$r_V = -305.775864(t_0')^3 + 863.428549(t_0')^2 - 813.609546t_0' + 257.011523 \quad (R^2 = 0.9860) \tag{6.5}$$

where t' is calculated from Eq. 1.9 using $a_{pc(exptl.)}$ at the $x = 0$ composition for each system (*i.e.* the composition with no extrinsic vacancies). Fig. 6.5b shows that the bond deformation, D_B, is a linear function of the modified tolerance factor:

$$D_B = 0.712022t_0' - 0.716288 \quad (R^2 = 0.9986) \tag{6.6}$$

Thus, the effective anion-site size can now be predicted using Eq. 6.7:

$$r_X = r_{X(id)} + D_B + r_V[V_O] \tag{6.7}$$

where $r_{X(id)}$ is calculated from the Shannon tables[26] and stoichiometry, D_B is obtained from Eq. 6.6, r_V from Eq. 6.5, and $[V_O] = x/6$ is the effective oxygen vacancy concentration. Unfortunately, in order to invoke this equation, it is first necessary to calculate t', which would seem to require a foreknowledge of a_{pc} (Eq. 1.9). In order to circumvent this problem, a relationship between t' and $r_{X(id)}$ was established (Fig. 6.6).

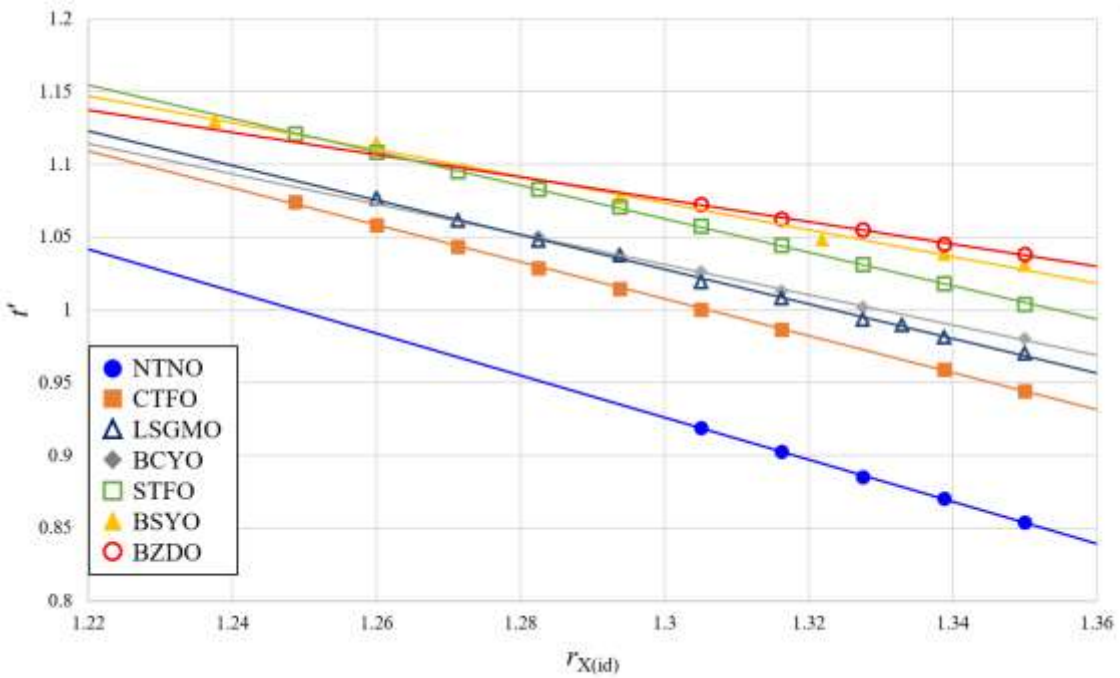

Figure 6.6 The modified tolerance factor, *t′* (Eq. 1.9), as a function of the ideal Shannon[25] anion size, $r_{X(id)}$.

Fig. 6.6 shows that the relationship between the modified tolerance factor, *t′*, and the ideal Shannon[26] anion size, $r_{X(id)}$, for all 7 oxygen-deficient perovskite systems can be represented by the same linear expression:

$$t' = Ar_{X(id)} + B \tag{6.8}$$

where $r_{X(id)}$ is the effective Shannon[26] size of the X-site species in two-fold coordination.

For the purpose of finding an appropriate function to find a trend for *A* and *B*, the function *G* was defined as:

$$G = \frac{r_{A(x=0)} + r_{X(id)(x=0)}}{\sqrt{2}\left(r_{B(x=0)} + r_{X(id)(x=0)}\right)^{1/3}} \tag{6.9}$$

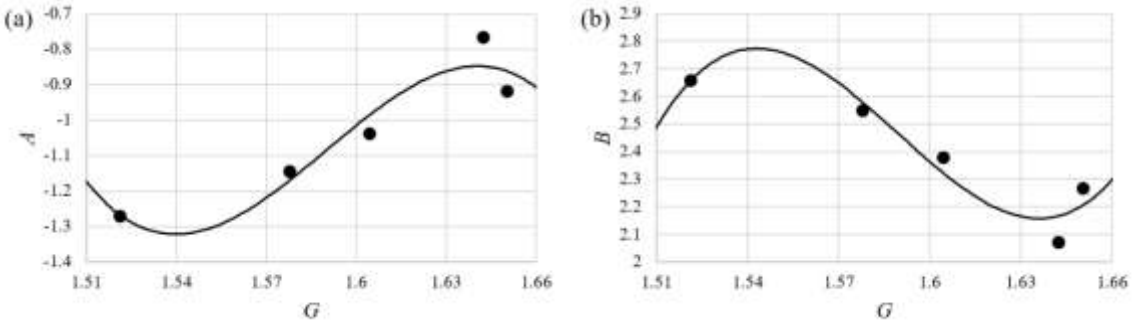

Figure 6.7 Coefficients of Eq. 6.8.

Fig. 6.7 shows that the relationships between the coefficients (*A* and *B*) of Eq. 6.8 as functions of *G* (Eq. 6.9) can be represented by Eqs. 6.10 and 6.11:

$$A = -929.413997(G)^3 + 4433.65433(G)^2 - 7043.016170(G) + 3724.521276 \quad (R^2 = 0.9138) \tag{6.10}$$

$$B = -1527.992999(G)^3 - 7286.513754(G)^2 + 11572.422503(G) - 6118.697145 \quad (R^2 = 0.9209) \tag{6.11}$$

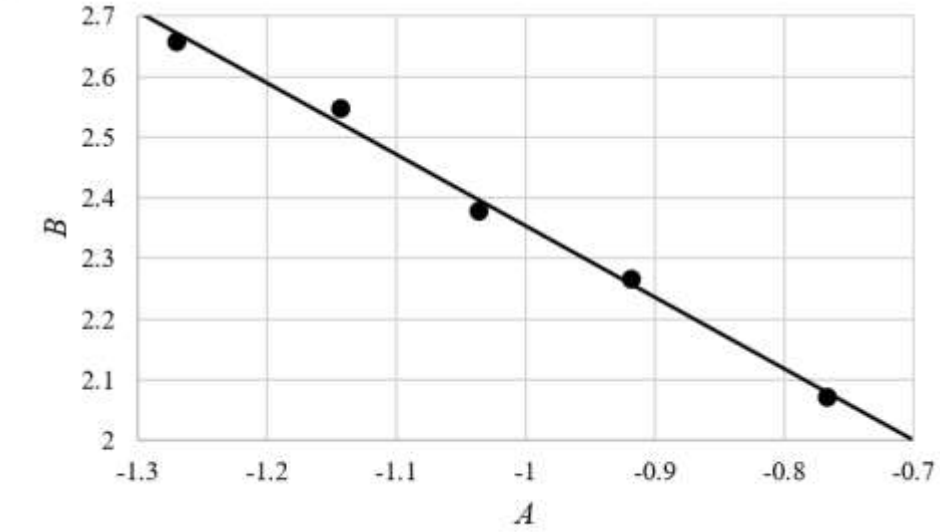

Figure 6.8 Correlation between the coefficients of Eq. 6.8.

Fig. 6.8 shows that the coefficients of Eq. 6.8 are not independent parameters but are in fact highly linearly correlated, as shown by Eq. 6.12:

$$B = -1.179372A + 1.173984 \quad \left(R^2 = 0.9938\right) \tag{6.12}$$

Thus, Eq. 6.8 can be simplified as follows:

$$t' = A\left(r_{X(id)} - 1.179372\right) + 1.173984 \tag{6.13}$$

Tables 6.4, 6.6, 6.8, 6.10, 6.12, 6.14, and 6.16 show the experimental and calculated tolerance factor, t', and anion sizes, r_X, using Eqs. 6.13 and 6.7 for all 7 oxygen-deficient perovskite systems. Additionally, tables 6.5, 6.7, 6.9, 6.11, 6.13, 6.15, and 6.17 show the experimental and calculated pseudocubic lattice constants for all 7 oxygen-deficient perovskite systems. The values for a_{pc} in Tables 6.5, 6.7, 6.9, 6.11, 6.13, 6.15, and 6.17 are calculated by first predicting t' using Eq. 6.13, then plugging that value into Eq. 1.19. Similarly, a'_{pc} and a''_{pc} are calculated by first predicting t' using Eq. 6.13, then using that value to predict r_X using Eqs. 6.5-6.7. This value of r_X is used along with the ideal Shannon size of the B-site cation to predict a''_{pc} using Eq. 1.5, whereas a'_{pc} is calculated from Eq. 1.4 using this value of r_X but the value of r_A used in Eq. 1.4 is determined from another empirical model (Eq. 6.14) developed by Ubic *et al.*[27]:

$$\begin{aligned} r_A = r_{A(id)} + \left(7.4801 - 12.3139 t_{0([V_A]=0)} + 4.8257 t^2_{0([V_A]=0)}\right) + \\ \left(-20.8983 + 36.9417 t_{0([V_A]=0)} - 14.4771 t^2_{0([V_A]=0)}\right)[V_A] \end{aligned} \tag{6.14}$$

where $t_{0([V_A]=0)}$ is the Goldschmidt the tolerance factor corresponding to the composition in a given $\left(A^{2+}_{1-3x}A^{3+}_{2x}\right)B^{4+}X_3$ system where $x = 0$ (with no extrinsic vacancies) and $[V_A]$ is the concentration of A-site vacancies. Thus, all three versions of the pseudocubic lattice constant can be predicted using only published ionic radii data.

It should be noted that while the model has been applied to all 7 oxygen-deficient systems, the model for t' was derived using data from $A^{2+}B^{4+}_{1-x}B^{3+}_{x}O_{3-x/2}$ perovskites exclusively; thus, this model cannot necessarily be accurately applied to oxygen-deficient perovskite systems. In fact, when this model is applied to the $NaNb_{1-x}Ti_xO_{3-x/2}$ (NNTO) system, which has the form $A^{1+}B^{5+}_{1-x}B^{4+}_{x}O_{3-x/2}$, the t' and r_X models produce very large errors; however, the model appears to be surprisingly accurate when applied to the $La_{1-x}Sr_xGa_{1-y}Mg_yO_{3-(x+y)/2}$ (LSGMO) system (0.3186% absolute average error for t' and 0.2084% absolute average error for r_X), which has the form $A^{3+}_{1-y}A^{2+}_{y}B^{3+}_{1-x}B^{2+}_{x}O_{3-(x+y)/2}$. This fact does not mean that the model is necessarily accurate for all perovskites of the type $A^{3+}B^{3+}_{1-x}B^{2+}_{x}O_{3-x/2}$. In order to fully explain this trend, correlative models would need to be developed for the $A^{1+}B^{5+}_{1-x}B^{4+}_{x}O_{3-x/2}$ and $A^{3+}B^{3+}_{1-x}B^{2+}_{x}O_{3-x/2}$ perovskite systems in addition to the models developed in this work for $A^{2+}B^{4+}_{1-x}B^{3+}_{x}O_{3-x/2}$ perovskites.

These tables show that the model is very accurate overall with the smallest absolute relative errors coming from the $CaTi_{1-x}Fe_xO_{3-x/2}$ system (0.0809% for t' and 0.1593% for r_X), and the largest errors coming from the $BaZr_{1-x}Dy_xO_{3-x/2}$ system (1.5039% for t' and 0.8132% for r_X). The larger errors could possibly be due to the fact that these compositions were only analyzed[18] via X-ray diffraction, which may not be able to detect deviations from stoichiometry; however, deviations in oxygen vacancy concentrations in this system are unliklely because Zr and Dy generally have oxidation states of 4+ and 3+, respectively. Thus, the only way for oxygen occupancy to deviate from stoichiometry and still maintain charge neutrality would be for A-site vacancies to occur. Although X-ray diffraction can be used to detect A-site vacancies, the X-ray patterns from these samples were only

analyzed[18] via Le Bail, not Rietveld, refinements. For this reason, it is possible that A-site vacancies were present in these samples causing the oxygen vacancy concentration to be greater than the concentration reported.

Table 6.4 Experimental and predicted t' and r_X for $CaTi_{1-x}Fe_xO_{3-x/2}$.

Composition	t' (Eq 1.9)	t' (Eq 6.13)	|Error%|	$r_{X(exptl)}$ (Å) (Eq 6.1)	r_X (Å) (Eq 6.7)	|Error%|
$x = 0$[a]	0.9444	0.9445	0.0171	1.3073	1.3062	0.0840
$x = 0.05$	0.9593	0.9588	0.0580	1.3068	1.3047	0.1612
$x = 0.15$	0.9864	0.9873	0.0883	1.3035	1.3017	0.1408
$x = 0.20$	1.0002	1.0016	0.1406	1.3018	1.3001	0.1296
$x = 0.25$	1.0148	1.0158	0.1010	1.3007	1.2986	0.1598
$x = 0.30$	1.0290	1.0301	0.1038	1.2992	1.2971	0.1602
$x = 0.35$	1.0436	1.0444	0.0736	1.2979	1.2956	0.1713
$x = 0.40$	1.0583	1.0586	0.0307	1.2964	1.2940	0.1825
$x = 0.45$	1.0741	1.0729	0.1150	1.2957	1.2925	0.2441
Average Absolute Relative Error			0.0809			0.1593

[a] Ref. [28].

Table 6.5 Experimental and predicted pseudocubic lattice constants for $CaTi_{1-x}Fe_xO_{3-x/2}$.

Composition	$a_{pc(exptl)}$ (Å)	a_{pc} (Å) (Eq 1.19)	|Error%|	a'_{pc} (Å) (Eq 1.4)	|Error%|	a''_{pc} (Å) (Eq 1.5)	|Error%|
$x = 0$[a]	3.8246	3.8249	0.0060	3.8377	0.3417	3.8225	0.0575
$x = 0.05$	3.8276	3.8268	0.0204	3.8348	0.1874	3.8255	0.0566
$x = 0.15$	3.8290	3.8302	0.0316	3.8282	0.0217	3.8304	0.0372
$x = 0.20$	3.8297	3.8316	0.0508	3.8244	0.1359	3.8324	0.0711
$x = 0.25$	3.8314	3.8328	0.0368	3.8205	0.2851	3.8340	0.0676
$x = 0.30$	3.8324	3.8338	0.0382	3.8162	0.4209	3.8352	0.0754
$x = 0.35$	3.8336	3.8346	0.0273	3.8117	0.5707	3.8351	0.0667
$x = 0.40$	3.8348	3.8353	0.0115	3.8069	0.7274	3.8367	0.0490
$x = 0.45$	3.8374	3.8357	0.0434	3.8019	0.9247	3.8369	0.0120
Average Absolute Relative Error			0.0295		0.4017		0.0548

[a] Ref. [28].

Table 6.6 Experimental and predicted t' and r_X for $SrTi_{1-x}Fe_xO_{3-x/2}$.

Composition	t' (Eq 1.9)	t' (Eq 6.13)	|Error%|	$r_{X(exptl)}$ (Å) (Eq 6.1)	r_X (Å) (Eq 6.7)	|Error%|
$x = 0$	1.0041	0.9993	0.4785	1.3494	1.3452	0.3110
$x = 0.025$	1.0104	1.0058	0.4543	1.3483	1.3440	0.3178
$x = 0.05$	1.0191	1.0124	0.6571	1.3487	1.3428	0.4432
$x = 0.10$	1.0312	1.0256	0.5453	1.3459	1.3403	0.4152
$x = 0.15$	1.0438	1.0388	0.4844	1.3434	1.3379	0.4071
$x = 0.20$	1.0575	1.0519	0.5241	1.3415	1.3355	0.4469
$x = 0.25$	1.0699	1.0651	0.4469	1.3386	1.3330	0.4162
$x = 0.30$	1.0832	1.0783	0.4577	1.3363	1.3306	0.4271
$x = 0.35$	1.0953	1.0914	0.3561	1.3331	1.3282	0.3686
$x = 0.40$	1.1086	1.1046	0.3610	1.3305	1.3257	0.3626
$x = 0.45$	1.1191	1.1178	0.1129	1.3260	1.3233	0.2060
Average Absolute Relative Error			0.4435			0.3747

Table 6.7 Experimental and predicted pseudocubic lattice constants for $SrTi_{1-x}Fe_xO_{3-x/2}$.

Composition	$a_{pc(exptl)}$ (Å)	a_{pc} (Å) (Eq 1.19)	|Error%|	a'_{pc} (Å) (Eq 1.4)	|Error%|	a''_{pc} (Å) (Eq 1.5)	|Error%|
$x = 0$	3.9088	3.9020	0.1732	3.8954	0.3433	3.9029	0.1521
$x = 0.025$	3.9085	3.9021	0.1651	3.8930	0.3984	3.9033	0.1349
$x = 0.05$	3.9115	3.9021	0.2401	3.8905	0.5366	3.9036	0.2017
$x = 0.10$	3.9098	3.9020	0.2008	3.8854	0.6258	3.9040	0.1489
$x = 0.15$	3.9087	3.9017	0.1797	3.8800	0.7350	3.9041	0.1180
$x = 0.20$	3.9089	3.9012	0.1961	3.8744	0.8833	3.9039	0.1283
$x = 0.25$	3.9072	3.9006	0.1684	3.8685	0.9897	3.9033	0.0983
$x = 0.30$	3.9066	3.8998	0.1738	3.8624	1.1309	3.9025	0.1052
$x = 0.35$	3.9041	3.8988	0.1362	3.8561	1.2315	3.9013	0.0728
$x = 0.40$	3.9031	3.8977	0.1391	3.8494	1.3741	3.8998	0.0847
$x = 0.45$	3.8980	3.8963	0.0437	3.8426	1.4218	3.8979	0.0021
Average Absolute Relative Error			0.1651		0.8791		0.1134

Table 6.8 Experimental and predicted t' and r_X for $NaNb_{1-x}Ti_xO_{3-x/2}$.

Composition	t' (Eq 1.9)	t' (Eq 6.13)	|Error%|	$r_{X(exptl)}$ (Å) (Eq 6.1)	r_X (Å) (Eq 6.7)	|Error%|
$x = 0$[a]	0.8540	0.9868	15.5588	1.2416	1.3364	7.6302
$x = 0.05$[a]	0.8702	1.0017	15.1077	1.2427	1.3343	7.3680
$x = 0.10$[a]	0.8855	1.0166	14.8011	1.2429	1.3322	7.1797
$x = 0.15$[a]	0.9029	1.0314	14.2330	1.2445	1.3301	6.8741
$x = 0.20$[a]	0.9189	1.0463	13.8679	1.2450	1.3280	6.6710
Average Absolute Relative Error			14.7137			7.1446

[a] Ref. [19].

Table 6.9 Experimental and predicted pseudocubic lattice constants for $NaNb_{1-x}Ti_xO_{3-x/2}$.

Composition	$a_{pc(exptl)}$ (Å)	a_{pc} (Å) (Eq 1.19)	|Error%|	a'_{pc} (Å) (Eq 1.4)	|Error%|	a''_{pc} (Å) (Eq 1.5)	|Error%|
$x = 0$[a]	3.7632	3.9538	5.0651	3.9497	4.9543	3.9546	5.0852
$x = 0.05$[a]	3.7619	3.9493	4.9810	3.9395	4.7196	3.9505	5.0125
$x = 0.10$[a]	3.7589	3.9445	4.9369	3.9289	4.5239	3.9460	4.9776
$x = 0.15$[a]	3.7586	3.9394	4.8092	3.9181	4.2440	3.9411	4.8568
$x = 0.20$[a]	3.7559	3.9340	4.7402	3.9070	4.0217	3.9359	4.7925
Average Absolute Relative Error			4.9065		4.4927		4.9449

[a] Ref. [19].

Table 6.10 Experimental and predicted t' and r_X for $BaCe_{1-x}Y_xO_{3-x/2}$.

Composition	t' (Eq 1.9)	t' (Eq 6.13)	|Error%|	$r_{X(exptl)}$ (Å) (Eq 6.1)	r_X (Å) (Eq 6.7)	|Error%|
$x = 0$[a]	0.9803	0.9902	1.0113	1.3295	1.3388	0.6962
$x = 0.10$[a]	1.0022	1.0124	1.0216	1.3246	1.3344	0.7427
$x = 0.15$[a]	1.0132	1.0235	1.0147	1.3221	1.3322	0.7676
$x = 0.20$[a]	1.0263	1.0346	0.8067	1.3212	1.3301	0.6760
$x = 0.25$[a]	1.0367	1.0457	0.8709	1.3180	1.3279	0.7556
$x = 0.30$[a]	1.0507	1.0568	0.5843	1.3175	1.3257	0.6241
Average Absolute Relative Error			0.8849			0.7104

[a] Ref. [20].

Table 6.11 Experimental and predicted pseudocubic lattice constants for $BaCe_{1-x}Y_xO_{3-x/2}$.

Composition	$a_{pc(exptl)}$ (Å)	a_{pc} (Å) (Eq 1.19)	|Error%|	a'_{pc} (Å) (Eq 1.4)	|Error%|	a''_{pc} (Å) (Eq 1.5)	|Error%|
$x = 0$[a]	4.3990	4.4149	0.3607	4.3978	0.0267	4.4196	0.4673
$x = 0.10$[a]	4.3952	4.4114	0.3695	4.3838	0.2582	4.4130	0.4049
$x = 0.15$[a]	4.3932	4.4094	0.3696	4.3765	0.3804	4.4092	0.3653
$x = 0.20$[a]	4.3943	4.4073	0.2963	4.3690	0.5767	4.4053	0.2497
$x = 0.25$[a]	4.3909	4.4050	0.3219	4.3612	0.6762	4.4010	0.2303
$x = 0.30$[a]	4.3930	4.4026	0.2178	4.3433	0.9055	4.3965	0.0787
Average Absolute Relative Error			0.3226		0.4706		0.2994

[a] Ref. [20].

Table 6.12 Experimental and predicted t' and r_X for $BaSn_{1-x}Y_xO_{3-x/2}$.

Composition	t' (Eq 1.9)	t' (Eq 6.13)	|Error%|	$r_{X(exptl)}$ (Å) (Eq 6.1)	r_X (Å) (Eq 6.7)	|Error%|
$x = 0$[a]	1.0311	1.0398	0.8428	1.3690	1.3741	0.3698
$x = 0.05$[a]	1.0382	1.0495	1.0829	1.3630	1.3694	0.4679
$x = 0.125$[a]	1.0486	1.0640	1.4689	1.3538	1.3623	0.6352
$x = 0.25$[a]	1.0771	1.0883	1.0384	1.3465	1.3506	0.3071
$x = 0.40$[a]	1.1150	1.1174	0.2126	1.3405	1.3366	0.2925
$x = 0.50$[a]	1.1294	1.1368	0.6523	1.3285	1.3272	0.0972
Average Absolute Relative Error			0.8830			0.3616

[a] Ref. [17].

Table 6.13 Experimental and predicted pseudocubic lattice constants for $BaSn_{1-x}Y_xO_{3-x/2}$.

Composition	$a_{pc(exptl)}$ (Å)	a_{pc} (Å) (Eq 1.19)	|Error%|	a'_{pc} (Å) (Eq 1.4)	|Error%|	a''_{pc} (Å) (Eq 1.5)	|Error%|
$x = 0$[a]	4.1180	4.1308	0.3104	4.1184	0.0093	4.1324	0.3494
$x = 0.05$[a]	4.1270	4.1435	0.4005	4.1243	0.0664	4.1446	0.4261
$x = 0.125$[a]	4.1400	4.1626	0.5467	4.1331	0.1669	4.1624	0.5418
$x = 0.25$[a]	4.1780	4.1944	0.3930	4.1479	0.7211	4.1910	0.3109
$x = 0.40$[a]	4.2290	4.2325	0.0822	4.1657	1.4966	4.2233	0.1348
$x = 0.50$[a]	4.2470	4.2578	0.2542	4.1777	1.6326	4.2437	0.0789
Average Absolute Relative Error			0.3311		0.6822		0.3070

[a] Ref. [17].

Table 6.14 Experimental and predicted t' and r_X for $BaZr_{1-x}Dy_xO_{3-x/2}$.

Composition	t' (Eq 1.9)	t' (Eq 6.13)	|Error%|	$r_{X(exptl)}$ (Å) (Eq 6.1)	r_X (Å) (Eq 6.7)	|Error%|
$x = 0$[a]	1.0382	1.0198	1.7694	1.3745	1.3599	1.0652
$x = 0.05$[a]	1.0451	1.0294	1.5073	1.3684	1.3565	0.8677
$x = 0.10$[a]	1.0554	1.0389	1.5637	1.3648	1.3532	0.8503
$x = 0.15$[a]	1.0624	1.0485	1.3095	1.3587	1.3499	0.6505
$x = 0.20$[a]	1.0727	1.0580	1.3697	1.3551	1.3465	0.6324
Average Absolute Relative Error			1.5039			0.8132

[a] Ref. [18].

Table 6.15 Experimental and predicted pseudocubic lattice constants for $BaZr_{1-x}Dy_xO_{3-x/2}$.

Composition	$a_{pc(exptl)}$ (Å)	a_{pc} (Å) (Eq 1.19)	|Error%|	a'_{pc} (Å) (Eq 1.4)	|Error%|	a''_{pc} (Å) (Eq 1.5)	|Error%|
$x = 0$[a]	4.1890	4.1616	0.6544	4.1499	0.9337	4.1631	0.6186
$x = 0.05$[a]	4.1960	4.1725	0.5598	4.1547	0.9839	4.1735	0.5363
$x = 0.10$[a]	4.2080	4.1834	0.5843	4.1595	1.1520	4.1837	0.5781
$x = 0.15$[a]	4.2150	4.1943	0.4914	4.1643	1.2026	4.1936	0.5073
$x = 0.20$[a]	4.2270	4.2051	0.5170	4.1691	1.3702	4.2033	0.5601
Average Absolute Relative Error			0.5614		1.1285		0.5601

[a] Ref. [18].

Table 6.16 Experimental and predicted t' and r_X for $(La_{1-x}Sr_x)(Ga_{1-y}Mg_y)O_{3-(x+y)/2}$.

Composition	t' (Eq 1.9)	t' (Eq 6.13)	|Error%|	$r_{X(exptl)}$ (Å) (Eq 6.1)	r_X (Å) (Eq 6.7)	|Error%|
$y = 0$, $x = 0$[a]	0.9705	0.9650	0.5704	1.3255	1.3208	0.3570
$y = 0$, $x = 0.05$[b]	0.9811	0.9796	0.1528	1.3219	1.3191	0.2127
$y = 0$, $x = 0.076$[c]	0.9896	0.9872	0.2401	1.3221	1.3182	0.2948
$y = 0.10$, $x = 0$[d]	0.9934	0.9943	0.0906	1.3194	1.3174	0.1569
$y = 0.10$, $x = 0.05$[d]	1.0082	1.0089	0.0706	1.3186	1.3156	0.2252
$y = 0$, $x = 0.20$[e]	1.0193	1.0236	0.4244	1.3151	1.3139	0.0890
$y = 0.15$, $x = 0.10$[d]	1.0376	1.0383	0.0664	1.3165	1.3122	0.3248
$y = 0.15$, $x = 0.15$[d]	1.0479	1.0529	0.4849	1.3123	1.3105	0.1358
$y = 0.20$, $x = 0.15$[d]	1.0614	1.0676	0.5853	1.3102	1.3088	0.1069
$y = 0.20$, $x = 0.20$[d]	1.0769	1.0823	0.5002	1.3095	1.3071	0.1804
Average Absolute Relative Error			0.3186			0.2084

[a] Ref. [29]; [b] Ref. [30]; [c] Ref. [31]; [d] Ref. [32]; [e] Ref. [33].

Table 6.17 Experimental and predicted pseudocubic lattice constants for $(La_{1-x}Sr_x)(Ga_{1-y}Mg_y)O_{3-(x+y)/2}$.

Composition	$a_{pc(exptl)}$ (Å)	a_{pc} (Å) (Eq 1.19)	|Error%|	a'_{pc} (Å) (Eq 1.4)	|Error%|	a''_{pc} (Å) (Eq 1.5)	|Error%|
$y = 0$, $x = 0$[a]	3.8910	3.8832	0.2021	3.8882	0.0731	3.8825	0.2198
$y = 0$, $x = 0.05$[b]	3.8938	3.8916	0.0545	3.8917	0.0537	3.8918	0.0501
$y = 0$, $x = 0.076$[c]	3.8994	3.8960	0.0861	3.8934	0.1527	3.8965	0.0725
$y = 0.10$, $x = 0$[d]	3.8789	3.8801	0.0326	3.8625	0.4212	3.8808	0.0498
$y = 0.10$, $x = 0.05$[d]	3.8872	3.8882	0.0256	3.8654	0.5619	3.8894	0.0561
$y = 0$, $x = 0.20$[e]	3.9102	3.9163	0.1551	3.9008	0.2395	3.9177	0.1908
$y = 0.15$, $x = 0.10$[d]	3.8930	3.8940	0.0245	3.8542	0.9970	3.8956	0.0661
$y = 0.15$, $x = 0.15$[d]	3.8946	3.9016	0.1803	3.8563	0.9828	3.9031	0.2190
$y = 0.20$, $x = 0.15$[d]	3.8904	3.8989	0.2195	3.8419	1.2475	3.9003	0.2544
$y = 0.20$, $x = 0.20$[d]	3.8989	3.9063	0.1892	3.8435	1.4218	3.9071	0.2109
Average Absolute Relative Error			0.1170		0.6151		0.1389

[a] Ref. [29]; [b] Ref. [30]; [c] Ref. [31]; [d] Ref. [32]; [e] Ref. [33].

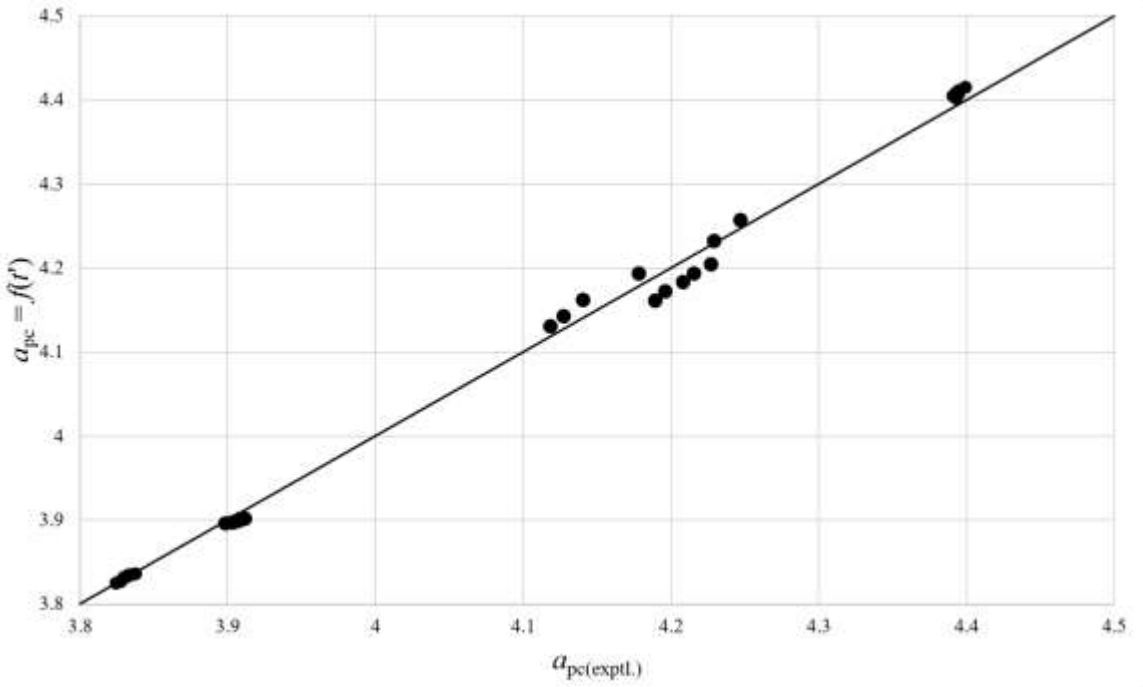

Figure 6.9 Experimental pseudocubic lattice constants, $a_{pc(exptl.)}$, versus the predicted pseudocubic lattice constants, a_{pc} (Eq. 1.19), for all 5 $A^{2+}B^{4+}_{1-x}B^{3+}_{x}O_{3-x/2}$ oxygen-deficient perovskite systems.

Fig. 6.9 shows the results of the predicted pseudocubic lattice constant, a_{pc}, by inserting the predicted t' from Eq. 6.13 into Eq. 1.19. It clearly shows that this modeling technique can accurately predict the pseudocubic lattice constants within a very wide range ($3.8246 \leq a_{pc} \leq 4.3990$). Although the models for r_V and D_B were derived using the data from all 7 oxygen-deficient perovskite systems analyzed in this work, it should be noted that the modeling technique can so far only be applied reliably to $A^{2+}B^{4+}_{1-x}B^{3+}_{x}O_{3-x/2}$ perovskites due to the fact that the predictive model for t' was developed using only those types of perovskite systems. Thus, the models developed in this work cannot be applied to any other type of perovskite system with any degree of certainty.

For this reason, the values for r_X and a_{pc} in tables 6.18-6.20 were calculated with Eq. 6.7 using $t'_{(exptl)}$ instead of calculating t' using Eq. 6.13. Tables 6.18-6.20 show the

results when this modeling technique is applied to $LaFeO_3$, $La_{0.9}Ca_{0.1}FeO_{3-\delta}$, $La_{0.9}Sr_{0.1}FeO_{3-\delta}$, and $La_{0.9}Ba_{0.1}FeO_{3-\delta}$ as produced by Beausoleil *et al*.[13] In particular, Table 6.18 shows the results when the model is applied to all four compositions where charge compensation is accounted for purely via oxygen vacancies. The results show that, while the error in a_{pc} might be acceptable, there are large errors in the predicted anion sizes, r_X. Table 6.19 shows the results assuming charge compensation purely by an increase in the iron oxidation state from Fe^{3+} to Fe^{4+}. In this case the errors in both a_{pc} and r_X look acceptable, but even better results can be obtained by allowing for both Fe^{3+} oxidation and oxygen vacancies as shown in Table 6.20. Indeed, the error in r_X for $La_{0.9}Ca_{0.1}FeO_{3-\delta}$, $La_{0.9}Sr_{0.1}FeO_{3-\delta}$, and $La_{0.9}Ba_{0.1}FeO_{3-\delta}$ can effectively be reduced to zero if there are some anion vacancies in addition to some Fe^{4+} present in each composition. The errors for pure $LaFeO_3$ can also be reduced to zero by allowing for a La^{3+} vacancy concentration of 0.2% and a charge-balancing amount of oxygen vacancies (0.1%).

Table 6.18 Experimental and predicted anion sizes and pseudocubic lattice constants for the lanthanum ferrites with charge compensation via oxygen vacancies alone.

Composition	[V_O]	$r_{X(exptl)}$ (Eq. 6.1)	r_X (Eq. 6.7)	|Error%|	$a_{pc(exptl)}$	a''_{pc} (Eq. 1.5)	Error%
$LaFeO_3$	0	1.3210	1.3207	0.0276	3.9321	3.9323	0.0045
$La_{0.9}Ca_{0.1}Fe^{3+}O_{2.95}$	0.017	1.3130	1.3307	1.3477	3.9159	3.9167	0.0203
$La_{0.9}Sr_{0.1}Fe^{3+}O_{2.95}$	0.017	1.3167	1.3342	1.3251	3.9235	3.9244	0.0232
$La_{0.9}Ba_{0.1}Fe^{3+}O_{2.95}$	0.017	1.3190	1.3363	1.3100	3.9281	3.9290	0.0250

Table 6.19 Experimental and predicted anion sizes and pseudocubic lattice constants for the lanthanum ferrites with charge compensation via Fe^{3+} oxidation alone.

Composition	[V_O]	$r_{X(exptl)}$ (Eq. 6.1)	r_X (Eq. 6.7)	|Error%|	$a_{pc(exptl)}$	a''_{pc} (Eq. 1.5)	Error%
$LaFeO_3$	0	1.3210	1.3207	0.0276	3.9321	3.9323	0.0045
$La_{0.9}Ca_{0.1}Fe^{3+}_{0.9}Fe^{4+}_{0.1}O_3$	0	1.3190	1.3185	0.0345	3.9159	3.9158	-0.0036
$La_{0.9}Sr_{0.1}Fe^{3+}_{0.9}Fe^{4+}_{0.1}O_3$	0	1.3227	1.3223	0.0363	3.9235	3.9235	0.0011
$La_{0.9}Ba_{0.1}Fe^{3+}_{0.9}Fe^{4+}_{0.1}O_3$	0	1.3250	1.3245	0.0375	3.9281	3.9282	0.0040

Table 6.20 Experimental and predicted anion size and pseudocubic lattice constant for the four lanthanum ferrites with the errors optimized using both oxygen vacancies and Fe^{4+} as charge compensating mechanisms.

Composition	[V_O]	$r_{X(exptl)}$ (Eq. 6.1)	r_X (Eq. 6.7)	|Error%|	$a_{pc(exptl)}$	a''_{pc} (Eq. 1.5)	Error%
$La_{0.998}FeO_{2.997}$	0.00033	1.3210	1.3207	0.0000	3.9321	3.9323	0.0050
$La_{0.9}Ca_{0.1}Fe^{3+}_{0.9024}Fe^{4+}_{0.0976}O_{2.9988}$	0.00041	1.3188	1.3188	0.0000	3.9159	3.9158	-0.0028
$La_{0.9}Sr_{0.1}Fe^{3+}_{0.9026}Fe^{4+}_{0.0974}O_{2.9987}$	0.00043	1.3226	1.3226	0.0000	3.9235	3.9235	0.0019
$La_{0.9}Ba_{0.1}Fe^{3+}_{0.9027}Fe^{4+}_{0.0973}O_{2.9986}$	0.00045	1.3249	1.3249	0.0000	3.9281	3.9282	0.0047

These results are in general agreement with the conclusions of Beausoleil *et al.*[13], who suggested that both oxygen vacancies and iron oxidation (to Fe^{4+}) occur in Sr- or Ba-doped lanthanum ferrites; however, where they found only iron oxidation in Ca-doped lanthanum ferrite, this model shows that there may also be a small concentration (~0.04%) of oxygen vacancies in this composition. Such a small concentration of vacancies would be difficult to detect via x-ray or neutron diffraction. Similarly, the very small concentration of A-site vacancies (0.2%) in $LaFeO_3$ would be difficult to demonstrate experimentally.

6.4 Conclusions

Eight compositions within the $CaTi_{1-x}Fe_xO_{3-x/2}$ system and eleven compositions within the $SrTi_{1-x}Fe_xO_{3-x/2}$ system were successfully synthesized, and their respective XRD patterns show that all compositions are single-phase. Data corresponding to compositions in five other homologous series were also analyzed, and system-specific models for r_V and D_B were developed for all seven series. Based upon these system-specific models, general models were developed which allow for the accurate prediction of the vacancy size and the bond deformation in oxygen-deficient perovskites. Furthermore, five system-specific models were developed which describe the modified tolerance factor, t', as a function of the ideal anion size, $r_{X(id)}$, in $A^{2+}B^{4+}_{1-x}B^{3+}_{x}O_{3-x/2}$ perovskites. A general model was then developed based upon these specific ones. Results also suggest that both oxygen vacancies and Fe^{3+} oxidation to Fe^{4+} occur in $La_{0.9}M_{0.1}FeO_{3-\delta}$ (M=Ca, Sr, Ba) and that La vacancies probably occur with oxygen vacancies in pure $LaFeO_3$. A major implication of this modeling technique is that it allows for the accurate prediction of the tolerance factor in

oxygen-deficient perovskites, which in turn allows for the accurate prediction of the effective anion size and pseudocubic lattice constants in oxygen-deficient perovskites.

6.5 References

[1] Miller V, Tidrow S. Perovskites: Temperature and coordination dependent ionic radii. Integrated Ferroelectrics. 2013;148:1-16.

[2] Feng X, Fan Y, Nomura N, Kikuchi K, Wang L, Jian W, Kawasaki A. Graphene promoted oxygen vacancies in perovskite for enhanced thermoelectric properties. Carbon. 2017;112:169-176.

[3] Scott JF, Dawber M. Oxygen-vacancy ordering as a fatigue mechanism in perovskite ferroelectrics. Appl Phys Lett. 2000;76(25):3801-3803.

[4] Eom K, Choi E, Choi M, Han S, Zhou H, Lee J. Oxygen vacancy linear clustering in a perovskite oxide. J Phys Chem Lett. 2017;8:3500-3505.

[5] Glinchuk M, Eliseev E, Li G, Zeng J, Kalinin S, Morozovska A. Ferroelectricity induced by oxygen vacancies in relaxors with perovskite structure. Phys Rev B. 2018;98:094102.

[6] Deng G, Li G, Ding A, Yin Q. Evidence for oxygen vacancy inducing spontaneous normal-relaxor transition in complex perovskite ferroelectrics. Appl Phys Lett. 2005;87:192905.

[7] Yu C, Scullin M, Huijben R, Ramesh R, Majamdar A. The incluence of oxygen deficiency on the thermoelectric properties of strontium titanate. Appl Phys Lett. 2008;92(9):092118.

[8] Liu G, Yang B, Liu B, Zhang C, Xiao S, Yuan Y, *et al*. Irreversible light-soaking effect of perovskite solar cells caused by light-induced oxygen vacancies in titanium oxide. Appl Phys Lett. 2017;111:153501.

[9] Kim C, Perry N, Bishop S, Tuller H. Electro-chemo-mechanical studies of perovskite-structured mixed ionic-electronic conducting $SrSn_{1-x}Fe_xO_{3-x/2+\delta}$ part II: Electrical conductivity and cathode performance. J Electroceram. 2018;40:57-64.

[10] Hao Z, Zeng R, Yuan L, Bing Q, Liu J, Xiang J, Huang Y. Perovskite $La_{0.6}Sr_{0.4}CoO_{3-\delta}$ as a new polysulfide immobilizer for high-energy lithium-sulfur batteries. Nano Energy 2017;40:360-368.

[11] Zhu J, Thomas A. Perovskite-type mixed oxides as catalytic material for NO removal. Appl Catal B: Environ. 2009;92:225-233.

[12] Kim CH, Ahn Y, Son JY. $SrTiO_3$ - Based Resistive Switching Memory Device with Graphene Nanoribbon Electrodes. J Am Ceram Soc 2016;99(1):9–11.

[13] Beausoleil G, Price P, Thomsen D, Punnoose A, Ubic R, Misture S, Butt D. Thermal expansion of alkaline-doped lanthanum ferrite near the Neel temperature. J Am Ceram Soc. 2014;97(1): 228-234.

[14] Ubic R. Revised method for the prediction of lattice constants in cubic and pseudocubic perovskites. J Am Ceram Soc. 2007;90(10):3326-3330.

[15] Enriquez E, Chen A, Harrell Z, Dowden P, Koskelo N, Roback J, *et al*. Oxygen Vacancy-Tuned Physical Properties in Perovskite Thin Films with Multiple B-site Valance States. Sci Rep 2017;7(1):46184.

[16] Schmidt M, Campbell SJ. In situ neutron diffraction study (300–1273 K) of non-stoichiometric strontium ferrite $SrFeO_x$. Phys Chem Solids 2002;63(11):2085–92.

[17] Wang Y, Chesnaud A, Bevillon E, Dezanneau G. Properties of Y-doped $BaSnO_3$ proton conductors. Solid State Ionics. 2012;214:45-55.

[18] Gu Y, Liu Z, Ouyang J, Zhou Y, Yan F. Synthesis, structure and electrical conductivity of $BaZr_{1-x}Dy_xO_{3-x/2}$ ceramics. Electrochemica Acta 2012;75:332-338.

[19] Xu H, Su Y, Balmer M, Navrotsky A. A new series of oxygen-deficient perovskites in the $NaTi_xNb_{1-x}O_{3-0.5x}$ system: Synthesis, crystal chemistry, and energetics. Chem Mater. 2003; 15:1872-1878.

[20] Takeuchi K, Loong C, Richardson J, Guan J, Dorris S, Balachandran U. The crystal structures and phase transitions in Y-doped $BaCeO_3$: their dependence on Y concentration and hydrogen doping. Solid State Ionics. 2000;138:63-77.

[21] Marrocchelli D, Perry N, Bishop S. Understanding chemical expansion in perovskite-structured oxides. Phys Chem Chem Phys. 2015;17:10028.

[22] Toby BH, Von Dreele RB. GSAS-II: the gensis of a modern open-source all purpose crystallography software package. J Appl Crystallography 2013;46(2):544-549.

[23] Howard C, Knight K, Kennedy B, Kisi E. The structural phase transitions in strontium zirconate revisited. J Phys: Condensed Matter. 2000;12:L677

[24] Woodward P, Cox D, Moshopoulou E, Sleight A, Morimoto S. Structural studies of charge disproportionation and magnetic order in $CaFeO_3$. Phys Rev B. 2000;62:844

[25] Takeda Y, Naka S, Takano M. Preparation and characterization of $CaFeO_3$ and its solid solution with $SrFeO_3$. Journal de Physique Colloques. 1979;40(C2):331-332.

[26] Shannon R. Revised effective ionic-radii and systematic studies of interatomic distances in halides and chalcogenides. Acta Crystallogr Sec A. 1976;32:751-767.

[27] Ubic R, Tolman K, Talley K, *et al*. Lattice-constant prediction and effect of vacancies in aliovalently doped perovskites. J Alloys Compd. 2015;644:982-995.

[28] Takani N, Yamane H. Structure analysis of $CaTi_{1-x}Sn_xO_3$ (x = 0.0-1.0) solid solutions. Powder Diffraction. 2014;29(3):254-259.

[29] Vasylechko L, Berkowski M, Matkovski A, Savytskii D, Fink-Finowicki J. Crystal structure of $La_{1-x}Nd_xGaO_3$ single crystals ($0<x<0.2$). Mater Res Bull. 2000;35:333-340.

[30] Rozumek M, Majewski P, Aldinger F. Metastable crystal structure of strontium and magnesium substituted $LaGaO_3$. J Am Ceram Soc. 2004;87:656-661.

[31] Lapina A, Li S, Bergman B, Zhao Z. Synthesis of $La_{0.9}Sr_{0.1}Ga_{0.8}Mg_{0.2}O_{2.85}$ powder by gel combustion route with two-step strategy. J Eur Ceram Soc. 2012;32:2325-2331.

[32] Datta P, Majewski P, Aldinger F. Structural studies of Sr- and Mg-doped $LaGaO_3$. J Alloy Compd. 2007;438:232-237.

[33] Kajitani M, Matsuda M, Hoshikawa A, Harjo S, Kamiyama T, Ishigaki T, *et al*. Doping effect on crystal structure and conduction property of fast oxide ion conductor $LaGaO_3$-based perovskite. J Phys Chem Solids. 2007;68:758-764.

CHAPTER SEVEN: CONCLUSIONS AND FUTURE WORK

7.1 Concluding Remarks

The correlative modeling techniques presented in this work significantly impact the electroceramics industry in that they allow for the accurate prediction of several structural distortions (*e.g.*, trigonal as well as those caused by layered A-site cation ordering, rock salt B-site cation ordering, and oxygen vacancies) in perovskite electroceramics. They can also be used in some cases to link structural aspects (*e.g*, trigonal distortion) to properties (*e.g.*, polarization). These models have the potential to save researchers significant amounts of time and save industry significant amounts of money developing new perovskite materials.

Chapter one described perovskites generally. It was observed that perovskites possess more functional properties than almost any other type of crystal structure due to the various structural distortions that can occur within the perovskite structure. Correlative models based on empirical evidence which can predict these various structural distortions are very powerful tools indeed, yet few models currently exist outside this work for perovskites with A-site cation ordering, B-site cation ordering, trigonality, or oxygen vacancies. This knowledge gap was filled by developing predictive models for each of these structural distortions based entirely on structural data from compositions produced in this work and from structural data mined from published scientific literature.

Chapter two investigated the effects of layered A-site ordering on the perovskite structure. The structural effect of A-site ordering was studied in the $(Na_yLi_{1-y})_{(1-}$

$_{3x)/2}La_{(1+x)/2}TiO_3$ (NLLT) system. 15 compositions in the NLLT system were synthesized using a conventional solid-state mixed-oxide method, and structural parameters were determined from X-ray diffraction patterns. X-ray diffraction shows evidence of long-range ordering at higher *x* values, but electron-diffraction shows that some degree of order exists for all compositions. It was observed that this ordering causes an increase in the unit cell volume as compared to the disordered state. A general model was developed which effectively accounts for this volume expansion, which allows for the accurate prediction of the degree of ordering in layered A-site ordered perovskite titanates using only published ionic radii data.

Chapter three explored the effects of 1:2 B-site ordering in the $BaMg_{1/3}Ta_{2/3}O_3$ (BMT) perovskite compound. BMT is first synthesized using a conventional solid-state mixed-oxide method in its disordered state, then subsequently annealed for up to 40 hours in order to gain insight into how the structure is distorting as the B-site is becoming more and more ordered. It was observed that as the degree of ordering increased, the unit cell volume decreased. It was also shown that the structure contracts within the ordering planes yet expands perpendicular to the ordering planes due to ionic demixing. A general model was developed for this volume shrinkage, which allows for the accurate prediction of the volume contraction resulting from 1:2 B-site ordering in BMT. It may even be possible to extend this model to predict the effects of 1:2 B-site ordering in general.

Chapter four further investigated the effects of B-site ordering in 1:1 rock salt B-site ordered perovskites. The rock salt B-site ordered $NdZn_{0.5}Ti_{0.5}O_3$, $SmZn_{0.5}Ti_{0.5}O_3$, $(Nd_{0.5}La_{0.5})(Zn_{0.5}Ti_{0.5})O_3$, and $(Nd_{0.5}Gd_{0.5})(Zn_{0.5}Ti_{0.5})O_3$ perovskites were synthesized using a conventional solid-state mixed-oxide route. Evidence of long-range range ordering

in all four compositions was shown via XRD. Additional data for rock salt B-site ordered structures was mined from literature, and system-specific models were initially developed for the B-site size adjustment factor, Δr_B. A general model was then developed for Δr_B which allows for the accurate prediction of the B-site ordering induced volume contraction in rock salt B-site ordered perovskites using only published ionic radii data. It may be possible to extend this model, in conjunction with the model for BMT, to predict this effect in 1:2 B-site ordered perovskites in general.

Chapter five proposed predictive models for the effects of trigonlity in perovskites and the polarization in trigonally distorted perovskites in space group *R*3*c*. Data was mined from scientific literature, and general models were developed based upon this data. The general models developed for perovskite trigonality successfully predicted the trigonal-to-cubic phase transition at room temperature, which means that it may be possible, with the use of additional correlative models, to extend these models to predict trigonal phase transitions which are temperature-dependent (*e.g.*, T_C). Additionally, a general model was developed for polarization in $A^{1+}B^{5+}O_3$, $A^{2+}B^{4+}O_3$, and $A^{3+}B^{3+}O_3$ perovskites; which allows for the accurate prediction of the intrinsic polarization in *R*3*c* trigonal perovskites using only the degree of trigonality, *c*/*a*.

Chapter six investigated the effect of oxygen vacancies on the perovskite structure. Eight $CaTi_{1-x}Fe_xO_{3-x/2}$ compositions and eleven $SrTi_{1-x}Fe_xO_{3-x/2}$ compositions were synthesized via a solid-state mixed-oxide method. Structural data for additional oxygen vacant perovskites were mined from literature. The effective oxygen vacancy size and the resultant bond deformation were modeled for each system. A general model was then developed for the modified tolerance factor, *t*′, which allows for the accurate prediction of

the tolerance factor in oxygen-deficient perovskites. In turn, this allows for the accurate prediction of the effective anion size and pseudocubic lattice constants in oxygen-deficient perovskites using only published ionic radii data.

7.2 Future Work

7.2.1 Extend empirical model for A-site vacancies to perovskites with $r_A < 1.34$ Å (Ca^{2+})

The proposed system for this study is $(Ca_{1-y}Mg_y)_{1-3x}La_{2x}TiO_3$ ($0 \leq x \leq ⅓$, $0 < y \leq 1$) because $MgTiO_3$ forms in the ilmenite structure. Thus, doping $Ca_{1-3x}La_{2x}TiO_3$ with Mg^{2+} should effectively reduce r_A until the perovskite structure destabilizes. An alternative could be $MgSiO_3$, which is a perovskite, but there may be difficulties with eliminating amorphous phases during synthesis.

7.2.2 Extend all models with thermal variations

All of the empirical models derived in this work use characterization data that was collected at room temperature and ambient pressure. Ionic sizes will likely change significantly with temperature, but the degree of that change is not yet known for the systems analyzed in this work. So, it is necessary to first develop empirical models which describe the relationship between ionic size and temperature by determining the bond lengths from neutron or X-ray diffraction experiments. It may then be possible to extend the empirical models in this work to predict meaningful phase-transition temperatures such as the ferroelectric T_C.

7.2.3 Develop an empirical model for simultaneous A- and B-site ordering

This work focuses on developing empirical models for A- and B-site ordering separately. However, it is desirable to have a single model that can account for both A- and B-site ordering. The proposed systems for this study are $Na_{0.5}Ln_{0.5}Mg_{0.5}W_{0.5}O_3$ and $K_{0.5}Ln_{0.5}Mg_{0.5}W_{0.5}O_3$ (Ln = La, Nd, Sm, Eu, Gd, Tb, Dy, Ho, Er) because these systems contain simultaneous layered ordering between the Na^+, K^+ and Ln^{3+} cations on the A-site and rock salt ordering between the Mg^{2+} and W^{6+} cations on the B-site.

7.2.4 Develop a correlative model for simultaneous vacancies on both A and X

A model for oxygen vacancies was developed in this work; however, it is desirable to produce an empirical model that accounts for both A-site and X-site vacancies. The proposed system for this study is $((Ca,Sr,Ba)_xLa_{1-xy})FeO_{3+x-3xy/2}$, ($0 \leq x \leq 1$, $1 \leq y \leq 1/x$) because A- and O-vacancies can be simultaneously engineered into the structure. Theoretically, 50% A-site and 33% oxygen vacancies can be achieved in this system, but an increase in iron valence from Fe^{3+} to Fe^{4+} may be possible at higher x and y values. Thus, X-ray photoelectron spectroscopy (XPS) should be performed to verify the valence state of the iron atoms. It should also be noted that at $x = 0$ or $y = 1$ only oxygen vacancies will be produced. Also, the same $[V_O]$ or $[V_A]$ may be achieved by using different compositions with different tolerance factors.

7.2.5 Extend B-site ordering model to include 1:2 and 1:3 B-site ordered perovskites

A general correlative model was developed for 1:1 rock salt B-site ordering and a model was developed for 1:2 B-site ordered $BaMg_{1/3}Ta_{2/3}O_3$ in this work. However, it would be useful to develop a general model for 1:2 and 1:3 B-site ordered perovskites as well. The proposed method for this study is a data mining approach due to the large quantity of published structural data that currently exists for these types of perovskites. This could potentially allow for the development of a single general empirical model which encompasses 1:1, 1:2, and 1:3 B-site ordered perovskites.